Structural Relationships within Bismuth-containing Ternary Metal Oxide Systems

by

Christopher David Ling

A thesis submitted for the degree of Doctor of Philosophy

of

The Australian National University

March 1999

Declaration

The work presented in this thesis is the original work of the candidate, with the exception of Section 4.2 and the Appendix, which were carried out in collaboration with Dr Ray L. Withers.

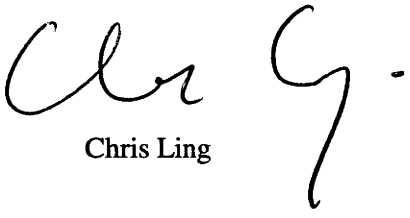

Chris Ling

Acknowledgements

The author is extremely grateful for the advice and assistance over the last few years of his supervisors Dr Ray Withers, Dr John Thompson and Dr Siegbert Schmid. Many thanks also for the help of Dr Philip Reynolds and Dr Richard Welberry in their capacity as advisors, and Professor A. David Rae for advice on crystallographic matters.

The author also gratefully acknowledges: the assistance of Dr David J. Cookson at the Australian National Beamline Facility in collection of synchrotron XRD data; Ms Zhongli Li of the Electronic Materials Engineering group at the Research School of Physical Sciences and Engineering, Australian National University, for collecting DTA data; Mr Frank Brink of the Electron Microscope Unit at the ANU for assistance in EDXA data processing; Dr Ron Smith at ISIS for assistance with collection of time-of-flight neutron powder diffraction data; Dr Shane Kennedy of the Australian Nuclear Science and Technology Organisation for assistance in collecting of constant-wavelength neutron powder diffraction data; and Dr Shunji Kishimoto and Professor Nobuo Ishizawa for assistance in collection of single-crystal synchrotron X-ray data.

Gratitude for financial assistance is due to: the Australian Synchrotron Radiation Program; the Ministry of Education (Japan) Grant-in-Aid for International Scientific Research; the Access to Major Research Facilities Program; the Australian Institute for Nuclear Science and Engineering; the Society for Crystallographers in Australia; the Australian Postgraduate Award scheme; and the Research School of Chemistry at the ANU.

Table of Contents

List of Figures

List of Tables

Abstract

Bismuth-rich phases in the Bi_2O_3-M_2O_x (M = Nb, Ta, V, W, Mo) systems are investigated using synchrotron X-ray powder diffraction and electron diffraction to resolve outstanding problems concerning phase relationships, unit cells and symmetry. Single-phase powder specimens are prepared for most phases and a temperature-composition phase diagram presented for the Bi_2O_3-Nb_2O_5 system. A modulated structure approach is applied to the characterisation of phases, based on a fluorite-type δ-Bi_2O_3-related parent structure, and space groups or superspace groups assigned. The most appropriate description (superstructure or incommensurate modulation) for the structure of each phase is discussed.

The crystal structure of each phase is considered and the most probable model proposed on the basis of all available data from the present as well as previous studies, including X-ray powder diffraction, electron diffraction, high-resolution transmission electron microscopy, neutron powder diffraction data and single crystal X-ray diffraction. Some structural models are tested against observed data, and some are fully refined. The structures vary both in their absolute configurations and in their relationships (strong, weak or non-existent) to an archetypal fluorite-type δ-Bi_2O_3-related parent structure.

A crystal-chemical scheme is proposed, unifying key features of the various structures in terms of their relationships to fluorite-type δ-Bi_2O_3. The scheme is based on the incorporation of pyrochlore-type structural motifs (such as strings of M atoms along $<1\ 1\ 0>_f$ directions) into an underlying fluorite-type average structure. The orientations of these M atom strings and the way they interact are driven by the competing requirements of overall charge-balance (a function of mol% M_2O_x) and local coordination environment (a function of the element M) within the flexible fluorite-type oxygen atom array. These interactions inter-relate the oxygen atom array, the metal atom array, and composition. As the composition moves further from Bi_2O_3, the interactions force the abandonment of the pyrochlore-type structural motif, and hence any meaningful relationship to a fluorite-type δ-Bi_2O_3-related parent structure is lost. The descriptive and predictive utilities of this crystal-chemical scheme are discussed.

Chapter 1

Introduction

The study of phase relationships and crystal structures in ternary metal oxide systems containing heavy metals provides serious challenges to test the knowledge and skills of solid state inorganic chemists and crystallographers.

Chemical challenges stem from the complex phase diagrams found in such systems, where often only subtle distinctions exist between adjacent phases. They may involve homologous series of line phases, solid solution fields or both. Identifying the compositions of line phases and the extent of solid solutions using X-ray powder diffraction requires great care due to the dominant contribution to X-ray patterns made by the metal atom array.

Crystallographic challenges are exacerbated by these synthetic chemical difficulties. The ability to definitively solve and refine the crystal structures of ternary metal oxides usually depends on whether it is possible to grow single crystals. Solving structures *ab initio* from powder diffraction data is, in most cases, an impossible or at least intractable problem even with the highest resolution synchrotron X-ray and time-of-flight neutron data available. Even with single crystal X-ray diffraction data, problems with correction for absorption and secondary extinction, weak scattering by the oxygen atoms, pseudo-symmetry, twinning and disorder can often foil attempts at solving and refining structures.

It is only by meeting these challenges and maximizing the amount of reliable crystallographic information about such phases that the crystal-chemical principles underlying ternary metal oxide systems containing heavy metals can be determined.

The ternary metal oxide systems described in this study are the Bi_2O_3-rich ends of the pseudo-binary systems Bi_2O_3-Nb_2O_5, Bi_2O_3-Ta_2O_5, Bi_2O_3-V_2O_5, Bi_2O_3-WO_3 and Bi_2O_3-MoO_3. These systems exemplify the challenges stated above. The dominant heavy metal atom, bismuth, is the highest atomic number non-radioactive element. An initial literature survey (Chapter 3) reveals that while a large amount of work has been done in these systems, it is to a large extent neither mutually consistent nor definitive. Very few single crystals have been obtained, and there are serious difficulties associated with synthesising single-phase powder samples, such that the most comprehensive studies have been carried out using transmission electron microscopy to study individual crystallites. The challenges of the present study are therefore twofold; synthetic (to document these phases definitively and obtain sufficiently

high quality samples for the best crystallographic data to be obtained) and crystallographic (to determine their structures as accurately and precisely as possible given that data).

Interest in these particular systems stems from the high-temperature form of bismuth oxide, δ-Bi_2O_3, one of the best solid-state oxygen ion conductors known (1, 2). Bismuth oxide is strongly polymorphic (α-, β-, γ- and δ- forms are known) (3) and pure δ-Bi_2O_3 cannot be quenched to room temperature. However, certain transition metal oxides (in particular those listed above), when added to Bi_2O_3 as the minor component, are known to form phases which often preserve a structure related to that of δ-Bi_2O_3 and retain much of its anionic conduction properties. This study therefore focuses on δ-Bi_2O_3-related phases found at the bismuth-rich ends of the respective phase diagrams.

The structure of δ-Bi_2O_3 itself is not unambiguous. To a first approximation, it has a face-centred cubic (fcc) structure akin to that of fluorite (CaF_2) with an average oxygen occupancy of 75 % (3) (Figure 1). The metal atoms thus form an fcc cation array with the oxygen atoms (at the 75 % level) occupying the tetrahedral sites therein. The oxygen vacancies in this model are supposed to account for its ionic conduction properties. More sophisticated oxygen vacancy ordering models have also been proposed and tested by the refinement of neutron powder diffraction data (4), but no definitive, fully ordered structure has yet been established. Battle *et al.* (5) have refined a disordered variant of this model, in which 43 % of the oxygen atoms move ~ 1 Å from the exact tetrahedral site along $<1\ 1\ 1>_f$ directions.

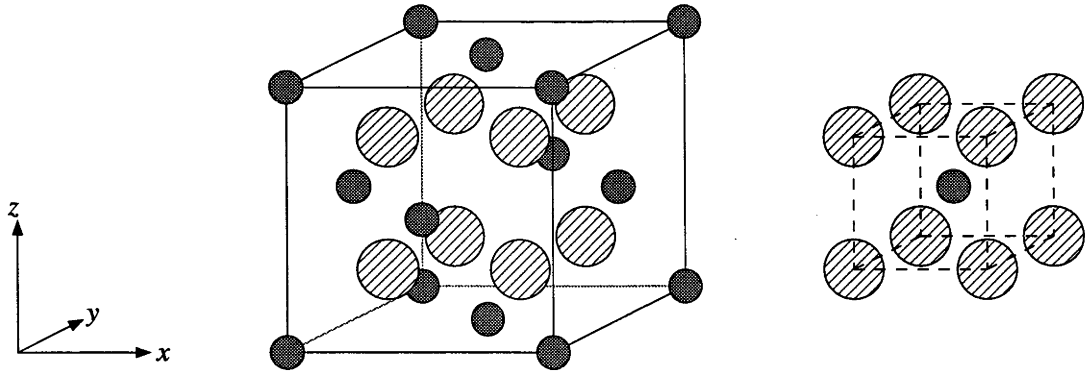

Figure 1. The average fluorite-type structure of δ-Bi_2O_3 (Fm3m, a = 5.6595(4) Å) showing the average cubic coordination environment (dashed lines) of bismuth atoms (dark grey). Oxygen sites (striped) are 75 % occupied.

The disordered average coordination environment of bismuth atoms within this fluorite-type model for δ-Bi_2O_3 (cubic, with 75 % occupancy of each site) (Figure 1), and its oxygen ion conductivity, imply that the actual local coordination environments of bismuth atoms must be highly variable. This flexibility in the oxygen atom array means that when considering the relationships to fluorite-type of individual phases in this study, it is most appropriate to consider the metal atom array before the oxygen atom array.

X-ray diffraction and transmission electron microscopy, techniques most sensitive to the metal atom array, often appear to indicate that the phases with which this study is concerned do form modulated variants of a fluorite-type δ-Bi_2O_3 structure. This implies that the structures should be characterised most succinctly by an underlying fluorite-type δ-Bi_2O_3-related average structure plus compositional and/or displacive modulations thereof. One of two central questions that this study seeks to answer is to what extent each phase can be meaningfully described as a modulated variant of δ-Bi_2O_3. The observation of satellite reflections in addition to the strong Bragg reflections of an underlying δ-Bi_2O_3-related average structure (or at least fcc cation array) usually indicate the presence of metal atom compositional ordering. Whether, and to what extent, this is accompanied by oxygen vacancy ordering and displacive relaxation of the remaining oxygen atoms is the other central question of this study.

This second question will have a strong bearing on the level of detail to which the structures can be determined by diffraction methods. If the oxygen atoms are fully ordered, and useful single crystals can be grown, it ought to be possible to obtain a complete structural solution from standard crystallographic methods in which the coordination environment of each atom is chemically plausible. If the oxygen atoms are fully disordered then an average fluorite-type array should satisfactorily fit the diffraction data. If, however, the oxygen atoms are only partially ordered, then determining chemically and crystallographically satisfactory structural solutions will be extremely difficult.

The highly polymorphic nature of bismuth oxide itself, in conjunction with the ability of small proportions of transition metal atoms to influence the structure type adopted, clearly indicates that these δ-Bi_2O_3-related structures are the result of a delicate balance of competing crystal chemical interactions. The structure type adopted by a given phase will be a function of the interaction between the ability of Bi^{3+} to adopt a variety of coordination environments, and the tendency of the transition metal cations to adopt more rigidly defined octahedral or tetrahedral coordination environments. In order to understand these phases it will be necessary to understand the relationship between the concentration of the transition metal atoms and the structure types adopted; this relationship, and the interactions that govern it, may be played out within the context of a unifying crystal chemical scheme.

Such a unifying crystal chemical scheme might well be based upon the incorporation of pyrochlore-type structural motifs into an underlying fluorite-type average structure, following the use by Zhou *et al.* (15) of a pyrochlore-type structural motif in modelling some of these phases. (The pyrochlore-type structure, ideal stoichiometry $A_2B_2O_7$, can be described as a 2 x 2 x 2 metal atom ordered fluorite-type superstructure phase (78).) In these models, transition metal atoms condense in tetrahedra of nearest-neighbour metal atoms within the fcc fluorite-type metal atom array. When the transition metal atoms prefer octahedral

coordination environments, an ordered pattern of fluorite-type oxygen vacancies follows this metal atom compositional ordering pattern (Figure 2*(a)*), creating a tetrahedron of (somewhat distorted) octahedra (Figure 2*(b)*). Oxygen atom displacements from fluorite-type positions obviously follow, in order to satisfy chemical bonding requirements. In pyrochlore-type itself, these tetrahedral metal atom clusters (Figure 2*(c)*) are infinitely corner-connected as shown in Figure 2*(d)*. A scheme built around this motif could therefore provide a framework within which to model metal atom compositional ordering, and subsequently oxygen vacancy ordering and oxygen atom displacements, from a fluorite-type δ-Bi_2O_3 archetype.

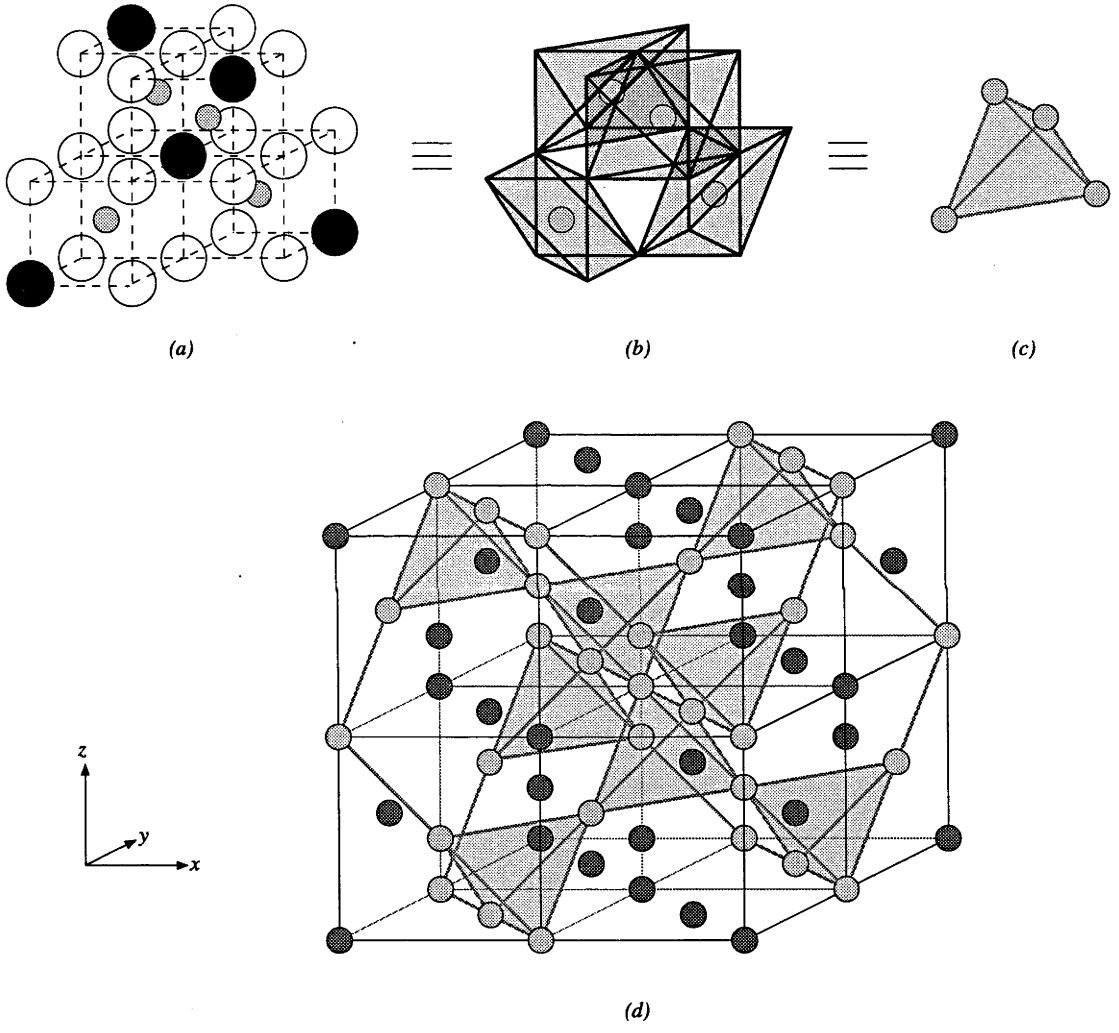

Figure 2. Scheme for the incorporation of a pyrochlore-type structural motif into a fluorite-type average structure. (a) The arrangement of vacancies (black) within the fluorite-type oxygen lattice (white) surrounding a tetrahedron of transition metal atoms (light grey). This reduces the cubic coordination of metal atoms in fluorite-type (dashed lines) to octahedral coordination (b) (oxygen atom displacive relaxations are not shown). These tetrahedral clusters (c) are then infinitely corner-connected in pyrochlore-type itself (d).

These 'tetrahedra of octahedra' are in fact only one of several structural motifs which can be identified in pyrochlore-type, any of which could form the basis of the a crystal-chemical scheme incorporating pyrochlore-type structural motifs into a fluorite-type average structure. Figure 3*(a)* shows the B_2O_6 array in pyrochlore-type, from which a variety of structural motifs can be drawn, including isolated BO_6 octahedra (Figure 3*(b)*), B_4O_{18}

tetrahedra of BO_6 octahedra (Figure 3*(c)*) and B_nO_{5n+1} strings of n corner-connected BO_6 octahedra (Figure 3*(d)*). Potential crystal chemical schemes based on all such motifs will be considered as supporting structural evidence is accumulated during this study.

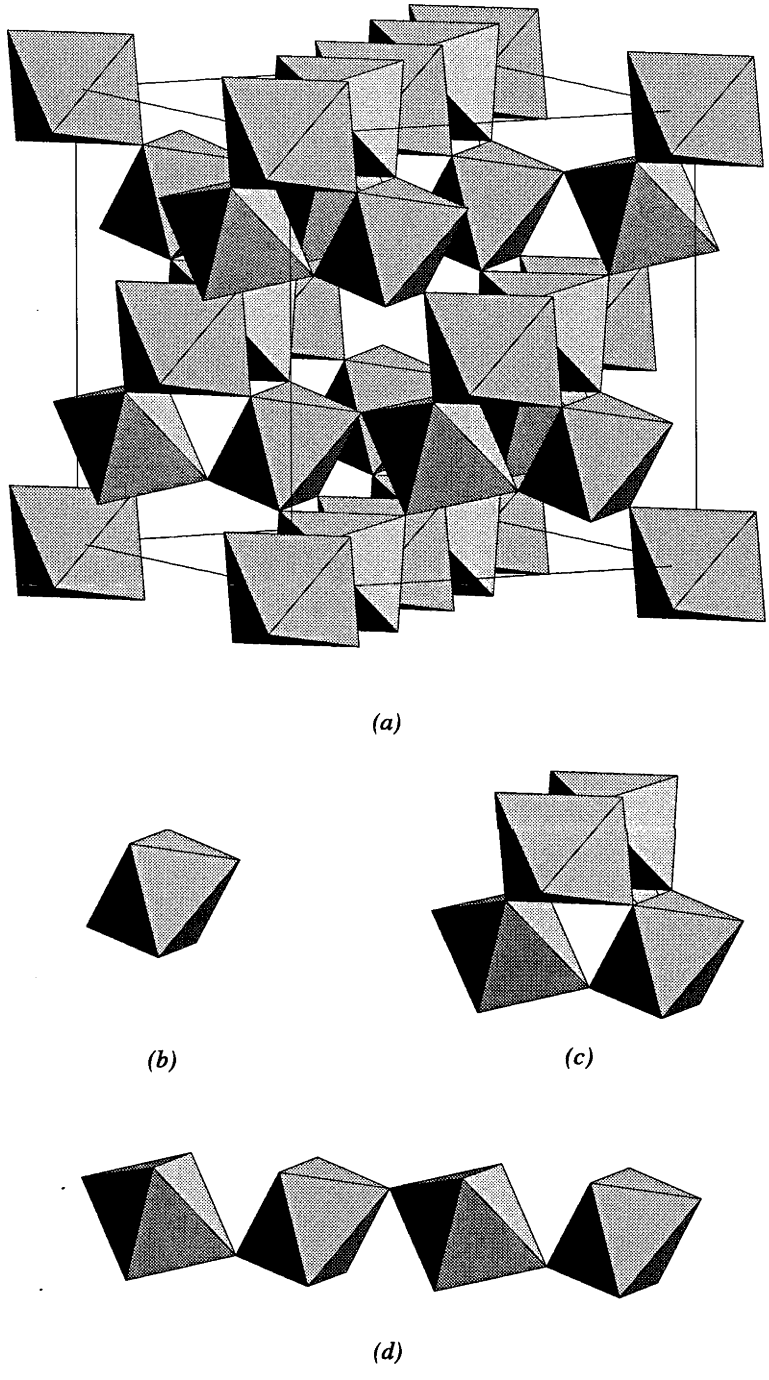

Figure 3. (a) The B_2O_6 array in ideal pyrochlore-type $A_2B_2O_7$, and some of the structural motifs that can be drawn from it; (b) isolated BO_6 octahedra, (c) B_4O_{18} tetrahedra of BO_6 octahedra and (d) B_nO_{5n+1} strings of n corner-connected BO_6 octahedra.

The ultimate aim of this study is to arrive at an understanding of the crystal chemistry of δ-Bi_2O_3-related phases containing small amounts of certain transition metal oxides. This is to be brought within reach by: reviewing previously studied ternary oxide systems, in order to confirm or establish phase relationships, unit cells and modulation types; solving as many

crystal structures as possible within these systems, either completely or partially; determining some general underlying structural principles of these solved phases; and considering the probable structures of the remaining phases on the basis of these principles.

The structure of the thesis itself, following the above outline, reflects the fact that the bulk of the work was published or in press prior to the thesis being submitted for examination. The text and structure of the papers have, however, been adapted to provide continuity and amplified to include later research results, or results which were inappropriate for inclusion in a self-contained paper. Chapter 2 introduces the experimental and analytical techniques and equipment used throughout, including the chemistry described in Chapter 3 and the crystallography described in Chapter 4. This has allowed a consistent style and notation to be used throughout Chapters 3 and 4, which are principally derived from self-contained papers originally prepared in a variety of journal formats. Chapter 5 unifies the chemical and crystallographic work in order to arrive at an understanding of the structural principles of the phases investigated, and the concluding Chapter 6 considers the understanding thereby gained of their crystal chemistry.

Chapter 2

Experimental and Analytical Techniques

2.1 Synthesis

The ternary metal oxides synthesised during this research were all prepared from their component oxides (Bi_2O_3 Koch-Light 99.998 %, Nb_2O_5 Koch-Light 99.9 %, Ta_2O_5 Aldrich 99.99 %, WO_3 Koch-Light 99.9 %, MoO_3 Halewood 99.999 %, V_2O_5 Cerac 99.9 %) by solid-state reaction using platinum vessels. Details of individual syntheses (polycrystalline powder or single crystal growth) are included in Chapters 3 and 4 adjacent to the results and discussion for each.

2.2 Differential Thermal Analysis

Differential thermal analysis (DTA) was used in this study to obtain data points for the construction of phase diagrams from the relatively small (< 100 mg) samples available. DTA experiments were performed in a Shimadzu DTA-50 instrument using a 20 mg sample in an alumina crucible with a platinum lid. A 20 mg sample of alumina was used in the second crucible. Dry argon was used to purge the system of oxygen for 20 min prior to heating and flowed through the furnace chamber at 50 ml/min throughout the heating cycle. The sample was heated to 100 °C above the liquidus at 20 °C/min and allowed to cool at the same rate.

2.3 Scanning Electron Microscopy

Energy dispersive X-ray analyses (EDXA) were used to compare the compositions of individual crystallites in powders, and of different regions of individual larger crystals. It was thereby possible to confirm that the composition at which a particular sample was synthesised corresponded to the composition of the crystalline regions producing diffraction data. EDXA was carried out in a JEOL 6400 scanning electron microscope (SEM) equipped with a Link ATW detector, at 15 kV and 1 nA with data processed using the Link ISIS system. ZAF corrections were made using the SEM-QUANT software package.

2.4 X-ray Powder Diffraction

X-ray powder diffraction (XRD) was the principal means of phase identification in this study. Comparison of conventional XRD data from samples synthesised at different compositions and temperatures was used to identify line phases, solid-solutions and two-phase regions within the phase diagrams studied.

XRD was also used in the accurate determination of unit cell parameters and, in some cases, for Rietveld-refinement of metal atom parameters. For these purposes it was necessary to collect extremely high-resolution data (using a synchrotron source) in order to observe splitting of diffraction peaks associated with small distortions from 90 ° angles, as observed in many of these phases as a consequence of pseudo-symmetry.

Conventional source XRD data were collected on film using Cu $K\alpha$ radiation ($\lambda = 1.54059$ Å) and a Jungner XDC-700 Guinier-Hägg camera. Synchrotron XRD data were collected on Beam Line 20B at the Photon Factory in Tsukuba, Japan. Each pattern was collected across three image plates at a wavelength of 1.4986 (4) Å, from $2\theta \sim 5$ to 125 °. Si (NBS # 640) was used as an internal standard in both cases.

2.5 Electron Diffraction

For many of the large unit cell, low-symmetry phases found in this study, unit cell determination and indexation was only possible using electron diffraction (ED) in conjunction with XRD data. While the resolution of ED is not as high as XRD, the fact that a consecutive series of electron diffraction patterns (DPs) can be obtained from different orientations of the same crystallite means that an internally consistent set of unit cell dimensions is more easily obtained.

ED analyses were carried out using JEOL 100CX and Philips EM 430 transmission electron microscopes (TEMs) operating at 100 and 300 kV respectively. DPs were collected on film.

2.6 Single-Crystal X-ray Diffraction

Single-crystal X-ray diffraction was used in this study to determine the crystal structure of one phase, and provided useful insight into the symmetry of others. The difficulties experienced in obtaining large (untwinned) single crystals, and the high absorption coefficients of the heavy metals involved, necessitated the collection of data from very small crystals using an intense synchrotron source.

Single-crystal X-ray diffraction data were collected on Beam Line 14A at the Photon Factory in Tsukuba, Japan. Experimental details are summarised in Table 10.

2.7 Neutron Powder Diffraction

Neutron powder diffraction data were used in conjunction with XRD data in the Rietveld-refinement of some of the phases studied. The greater relative contribution of oxygen atoms to neutron diffraction intensities (compared with their contribution to XRD intensities) allowed the modelling and refining of oxygen atom parameters as well as those of metal atoms.

Medium resolution neutron powder diffraction data were collected on POLARIS (6), the high flux, medium resolution time-of-flight (TOF) instrument at ISIS (Rutherford Appleton Laboratories, UK). Specimens were mounted in a vanadium can and data collected on three resolution-focussed banks using ^{3}He gas (at 35 ° and 145 °) and ZnS scintillation (at 90 °) counters.

High resolution TOF neutron powder diffraction data were collected on the high-resolution powder diffractometer (HRPD) at the same facility (7). Specimens were mounted in a vanadium can and data collected on a ^{6}Li-doped glass scintillation counter (at 90 °) over two overlapping TOF ranges, 30 - 130 and 100 - 200 ms.

2.8 Bond Valence Calculations

Empirical calculations of bond valence sums were made using the bond length-bond valence formulation of Brown and Altermatt (76) as a test of the chemical plausibility of refined structures. This approach is based on the assumption that the valence V of an atom i is the sum of the valences v_{ij} between it and all other atoms j, *i.e.* $\Sigma_j v_{ij} = V_i$. An empirical equation is then used to relate bond valences v_{ij} to bond distances d_{ij}, that of Brown and Altermatt being $v_{ij} = \exp[(R_{ij} - d_{ij})/0.37]$.

Calculations were made using the bond valence parameters R_{ij} of Brese and O'Keefe (52) in the program EUTAX (77), with maximum bond distances of 3.5 Å.

Chapter 3

A Review of Bismuth-Rich Phases in the Systems Bi_2O_3-Nb_2O_5, Bi_2O_3-Ta_2O_5, Bi_2O_3-WO_3, Bi_2O_3-MoO_3 and Bi_2O_3-V_2O_5 (8)

3.1 Literature Survey

The Bi_2O_3-rich ends of binary oxide phase diagrams involving a range of transition metal oxides have previously been investigated on several levels. Studies using XRD as the principal means of phase identification have been carried out in many systems. This approach generally identified sillenite-related phases (ideal stoichiometry $Bi_{12}SiO_{20}$) (9) at very low transition metal oxide concentration (below ~ 5 mol%) succeeded by a series of solid solution fields of pseudo-fcc, fluorite-related phases (up to ~ 30 mol%). Higher concentrations led to non-fluorite-related structures such as the $SbNbO_4$-type (10) α-$BiTaO_4$ and α-$BiNbO_4$, the (perovskite related) Aurivillius phases Bi_2WO_6 and γ-Bi_2MoO_6 (11) and the Aurivillius-related $Bi_2VO_{5.5}$ (12). Despite similarities in phase behaviour between different transition metal oxides, sufficient differences have been observed to indicate that more complex mechanisms are involved than simple substitution of transition metal atoms for bismuth atoms.

These subtleties were more clearly elucidated by a series of TEM studies in the Bi_2O_3-MoO_3 (13), Bi_2O_3-WO_3 (14), Bi_2O_3-Nb_2O_5 (15-20), Bi_2O_3-Ta_2O_5 (19, 21) and Bi_2O_3-V_2O_5 (22- 24) systems. In the TEM approach, the ability of ED to detect weak features of reciprocal space often missed by conventional powder diffraction methods is used to identify the modulations by which the average fluorite-type substructure is distorted, and to index reciprocal space in terms of fluorite-type superstructures. A greater number of discrete phases were thereby identified as possessing characteristic superstructures than had previously been identified by XRD. Furthermore, image contrast between metal atom sites in high-resolution TEM (HRTEM) images was used to propose models for the superstructures in real space. The observed HRTEM image contrast suggested in many cases a close relationship to the *A/B* metal atom ordering pattern characteristic of pyrochlore-type $A_2B_2O_7$ phases (25) (Figure 2). As oxygen atoms were unresolved by HRTEM, the oxygen atom vacancies were usually modelled such that the substituting metal atoms (Nb, Ta, Mo, W, V) were

octahedrally coordinated as for the *B* atoms in $A_2B_2O_7$ pyrochlore oxides. Oxygen atoms coordinated only by Bi^{3+} were considered to remain in average fluorite-type positions.

The final class of experiment carried out in these systems has been single-crystal X-ray diffraction. To date, there have been very few actual single-crystal structure refinements. The average structure of Bi_3NbO_7 has been refined as being of fluorite-type (26), precession photography has been used to derive a cation ordering model for $Bi_{14}W_2O_{27}$ (27), a single-crystal structure refinement has been published for $Bi_{26}Mo_{10}O_{69}$ (28), a cation ordering scheme related to one proposed on the basis of TEM work has been refined for $Bi_{12}V_2O_{23}$ (29) and an independent study (30) determined possible space groups from a single crystal of $Bi_{12}V_2O_{23}$.

The most studied of these systems is Bi_2O_3-Nb_2O_5. The volume of work published does not, however, appear to have resulted in consensus; it has in fact highlighted some ambiguities and uncertainties, as a critical review of the literature shows. Published phase diagrams (31, 32) describe two solid-solution phases (approximately 0-20 and 20-23 mol% Nb_2O_5) and one line phase (37.5 mol% Nb_2O_5) between Bi_2O_3 and $BiNbO_4$. Subsequent ED studies (15-20) showed that the solid solutions described oversimplified the system, and suggested the existence of at least four distinct structure types in this composition range. Type I was reported to exist between $Bi_{19}NbO_{31}$ and Bi_9NbO_{16} (15), but to predominate at $Bi_{15}NbO_{25}$. Type II was variously reported to exist between Bi_9NbO_{16} and Bi_3NbO_7 (15), $Bi_{24}Nb_2O_{41}$ and $Bi_8Nb_2O_{17}$ (16), or $Bi_{19}NbO_{31}$ and $Bi_{23}Nb_7O_{52}$ (18). An independent ED study (48) reported a composition range 11.2-26.6 mol% Nb_2O_5. Type III was reported to exist around 30 mol% Nb_2O_5 (with a disordered variant around 32 mol% Nb_2O_5), although EDXA analysis (in the TEM) by the same authors suggested a composition closer to 25 mol% Nb_2O_5 (*i.e.* Bi_3NbO_7) (16). A single-crystal X-ray study (26), however, found a cubic phase (presumably type II) at the latter composition. Type IV, in accordance with the earlier XRD work, was found to occur at 37.5 mol% Nb_2O_5 (*i.e.* $Bi_5Nb_3O_{15}$) (19, 20).

In general, inconsistencies within the published work on the Bi_2O_3-rich end of the Bi_2O_3-Nb_2O_5 system are linked to inconsistencies between phase characterisation on the macroscopic (starting materials, XRD) and microscopic (ED, EDXA) scales. Phases characterised by TEM need not originate from a homogeneous sample, and although their compositions may be determined *in situ* by EDXA doubts will persist as to their exact compositions in bulk specimens. A pivotal aspect of the present study is therefore the requirement that results obtained by XRD (which provide structural and phase information on bulk specimens) are completely consistent with ED results (which provide structural and phase information from individual microcrystals within a specimen).

Given that most known phases at the Bi_2O_3-rich ends of the Bi_2O_3-Nb_2O_5, Bi_2O_3-Ta_2O_5, Bi_2O_3-WO_3, Bi_2O_3-MoO_3 and Bi_2O_3-V_2O_5 systems were initially characterised

by TEM alone, the present work aims to review critically the results of previous studies on these systems, drawing together the information obtained using disparate techniques. There follows a reinvestigation of these systems involving synthesis, characterisation using a combination of XRD and ED and redescription of the various phases using a modulated structure approach. It is felt that the modulated structure approach allows more concise descriptions of some of the very large line-phase superstructures reported, as well as providing insight into how the solid-solution structures accommodate the range of compositions in each case.

3.2 Experimental

3.2.1 Synthesis

Preliminary synthetic experiments carried out in the Bi_2O_3-Nb_2O_5 system using platinum crucibles as reaction vessels yielded inconsistent results. Single-phase bulk samples were elusive despite regrinding and annealing of reagents, and the unit cell dimensions of solid-solution phases were not reproducible. Quantitative EDXA analyses (using $BiNbO_4$ as a standard) of samples indicated significantly higher Nb_2O_5 content than expected based on the starting ratio of reagents, *e.g.* starting materials with 14.3 mol% Nb_2O_5 heated to 1323 K for 3 days formed material analysing at 16.7 mol% Nb_2O_5, and starting materials at 16.7 mol% Nb_2O_5 heated to 1173 K for 2 days formed products analysing at 23.0 mol% Nb_2O_5. This indicated that the open system in which the reaction was taking place was allowing the uncontrolled loss of Bi_2O_3 through volatilisation. The use of open reaction systems in earlier studies may explain some of the confusion concerning compositions of bulk specimens, *e.g.* the type III phase reportedly synthesised at 30 mol% Nb_2O_5 but determined by EDXA to be 25 mol% Nb_2O_5 (16).

In order to achieve homogeneous, single-phase material, it was therefore necessary to limit the loss of starting materials through volatilisation (in particular of Bi_2O_3) and reduction (in particular of V_2O_5). A simple and effective way of achieving this was to seal the reactants in platinum tubing (silica vessels being impractical due to the possible formation of sillenite, $Bi_{12}SiO_{20}$). Although this limited the quantity of material reacted at any one time to hundreds of milligrams, sufficient material for analysis could easily be produced. In addition, to ensure complete mixing of components without opening the sealed vessels for regrinding, samples were subjected to an initial annealing at 1103 K (just above the melting point of Bi_2O_3, 1098 K) in an open platinum vessel for 0.5 hours before being reground and sealed in platinum tubing.

Binary System (+ Bi_2O_3)	Minor Oxide (Mol %)	Final Annealing Temp (K)	Final Annealing Time (h)	Phases Identified by XRD	Comments
Nb_2O_5	1.00	1073	48	β-Bi_2O_3, S	
	1.96	1173	120	S, (II)	
	4.76	1098	144	(S), II	
	4.76	1173	120	(S), II	
	6.25	1173	120	II	type I nominal composition : II ss
	6.25	1273	120	(S), II	type II end-member unstable at 1000 °C
	7.69	1093	24	II	type II ss
	9.09	1093	24	II	type II ss
	10.00	1093	96	II	type II ss
	11.11	1093	24	II	type II ss
	15.00	1093	96	II	type II ss
	16.67	1173	48	II	type II ss
	20.00	1093	96	II	type II ss
	22.22	1173	48	II	type II ss
	23.53	1173	48	II, III	
	25.00	1173	96	III	type III nominal composition
	28.57	1173	96	III, (IV)	
	36.36	1173	24	(III), IV	
	37.50	1173	240	IV	type IV nominal composition
	37.50	1273	96	IV	type IV nominal composition
	37.50	1343	120	III, H-$BiNbO_4$	type IV unstable at 1050 °C
	40.00	1173	24	IV, (L-$BiNbO_4$)	
Ta_2O_5	6.25	1098	72	I	type I nominal composition
	19.53	1173	360	II	type II nominal ss composition
	19.53	1273	72	(I), II	type II unstable at 1000 °C
	30.00	1173	192	II*	type II* nominal composition
	30.00	1273	72	(II), II*	type II* unstable at 1000 °C
	33.33	1173	192	III	type III nominal composition
	33.33	1273	72	(II*), III	type III unstable at 1000 °C
	35.42	1273	168	IV	type IV nominal composition
	37.50	1173	144	III, L-$BiTaO_4$	type IV not formed at 900 °C
	37.50	1273	144	IV, (H-$BiTaO_4$)	
W_2O_6	6.67	1103	192	Ia	type Ia nominal composition
	12.50	1173	192	Ib	type Ib nominal composition
	14.81	1073	48	Ib	type Ib ss : II nominal composition
	14.81	1173	168	Ib	type Ib ss : II nominal composition
	15.38	1173	192	Ib	type Ib ss
	16.00	1173	168	Ib	type Ib ss
	16.67	1098	120	Ib, II	
	18.19	1173	192	II, (Bi_2WO_6)	

Binary System (+ Bi_2O_3)	Minor Oxide (Mol %)	Final Annealing Temp (K)	Final Annealing Time (h)	Phases Identified by XRD	Comments
Mo_2O_6	6.67	1073	168	Ia	type Ia nominal composition
	12.50	1173	96	38:7	38:7 highly disordered ss
	14.29	1173	96	38:7	38:7 partially disordered ss
	15.55	1113	168	38:7	38:7 nominal composition
	16.66	1173	96	38:7, (26:10)	
	25.00	1113	168	(38:7), 26:10	
	27.78	1173	168	26:10	26:10 nominal composition
V_2O_5	7.41	1173	168	β-Bi_2O_3, I	type I nominal composition
	10.00	1173	168	(β-Bi_2O_3), I	
	12.50	1173	168	I	type IIe nominal composition
	12.50	1093	168	variant on I	type IIe nominal composition
	13.89	1093	192	(I), IIa	type IId nominal composition
	14.81	1093	192	IIa	type IIa/b/c nominal compositions
	20.37	1093	192	(IIa), ?	type IIf nominal composition

Table 1. Selective summary of syntheses carried out in this study. Parenthesised phases have a trace presence. 'S' indicates sillenite-related phases, '38:7' and '26:10' represent $Bi_{38}Mo_7O_{78}$ and $Bi_{26}Mo_{10}O_{69}$ respectively, and '?' represents a highly disordered phase.

In studies of the systems Bi_2O_3-Nb_2O_5, Bi_2O_3-Ta_2O_5, Bi_2O_3-WO_3, Bi_2O_3-MoO_3 and Bi_2O_3-V_2O_5, homogeneous samples of discrete line-phases and representatives of solid-solution phases reported in the literature were synthesised in quantities sufficient for XRD analysis. The results of previous XRD and ED / EDXA studies were used to suggest ratios of starting materials for syntheses. A summary of key syntheses is presented in Table 1. Note that in order to ensure consistency, compositions are always formulated in terms of mol% M_2O_x (*i.e.* W_2O_6 and Mo_2O_6 instead of WO_3 and MoO_3). The results of syntheses excluded from Table 1 were consistent with those included, but redundant in terms of the conclusions drawn (*e.g.* additional syntheses in two-phase regions).

3.2.2 Characterisation

Identification of phases during synthetic work was based on XRD films collected using a Guinier-Hägg camera. This method allowed collection of patterns from very small amounts of reaction products (< 1 mg), easy comparison of patterns by overlaying films and visual identification of extremely weak satellite reflections. The necessity to measure line spacings manually and estimate intensities, however, made it a less attractive method for indexing the complex patterns that arise from large supercells.

Indexing of patterns was carried out using ED in conjunction with conventional XRD, while accurate refinement of unit cell dimensions was for the most part carried out from synchrotron XRD. The General Structure Analysis System (GSAS) (34) was used for this purpose, by fitting a model in which metal atoms of the substructure, fluorite-type δ-Bi_2O_3,

were placed into the supercell. As the strongest lines in most patterns correspond to the substructure dominated by metal atom scattering, this approach provided confirmation that the relationships to fluorite-type subcells were correct. The sensitivity of ED to weak features in reciprocal space was used to ensure that all satellite reflections had been detected. Misindexing may otherwise easily occur when a large unit cell is used to index XRD reflections.

3.3 Phase Relationships

3.3.1 Bi_2O_3–Nb_2O_5

A partial temperature-composition phase diagram of the system was prepared from the results in the system Bi_2O_3-Nb_2O_5 (Figure 4). Data for the temperature axis were obtained from DTA. This phase diagram deviates from the findings of the previous ED studies significantly. At the Bi_2O_3-rich end, a type I phase was not observed; rather, a sillenite-related phase of composition $Bi_{12}Nb_{0.29}O_{18.7+x}$ (35) was found to be responsible for ED patterns qualitatively identical to those reported for type I (body-centered cubic). It became clear that this Bi_2O_3-rich phase was not δ-Bi_2O_3-related when the unit cell dimension was refined from XRD data as a = 10.048(1) Å, too small for a $2\mathbf{a}_f$, $2\mathbf{b}_f$, $2\mathbf{c}_f$ supercell of fluorite-type δ-Bi_2O_3 (a = 5.6595(4) Å) as had previously been suggested for type I (15).

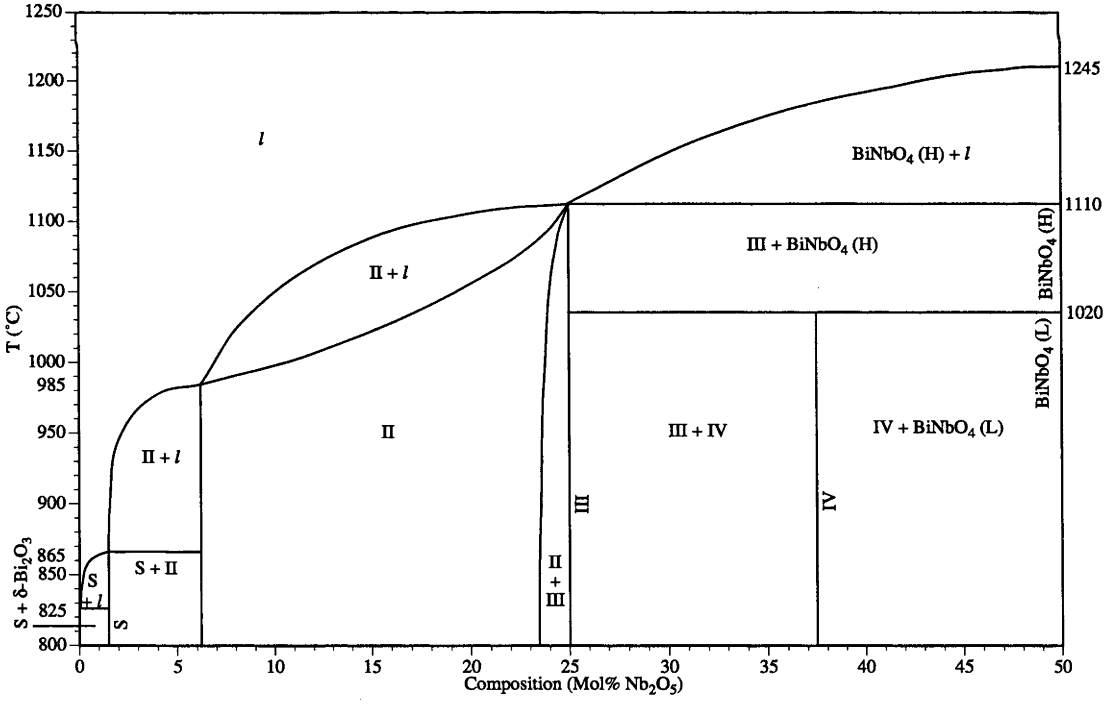

Figure 4. Partial phase diagram of the Bi_2O_3-Nb_2O_5 system. 'S' is a sillenite-type phase, 'L' and 'H' are the low- and high- temperature forms of $BiNbO_4$, respectively.

The Bi_2O_3-rich end member of the type II solid-solution was found to be $Bi_{15}NbO_{25}$. A plot of the underlying fluorite subcell dimension of the type II phase as a function of

composition showed an approximately linear relationship, in agreement with Vegard's law, (Figure 5) from $Bi_{15}NbO_{25}$ up to a narrow two phase region with type III, consistent with type II being a solid solution. Quantitative EDXA analyses of specimens within the type II + type III two-phase region gave end-member compositions of 23.4(4) and 25.5(2) mol% Nb_2O_5 respectively, using $BiNbO_4$ as a standard.

Syntheses spanning the composition 25 mol% Nb_2O_5 confirmed that type III is a line phase of composition very close to Bi_3NbO_7; previous syntheses with contradictory results (16) presumably suffered from loss of Bi_2O_3 and therefore arrived at more Nb_2O_5-rich compositions (30 mol%). Type IV was also found to be a line phase ($Bi_5Nb_3O_{15}$) with an upper temperature limit of stability; in this study, above the transition temperature between the high- and low-temperature modifications of $BiNbO_4$ (1020 °C) (10), type IV was found to unmix into type III and $BiNbO_4$ (H) (36).

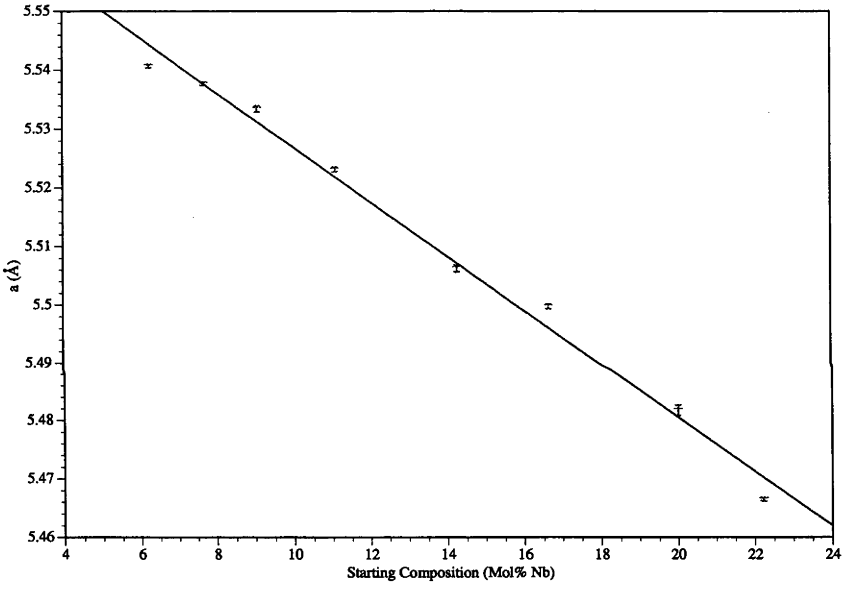

Figure 5. Vegard's law behaviour of the type II solid-solution phase in the Bi_2O_3-Nb_2O_5 system.

3.3.2 Bi_2O_3–Ta_2O_5

Four line phases were found between Bi_2O_3 and $BiTaO_4$, at $Bi_{15}TaO_{25}$, $Bi_7Ta_3O_{18}$, $Bi_4Ta_2O_{11}$ and $Bi_{31}Ta_{17}O_{89}$, and a solid-solution between Bi_9TaO_{16} and Bi_3TaO_7. The only published phase diagram in this system (31) focussed on the extremely Bi_2O_3-rich region, dominated by a sillenite-related solid-solution phase, and does not discuss the additional phases at higher mol% Ta_2O_5.

Previous ED studies (19, 21) described these additional phases as δ-Bi_2O_3-related, labelling them types I ($Bi_{15}TaO_{25}$), II (Bi_9TaO_{16} to Bi_3TaO_7), II* ($Bi_7Ta_3O_{18}$), III ($Bi_4Ta_2O_{11}$) and IV ($Bi_{31}Ta_{17}O_{89}$). Type III was reported as metastable (19). The synthetic regime used in

this study, however, allowed preparation of single-phase powder specimens of this phase as well as of types I, II, II* and IV.

3.3.3 Bi_2O_3–WO_3

Three phases were observed between Bi_2O_3 and Bi_2WO_6. In addition to a γ-Bi_2O_3-related solid-solution at compositions close to Bi_2O_3, a line phase was observed at $Bi_{14}WO_{24}$, a solid-solution phase between $Bi_{42}W_8O_{87}$ and $Bi_{30}W_4O_{57}$ and a line phase at approximately $Bi_{38}W_8O_{73}$. The latter was not obtained as a single-phase specimen, but was observed by XRD in a two-phase mixture with trace amounts of the solid-solution phase for the synthesis at 16.67 mol% W_2O_6 and with trace amounts of Bi_2WO_6 at 18.19 mol% W_2O_6.

The most recent published phase diagram of this system (37) reports line phases at $Bi_{12}WO_{21}$ and Bi_4WO_9, most likely corresponding to the line phases observed (at similar compositions) in this study. A solid-solution is reported, centered on Bi_6WO_{12}, with a subsequent investigation (27) placing its range between 11.90 and 15.15 mol% W_2O_6 in reasonable agreement with our results. Recent ED work (14) describes types Ia ($Bi_{14}WO_{24}$), Ib ($Bi_{24}W_2O_{33}$-Bi_6WO_{12}) and II (Bi_6WO_{12}-$Bi_{18}W_4O_{39}$). Type Ia clearly corresponds to the phase observed in this study at the same composition, and type Ib to the solid-solution phase. The higher Bi_2O_3 content previously reported for the solid-solution range may again be due to the use of open vessels and subsequent Bi_2O_3 loss. The reported composition range of type II encompasses (at the Bi_2O_3-rich end) the phase observed in this study at approximately 17.5 mol% W_2O_6, which appears to correspond to type II according to ED results discussed below. It should be noted that a structural model for type II proposed in the ED study has composition $Bi_{46}W_8O_{93}$, which falls within the type Ib solid-solution range observed in the present study.

3.3.4 Bi_2O_3–MoO_3

Three line phases were observed between Bi_2O_3 and Bi_2MoO_6, at $Bi_{14}MoO_{24}$, $Bi_{38}Mo_7O_{78}$ and $Bi_{26}Mo_{10}O_{69}$. Between 14.29 and 15.56 mol% Mo_2O_6 (*i.e.* $Bi_{38}Mo_7O_{78}$), reaction kinetics were found to be sufficiently slow that well crystallised material could not be obtained, however, below 14.29 mol% Mo_2O_6 a clear two-phase region with $Bi_{14}MoO_{24}$ was observed as expected. The presence of three phases is in agreement with the most recent XRD-based phase diagram of this system (33), which reported line phases $Bi_{14}MoO_{24}$, Bi_6MoO_{12} and $Bi_6Mo_2O_{15}$. The first of these has been neither indexed nor investigated by ED, however, its composition and XRD pattern suggest a close relationship to the type Ia phase in the Bi_2O_3–WO_3 system. A single-crystal X-ray structure of $Bi_{26}Mo_{10}O_{69}$ has recently been published (28). $Bi_{38}Mo_7O_{78}$ has been reported as a line phase in an ED study (13).

3.3.5 Bi_2O_3–V_2O_5

This was by far the most complex system investigated. The large number of studies concerning $Bi_2VO_{5.5}$ (12, 38, 39) give some indication of the difficulties involved. In particular, it appears that variability in the oxidation state of V adds a degree of freedom to the whole system (38). No phase diagrams are available covering the region Bi_2O_3-$Bi_2VO_{5.5}$, although a number of phases have been reported based on XRD studies (40-42). ED studies (23, 24) describe a plethora of δ-Bi_2O_3-related phases; types I ($Bi_{50}V_4O_{85}$), IIa ($Bi_{46}V_8O_{89}$), IIb ($Bi_{46}V_8O_{89}$), IIc ($Bi_{46}V_8O_{89}$), IId ($Bi_{31}V_5O_{59}$), IIe (Bi_7VO_{13}) and IIf ($Bi_{43}V_{11}O_{92}$). A further reported phase, $Bi_{17}V_3O_{33}$, has been obtained *via* hydrothermal synthesis (22).

It is possible that the different reported phases at the same composition represent different net oxidation states of V in the crystallites examined by TEM. By carrying out syntheses for this study in sealed Pt tubes, it proved possible to obtain single-phase powder samples of Bi_7VO_{13} and $Bi_{12}V_2O_{23}$, equated by ED with the reported types I and IIa respectively. At higher V_2O_5 content, a range of phases were observed reminiscent of the previous ED studies, possibly due to redox disproportionation processes. An approximately single-phase powder was obtained at $Bi_8V_2O_{17}$, however, it was too poorly ordered crystallographically to identify with a specific reported phase. More exotic synthetic methods are probably needed to control reduction in this system sufficiently for a complete study, as suggested by the recent study of Pang *et al.* (22) in which hydrothermal and solid-state synthetic routes produced completely different phases at approximately the same composition.

3.4 Reciprocal Space Characterisation

3.4.1 Electron Diffraction

3.4.1.1 Bi_2O_3–Nb_2O_5

Integer indexation of the reciprocal lattice of the type II solid-solution phase (Figure 6) requires six basis vectors given by $\mathbf{M}^* = \mathbf{a}_f^*$, $\mathbf{b}_f^*$, $\mathbf{c}_f^*$, $\varepsilon\mathbf{a}_f^*$, $\varepsilon\mathbf{b}_f^*$ and $\varepsilon\mathbf{c}_f^*$ respectively, where the subscript (f) refers to the fluorite-type substructure and $\varepsilon \sim 0.37$ (43, 44). Any Bragg reflection $\mathbf{H}$ can therefore be written in the form $\mathbf{H} = h\mathbf{a}_f^* + k\mathbf{b}_f^* + l\mathbf{c}_f^* + m\varepsilon\mathbf{a}_f^* + n\varepsilon\mathbf{b}_f^* + p\varepsilon\mathbf{c}_f^* = [h\,k\,l\,m\,n\,p]^*$ with h, k, l, m, n and p all integers. The structure at any particular composition within the solid solution is thus a three-dimensional incommensurately modulated structure characterised by a six-dimensional superspace group symmetry (44, 45). There are very few other known examples of three-dimensional incommensurately modulated structures (46, 47).

The observed characteristic extinction conditions $F([h\,k\,l\,m\,n\,p]^*) = 0$ unless $h + k$, $k + l$, $h + l$, $m + n$, $n + p$, $m + p$ are all even and $F(<h\,k\,0\,m\,n\,0>^*) = 0$ unless $m + n = 4J$, J an

integer (Figure 6*(d)*), in conjunction with the overall *m*3*m* Laue symmetry of reciprocal space, imply a six-dimensional superspace group symmetry $P{:}Fm\bar{3}m{:}Fd\bar{3}m$ (in the notation of Yamamoto (47)). The first *F* in this superspace group symbol implies that the allowed Bragg reflections, $\mathbf{G}_f = h\mathbf{a}_f^* + k\mathbf{b}_f^* + l\mathbf{c}_f^*$, of the underlying fluorite-type substructure obey fcc extinction rules. The second *F* implies that the allowed satellite reflections decorating these allowed substructure reflections also obey fcc extinction rules (Figure 6*(c), (d)*). The first allowed, or 'primary', modulation wave-vectors are thus of the form $\mathbf{q}_i = \varepsilon\langle 1\ 1\ 1\rangle^*$. Note that the most intense satellite reflections (Figure 6) are invariably first order harmonic (*i.e.* of the form $\mathbf{G}_f \pm \mathbf{q}_i$) and decay rapidly with increasing harmonic order. A characteristic diamond-like pattern of image contrast in $\langle 1\ 1\ 0\rangle_f$ HRTEM images of this phase (15) clearly shows that the incommensurate satellite reflections are associated with metal atom compositional ordering.

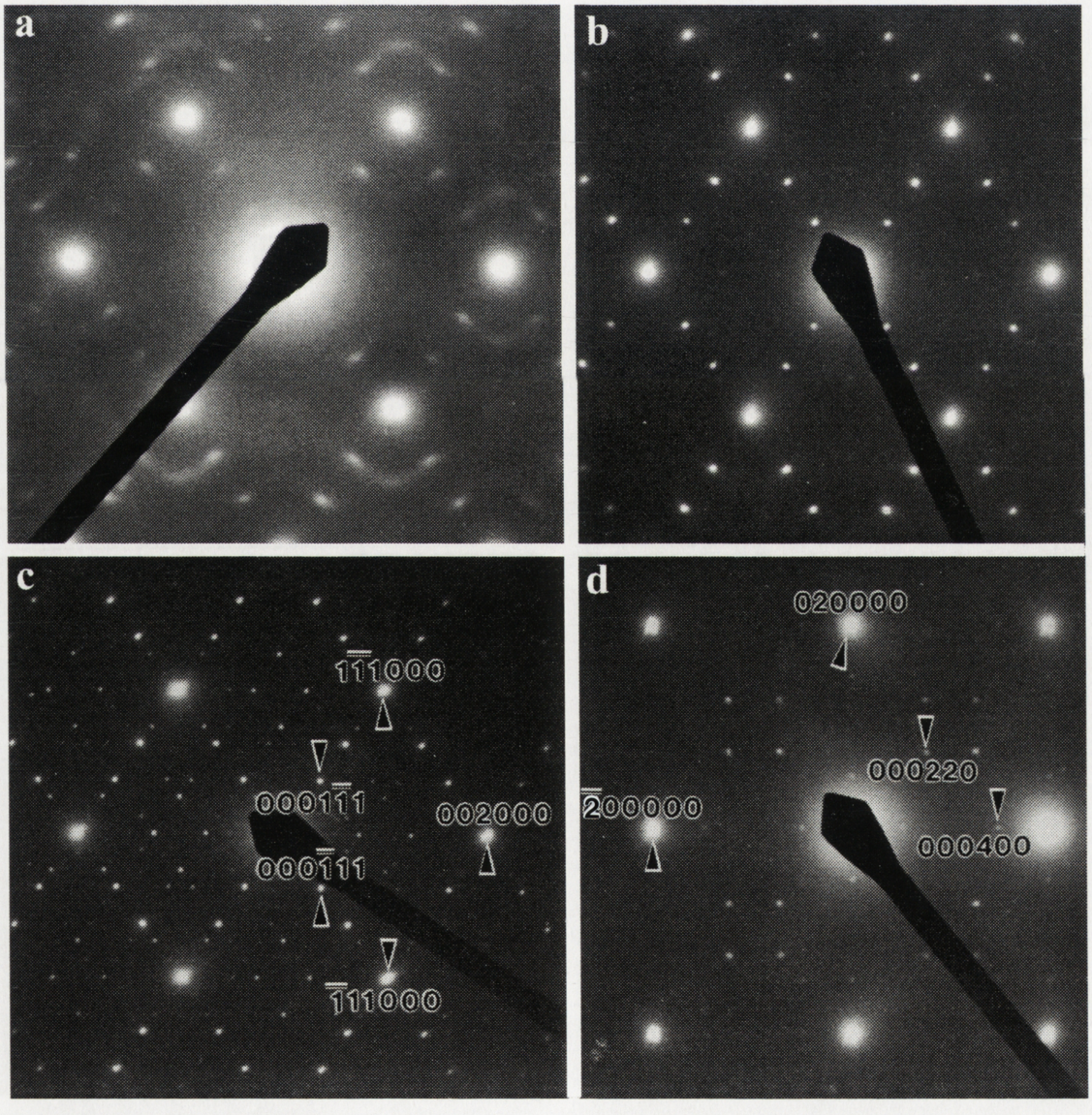

Figure 6. $\langle 1\ 1\ 0\rangle_f$ zone axis DPs of the type II phase in the Bi_2O_3-Nb_2O_5 system at compositions $Bi_{15}NbO_{25}$ (a), $Bi_{17}Nb_3O_{33}$ (b) and $Bi_8Nb_2O_{17}$ (c). (d) $\langle 0\ 0\ 1\rangle_f$ zone axis of $Bi_{17}Nb_3O_{33}$ showing extinctions due to a d-hyperglide in superspace.

The *d*-hyperglide superspace symmetry operations of the form $\{x_1, x_2, -x_3, x_4 + \frac{1}{4}, x_5 + \frac{1}{4}, -x_6\}$ (responsible for the $F(<h\ k\ 0\ m\ n\ 0>^*) = 0$ unless $m + n = 4J$ extinction condition) provides an important constraint on the form of the compositional and displacive Atomic Modulation Functions (AMFs), which describe the deviation of the actual crystal structure at any particular composition from its underlying fluorite-type substructure (44, 46, 47). For an example of how such a hyperglide symmetry operation constrains the form of the corresponding AMFs see Withers *et al.* (46).

Careful measurement of DPs such as those of Figure 6 suggests that the magnitude of ε increases smoothly and monotonically with composition across the whole composition range, from 6.25 to 23.4 mol% Nb_2O_5. Miida and Tanaka (48) reported that ε increased smoothly and monotonically for $0.13 \leq x \leq 0.24$, but was nearly constant outside this range. The intensity of the primary $\mathbf{G}_f \pm \mathbf{q}_i$ satellite reflections, as well as the anharmonic character of the modulated structure (*i.e.* the visibility of higher order harmonic satellite reflections), also appear to increase smoothly and monotonically across the whole composition range (Figure 6*(a-c)*). Note also the disorder evident in the diffuse streaking accompanying the primary $\mathbf{G}_f \pm \mathbf{q}_i$ satellite reflections at low Nb_2O_5 content (Figure 6*(a)*).

Previous authors (15, 18) have used image simulation techniques at high Nb_2O_5 content and DP simulation at low Nb_2O_5 content to propose plausible commensurate (superstructure) models based on idealised cubic $8\mathbf{a}_f$, $8\mathbf{b}_f$, $8\mathbf{c}_f$ ($Bi_8Nb_2O_{17}$) or $11\mathbf{a}_f$, $11\mathbf{b}_f$, $11\mathbf{c}_f$ (Bi_9NbO_{16}, $Bi_{17}Nb_3O_{33}$) supercells of fluorite-type δ-Bi_2O_3. It is important to realise, however, that compositions at which ε apparently coincides with rational fractions such as $\frac{3}{8}$ or $\frac{4}{11}$ do not imply that ε has 'locked in' to a commensurate value. The real test of commensurability is rather whether or not all possible higher order harmonic satellite reflections can be observed, *i.e.* whether there is 'overlap' or interaction between modulated intensity arising from independent subcell reflections (44). In the current case, this would necessitate observation of at least fourth-order harmonics of $\mathbf{q}_i$ (when $\varepsilon = \frac{3}{8}$). In fact, only a maximum of third order satellite reflections are ever actually observed in DPs (Figure 6*(c)*), even fewer in XRD data (Figure 14). These structures are effectively incommensurate regardless of the apparent value of ε.

While the type II phase is clearly an incommensurate, 'infinitely adaptive' solid solution, it is interesting to note that the disordered fluorite-type to pyrochlore-type ($A_2B_2O_7$) transformation involving coupled *A*/*B* metal atom compositional and oxygen vacancy ordering (49), on which structural models for this type II phase have been based (15, 18), can be described by the same three-dimensional modulation and six-dimensional superspace group but with ε genuinely 'locked in' at $\varepsilon = \frac{1}{2}$.

<1 1 0>, <1 0 0> and [0 0 1] zone axis DPs characteristic of the tetragonal type III line phase Bi_3NbO_7 are shown indexed with respect to an $\mathbf{a} = 3\mathbf{a}_f$, $\mathbf{b} = 3\mathbf{b}_f$, $\mathbf{c} = 7\mathbf{c}_f$ supercell of

fluorite-type in Figure 7*(a)*, *(c)* and *(d)* respectively. Similar, but unindexed, selected area DPs have been published previously (16). This 3 x 3 x 7 cell is clearly *F*-centered with a most probable space group symmetry of *F*4/*mmm*. As pointed out by Zhou *et al.* (16), the standard setting for this space group is *I*4/*mmm* with $\mathbf{a}' = \frac{3}{2}(\mathbf{a}_f - \mathbf{b}_f)$, $\mathbf{b}' = \frac{3}{2}(\mathbf{a}_f + \mathbf{b}_f)$, $\mathbf{c}' = 7\mathbf{c}_f$.

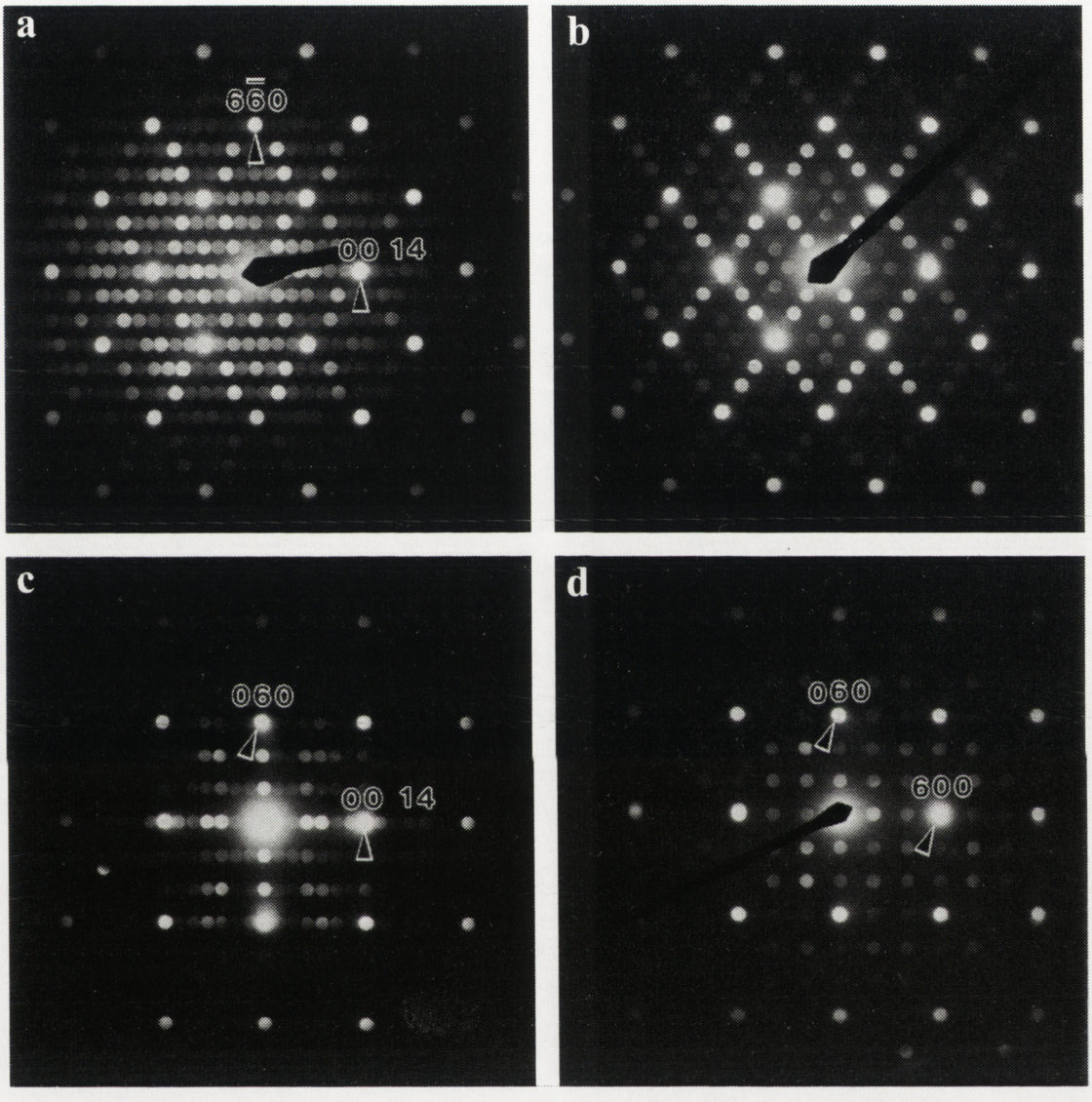

Figure 7. (a) <1 1 0>$_f$, (c) <1 0 0>$_f$ and (d) [0 0 1]$_f$ zone axis DPs of the type III phase in the Bi_2O_3-Nb_2O_5 system. (b) Shows a <1 1 0>$_f$ zone axis DP of the type II phase at the composition $Bi_8Nb_2O_{17}$.

The non-standard setting for type III is used in order to emphasise the close relationship of type III to Nb_2O_5-rich type II, as shown by a comparison of the <1 1 0> zone axis DP of type II at 20 mol% Nb_2O_5 (Figure 7*(b)*) with the corresponding [1 1 0] zone axis DP of type III (Figure 7*(a)*). The reciprocal lattices of both phases are characterised by a very similar hierarchical intensity distribution. The only obvious distinction is that the $\mathbf{q}_i \sim 0.38\langle 1\ 1\ 1\rangle^* = \langle 0.38\ 0.38\ 0.38\rangle^*$ 'primary' modulation wave-vectors of type II have rotated slightly and 'locked in' to $\langle \frac{1}{3}\ \frac{1}{3}\ \frac{3}{7}\rangle^*$ positions in the case of (tetragonal) type III (*cf.* Figure 7*(a) vs.* Figure 7*(b)*). An orientationally variable primary modulation wave-vector has

recently also been reported in the case of the sulfosalt mineral sartorite (50). It seems clear that a successful structure refinement of type III would necessarily provide great insight into the nature of type II.

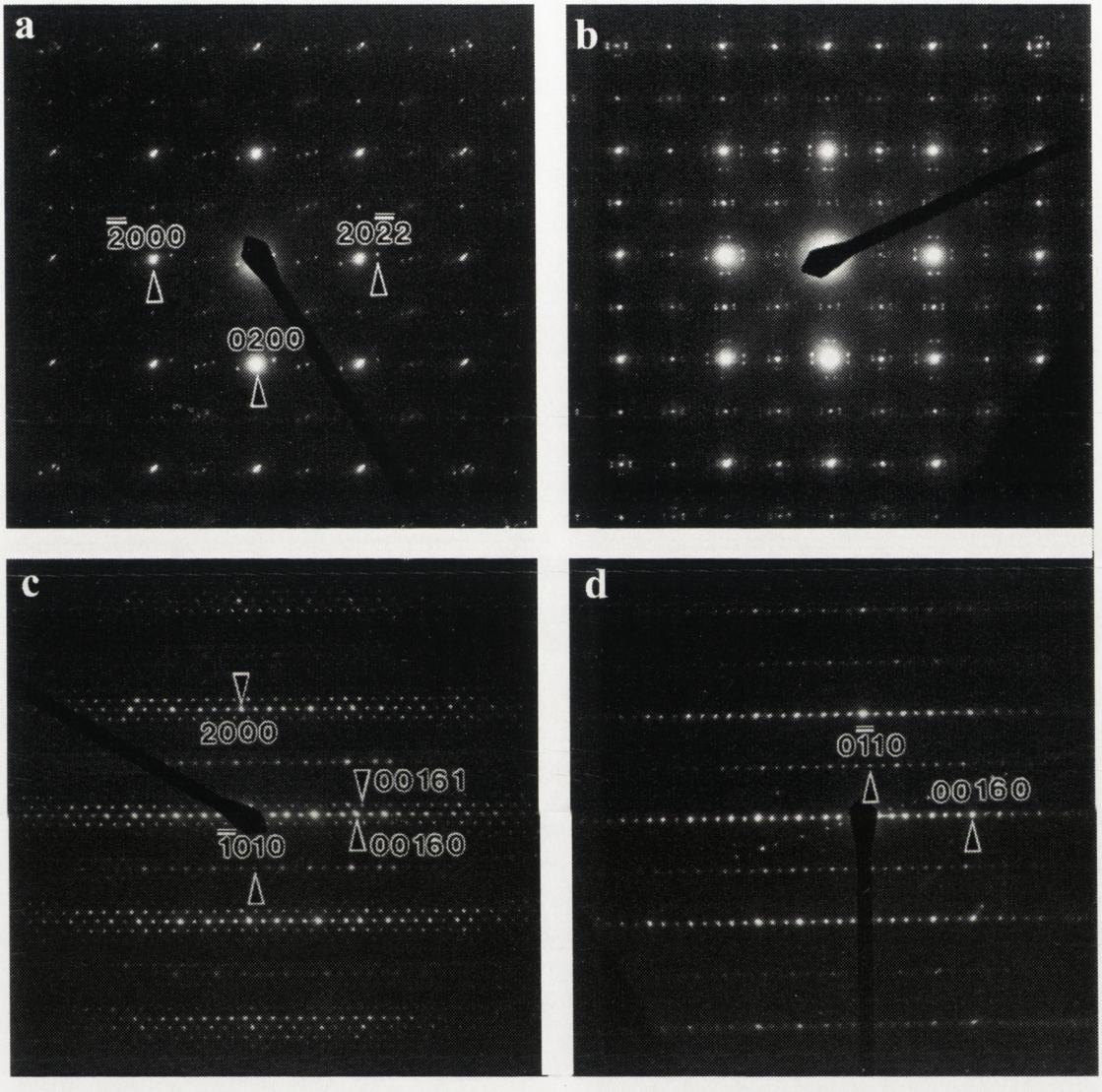

Figure 8. (a) [0 0 1]$_f$, (c) [0 1 0]$_f$ and (d) [1 0 0]$_f$ zone axis DPs of the type IV phase in the Bi_2O_3-Nb_2O_5 system. (b) Shows a multiply twinned [0 0 1]$_f$ zone axis DP of the same phase.

The type IV ($Bi_5Nb_3O_{15}$) line phase was found to be a one-dimensional, incommensurately modulated structure characterised by an incommensurate primary modulation wave-vector $\mathbf{q} \sim 0.18\mathbf{a}^* + 0.04\mathbf{b}^* + \mathbf{c}^*$ and by a very close to metrically tetragonal (no peak splitting is observed in XRD), body-centred cubic, average structure (Figure 8, Table 2). The incommensurate nature of the primary modulation wave-vector along both **a*** and **b*** was quite reproducible from grain to grain for the synthetic conditions used and necessarily lowers the average structure space group symmetry to at most monoclinic *I*112/*m*. The most probable superspace group symmetry is *I*112/*m*(0.18, 0.04, 1) $\bar{1}$ 1. Note that only up to second order satellite reflections are ever actually observed in DPs, rendering a superstructure description inappropriate. This is a non-standard superspace group setting; it is retained due to

the demonstrated relationship (19, 20) of this phase to the Aurivillius family of phases, making a change of setting inappropriate.

Zhou *et al.* (19) had previously reported two distinct type IV phases; an $a = 31.79$, $b = 5.45$, $c = 41.02$ Å orthorhombic structure (corresponding to the same pseudo-tetragonal body-centered cubic subcell plus a primary modulation wave-vector $\mathbf{q} = \frac{1}{6}\mathbf{a}^* + \mathbf{c}^*$, instead of the incommensurate primary modulation wave-vector $\mathbf{q} \sim 0.18\mathbf{a}^* + 0.04\mathbf{b}^* + \mathbf{c}^*$ described above) and a monoclinic type IV* variant. The DPs of Figure 8 are most closely related to those reported for the former, except for the incommensurability of the primary modulation wave-vector along $\mathbf{b}^*$. Exactly what factor controls the apparent variability in the observed primary modulation wave-vector remains unclear.

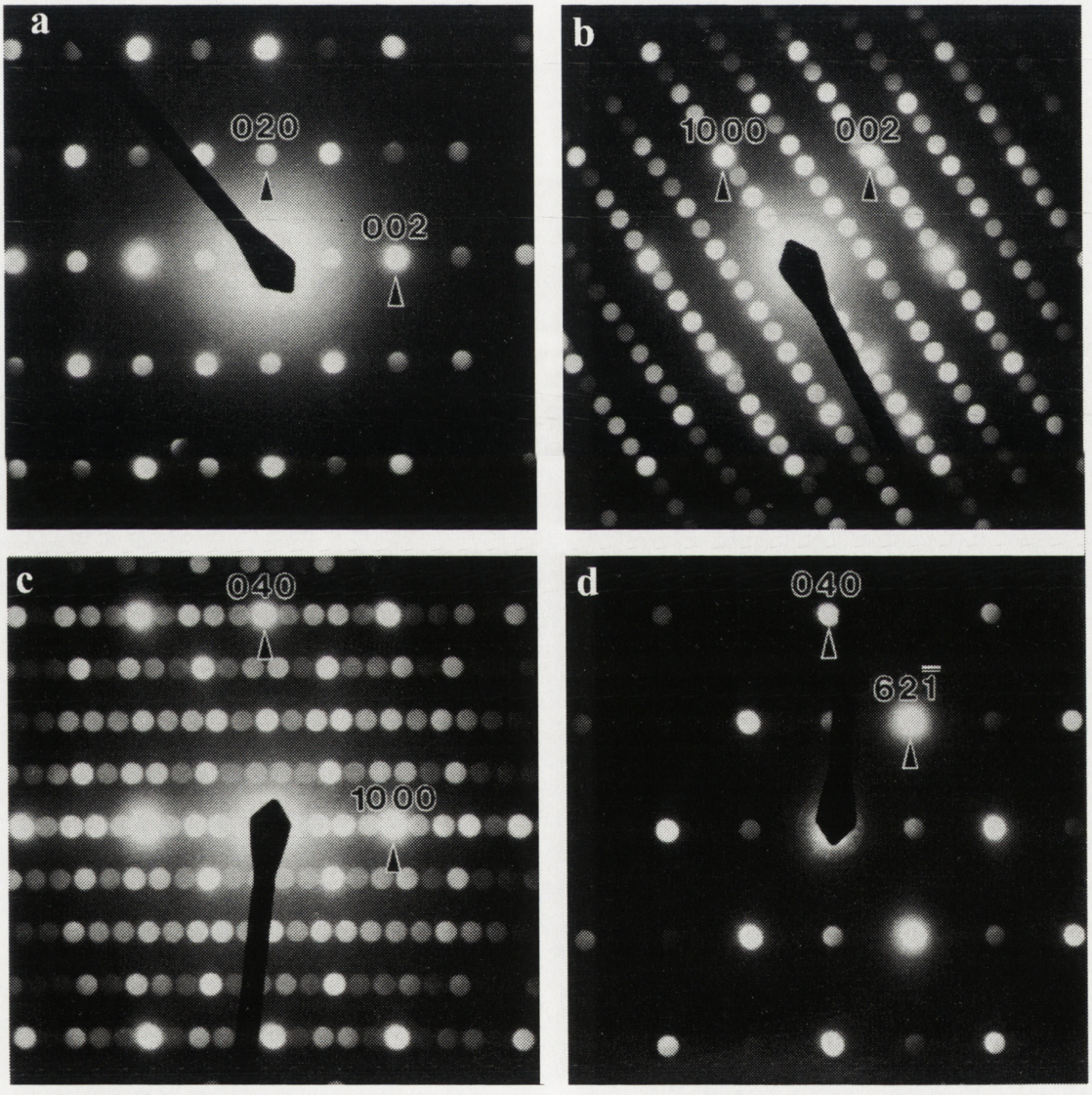

Figure 9. (a) [1 0 0], (b) [0 1 0], (c) [0 0 1] and (d) [$\bar{1}$ 0 6] zone axis DPs of the type II phase in the Bi_2O_3-Ta_2O_5 system.*

3.4.1.2 Bi_2O_3–Ta_2O_5

ED work with the type I phase in this system identified the commensurate modulation reported (21), leading to a $2\mathbf{a}_f$, $2\mathbf{b}_f$, $2\mathbf{c}_f$ *I*-centered supercell of fluorite-type δ-Bi_2O_3. The space group could not be uniquely determined (possible space groups were $I23$, $I2_13$, $Im\bar{3}$, $I432$, $I4\bar{3}m$ or $Im\bar{3}m$). The type II phase in this system was found to be isomorphous with the incommensurately modulated type II phase in the Bi_2O_3-Nb_2O_5 system described above (Section 3.4.1.1).

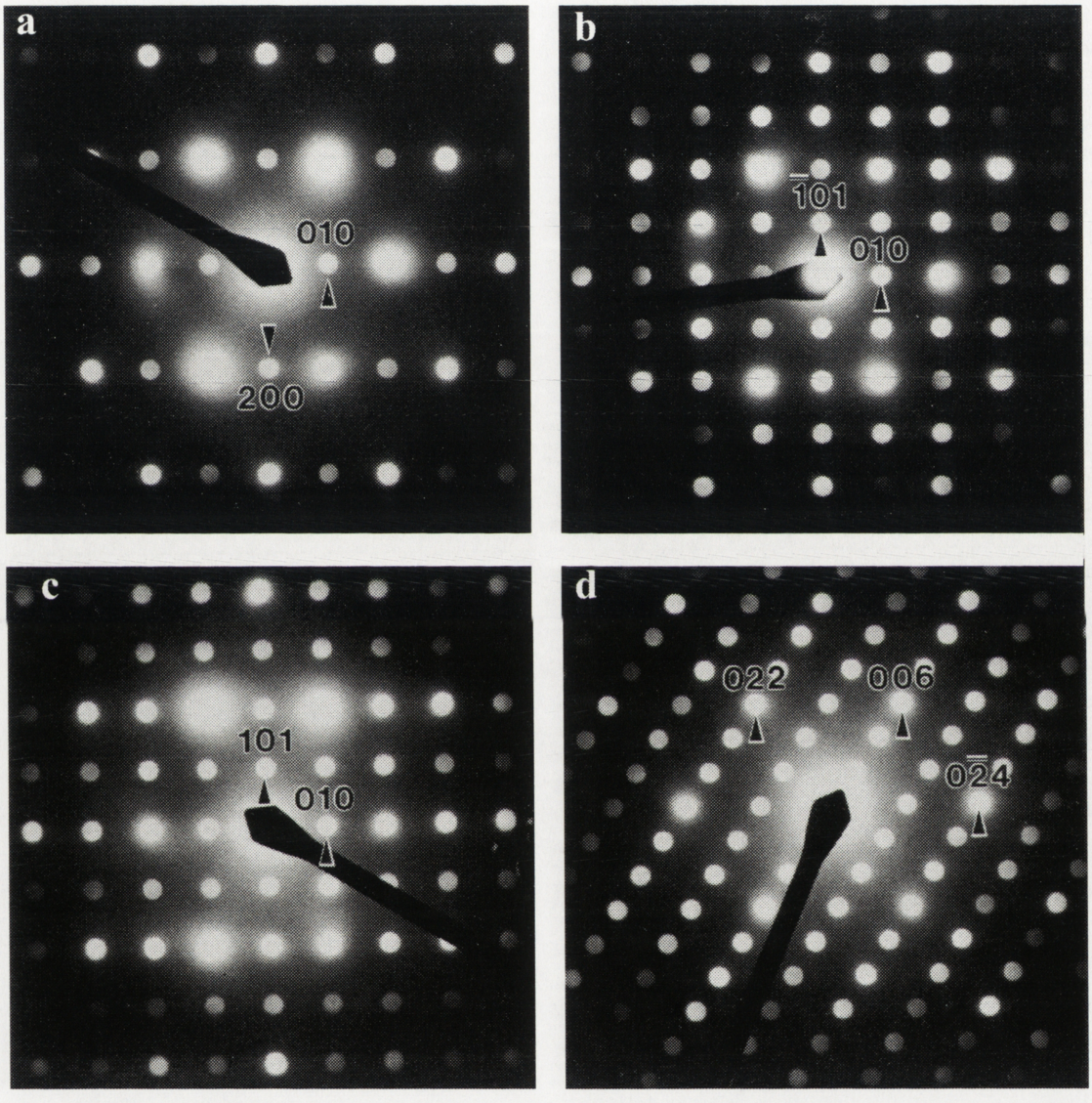

Figure 10. (a) [0 0 1], (b) [1 0 1], (c) [$\bar{1}$ 0 1] and (d) [1 0 0] zone axis DPs of the type III phase in the Bi_2O_3-Ta_2O_5 system.

Indexation of DPs of the large unit cell, low symmetry, type II* phase (Figure 9) was non-trivial and required close cross-correlation between XRD data (Figure 16) and ED data to ensure self-consistency. A unique *C*-centered monoclinic cell (most probable space group symmetry $C2/m$), $a \sim 34.0$, $b \sim 7.61$, $c \sim 6.63$ Å, $\beta \sim 109.2$ °, was found to be the only possible solution (Figure 9, Figure 16). These DPs could not be indexed to the previously

reported (21) simple fluorite-type superstructure ($\mathbf{a} = 5\mathbf{a}_f - 5\mathbf{b}_f$, $\mathbf{b} = \mathbf{a}_f + \mathbf{b}_f$, $\mathbf{c} = -\mathbf{a}_f + \mathbf{b}_f + 2\mathbf{c}_f$: $\mathbf{a}^* = \frac{1}{10}[1\ \bar{1}\ 1]_f^*$, $\mathbf{b}^* = \frac{1}{4}[2\ 2\ 0]_f^*$, $\mathbf{c}^* = \frac{1}{4}[0\ 0\ 2]_f^*$: $a = 38.5$, $b = 7.70$, $c = 13.64$ Å, $\beta = 124.33$ °), or indeed to any other simple fluorite-type superstructure, despite the observance of apparent fluorite-like zone axis DPs, *i.e.* zone axis DPs in which the strongest reflections appear to correspond to fluorite-type subcell reflections.

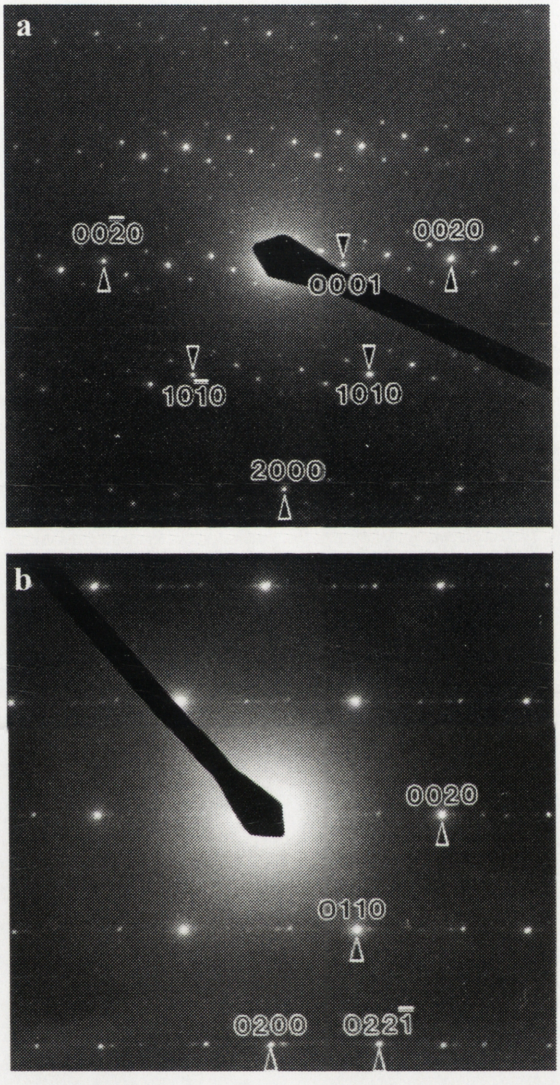

Figure 11. (a) [0 1 0] and (b) [1 0 0]$_f$ zone axis DPs of the type IV phase in the Bi_2O_3-Ta_2O_5 system.

Consider, for example, Figure 9*(b)* which resembles a <1 1 0>$_f$ zone axis DP and Figure 9*(c)* which resembles a $[\bar{1}\ 1\ 2]_f$ zone axis DP. The strong reflections labelled [10, 0, 0]* and [0 0 2]* in Figure 9*(b)* appear to correspond to <1 1 1>$_f$* average structure reflections (which should therefore be strong reflections, consistent with the XRD data in Figure 16) while the strong reflection labelled [0 4 0]* in Figure 9*(c)* appears to correspond to a <2 2 0>$_f$* average structure reflection (also consistent with XRD data). The implied relationship between the reciprocal lattice of the apparent fluorite type average structure and the actual reciprocal lattice is thus: $\mathbf{a}^* = \frac{1}{10}[1\ \bar{1}\ 1]_f^*$, $\mathbf{b}^* = \frac{1}{4}[2\ 2\ 0]_f^*$, $\mathbf{c}^* = \frac{1}{2}[1\ \bar{1}\ \bar{1}]_f^*$. The problem with this apparent fluorite-type supercell is that the other strong <1 1 1>$_f$* reflection

expected in XRD data for a resultant monoclinic supercell, namely $[1\ 1\ 1]_f^* = [5\ 2\ \bar{1}\ ]^*$, is forbidden by the *C*-centering of the resultant supercell. The third strong $<1\ 1\ 1>_f^*$ reflection observed in XRD and ED (Figure 9*(d)*) data indexes as $[6\ 2\ \bar{1}\ ]^* = \frac{1}{20}[22, 18, 22]_f^*$. Such problems were always encountered when the type II* phase was assumed to possess an underlying, fluorite-type average structure.

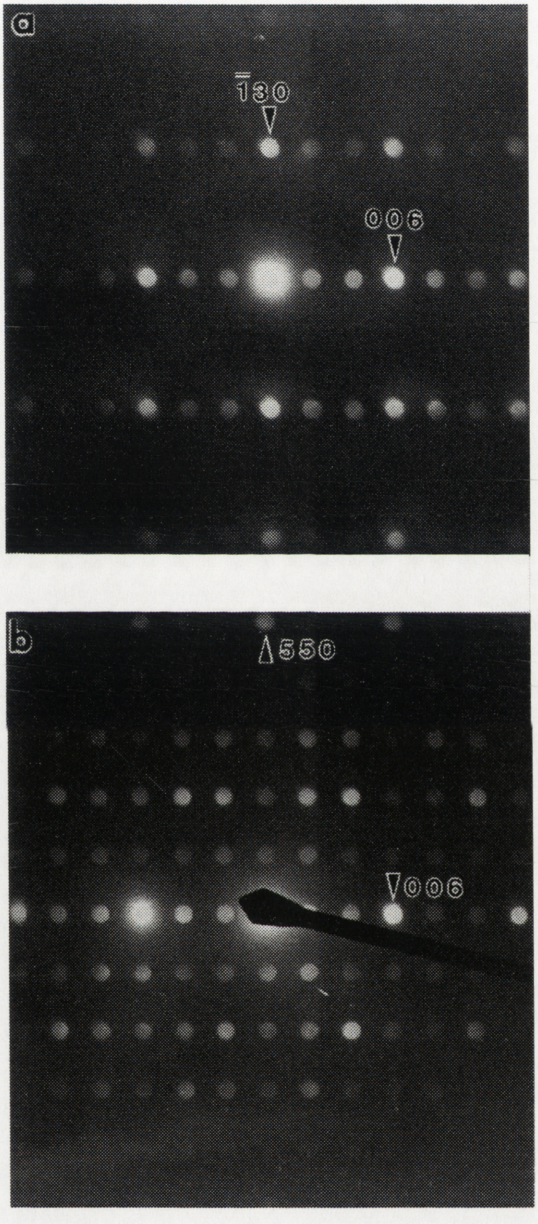

Figure 12. (a) [3 1 0] ≡ $[1\ 0\ 0]_f$ and (b) [1 $\bar{1}$ 0] ≡ $[2\ \bar{4}\ 0]_f$ zone axis DPs of the type Ia phase in the Bi_2O_3-MoO_3 system.

Similar problems were encountered interpreting DPs of type III (Figure 10). Indexation again required close cross-correlation between XRD (Figure 17) and ED data to ensure self-consistency. A unique *B*-centered triclinic, but pseudo-monoclinic, cell (most probable space group symmetry $B1$ or $B\bar{1}$), $a \sim 7.66$, $b \sim 6.61$, $c \sim 19.765$ Å, $\alpha \sim 89.8$, $\beta \sim 109.2$, $\gamma \sim 90.02$ °, was found to be the only possible solution. Again, DPs could not be

indexed to the previously reported (21) simple fluorite superstructure ($\mathbf{a} = 3\mathbf{a}_f - 3\mathbf{b}_f$, $\mathbf{b} = 2\mathbf{a}_f + 2\mathbf{b}_f$, $\mathbf{c} = -\mathbf{a}_f + \mathbf{b}_f + 2\mathbf{c}_f$; $\mathbf{a}^* = \frac{1}{6}[1\ \bar{1}\ 1]_f^*$, $\mathbf{b}^* = \frac{1}{8}[2\ 2\ 0]_f^*$, $\mathbf{c}^* = \frac{1}{4}[0\ 0\ 2]_f^*$, $a = 24.14$, $b = 14.63$, $c = 13.47$ Å, $\beta = 126.2$ °) or to any other simple fluorite type superstructure, despite the existence of apparent fluorite-like zone axis DPs *e.g.* Figure 10*(d)*. Correct indexation of this phase is seriously complicated by the fact that, to a very good approximation, $a^* = \frac{\sqrt{3}}{2} b^*$ and $c^* = 2a^*\cos\beta^*$.

Integer indexation of the reciprocal lattice of the final phase in this system, type IV, requires four basis vectors given by $\mathbf{M}^* = \mathbf{a}^*, \mathbf{b}^*, \mathbf{c}^*$ and $\mathbf{q}$ respectively (Figure 11). The *I*-centered monoclinic (pseudo-tetragonal) unit cell of the underlying average structure (most probable space group symmetry *I*12/*m*1) is given by $a \sim 3.90$, $b \sim 3.86$, $c \sim 5.20$ Å, $\beta \sim 91.3$ °. The incommensurate primary modulation wave-vector $\mathbf{q}$ is very close, but not exactly equal, to $\frac{1}{48}[2, 0, 36]^*$. The most probable superspace group symmetry is *I*12/*m*1(0.04 0 0.75)$\bar{1}$ 1. Typically, satellite reflections up to approximately eighth order are visible in [0 1 0] zone axis DPs (Figure 11*(a)*), rather less in XRD patterns. The reciprocal lattice of the previously published ($a_Z = 22.72$, $b_Z = 3.85$, $c_Z = 19.26$ Å, $\beta_Z = 101.9$ °) monoclinic cell of Zhou *et al.* (19) can be mapped onto this four-dimensional reciprocal lattice $\mathbf{M}^*$ by the relations $\mathbf{a}_Z^* = \frac{1}{2}[0\ 0\ \bar{6}\ 8]^*$, $\mathbf{b}_Z^* = \frac{1}{2}[0\ 2\ 0\ 0]^*$ and $\mathbf{c}_Z^* = \frac{1}{2}[0\ 0\ \bar{2}\ 2]^*$.

3.4.1.3 Bi_2O_3–WO_3

All phases synthesised in this system produced DPs corresponding to supercells of fluorite-type as reported (14). The space groups of types Ia and II could not be uniquely determined (choices of *I*4, $I\bar{4}$, *I*4/*m*, *I*422, *I*4*mm*, $I\bar{4}2m$ or *I*4/*mmm* and *F*4, $F\bar{4}$, *F*4/*m*, *F*422, *F*4*mm*, $F\bar{4}2m$ or *F*4/*mmm* respectively). Extinctions indicate $I4_1$ or $I4_122$ for type Ib. Note that an earlier XRD and single-crystal X-ray photographic study of type Ib (27) determined a higher symmetry, $I4_1/a$, for the same unit cell; this pseudo-symmetry condition rules out $I4_122$ (in a different Laue class to $I4_1/a$), therefore the space group must be $I4_1$.

3.4.1.4 Bi_2O_3–MoO_3

$Bi_{14}MoO_{24}$ was confirmed by ED to be isomorphous with the Bi_2O_3-WO_3 type Ia phase; a tetragonal superstructure of fluorite-type, $\mathbf{a} = \frac{3}{2}\mathbf{a}_f - \frac{1}{2}\mathbf{b}_f$, $\mathbf{b} = \frac{1}{2}\mathbf{a}_f + \frac{3}{2}\mathbf{b}_f$, $\mathbf{c} = 3\mathbf{c}_f$, space group *I*--- (Figure 12). ED results reported for $Bi_{38}Mo_7O_{78}$ (13) were reproduced, and the cell and space group symmetry confirmed (*Pccn*, uniquely determined from extinction conditions). $Bi_{26}Mo_{10}O_{69}$ was also investigated by ED, the *P*2/*c* cell reported (28) being observed. The relationship of this cell to a fluorite-type δ-Bi_2O_3 subcell (not previously reported) was determined as $\mathbf{a} = \frac{3}{2}\mathbf{a}_f + \frac{3}{2}\mathbf{c}_f$, $\mathbf{b} = \mathbf{b}_f$, $\mathbf{c} = -4\mathbf{a}_f + 2\mathbf{c}_f$.

3.4.1.5 Bi_2O_3–V_2O_5

ED investigation of this system highlighted the problems controlling synthetic products identified by XRD. Two single-phase powder samples of type I were found to have

slightly different primary modulation wave-vectors. Type I was reported as a relatively simple $3\mathbf{a}_f$, $3\mathbf{b}_f$, $3\mathbf{c}_f$ superstructure of fluorite-type δ-Bi_2O_3 (24). The first sample examined, however, was rather more complicated. The strongest satellite reflections corresponded to primary modulation wave-vectors given by $\mathbf{q}_1 = \frac{4}{13}(1\ \bar{1}\ 1)_f^*$, $\mathbf{q}_2 = \frac{1}{3}(1\ \bar{1}\ \bar{1})_f^* + \frac{1}{26}(1\ \bar{1}\ 1)_f^*$ (Figure 13*(c-d)*). Writing this in the form $\mathbf{q}_1 = (\frac{1}{3} + \varepsilon_1)(1\ \bar{1}\ 1)_f^*$, $\mathbf{q}_2 = \frac{1}{3}(1\ \bar{1}\ \bar{1})_f^* + \varepsilon_2(1\ \bar{1}\ 1)_f^*$ (with $\varepsilon_1 = -\frac{1}{13}$ and $\varepsilon_2 = \frac{1}{26}$) suggests the case $\varepsilon_1 = \varepsilon_2 = 0$ which describes the second sample examined and the reported type I (Figure 13*(a-b)*).

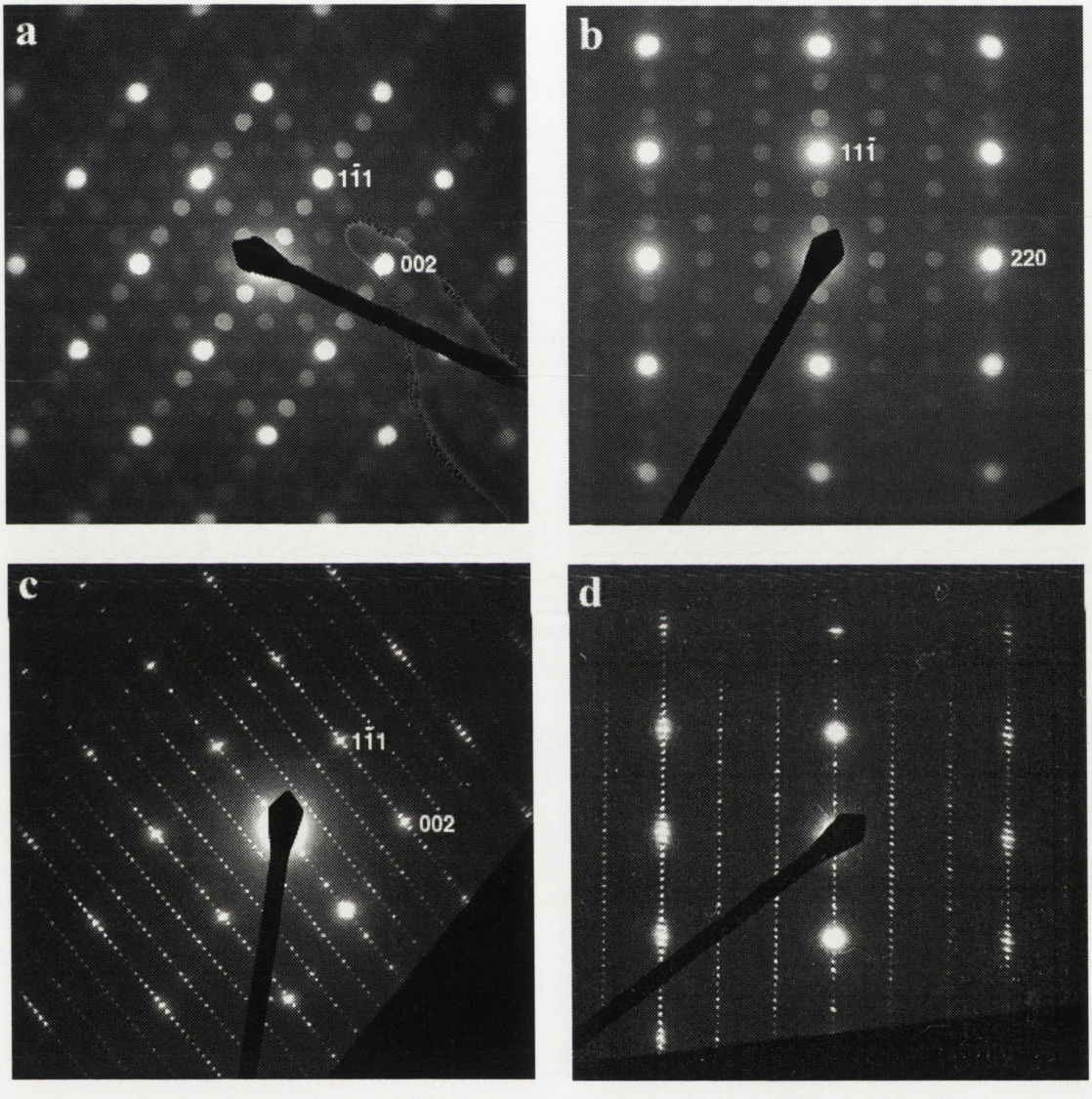

Figure 13. (a) $[1\ 1\ 0]_f$ and (b) $[1\ 1\ 2]_f$ zone axis DPs of the type I phase and (c) $[1\ 1\ 0]_f$ and (d) $[1\ 1\ 2]_f$ zone axis DPs of a commensurately modulated variant on the type I phase in the Bi_2O_3-V_2O_5 system.

Reported ED results for the type IIa phase (23) were successfully reproduced, indicating a tetragonal superstructure of fluorite-type δ-Bi_2O_3 where $\mathbf{a} = \frac{3}{2}\mathbf{a}_f + \frac{3}{2}\mathbf{c}_f$, $\mathbf{b} = \frac{3}{2}\mathbf{b}_f + \frac{3}{2}\mathbf{c}_f$, $\mathbf{c} = -\mathbf{a}_f - \mathbf{b}_f + 4\mathbf{c}_f$ (as reported). The type IIa single-crystal study published (29) used a permutation of this supercell; both are in space group $P\bar{1}$ or $P1$, the single-crystal study supporting $P\bar{1}$. At higher V_2O_5 concentrations, DPs were obtained which could only

sometimes be matched to reported types IIb-f. As for type I, it is possible that some or all of these are not line phases but variations on the theme of a modulated structure, related by shifts in the primary modulation wave-vectors. However, the endemically multi-phasic nature of the samples involved, and the incomplete ordering evident in the more complex phases, places a full investigation outside the range of this study (aimed as it is towards a practical knowledge-base for specimens able to be synthesised in bulk).

3.4.2 Unit Cell / Subcell Refinement

Results of unit cell refinements are presented in Table 2. All refinements used synchrotron data with the exception of $Bi_{15}TaO_{25}$ and $Bi_{31}Ta_{17}O_{89}$, for which conventional XRD data were used.

Representative XRD patterns collected using synchrotron radiation (λ = 1.4986 (4) Å) and presented below illustrate the various classes of structure (commensurately or incommensurately modulated, fluorite-type δ-Bi_2O_3-related or otherwise), exemplifying the quality of the data and the ability to index reflections with great confidence to high angle.

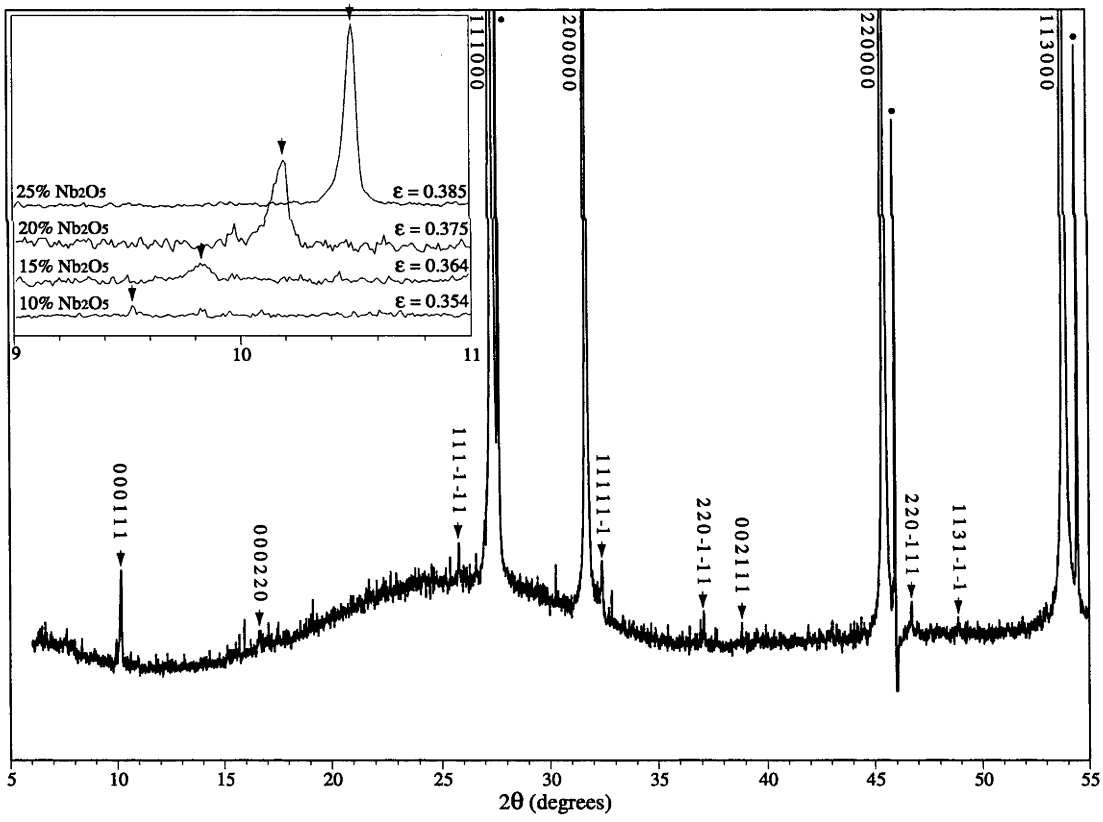

Figure 14. XRD pattern collected using a synchrotron source (λ = 1.4986 (4) Å) of type II $Bi_8Nb_2O_{17}$ indexed in six-dimensional notation. Silicon standard reflections are marked (•). The inset compares (0 0 0 1 1 1) reflections (normalised to (1 1 1 0 0 0)* reflections) across the type II solid solution.*

Composition	Type	Fluorite-type Supercell or Subcell Modulation	Space Group	Refined Supercell / Incommensurately Modulated Subcell Dimensions					
				a (Å)	b (Å)	c (Å)	α (°)	β (°)	γ (°)
Bi_9NbO_{16}	II	$\mathbf{q}_1 = \varepsilon\mathbf{a}_f^*, \mathbf{q}_2 = \varepsilon\mathbf{b}_f^*, \mathbf{q}_3 = \varepsilon\mathbf{c}_f^* : \varepsilon = 0.354$	$P{:}Fm\bar{3}m{:}Fd\bar{3}m$	5.53057(4)	5.53057(4)	5.53057(4)	90	90	90
$Bi_{17}Nb_3O_{33}$	II	$\mathbf{q}_1 = \varepsilon\mathbf{a}_f^*, \mathbf{q}_2 = \varepsilon\mathbf{b}_f^*, \mathbf{q}_3 = \varepsilon\mathbf{c}_f^* : \varepsilon = 0.364$	$P{:}Fm\bar{3}m{:}Fd\bar{3}m$	5.51044(3)	5.51044(3)	5.51044(3)	90	90	90
$Bi_8Nb_2O_{17}$	II	$\mathbf{q}_1 = \varepsilon\mathbf{a}_f^*, \mathbf{q}_2 = \varepsilon\mathbf{b}_f^*, \mathbf{q}_3 = \varepsilon\mathbf{c}_f^* : \varepsilon = 0.375$	$P{:}Fm\bar{3}m{:}Fd\bar{3}m$	5.48632(3)	5.48632(3)	5.48632(3)	90	90	90
Bi_3NbO_7	III	$\mathbf{a} = 3\mathbf{a}_f, \mathbf{b} = 3\mathbf{b}_f, \mathbf{c} = 7\mathbf{c}_f$	$F4/mmm$	16.3180(2)	16.3180(2)	38.5420(5)	90	90	90
$Bi_5Nb_3O_{15}$	IV	ambiguous : $\mathbf{q} = \pm (0.18\ 0.04\ 1)^*$	$I112/m\mathbf{q}\bar{1}1$	5.4663(13)	5.4663(13)	41.9658(4)	90.06(2)	89.96(4)	90.014(12)
$Bi_{15}TaO_{25}$	I	$\mathbf{a} = 2\mathbf{a}_f, \mathbf{b} = 2\mathbf{b}_f, \mathbf{c} = 2\mathbf{c}_f$	I---	11.078(2)	11.078(2)	11.078(2)	90	90	90
$Bi_{103}Ta_{25}O_{217}$	II	$\mathbf{q}_1 = \varepsilon\mathbf{a}_f^*, \mathbf{q}_2 = \varepsilon\mathbf{b}_f^*, \mathbf{q}_3 = \varepsilon\mathbf{c}_f^* : \varepsilon = 0.375$	$P{:}Fm\bar{3}m{:}Fd\bar{3}m$	5.47100(3)	5.47100(3)	5.47100(3)	90	90	90
$Bi_7Ta_3O_{18}$	II*	ambiguous	Cm, $C2/m$	33.9870(9)	7.5996(2)	6.6308(2)	90	109.148(1)	90
$Bi_4Ta_2O_{11}$	III	ambiguous	$B1$, $B\bar{1}$	7.6607(7)	6.6112(6)	19.762(2)	89.791(3)	101.060(3)	90.020(3)
$Bi_{31}Ta_{17}O_{89}$	IV	ambiguous : $\mathbf{q} = \pm (0.04\ 0\ 0.75)^*$	$I12/m1\mathbf{q}\bar{1}1$	3.9033(5)	3.8561(4)	5.2027(8)	90	91.318(12)	90
$Bi_{14}WO_{24}$	Ia	$\mathbf{a} = 1.5\mathbf{a}_f - \frac{1}{2}\mathbf{b}_f, \mathbf{b} = \frac{1}{2}\mathbf{a}_f + 1.5\mathbf{b}_f, \mathbf{c} = 3\mathbf{c}_f$	I---	8.71355(8)	8.71355(8)	17.3253(2)	90	90	90
$Bi_{14}W_2O_{27}$	Ib	$\mathbf{a} = 2\mathbf{a}_f + \mathbf{b}_f, \mathbf{b} = -\mathbf{a}_f + 2\mathbf{b}_f, \mathbf{c} = 2\mathbf{c}_f$	$I4_1$	12.4958(1)	12.4958(1)	11.2464(1)	90	90	90
$Bi_{46}W_8O_{93}$	II	$\mathbf{a} = 3\mathbf{a}_f, \mathbf{b} = 3\mathbf{b}_f, \mathbf{c} = 3\mathbf{c}_f$	F---	16.6877(2)	16.6877(2)	16.6451(2)	90	90	90
$Bi_{14}MoO_{24}$	Ia	$\mathbf{a} = 1.5\mathbf{a}_f - \frac{1}{2}\mathbf{b}_f, \mathbf{b} = \frac{1}{2}\mathbf{a}_f + 1.5\mathbf{b}_f, \mathbf{c} = 3\mathbf{c}_f$	I---	8.7142(5)	8.7142(5)	17.3305(9)	90	90	90
$Bi_{38}Mo_7O_{78}$	38:7	$\mathbf{a} = 3\mathbf{a}_f, \mathbf{b} = 5\mathbf{b}_f, \mathbf{c} = 3\mathbf{c}_f$	$Pccn$	16.8065(2)	28.6009(4)	16.8898(2)	90	90	90
$Bi_{26}Mo_{10}O_{69}$	26:10	$\mathbf{a} = 1.5\mathbf{a}_f + 1.5\mathbf{c}_f, \mathbf{b} = \mathbf{b}_f, \mathbf{c} = -4\mathbf{a}_f + 2\mathbf{c}_f$	$P2/c$	11.7413(1)	5.80071(6)	24.7940(2)	90	102.844(1)	90
Bi_7VO_{13}	I	$\mathbf{q}_1 = (\frac{1}{3} + \varepsilon_1)(1\ \bar{1}\ 1)_f^*$: $\mathbf{q}_2 = \frac{1}{3}(1\ \bar{1}\ \bar{1})_f^* + \varepsilon_2(1\ \bar{1}\ 1)_f^*$		5.629(4)	5.36977(9)	5.629(4)	89.79(5)	92.3439(9)	90.23(5)
$Bi_{12}V_2O_{23}$	IIa	$\mathbf{a} = 1.5\mathbf{a}_f + 1.5\mathbf{c}_f, \mathbf{b} = 1.5\mathbf{b}_f + 1.5\mathbf{c}_f,$ $\mathbf{c} = -\mathbf{a}_f - \mathbf{b}_f + 4\mathbf{c}_f$	$P1$, $P\bar{1}$	11.597(1)	11.774(1)	23.900(2)	57.656(6)	60.937(6)	60.362(6)

Table 2. Summary of data gathered in this study.

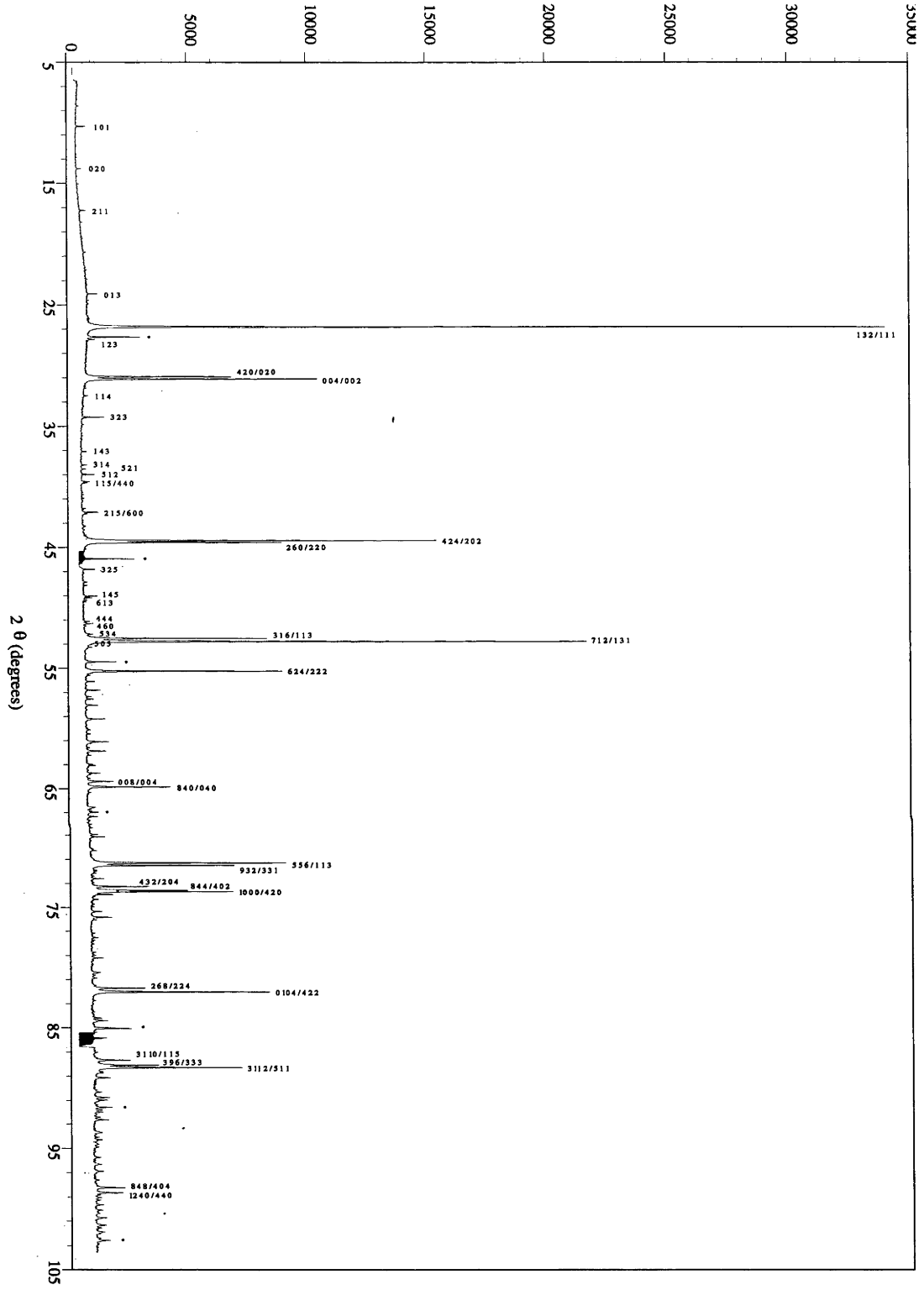

Figure 15. XRD pattern collected using a synchrotron source (λ = 1.4986 (4) Å) of type Ib $Bi_{14}W_2O_{27}$ indexed to a tetragonal cell. Silicon standard reflections are marked (•) and reflections of the fluorite-type subcell are indexed in bold type.

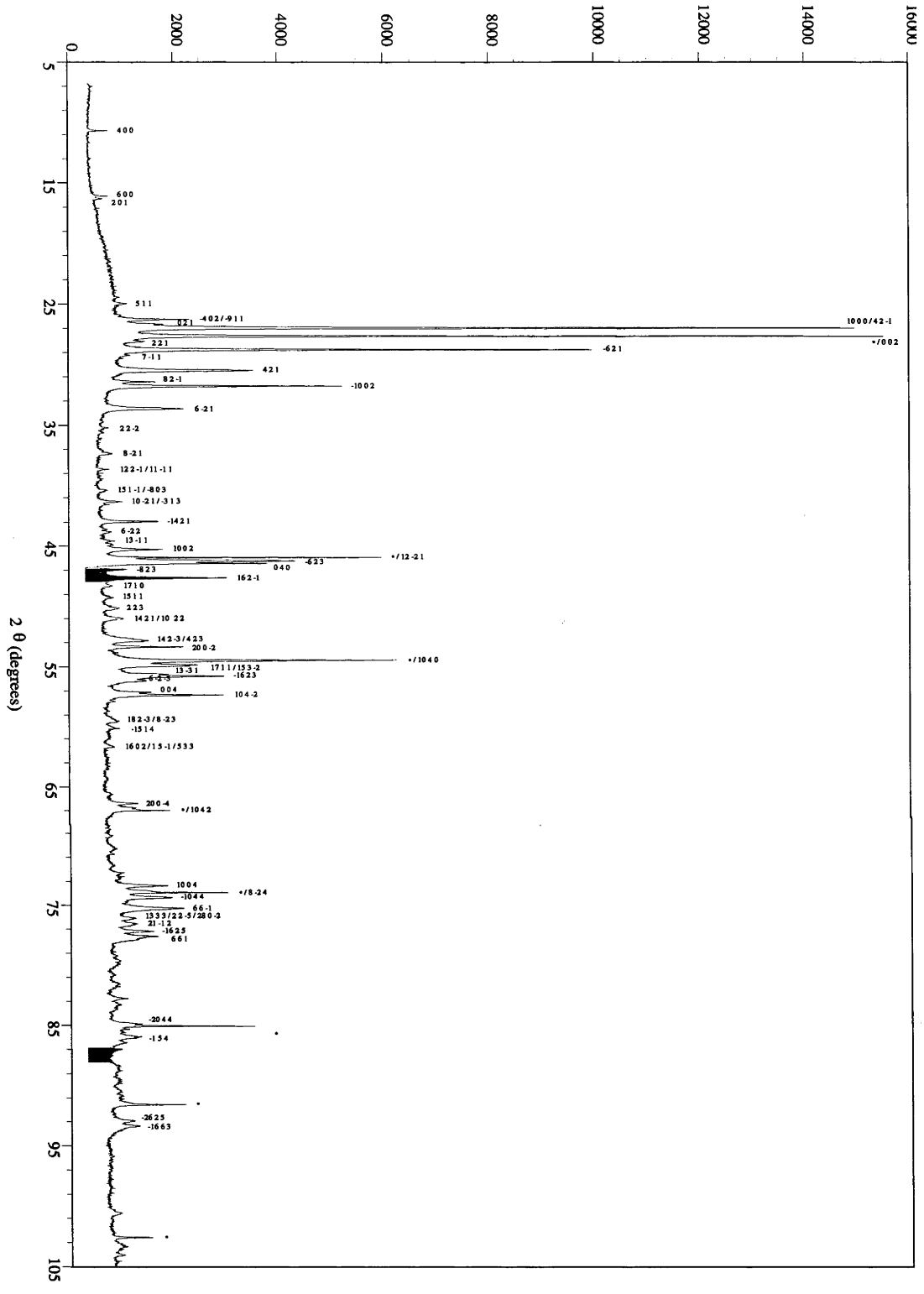

Figure 16. XRD pattern collected using a synchrotron source (λ = 1.4986 (4) Å) of type II $Bi_7Ta_3O_{18}$ indexed to a monoclinic cell. Silicon standard reflections are marked (•).*

Figure 14 shows the XRD pattern for $Bi_8Nb_2O_{17}$, part of the type II solid solution, enlarged for the benefit of the observed satellite reflections. Reflections are indexed in six-dimensional notation. The eight satellite reflections observed and indexed are extremely weak; consider that the subcell reflection (1 1 1 0 0 0)* is off-scale by a factor of twenty. The

weakness of the satellite reflections limited the ability of a previous study to model the structure using an incommensurate modulation wave approach (48).

The inset in Figure 14 shows enlarged sections of XRD patterns from a range of type II solid solution phases, normalised to (1 1 1 0 0 0)* reflections, including the Nb_2O_5-rich end-member (determined by EDXA to be 23.4(4) mol% Nb_2O_5). The reflection arrowed is (0 0 0 1 1 1)*, which is the most intense of the first-order satellite reflections. The series indicates the rapid increase in satellite reflection intensity with increasing Nb_2O_5 content. The patterns also quantitatively confirm ED evidence for a monotonic increase in the incommensurate modulation wave parameter ε with Nb_2O_5 content; measured values of ε are given in the inset to Figure 14.

A much greater number of satellite reflections are visible for type Ib $Bi_{14}W_2O_{27}$ (Figure 15), and the fluorite-type subcell is distorted to *F*-centered tetragonal. Nonetheless, fluorite-type subcell reflections dominate and clearly justify classification of this phase as a modulated structure.

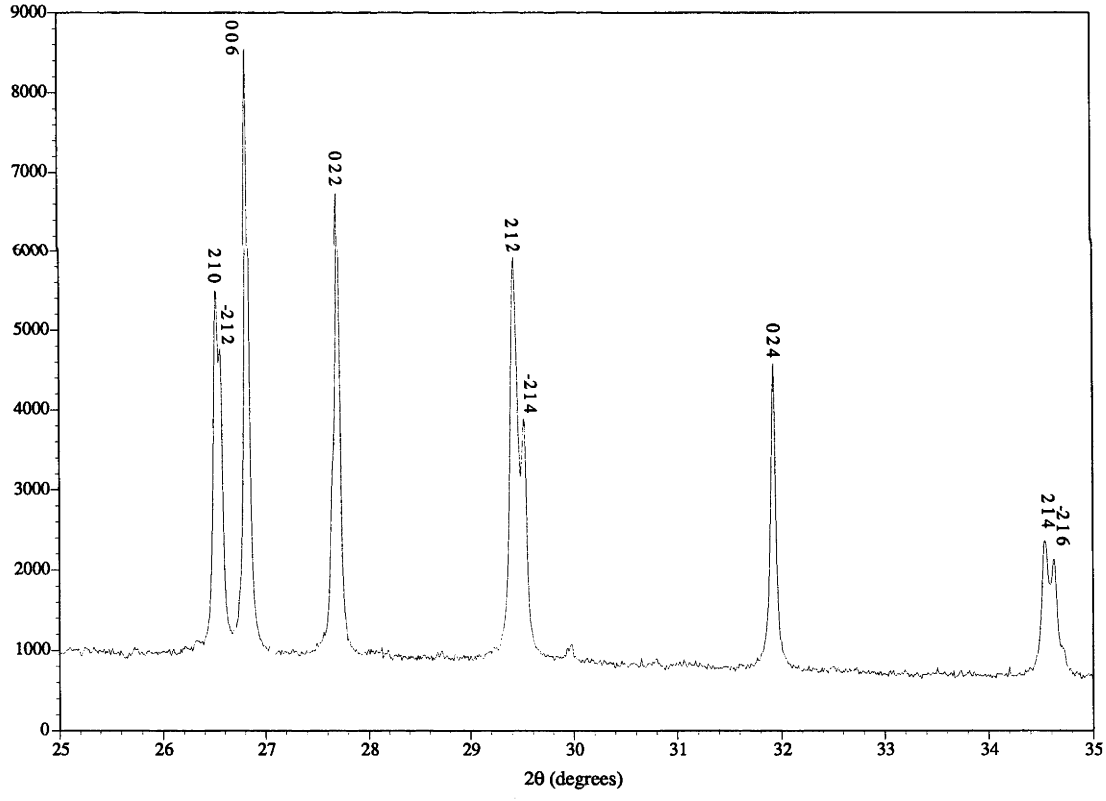

Figure 17. XRD pattern collected using a synchrotron source (λ = 1.4986 (4) Å) of type III $Bi_4Ta_2O_{11}$ indexed to a metrically monoclinic cell (ED indicating the actual structure to be triclinic).

The pattern for monoclinic type II* $Bi_7Ta_3O_{18}$ is shown in Figure 16. Although strong reflections are grouped near fluorite-type subcell reflection positions, the relationship to fluorite-type is no longer obvious. Strong reflections in XRD are also strong in DPs (Figure 10). As discussed above (Section 3.4.1.2), there is no unambiguous fluorite-type substructure

accounting for all strong reflections, bringing into question the previous assertion (21) that this phase is fluorite-related.

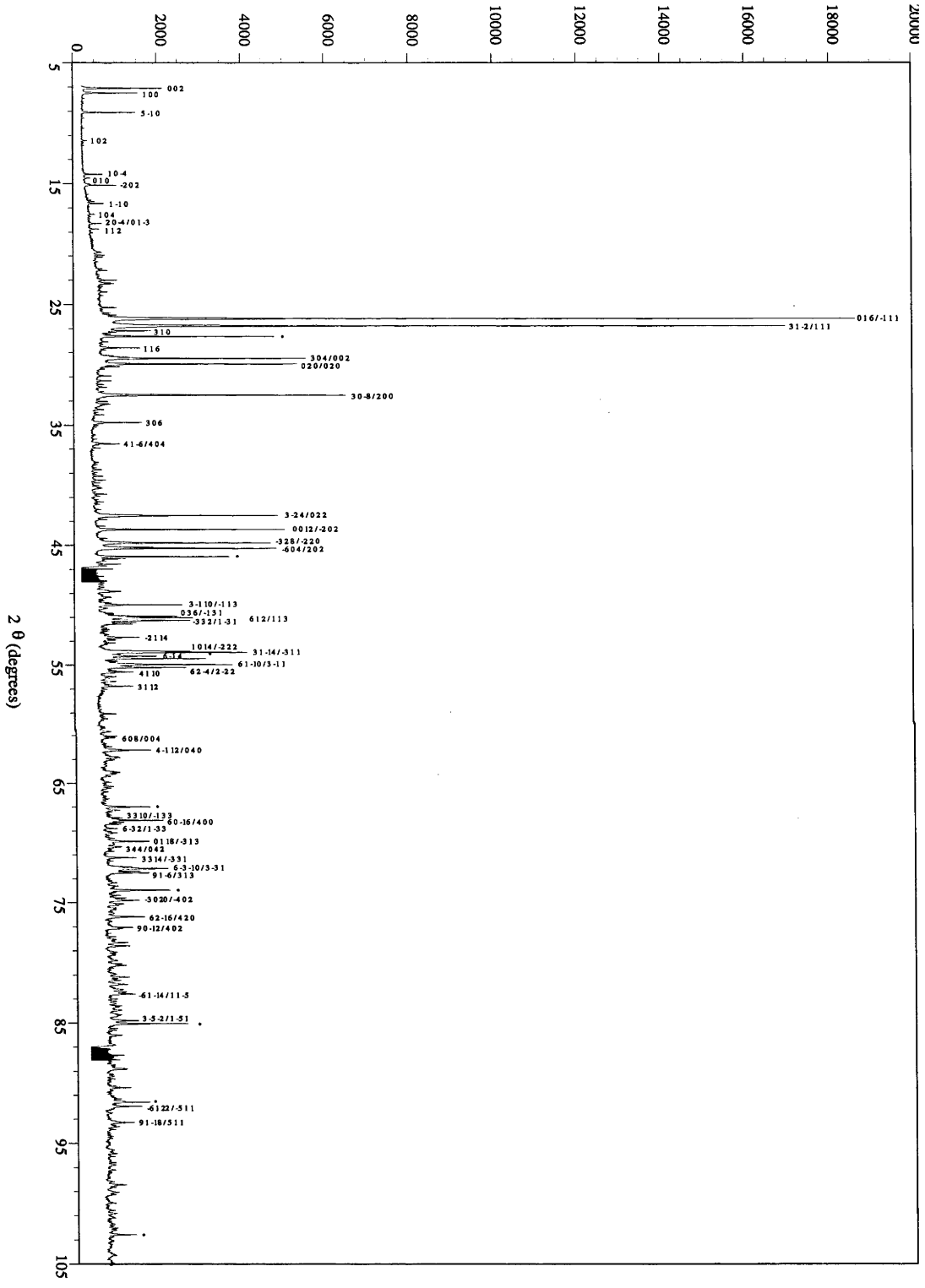

Figure 18. XRD pattern collected using a synchrotron source (λ = 1.4986 (4) Å) of $Bi_{26}Mo_{10}O_{69}$ indexed to a monoclinic cell. Silicon standard reflections are marked (•) and reflections of the fluorite-type subcell are indexed in bold type.

Figure 17 shows an enlarged section of the XRD pattern for type III $Bi_4Ta_2O_{11}$, highlighting (as for type II* $Bi_7Ta_3O_{18}$) the ambiguities involved in correct indexation and finding a unique underlying fluorite-type substructure for these phases. The cell is in fact triclinic, as discussed in Section 3.4.1.2, but very close to metrically monoclinic. In addition, $c^* = 2a^*\cos\beta^*$; this is the reason for the three narrowly split pairs of reflections in Figure 17. The nine reflections indexed in Figure 17 are of similar intensities, yet only seven unique reflections of any underlying fluorite-type substructure should be found in this region (four $<1\ 1\ 1>_f$ reflections and three $<2\ 0\ 0>_f$ reflections). The underlying substructure of this type III phase is therefore not (on average) of fluorite-type.

Figure 18 shows the pattern for $Bi_{26}Mo_{10}O_{69}$. Again, there are groupings of strong reflections about the fluorite-type subcell reflection positions. Some satellite reflections are, however, of comparable intensity to subcell reflections, devaluing the expedience of a modulated structure description. This observation is borne out by the structure of $Bi_{26}Mo_{10}O_{69}$ (28), the salient features of which are not (and need not be) discussed in terms of their relationship to fluorite-type δ-Bi_2O_3.

3.5 Discussion

This reinvestigation of the systems Bi_2O_3-Nb_2O_5, Bi_2O_3-Ta_2O_5, Bi_2O_3-MoO_3, Bi_2O_3-WO_3 and Bi_2O_3-V_2O_5 is founded on careful, systematic methodology and the application of a range of complementary analytical techniques. It aims to resolve most of the confusion that has arisen when the results of previous studies are considered together. Given the internal consistency of these results, it appears that most of the problems identified in the Introduction have been resolved.

It is extremely difficult to index reflections correctly for large unit cell, low symmetry, commensurately modulated phases *ab initio* using XRD, and the problem is effectively intractable for incommensurates without the aid of ED. At the same time, indexing reciprocal lattices from ED alone may fail to identify multiphasic specimens, or mistake impurity crystallites for those representative of the bulk specimen. Internal consistency between XRD and ED results is therefore essential.

The difficulties experienced in controlling the oxidation state of vanadium has led to the exclusion of the system Bi_2O_3-V_2O_5 from further investigation within the present study, in favour of a more concerted effort towards an understanding of the other systems. Both XRD and ED results have helped to indicate into which of two broad categories the remaining phases investigated in this study fall; those with a fluorite-type δ-Bi_2O_3-related substructure, and those for which the average structure appears to have moved too far from that prototype to be usefully described as a modulated variant thereof. Falling clearly in the former category

are the type II solid-solutions in the Bi_2O_3-Nb_2O_5 and Bi_2O_3-Ta_2O_5 systems, $Bi_{15}TaO_{25}$ (type I), Bi_3NbO_7 (type III), $Bi_{14}WO_{24}$ and $Bi_{14}MoO_{24}$ (type Ia), $Bi_{46}W_8O_{93}$ (type II) and $Bi_{38}Mo_7O_{78}$. In the latter category are $Bi_5Nb_3O_{15}$ and $Bi_{31}Ta_{17}O_{89}$ (type IV), $Bi_7Ta_3O_{18}$ (type II*), $Bi_4Ta_2O_{11}$ (type III) and $Bi_{26}Mo_{10}O_{69}$.

Where possible, a modulated structure approach should be used in structural studies of these phases. The important advantage of a modulated structure approach is the ability to recognise and index confidently complex XRD patterns by virtue of the hierarchy of intensities associated with such a modulated structure description. In crystallographic structural studies, this translates to a reduction in the number of variables by eliminating the need to consider structural degrees of freedom associated with higher order satellite reflections having zero observed intensity.

Chapter 4

Structure Determinations

4.1 Type Ia Bi_2O_3-WO_3 and Bi_2O_3-MoO_3 (51)

$Bi_{14}WO_{24}$ was described, in an ED study by Zhou (14), as a type Ia superstructure of fluorite-type δ-Bi_2O_3. In Section 3.4.1 (8), Zhou's ED results were reproduced for $Bi_{14}WO_{24}$ and it was found that $Bi_{14}MoO_{24}$ (33) appeared to be isostructural. For both phases, preliminary Rietveld-refinement of metal atom positions in Zhou's *I4/m* model using synchrotron XRD data indicated that the metal atom fractional coordinates were indeed very close to an fcc fluorite-type average structure. Zhou's model for oxygen atom positions lowers the symmetry from *I4/m* to *I*1 (*i.e. P*1) by removal of selected oxygen atoms (and their body-centred equivalents) from the model without displacing any remaining atoms from the fluorite-type average positions. The purpose of the study described here (Section 4.1) was to investigate the structures of these phases in terms of both displacive and occupational modulations away from a fluorite-type parent structure.

Successful synthesis of type Ia $Bi_{14}WO_{24}$ and $Bi_{14}MoO_{24}$ as nearly single phase powders on a sufficiently large scale allowed collection of TOF neutron powder diffraction data. The greater relative contribution of oxygen atoms to neutron diffraction intensities (compared to their contribution to X-ray diffraction intensities) allowed the modelling and refinement of oxygen atom parameters as well as those of the metal atoms. Solutions for the (isomorphous) structures of $Bi_{14}WO_{24}$ and $Bi_{14}MoO_{24}$ are reported and discussed in this Section, having been solved and refined using neutron powder diffraction data.

4.1.1 Experimental

Powder samples of type Ia $Bi_{14}WO_{24}$ and $Bi_{14}MoO_{24}$ were prepared by solid-state reaction of stoichiometric mixtures of Bi_2O_3 (Koch-Light 99.998 %), WO_3 (Koch-Light 99.9 %) and MoO_3 (Halewood 99.999 %) in platinum crucibles in air at 1103 K ($Bi_{14}WO_{24}$) or 1073 K ($Bi_{14}MoO_{24}$) for 0.5 hours. The samples were then quenched to room temperature, reground, annealed in sealed platinum vessels at 1103 K ($Bi_{14}WO_{24}$) or 1073 K ($Bi_{14}MoO_{24}$) for 168 hours and again quenched to room temperature. Homogeneous, pale yellow powders were obtained and identified as predominantly single-phase $Bi_{14}WO_{24}$ and $Bi_{14}MoO_{24}$ by XRD (Guinier-Hägg camera) (8). In neither case was it possible to eliminate small traces of a

γ-Bi_2O_3 type phase. This impurity was incorporated into both refinements using the model of Harwig (4), and refining only the phase fraction. Although XRD data indicated the samples were highly homogenous, the presence of small impurities and the fact that Zhou (14) reported a solid-solution between $Bi_{30}WO_{48}$ and $Bi_{14}WO_{24}$ meant that slight compositional inhomogeneities were possible.

Powder neutron diffraction data for $Bi_{14}MoO_{24}$ were collected on POLARIS (6), and for $Bi_{14}WO_{24}$ on HRPD (7); supplementary, high-*d*, data were collected on POLARIS. Experimental details for these diffraction experiments are summarised in Table 3 (POLARIS data for $Bi_{14}WO_{24}$ were collected under the same conditions as for $Bi_{14}MoO_{24}$). All refinements were carried out using *GSAS* (34).

Crystal data		
Chemical formula	$Bi_{14}WO_{24}$	$Bi_{14}MoO_{24}$
Chemical formula weight	3493.57	3404.66
Cell setting	Tetragonal	Tetragonal
Space group	*I4/m*	*I4/m*
a (Å)	8.71083(4)	8.70839(4)
c (Å)	17.32202(10)	17.31634(14)
V (Å^3)	1314.369(11)	1313.202(14)
Z	2	2
Radiation type	Neutron	Neutron
Temperature (K)	293	293
Specimen shape	Cylinder	Cylinder
Dimensions (mm)	30 x 15	25 x 8
Preparation conditions	101.3 kPa, 1103 K	101.3 kPa, 1073 K
Particle morphology	Plate	Plate
Colour	Yellow	Yellow
Data collection		
Diffractometer	HRPD, ISIS, RAL, UK	POLARIS, ISIS, RAL, UK
Detector	^{6}Li-doped glass scintillator	^{3}He gas and ZnS scintillators
Data collection method	Time-of-flight scans	Time-of-flight scans
Specimen mounting	Vanadium can	Vanadium can
Refinement		
R_p	0.0589	0.0387
wR_p	0.0605	0.0246
Profile function	Exponential pseudo-Voigt convolution	Exponential pseudo-Voigt convolution
No. of parameters used	56	56

Table 3. Experimental details.

4.1.2 Refinement

4.1.2.1 $Bi_{14}WO_{24}$

The relationship between the *I*-centred unit cells of $Bi_{14}WO_{24}$ and fluorite-type δ-Bi_2O_3 determined by Zhou (14) [$\mathbf{a} = \frac{3}{2}\mathbf{a}_f - \frac{1}{2}\mathbf{b}_f$, $\mathbf{b} = \frac{1}{2}\mathbf{a}_f + \frac{3}{2}\mathbf{b}_f$, $\mathbf{c} = 3\mathbf{c}_f$] was used to obtain a starting model for the structure of $Bi_{14}WO_{24}$. The supercell contains 30 metal atom sites, two of which are required to be occupied by W atoms. This requirement was satisfied by placing a W atom on the origin in the space group *I4/m*, the highest symmetry in which it is possible to obtain the correct Bi:W ratio. Full occupancy of all fluorite-type oxygen positions gave this model a stoichiometry $Bi_{14}WO_{30}$. This corresponds to the initial oxygen-rich model of Zhou (14).

Metal atom coordinates were then shifted slightly according to the results of the preliminary Rietveld refinement of the model using synchrotron XRD data. This provided an initial phasing of the modulation of the true structure away from fluorite-type. Fixing the metal atoms and refining oxygen atom positional and U_{iso} parameters led to unstable refinements and rapid growth in the error estimates and U_{iso} parameters for two of the five independent oxygen atom sites. Removal of these two atoms from the model led to a very stable refinement in which it was possible to simultaneously refine metal atom positional and U_{iso} parameters. The removed oxygen atoms were those closest to W. This led to an oxygen-poor model, $Bi_{14}WO_{20}$, in which W was clearly grossly underbonded (*i.e.* the bond valence sum for W was much less than 6).

Analysis of Fourier difference maps showed good agreement except in the vicinity of the W atom, and led to the clear identification of two oxygen atoms not in ideal fluorite-type positions bonding to W, one on the 4-fold axis (O1) and one on the mirror plane (O3). These appeared to form the axial and equatorial oxygen atoms respectively of a WO_6 octahedron. With full occupancy on both sites, however, the stoichiometry was once again oxygen-rich, $Bi_{14}WO_{28}$. It was possible to refine positional and U_{iso} parameters for these atoms, resulting in a significant improvement in refinement statistics over the purely fluorite-type model, however, large error estimates and U_{iso} parameters for O1 and O3 indicated that this model did not represent a perfectly ordered solution. The nature of the disorder was investigated by fixing U_{iso} parameters for all oxygen atoms to the same value and refining their occupancies. Occupancies for the fluorite-type oxygen atoms were found to remain close to 1.0, while for O1 and O3 occupancies refined to approximately 0.5.

At this stage it was noted that the required overall stoichiometry $Bi_{14}WO_{24}$ could be obtained with an occupancy for O1 of 0.50 and for O3 of 0.75, *i.e.* for each (average) WO_6 octahedron, one axial and one equatorial oxygen atom would be vacant. Fixing the

occupancies as such and freely refining all positional and U_{iso} parameters did indeed lead to the best refinement statistics thus far obtained.

Refinement of anisotropic atomic displacement parameters for O1 and O3 showed that the motion of these atoms was predominantly perpendicular to the W-O bonds. Refinement of anisotropic atomic displacement parameters for the remaining atoms did not yield sufficient improvements in refinement statistics to justify the increased number of variables. Consideration was also given to the possibility of correlation between atomic displacement parameters and other variables in Rietveld refinements, in particular absorption; clearly, however, the magnitude of the anisotropy observed for O1 and O3 made it unlikely that these were artefacts.

A series of attempts were made to find a fully ordered solution for the structure in lower-symmetry space groups. The tetragonal space groups $I\bar{4}$ and *I*4, and the monoclinic space group *I*2/*m*, were tried without success. In all cases, the refinements became less stable but the positions of O1 and O3 did not deviate significantly from the previously refined *I*4/*m* positions. Removing O1 and O3 from the model, refining the remainder of the structure and reinvestigating the Fourier difference map led to the identification of the same sites. In $I\bar{4}$ and *I*2/*m*, compatible with fully ordered WO_4 tetrahedra, attempts to constrain oxygen atoms around W into such tetrahedra produced unstable refinements with poor statistics.

Space group *I*4/*m* (no. 87), a = 8.71083(4), c = 17.32202(10) Å;

$U_{eq} = \frac{1}{3}\Sigma_i\Sigma_j U^{ij} a_i^* b_j^* \mathbf{a}_i.\mathbf{a}_j$ (Å^2).

	x (a)	y (b)	z (c)	Fraction	$100U_{iso/eq}$*
Bi1	0.4396(2)	0.2132(2)	0	1	1.75(5)
Bi2	0.39520(17)	0.2004(2)	0.32999(8)	1	1.46(3)
Bi3	0	0	0.34328(18)	1	3.13(10)
W1	0	0	0	1	4.0(2)
O1	0	0	0.1160(5)	0.50	3.9(3)*
O2	0	0.5	0.12133(2)	1	2.41(7)
O3	0.1937(9)	0.0173(14)	0	0.75	19.4(3)*
O4	0.6258(3)	0.3194(2)	0.07821(14)	1	2.28(5)
O5	0.2541(3)	0.0741(2)	0.25610(12)	1	2.33(5)
*	$100U_{11}$	$100U_{22}$	$100U_{33}$	$100U_{12}$	$100U_{13}$, U_{23}
O1	5.0(4)	5.0(4)	1.7(5)	0	0
O3	4.2(5)	30.9(15)	23.0(12)	-4.7(6)	0

Table 4. Structural parameters for the final Rietveld-refined structure of type Ia $Bi_{14}WO_{24}$.

The validity of the initial phasing of the refinement in *I*4/*m* was investigated by returning all atoms to fluorite-type positions and refining the positions of oxygen atoms before those of metal atoms. The same result was obtained, *i.e.* oxygen atoms phase metal atoms and *vice versa* in the same way therefore the refinement was not biased initially by the use of X-ray refined metal atom positions. It was concluded that none of the symmetry

lowering possibilities investigated resulted in sufficient deviations from the high symmetry case to justify the additional degrees of freedom. The disordered *I*4/*m* model appeared to fit all observable data, reflecting disorder in the true structure.

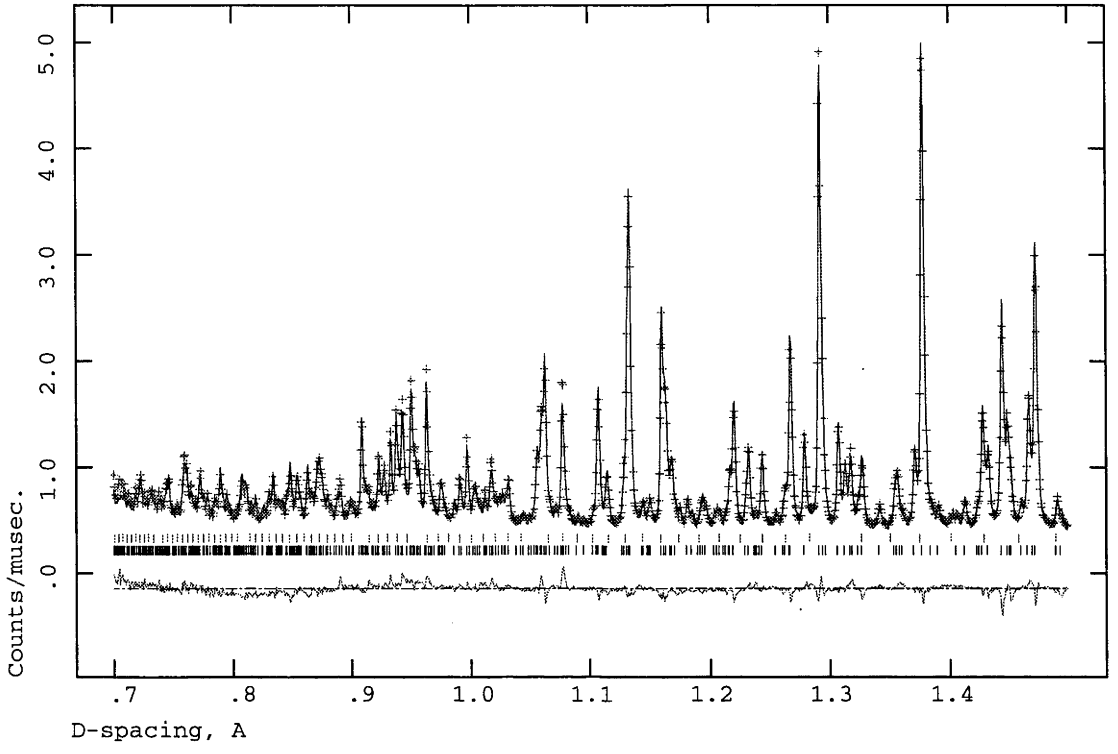

(a)

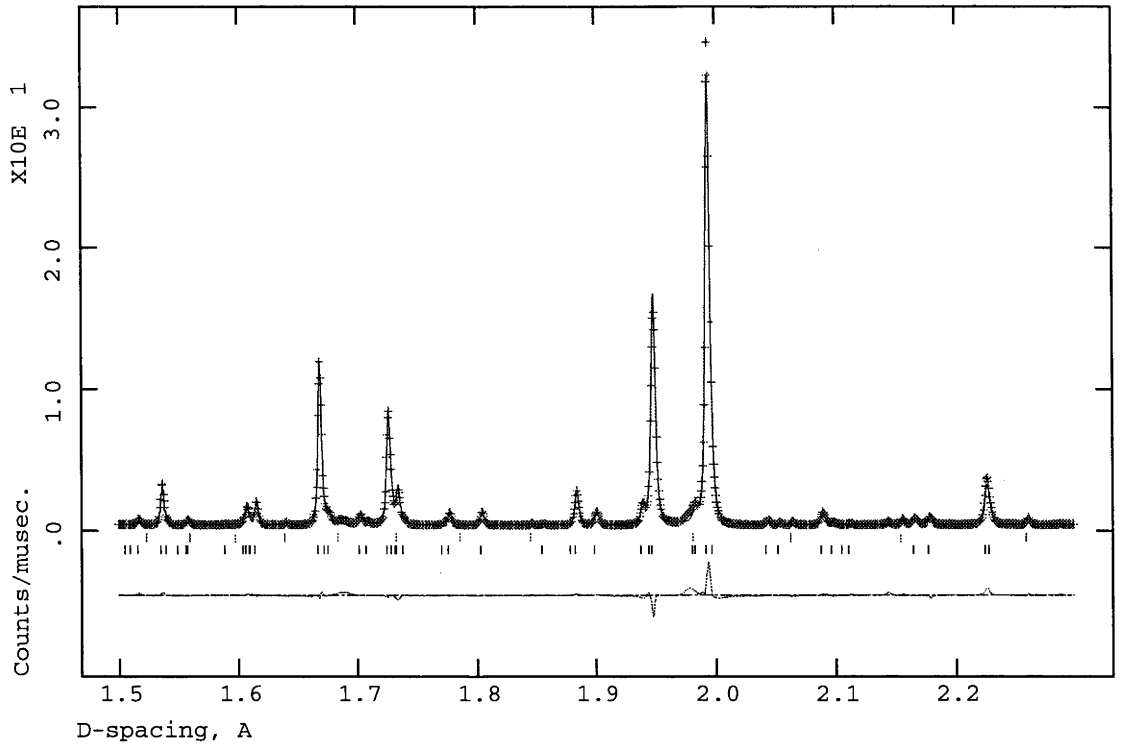

(b)

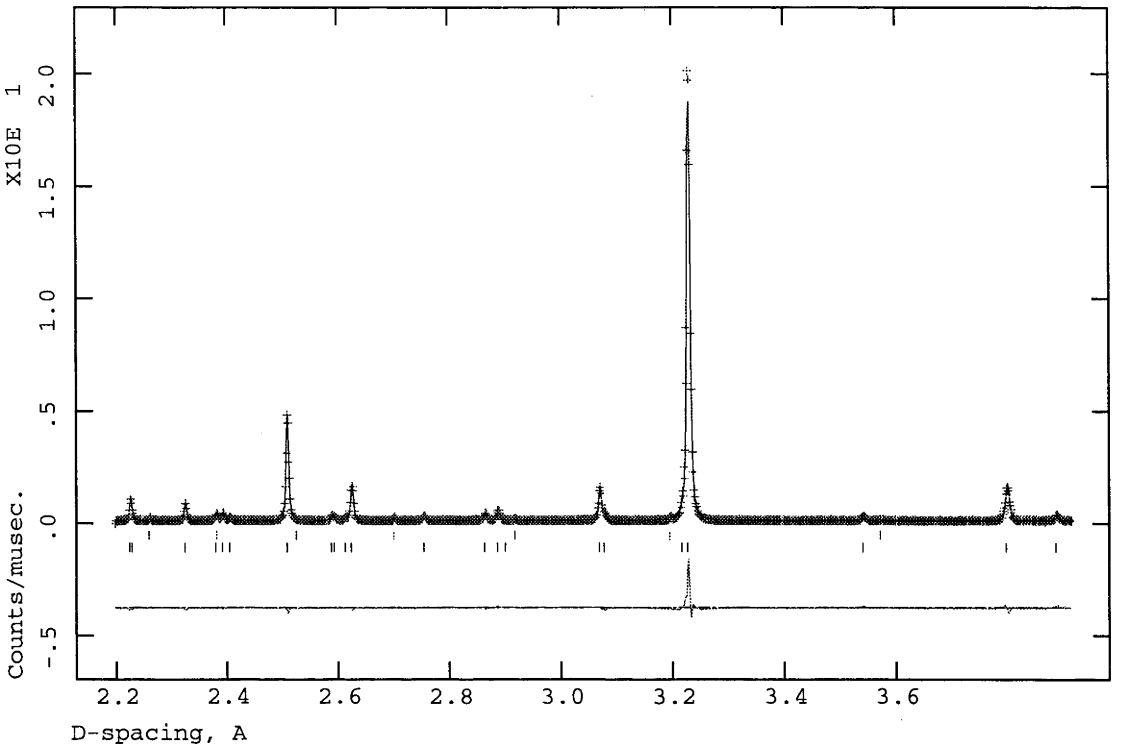

(c)

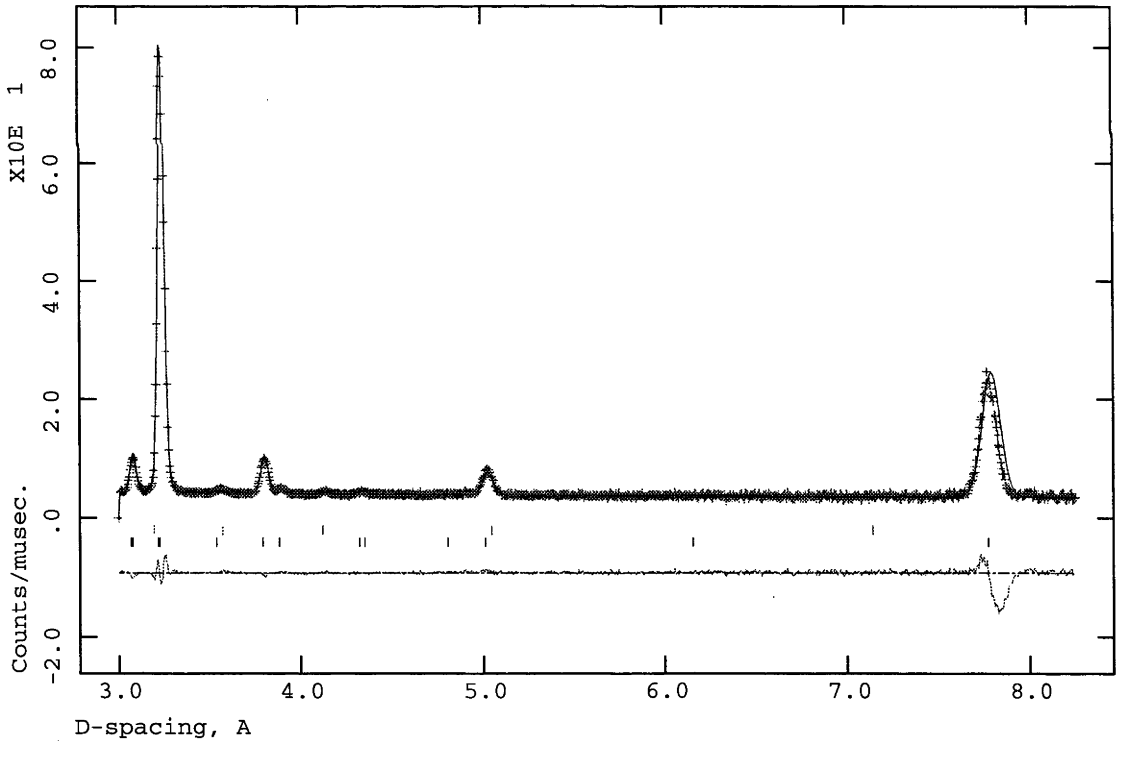

(d)

Figure 19. Observed (+), calculated and difference (bottom) neutron powder diffraction profiles for type Ia $Bi_{14}WO_{24}$ using (a, b) 30-130 ms, (c) 100-200 ms TOF windows with the backscattering detector of HRPD and (d) at the 135 ° detector bank of POLARIS. The top row of reflection markers refers to the γ-Bi_2O_3-type impurity.

Final refined values for the structural parameters are given in Table 4. Rietveld refinement statistics are summarised in Table 6. The refinement residuals for $Bi_{14}WO_{24}$, in particular $R(F^2)$, are in general higher than for $Bi_{14}MoO_{24}$, refined (Section 4.1.2.2) using lower resolution data. This tendency for higher-resolution data to give apparently worse refinement statistics (but better results) is a consequence of the weighting scheme used in the Rietveld method. Final observed, calculated and difference profiles are shown in Figure 19.

Space group *I4/m* (no. 87), a = 8.70839(4), c = 17.31634(14) Å;

$U_{eq} = \frac{1}{3}\Sigma_i\Sigma_j U^{ij} a_i^* b_j^* \mathbf{a}_i.\mathbf{a}_j$ (Å^2).

	x (a)	y (b)	z (c)	Fraction	$100U_{iso/eq}$*
Bi1	0.44022(13)	0.21306(15)	0	1	0.97(2)
Bi2	0.39542(11)	0.20048(13)	0.32975(5)	1	0.794(11)
Bi3	0	0	0.34376(13)	1	1.59(4)
Mo1	0	0	0	1	4.95(15)
O1	0	0	0.1189(4)	0.50	2.6(2)*
O2	0	0.5	0.12306(16)	1	1.76(3)
O3	0.1929(7)	0.9894(16)	0	0.75	19.8(8)*
O4	0.62344(18)	0.32173(17)	0.07786(10)	1	1.57(3)
O5	0.25313(15)	0.07313(15)	0.25669(8)	1	1.08(2)
*	$100U_{11}$	$100U_{22}$	$100U_{33}$	$100U_{12}$	$100U_{13}$, U_{23}
O1	3.3(2)	3.3(2)	1.2(3)	0	0
O3	4.8(5)	38.9(15)	15.6(8)	2.4(7)	0

Table 5. Structural parameters for the final Rietveld-refined structure of type Ia $Bi_{14}MoO_{24}$.

4.1.2.2 $Bi_{14}MoO_{24}$

The final structure of $Bi_{14}WO_{24}$ was used as a starting model for the Rietveld-refinement of POLARIS data for $Bi_{14}MoO_{24}$. The refinement rapidly converged from this starting model to a final refined structure clearly isomorphous to that of $Bi_{14}WO_{24}$. Final refined values for the structural parameters are given in Table 5. Rietveld-refinement statistics are summarised in Table 6. The final observed, calculated and difference powder neutron diffraction profiles are shown in Figure 20.

	Histogram	wR_p	R_p	$R(F^2)$	χ^2
$Bi_{14}WO_{24}$	30-130 ms	0.0598	0.0509	0.1365	
	100-200 ms	0.0822	0.0741	0.1342	
	35°	0.0512	0.0631	0.1279	
	Overall	0.0605	0.0589		7.362
$Bi_{14}MoO_{24}$	35°	0.0266	0.0383	0.0703	
	90°	0.0224	0.0337	0.0876	
	145°	0.0349	0.0474	0.0239	
	Overall	0.0246	0.0387		6.693

Table 6. Final Rietveld-refinement statistics for type Ia $Bi_{14}WO_{24}$ and $Bi_{14}MoO_{24}$.

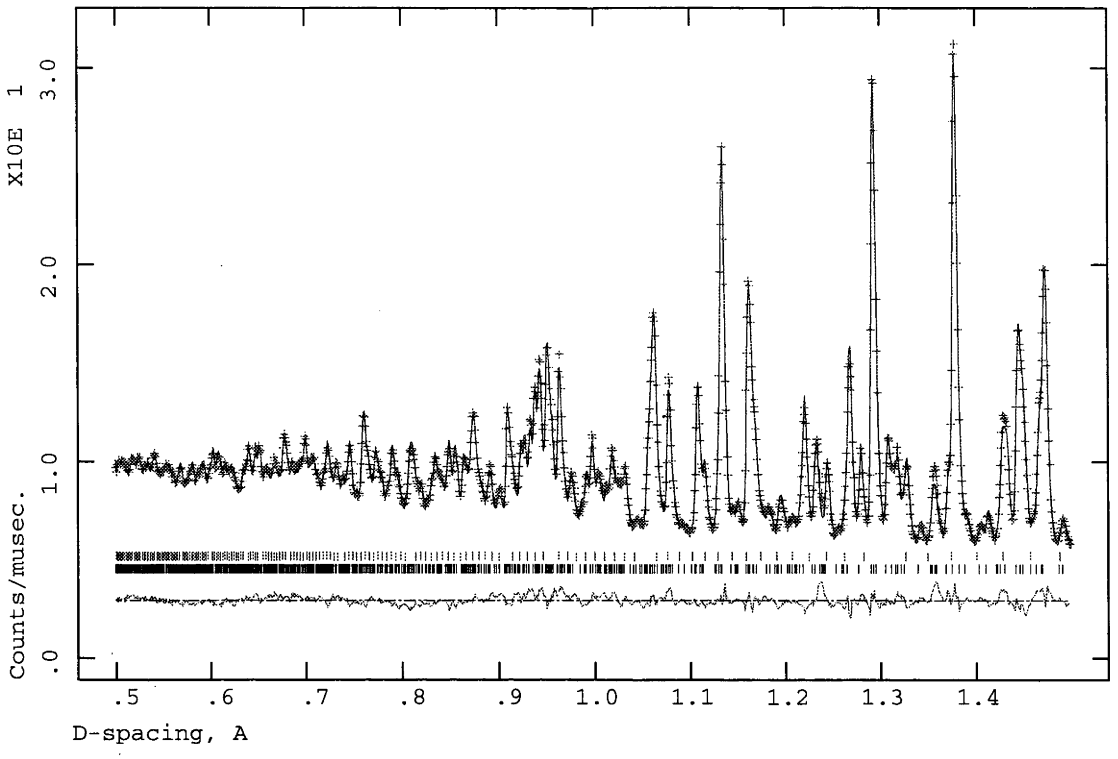
X10E 1
3.0
2.0
1.0
.0
Counts/musec.
.5
.6
.7
.8
.9
1.0
1.1
1.2
1.3
1.4
D-spacing, A

(a)

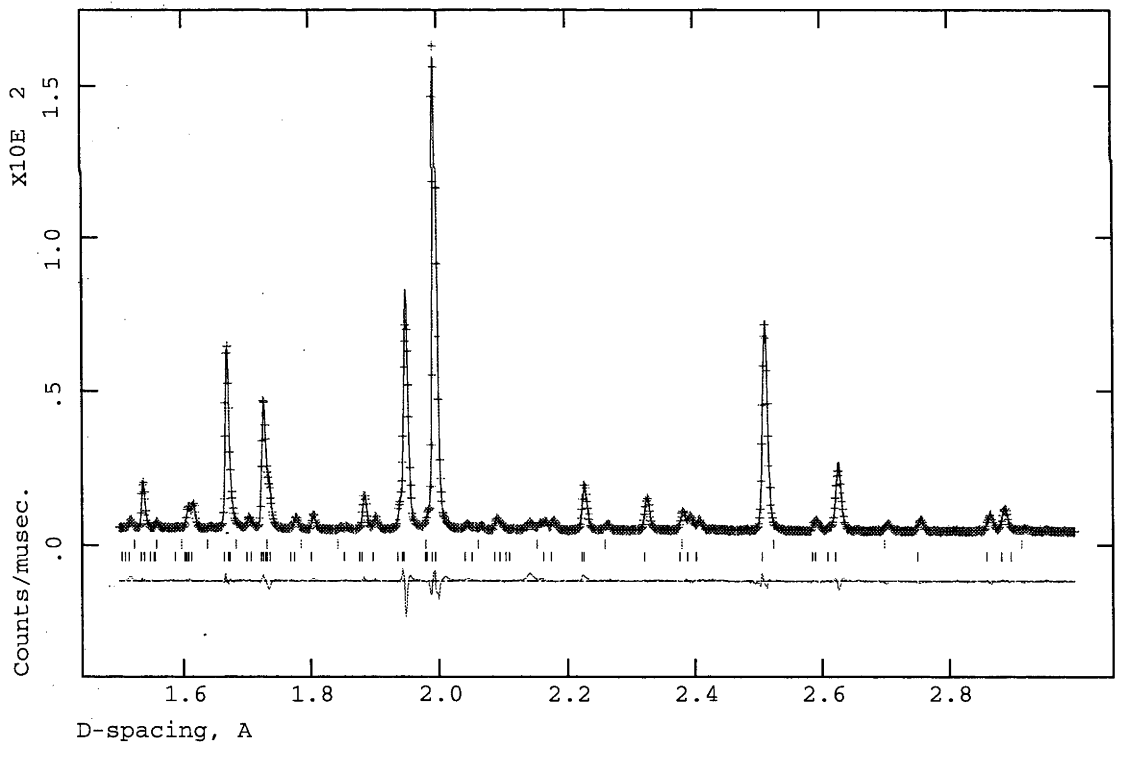
X10E 2
1.5
1.0
.5
.0
Counts/musec.
1.6
1.8
2.0
2.2
2.4
2.6
2.8
D-spacing, A

(b)

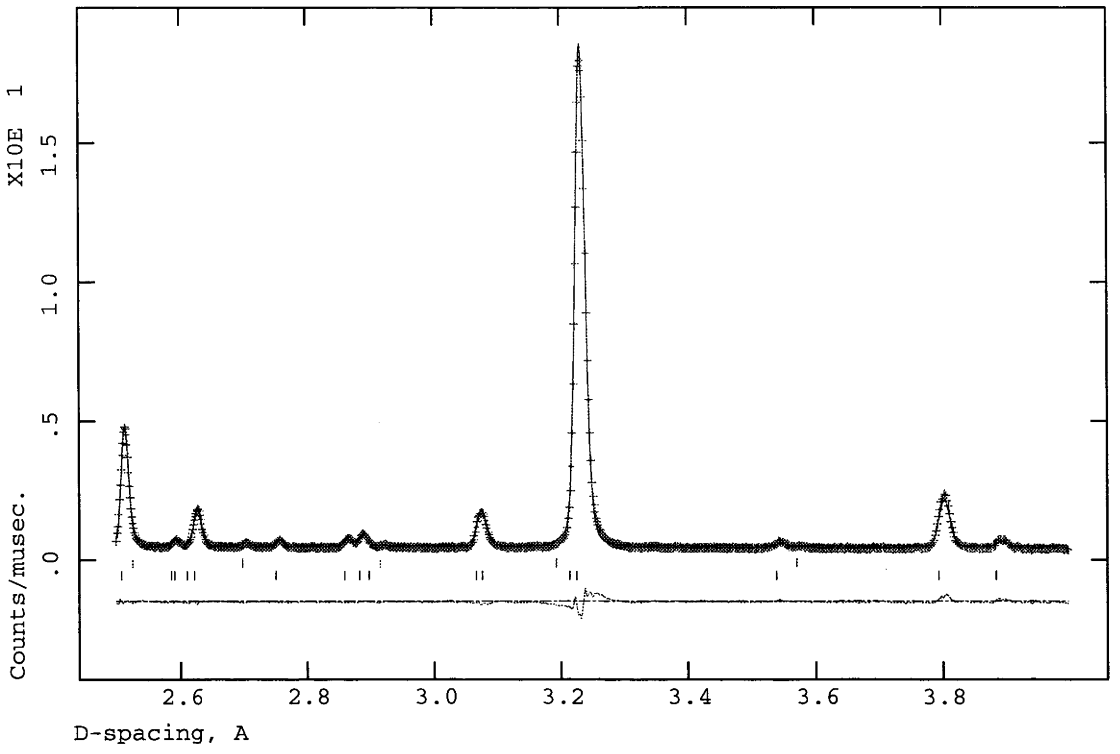

(c)

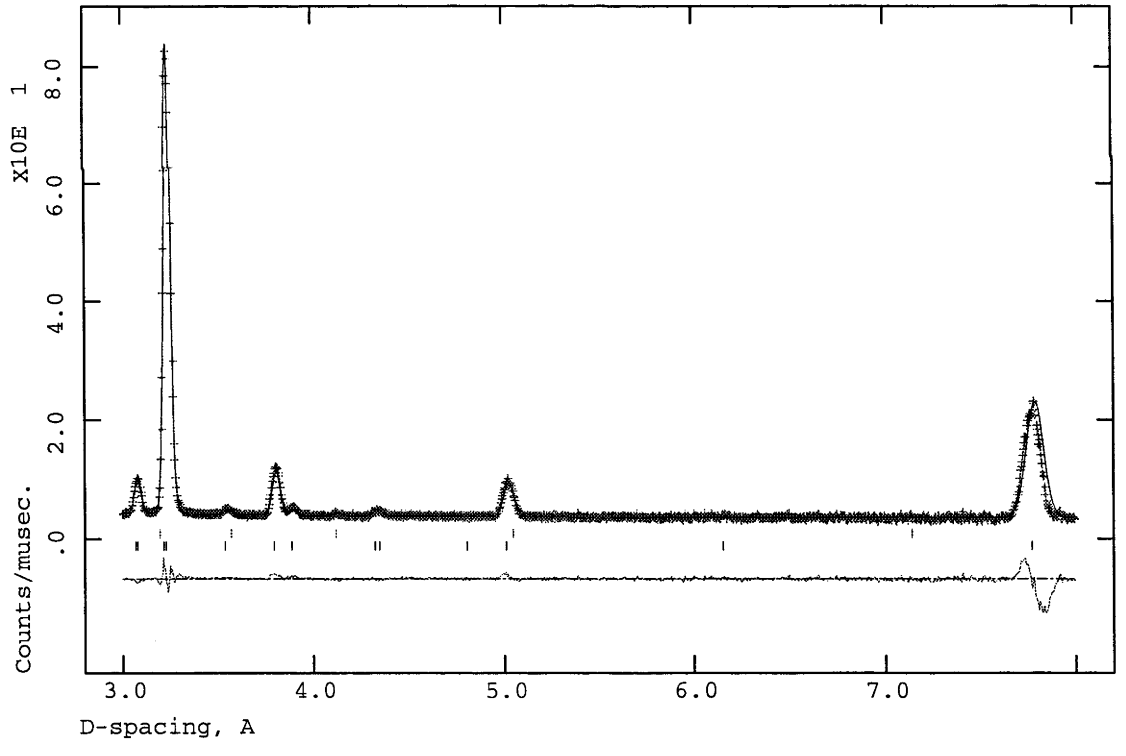

(d)

Figure 20. Observed (+), calculated and difference (bottom) neutron powder diffraction profiles for type Ia $Bi_{14}MoO_{24}$ at the (a, b) 145°, (c) 90° and (d) 35° detector banks of POLARIS. The top row of reflection markers refers to the γ-Bi_2O_3-type impurity.

4.1.3 Discussion

The final refined structure of $Bi_{14}WO_{24}$ is shown in Figure 21. That of $Bi_{14}MoO_{24}$ is completely isomorphous. Figure 21(*b*) and (*c*) are projections along the fluorite-type subcell directions according to the relationship described by Zhou (14). The metal atom array can be seen to closely preserve the fcc arrangement of the fluorite-type subcell. It is also clear that the oxygen atom array only deviates significantly from fluorite-type in the immediate vicinity of the W atoms, *i.e.* O1 and O3 are essentially the only non-fluorite-type oxygen atoms in the structure. These sites between them account for only 8 atoms out of 78 in the unit cell.

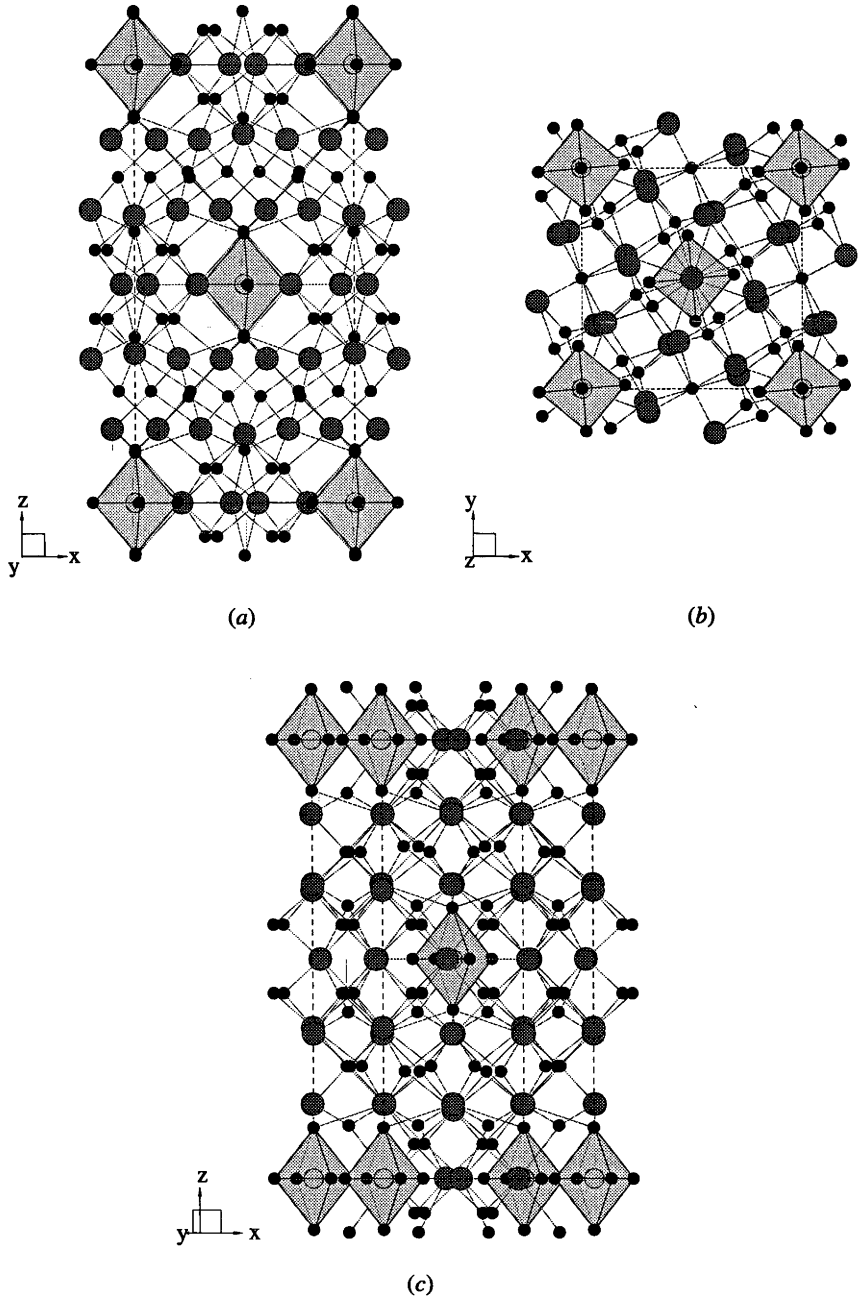

Figure 21. The final refined structure of type Ia $Bi_{14}WO_{24}$ viewed down the (a) [0 1 0], (b) [0 0 1] and (c) [1 3 0] directions. Bismuth atoms are darker than (average) WO_6 octahedra; oxygen atoms are black.

With such a bismuth-rich composition, the coordination environments of the Bi atoms (Figure 22) in $Bi_{14}WO_{24}$ may well be representative of those found in pure δ-Bi_2O_3. Discounting the long bonds to the non-fluorite type oxygen atoms O1 and O3, three different coordinations are seen to arise: Bi3 is surrounded by all eight oxygen atoms of this cube; Bi1 loses two adjacent oxygen atoms from the cube to form a distorted trigonal prism; and Bi2 loses two adjacent and one opposite oxygen atom from the cube to form a distorted square pyramid. The fact that all three have satisfactory calculated bond valences (Table 7), with the contributions of O1 and O3 being very small, indicates that all three coordination environments would be quite plausible in δ-Bi_2O_3 itself.

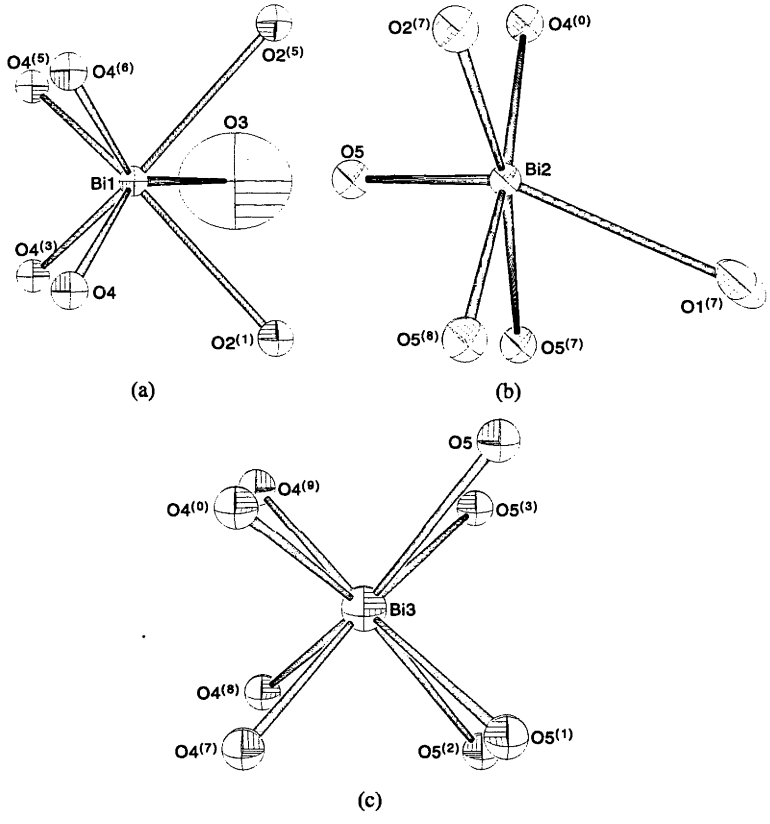

Figure 22. ORTEP plots (ellipsoid probability 50%) showing the coordination environments of (a) Bi1, (b) Bi2 and (c) Bi3 in the final refined structure of type Ia $Bi_{14}WO_{24}$. Symmetry codes: (1) –x, y, z; (2) –x, -y, z; (3) y, -x, z; (5) y, -x, -z; (6) x, y, -z; (7) –x + ½, -y + ½, -z + ½; (8) y + ½, -x + ½, -z + ½; (9) x + ½, y + ½, -z + ½; (0) –y + ½, x + ½, -z + ½.

In Figure 21, average WO_6 octahedra are depicted despite evidence from the refinement that only four out of six illustrated coordinating oxygen atoms are, on average, present around each W atom. This suggests that the coordination environment of W is in fact distorted tetrahedral. Clearly, a tetrahedron formed from one axial and three equatorial oxygen atoms of an average WO_6 octahedron would require serious local distortion to be chemically plausible. That such distortion may indeed occur is evidenced by the anisotropic displacement parameters perpendicular to the W-O bonds, which are large for O1 and extremely large for O3 (Figure 23).

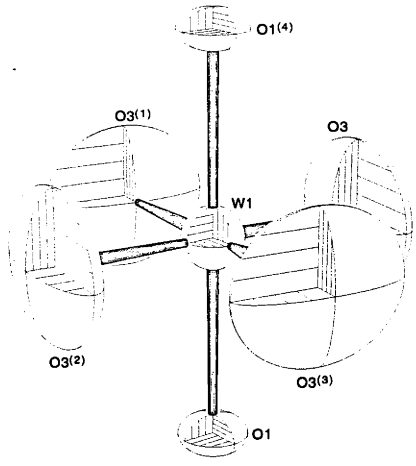

Figure 23. ORTEP plot (ellipsoid probability 50%) showing the coordination environment of W atoms in the final refined structure of type Ia $Bi_{14}WO_{24}$. Symmetry codes: (1) –x, y, z; (2) –x, -y, z; (3) y, -x, z; (4) -x, -y, -z.

The predominant motion of O1 and O3 perpendicular to W-O bonds is reasonable in terms of the bond valence sums (52) calculated for the final refined structure and presented in Table 7. When the occupancies of the O1 and O3 sites are taken into account, the bond valence requirements of W are fulfilled, *i.e.* no changes in W-O bond length are required for a WO_4 tetrahedron to be chemically plausible. Calculated bond valence sums for Bi and O atoms in pseudo-fluorite-type positions are also very reasonable. The only significant problem indicated by the bond valence sums is an apparent under-bonding of O1. No explanation can be offered other than to reiterate that this is a feature of the average position of O1, and not necessarily of its local position with respect to coordinating metal atoms.

Atom	$Bi_{14}WO_{24}$	$Bi_{14}MoO_{24}$
Bi1	2.96	2.96
Bi2	3.19	3.28
Bi3	2.67	2.83
W1 / Mo1	5.94	6.17
O1	1.22	1.13
O2	2.01	2.05
O3	2.11	2.05
O4	2.09	2.12
O5	2.10	2.11

Table 7. Bond valence sums for the final refined structures of type Ia $Bi_{14}WO_{24}$ and $Bi_{14}MoO_{24}$.

The finding that the crystal structures of type Ia $Bi_{14}WO_{24}$ and $Bi_{14}MoO_{24}$ are partially disordered is in itself significant. Their diffraction patterns contain large numbers of supercell reflections in addition to the fluorite-type subcell reflections, yet it appears that the majority of these are accounted for by small displacive modulations of those atoms remaining in pseudo-fluorite-type positions. The fact that a fully ordered model containing WO_4 tetrahedra could be proposed with only minor symmetry lowering (from $I4/m$ to $I\bar{4}$) strongly suggested such a model at the outset, however, insufficient evidence could be found in the observed

data. While it is possible that some of the disorder is a consequence of slight compositional inhomogeneities, the sharpness of the observed reflections is such that it still ought to be possible to refine a more ordered model (with larger atomic displacement parameters) if such order truly existed. The observation of such partial ordering for type Ia $Bi_{14}WO_{24}$ and $Bi_{14}MoO_{24}$ will inform subsequent structural studies in this Chapter.

As discussed in Chapter 1, a consequence of the disordered oxygen atom array of fluorite-type δ-Bi_2O_3 is that when considering the relationships of phases in this study to fluorite-type, it is appropriate to consider the metal atom array before the oxygen atom array. Such an approach is clearly justified in the case of type Ia $Bi_{14}WO_{24}$ and $Bi_{14}MoO_{24}$. In this context, the relationship of the metal atom array to that of fluorite-type is shown in Figure 24, by mapping the metal atom distribution in the supercell onto a 3 x 3 x 3 fluorite-type subcell array. The salient feature of Figure 24 is the absence of any nearest-neighbour W/Mo atoms; each is isolated from the others by the fluorite-type Bi atom array. Clearly, for phases with significantly higher *M* concentrations within a fluorite-type metal atom array, such isolation cannot persist.

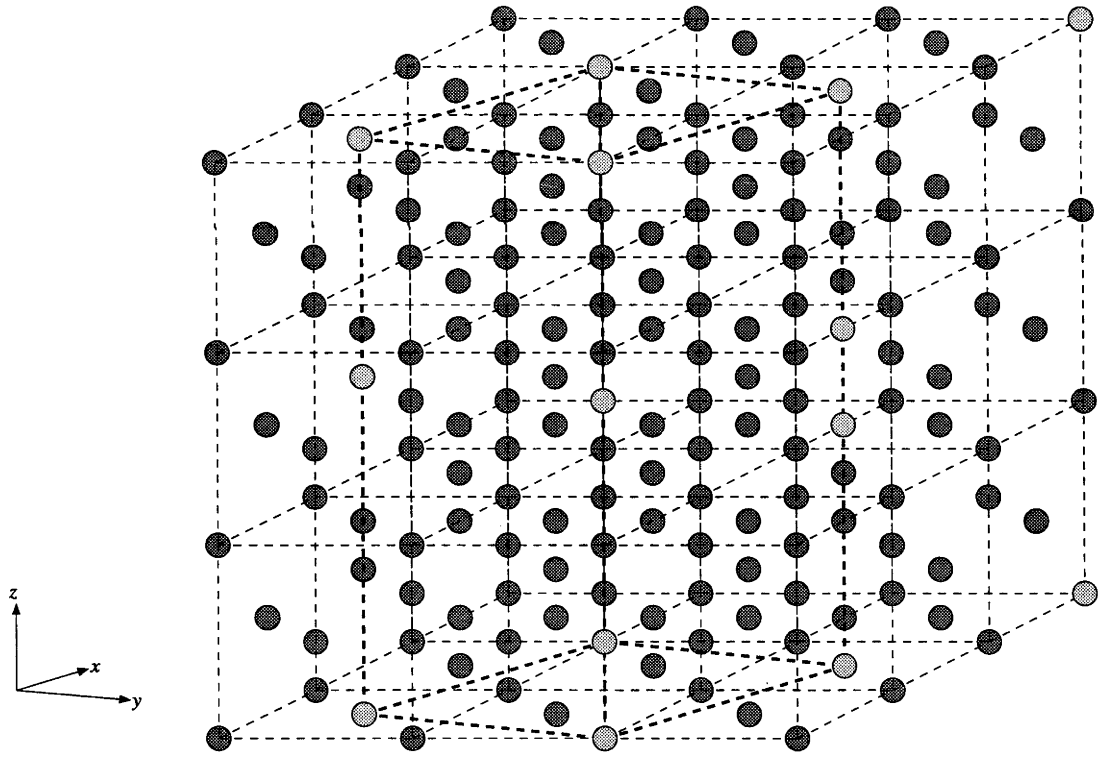

Figure 24. The metal atom array of type Ia $Bi_{14}(W/Mo)O_{24}$ mapped onto 3 x 3 x 3 average fluorite-type subcells. Dashed lines indicate the fluorite-type subcell grid, and heavy dashed lines indicate the supercell. Bismuth atoms are darker than W/Mo atoms.

4.2 Type II Bi_2O_3-Nb_2O_5 and Bi_2O_3-Ta_2O_5 (53)

Previous authors (15, 18) have proposed structural similarities between pyrochlore-type and type II phases in the Bi_2O_3-Nb_2O_5 and Bi_2O_3-Ta_2O_5 systems, based largely on a

characteristic diamond-like pattern of Bi/Nb or Bi/Ta metal atom ordering observed in projection along $<1\ 1\ 0>_f$ zone axis orientations in HRTEM. The proposed structural similarity was used, in conjunction with electron imaging and diffraction pattern simulation techniques, to produce superstructure models for various compositions within the solid solution. These models suggested that at any composition within the solid solution, niobium or tantalum atoms form M_7O_{30} or $M_{18}O_{72}$ clusters embedded within a fluorite-type δ-Bi_2O_3-related matrix. Both of these proposed clusters are extended, corner-connected, versions of the M_4O_{18} tetrahedral clusters depicted in Figure 2. The plausibility of these models has not been tested by any other techniques.

An inability to grow single crystals ruled out single crystal diffraction, while the difficulty in handling three-dimensional incommensurately modulated structures using a very small number of observed satellite reflections (8, 48) severely limited the structural information extracted from XRD. Miida and Tanaka (48) are the only authors to have attempted to refine compositional and displacive modulation wave amplitudes from XRD data, in a one-dimensional (along [1 1 1]*) rather than a fully three-dimensional refinement. An attempt was made to construct a three-dimensional model from the refined amplitudes of their one dimensional model, however, poor agreement was obtained for reflections not along <1 1 1>*. This was attributed to an incorrect relative phasing of the four lowest harmonic order, symmetry-allowed ε<1 1 1>* modulations, *i.e.* to a failure to properly take symmetry into account. Further structural characterisation of this phase clearly requires symmetry considerations to be properly accounted for.

4.2.1 Theory

In collaboration with Dr Ray Withers (53), the formalism of superspace symmetry has been exploited to parameterise both the underlying average structure as well as the compositional and displacive perturbations (or atomic modulation functions, AMFs) away from it which together define the $(1 - x)Bi_2O_3.xNb_2O_5$, $0.06 < x < 0.23$, incommensurately modulated structure. Expressions for the Bi/Nb and oxygen/vacancy ordering patterns characteristic of the solid solution have been derived in work due principally to Dr Withers, and are presented in the Appendix.

4.2.2 Discussion

Because the displacive relaxations of the metal and oxygen atoms will clearly be controlled by Bi/Nb metal atom and oxygen vacancy distributions, it is reasonable to focus on the metal atom and oxygen atom compositional AMFs defined in the Appendix. These AMFs are continuous three-dimensional functions of hyper-space, *i.e.* of $t_1 - \delta_1$ ($\equiv \varepsilon \mathbf{a}^*.(\mathbf{r}_\mu + \mathbf{T}) - \delta_1$), $t_2 - \delta_2$ ($\equiv \varepsilon \mathbf{b}^*.(\mathbf{r}_\mu + \mathbf{T}) - \delta_2$) and $t_3 - \delta_3$ ($\equiv \varepsilon \mathbf{c}^*.(\mathbf{r}_\mu + \mathbf{T}) - \delta_3$), as defined in Equations 6 and 7 (Appendix).

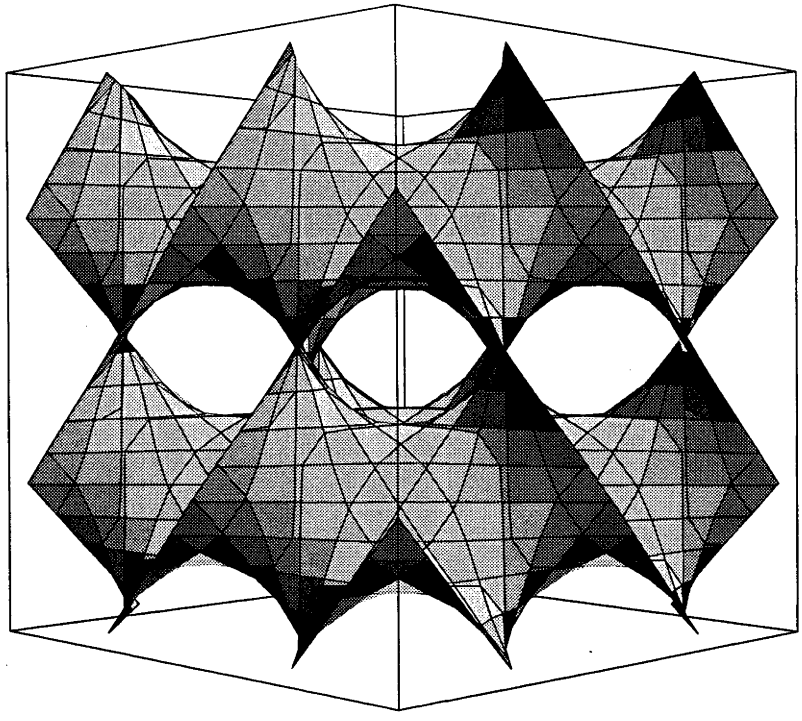

(a)

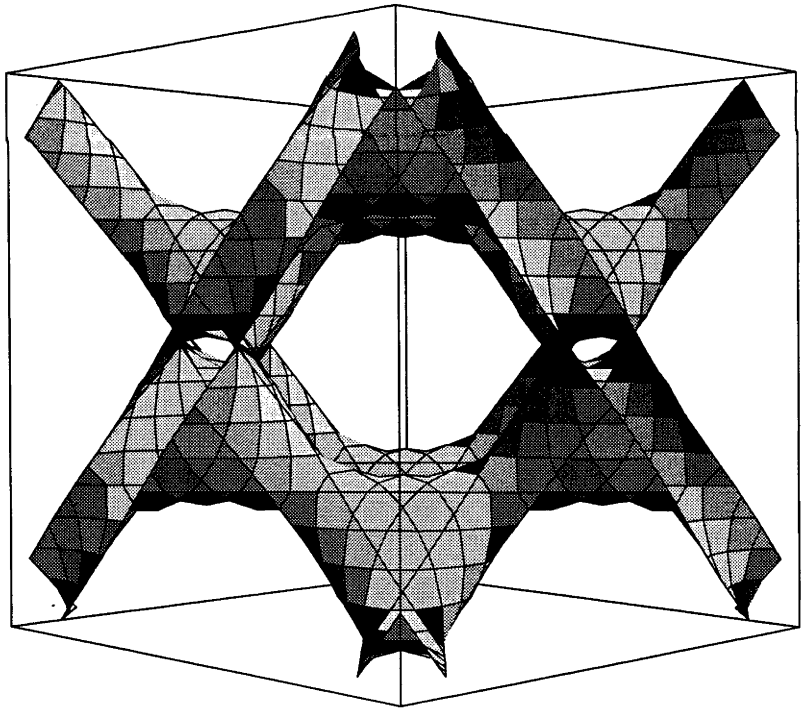

(b)

Figure 25. Perspective drawing along [1 1 0] in (t_1-δ_1), (t_2-δ_2), (t_3-δ_3), hyper-space of the metal atom compositional AMF defined by Equation 8 (Appendix) when (a) constant = 0 and (b) constant = -1.6.

The three-dimensional equivalent of a cosine-wave-like, one-dimensional AMF is a continuous three-dimensional surface. Consider, for example, the metal atom compositional

AMF describing Bi/Nb metal atom ordering defined in Equation 8 (Appendix). This equation describes surfaces parallel to one another in hyper-space on which metal atom composition is constant. It is intriguing to note that the surface describing the average metal atom composition (corresponding to setting the constant = 0 in Equation 8) has the same functional form as that given by von Schnering and Nesper (see Table 1 (54)) to describe the D Periodic Nodal Surface (PNS), and divides hyper-space into two congruent labyrinths of equal volume (54, 55). In this phase, the labyrinths will be bismuth-rich and niobium-rich with respect to the average metal atom composition (Figure 25*(a)*).

The metal atom compositional wave amplitude, $a_M(1\ 1\ 1)$ in Equation 6 (Appendix), determines the extent of the metal atom composition range as well as the rate at which it changes with the constant in Equation 8. Mathematically, it is the only parameter that needs to be determined for the metal atom compositional AMF to be fully characterised. Chemically, however, a fully characterised compositional AMF is unsatisfactory; a three-dimensional picture is needed of what a 'parallel to D PNS'-shaped, metal atom compositional AMF means.

Such a picture can be obtained by dividing hyper-space into fully occupied Bi and Nb regions by changing the value of the constant in Equation 8 such that the ratio of the hyper-space volumes on either side of the surface matches a desired Bi/Nb ratio. Figure 25*(b)* shows the surface which results when the constant = -1.6. (Note that this representation is imperfect because it assumes a sharp interface in hyper-space and hence generates too many higher order harmonics to be entirely consistent with experimental observation. (See Elcoro and Pérez-Mato (56) for a discussion of the effect of blurred AMF shapes and the corresponding real space consequences.) A three-dimensional (real space) representation of this 'parallel to D PNS' shape can then be obtained by placing a Bi atom at metal atom sites corresponding to the large volume side of the surface and Nb atoms at sites corresponding to the small volume side of the surface.

Figure 26 shows a projection along $[1\ 1\ 0]_f$ of the predicted Nb distribution corresponding to the AMF of Figure 25*(b)* for $\varepsilon = \frac{3}{8}$ and *(a)* $\delta_1 = \delta_2 = \delta_3 = 0$, *(b)* $\delta_1 = \delta_2 = \delta_3 = \frac{3}{16}$. In both cases the space group symmetry of the resultant 8 x 8 x 8 supercell is $Fd\bar{3}m$, but with the inversion centre on a metal atom in *(a)* and between metal atoms in *(b)*. Of 2048 metal atom sites in the supercell, 264 (12.89 %) are predicted to be Nb in *(a)* and 400 (19.53%) in *(b)*. (Note that if ε is irrational, the resultant Bi/Nb ratio is completely determined by the constant in Equation 8. If, however, ε is a rational fraction such as $\frac{3}{8}$, then the Bi/Nb ratio as well as the distribution of Nb atoms within the resultant supercell depends upon the choice of δ_1, δ_2 and δ_3). In both cases, isolated Nb atoms (*i.e.* those for which all twelve nearest neighbours in the fcc metal atom array are Bi) and two-coordinate Nb atoms (*i.e.* those with two nearest neighbour Nb atoms) are found. Also in evidence are infinite one-

dimensional strings of niobium atoms along three of the six $<1\ 1\ 0>_f$ directions, one perpendicular to each $<1\ 0\ 0>_f$ direction [*e.g.* the set $(1\ 1\ 0)_f$, $(1\ 0\ 1)_f$ and $(0\ 1\ 1)_f$].

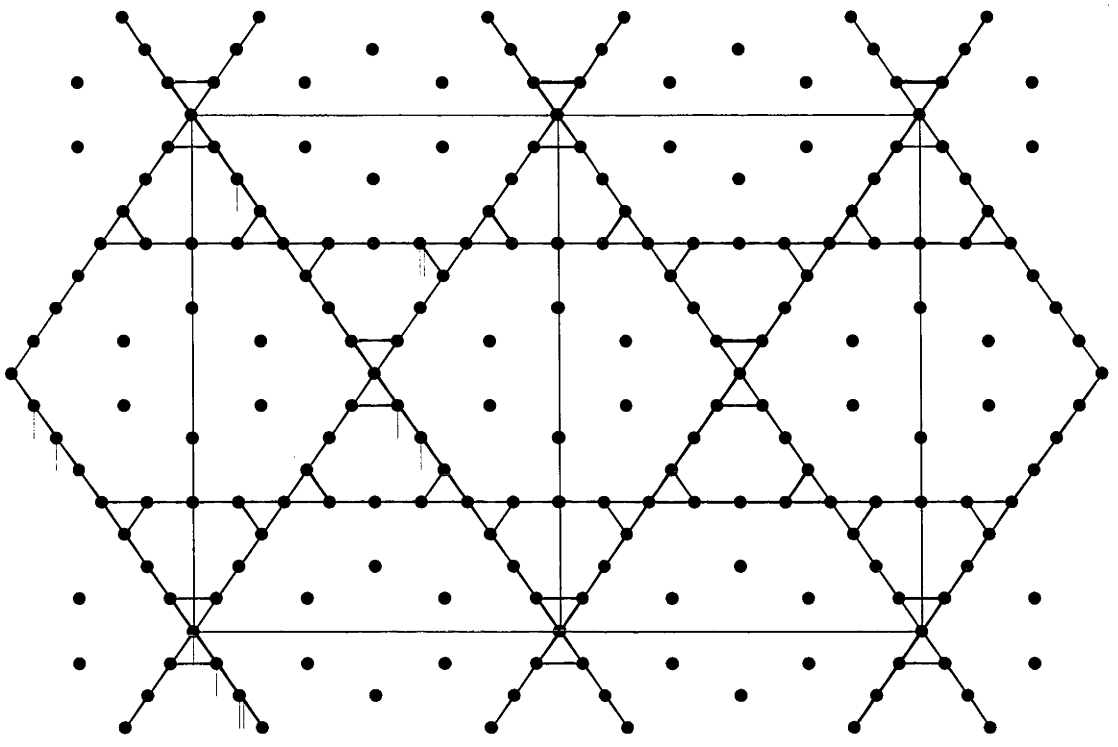

(a)

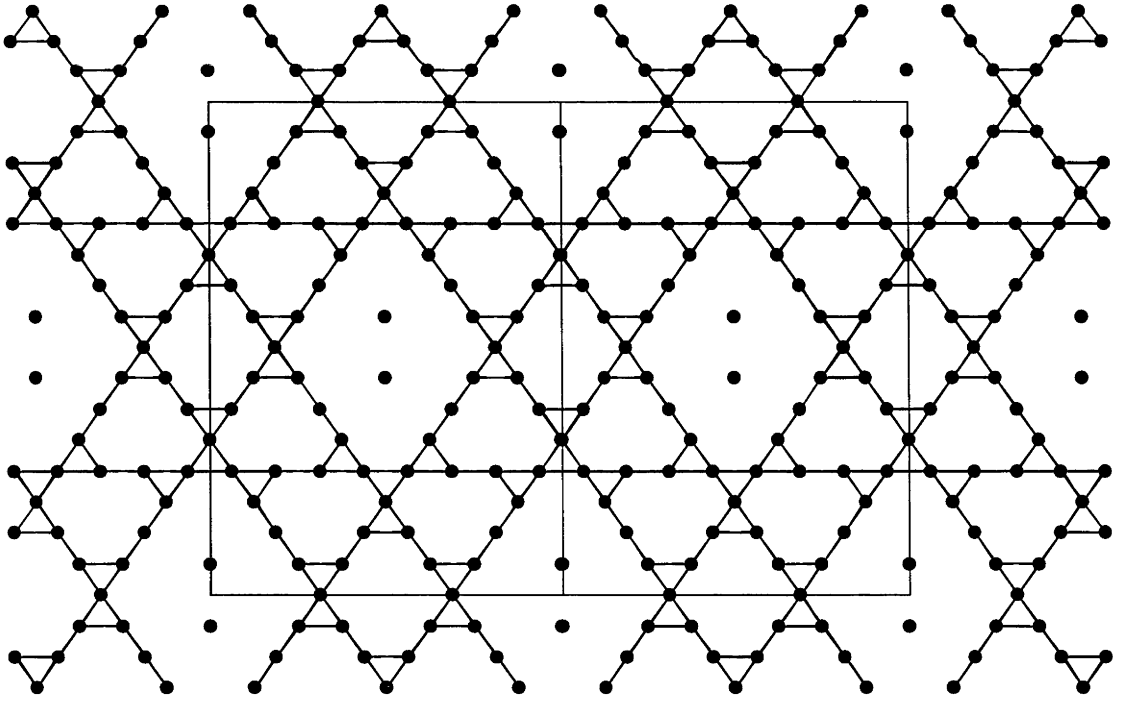

(b)

Figure 26. Projection along $[1\ 1\ 0]_f$ of the predicted Nb distribution corresponding to the AMF of Figure 25 for $\varepsilon = 3/8$ and (a) $\delta_1 = \delta_2 = \delta_3 = 0$, (b) $\delta_1 = \delta_2 = \delta_3 = 3/16$. Lines connecting nearest neighbour Nb atoms are marked.

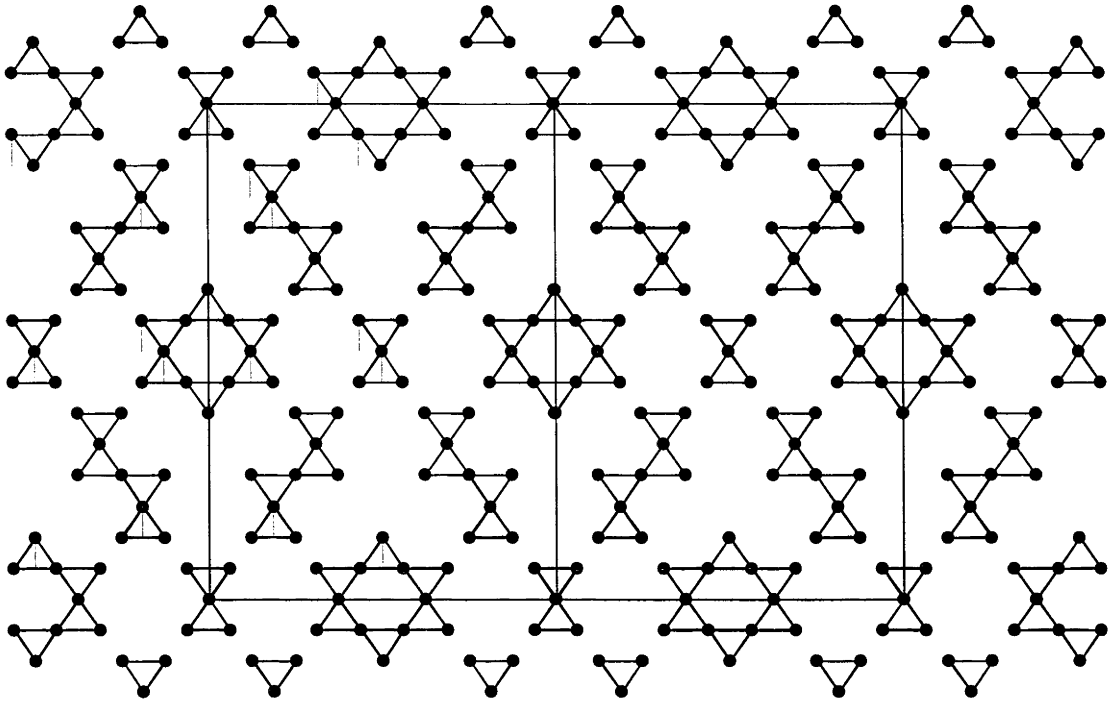

(a)

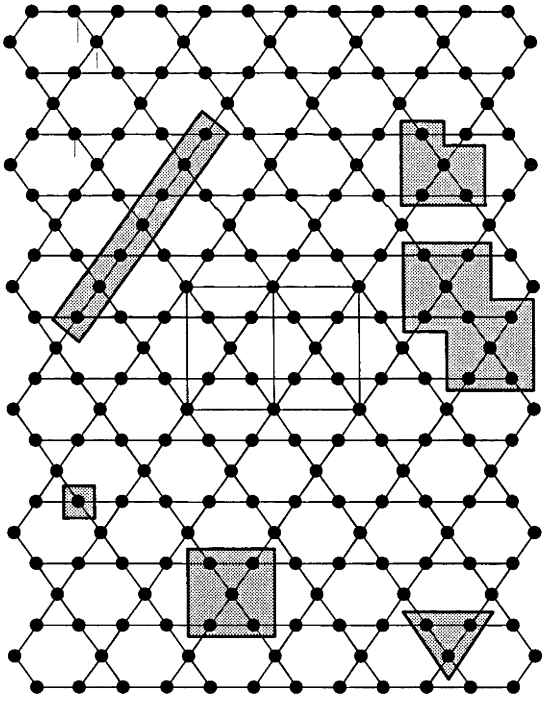

(b)

Figure 27. $[1\ 1\ 0]_f$ projections of Nb distributions in (a) the Tang and Zhou (18) model for type II $Bi_8Nb_2O_{17}$ (400/2048 metal atom sites are Nb) and (b) for $\varepsilon = ½$, $\delta_1 = \delta_2 = \delta_3 = 0$ corresponding to a hypothetical ideal $Bi_2Nb_2O_7$ pyrochlore. In (b), examples of various Nb_x clusters which occur within pyrochlore-type are highlighted.

Figure 27 shows $[1\ 1\ 0]_f$ projections of Nb distributions in *(a)* the Tang and Zhou (18) model for type II $Bi_8Nb_2O_{17}$ (400/2048 metal atom sites are Nb) and *(b)* for $\varepsilon = \frac{1}{2}$, $\delta_1 = \delta_2 = \delta_3 = 0$ corresponding to a hypothetical ideal $Bi_2Nb_2O_7$ pyrochlore. In *(b)*, examples

of various Nb_x clusters which occur within pyrochlore-type are highlighted. In the case of the Tang and Zhou model, all Nb atoms are either 3- or 6-coordinated by other Nb atoms such that each is part of at least one Nb_4 tetrahedron. The clusters thus formed do indeed occur within ideal pyrochlore-type (Figure 27*(b)*). The predicted Nb distributions of Figure 26*(a)* and *(b)*, however, show that these particular cluster types are not unique (Figure 27*(b)*) and that all cluster types (including isolated, two-, three-, four-, five- and six-coordinated Nb atoms) can be expected to occur at some point.

Given that each Nb atom is not necessarily part of an Nb_4 tetrahedron (Figure 26), it is not immediately obvious how oxygen vacancies should be distributed with respect to the Nb distribution (as it is in Figure 2). It is necessary to consider the oxygen atom compositional AMF defined in Equation 6 (Appendix) and approximated in Equation 9, which describes oxygen vacancy ordering, and how it might correlate with the metal atom ordering discussed above. This is complicated by the additional phase degree of freedom, $\varphi_O(1\ 1\ 1)$, in Equation 9. As a result of the complicated non-linear nature of Equation 9, a 'parallel to D PNS' shape only results if $\varphi_O(1\ 1\ 1)$ is a multiple of 90 °. Note that changing $\varphi_O(1\ 1\ 1)$ by 90 ° is equivalent to shifting the origin of the D PNS shape in Figure 25 by $(\frac{1}{4}\ \frac{1}{4}\ \frac{1}{4})$, as can be seen by substituting $\delta_i + \frac{1}{4}$, $i = 1, 2, 3$, for δ_i in Equation 9.

Direct evidence for the choice $\varphi_O(1\ 1\ 1) = +90$ ° or - 90 °, assuming $a_M(1\ 1\ 1)$ and $a_O(1\ 1\ 1)$ have the same sign, can be obtained by comparing experimental XRD and neutron powder diffraction data, particularly at high *d*-spacings ($\sin\theta/\lambda = \frac{1}{2}d < 0.1$) where compositional ordering is likely to make the major contribution to the structure factors of satellite reflections. In XRD data (Figure 14), the intensity of the <0 0 0 1 1 1>* reflection is relatively strong compared to the <1 1 1 $\bar{1}$ $\bar{1}$ $\bar{1}$>* reflection. In neutron powder diffraction data (Figure 28), however, <0 0 0 1 1 1>* is missing but <1 1 1 $\bar{1}$ $\bar{1}$ $\bar{1}$>* is relatively strong. It is not difficult to show (*e.g.* Equation 3 of Withers *et al.* (57)) that the compositional contribution to the structure factor of <0 0 0 1 1 1>* is proportional to $f_M^{av}a_M(1\ 1\ 1) + 2f_O^{av}a_O(1\ 1\ 1)\cos\varphi_O(1\ 1\ 1)$ whereas the equivalent contribution to the structure factor of <1 1 1 $\bar{1}$ $\bar{1}$ $\bar{1}$>* is given by $f_M^{av}a_M(1\ 1\ 1) + 2f_O^{av}a_O(1\ 1\ 1)\sin\varphi_O(1\ 1\ 1)$. The absence of <0 0 0 1 1 1>* and the strong presence of <1 1 1 $\bar{1}$ $\bar{1}$ $\bar{1}$>* in neutron powder diffraction data thus requires $\varphi_O(1\ 1\ 1)$ to be very close to either + 90 ° or - 90 °, assuming $a_M(1\ 1\ 1)$ and $a_O(1\ 1\ 1)$ have the same sign.

The O1 and O2 oxygen atom compositional AMFs therefore also have 'parallel to D PNS' shapes (Figure 25), although their origins in hyper-space are displaced by $(\pm\frac{1}{4} \pm\frac{1}{4} \pm\frac{1}{4})$ relative to the metal atom compositional AMF. Relative to the metal atom array, a real space picture of the effect of 'parallel to D PNS' shapes for oxygen atom AMFs can be obtained by setting $\varepsilon = \frac{3}{8}$, $\varphi_O(1\ 1\ 1) = +90$ ° or - 90 ° and constant = - 1.6 in Equation 8. Oxygen atoms are then placed on the large volume side of the corresponding

AMF and vacancies on the low volume side. Only the choice $\varphi_O(1\ 1\ 1) = +90°$ gives chemically plausible local NbO_x coordination polyhedra.

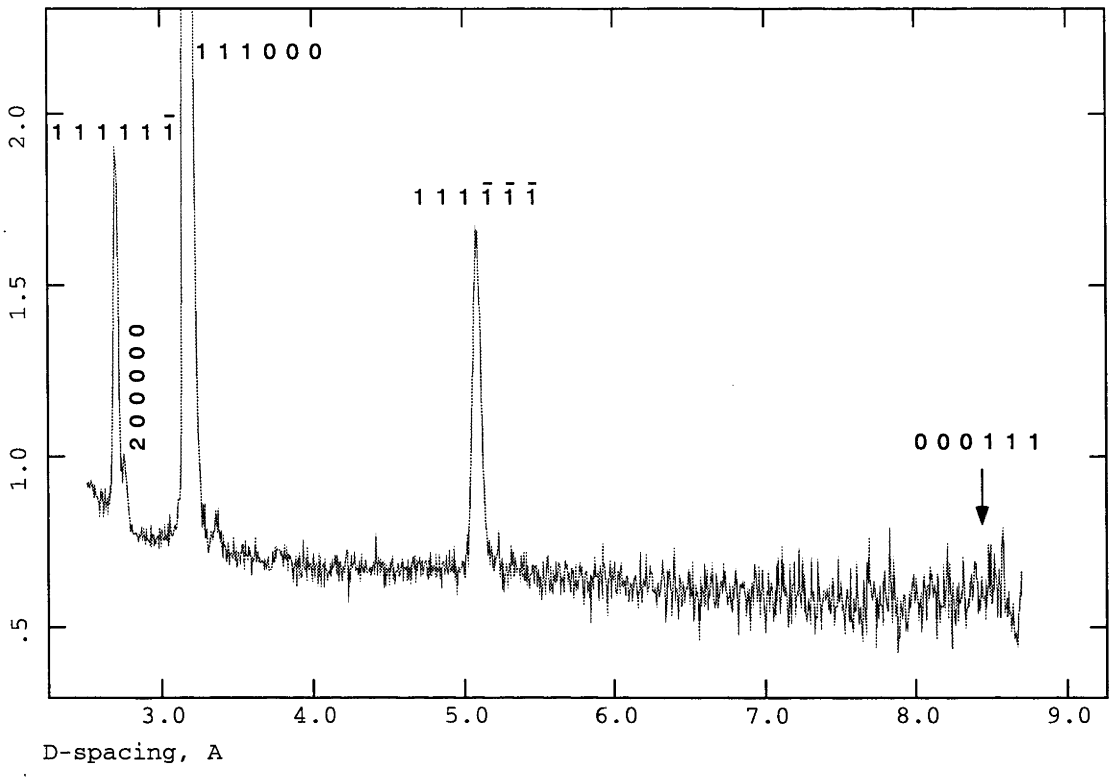

Figure 28. Neutron powder diffraction profile for type II $Bi_8Nb_2O_{17}$ collected at the 35 ° detector bank of POLARIS.

Figure 29 shows the predicted oxygen vacancy distributions corresponding to the Nb distributions of Figure 26, assuming $\varphi_O(1\ 1\ 1) = +90°$. In Figure 29*(a)* the 8 x 8 x 8 supercell contains 264 Nb atoms and 768 oxygen vacancies (assuming Bi^{3+} and Nb^{5+}, the nominal number of oxygen vacancies expected is 760), whereas in Figure 29*(b)* the supercell is predicted to contain 400 Nb atoms and 672 oxygen vacancies (assuming Bi^{3+} and Nb^{5+}, the nominal number of oxygen vacancies to be expected is 624). For $\varphi_O(1\ 1\ 1) = 90°$, the greatest number of oxygen vacancies surrounding a Nb atom is found to be 4 (corresponding to NbO_4 tetrahedral units), but if $\varphi_O(1\ 1\ 1) = 0°$ the same process predicts some Nb atoms surrounded by up to 5 and 6 nearest neighbour oxygen vacancies (corresponding to chemically unreasonable NbO_3 and NbO_2 units). Shaded tetrahedra correspond to oxygen vacancies which are tetrahedrally coordinated by Nb atoms. Two such units edge-connected form an Nb_7O_{30} cluster (favoured by Tang and Zhou (18)) and occur in Figure 29*(a)* and *(b)*. In addition, however, isolated NbO_4 tetrahedral units (rare but not unheard of, *e.g.* (58)) also occur in both Figure 29*(a)* and *(b)*, along with a range of other NbO_x coordination polyhedra. The resulting distributions are necessarily far more varied than the approach of Tang and Zhou (18) allowed.

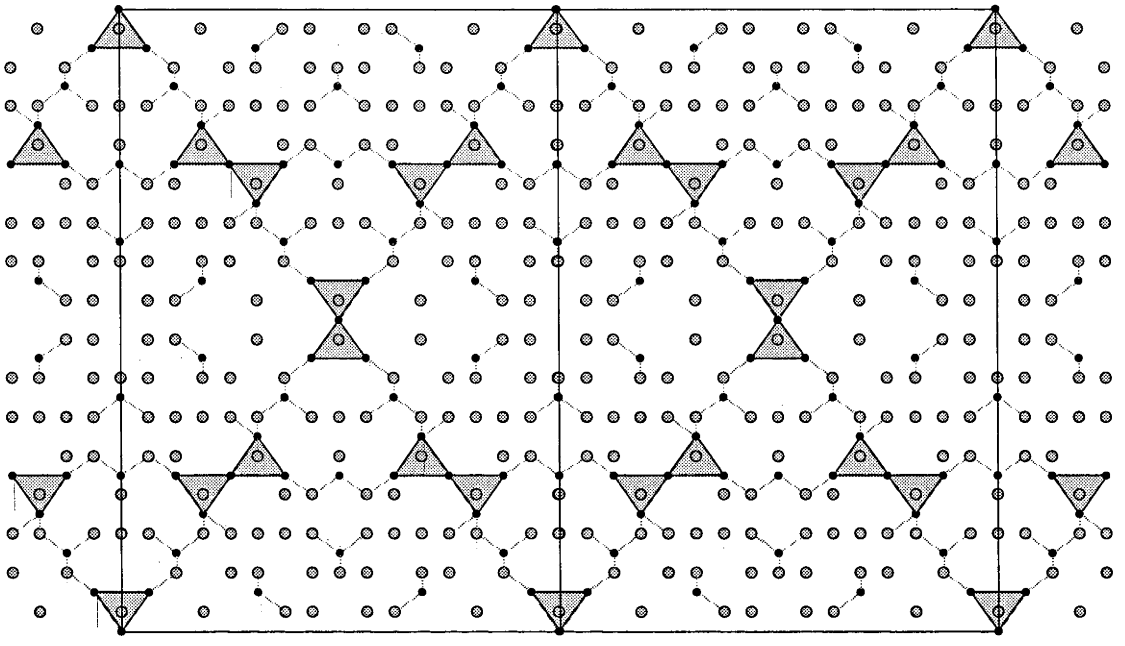

(a)

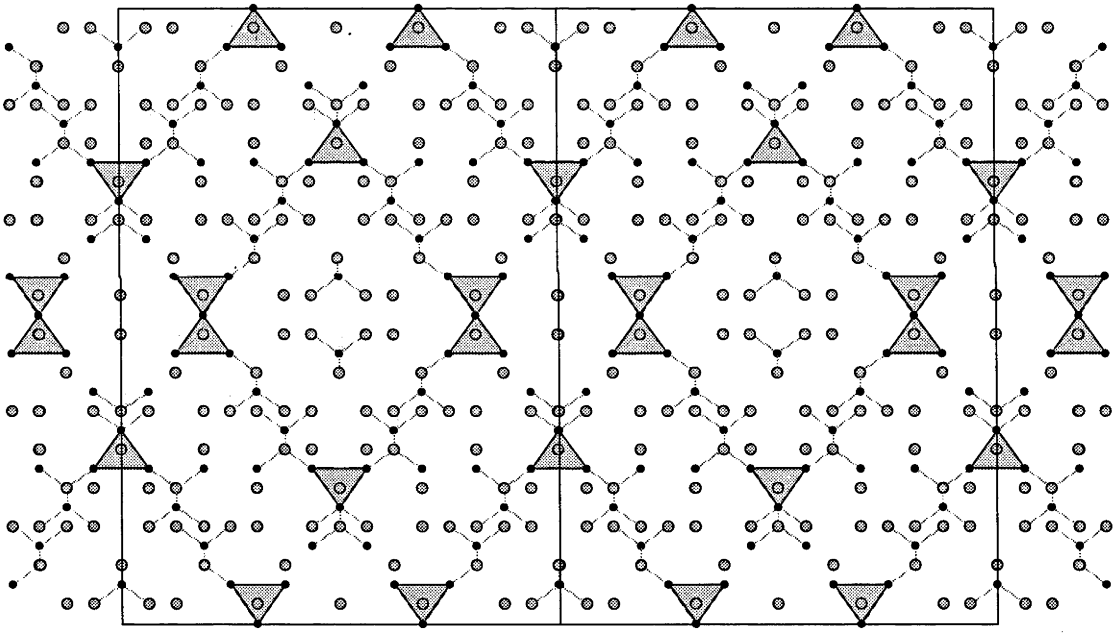

(b)

Figure 29. Predicted oxygen vacancy distributions (for $\varphi_O(1\ 1\ 1) = 90\ °$) accompanying the predicted Nb distributions of Figure 26 (and corresponding to the AMF of Figure 25(b) for $\varepsilon = 3/8$ and the choice (a) $\delta_1 = \delta_2 = \delta_3 = 0$ and (b) $\delta_1 = \delta_2 = \delta_3 = 3/16$. Shaded tetrahedra correspond to oxygen vacancies tetrahedrally coordinated by Nb atoms. Nb atoms are black and oxygen vacancies are grey.

Figure 30 shows part of the metal atom distribution for type II $Bi_8(Nb/Ta)_2O_{17}$, as shown in Figure 26*(b)*, mapped onto 3 x 3 x 3 fluorite-type subcells. This is the same projection shown for type Ia $Bi_{14}(W/Mo)O_{24}$ in Figure 24. In this case, however, *M* atoms are no longer isolated within the fluorite-type Bi atom array. The lines connecting nearest neighbour *M* atoms are shown, and extended to *M* atoms adjacent to the 3 x 3 x 3 fluorite-type block. These connections are continuous throughout the structure, creating two notable large-

scale motifs; infinite strings of M atoms along three of the six $<1\ 1\ 0>_f$ directions (one perpendicular to each $<1\ 0\ 0>_f$ direction), and corner-connected tetrahedral M_4 clusters. Both motifs are present in pyrochlore-type (Figure 2*(d)*), where each can be interpreted as a consequence of the other. In type II, however, it is clearly the string motif that leads to the cluster motif when strings intersect, as evidenced by the presence of incomplete tetrahedra (triangular faces) from complete strings. The importance of this $<1\ 1\ 0>_f$ string motif in such a wide-ranging solid solution strongly suggested that it would be of significance in other phases with similar compositions, and should therefore be considered in subsequent structure determinations.

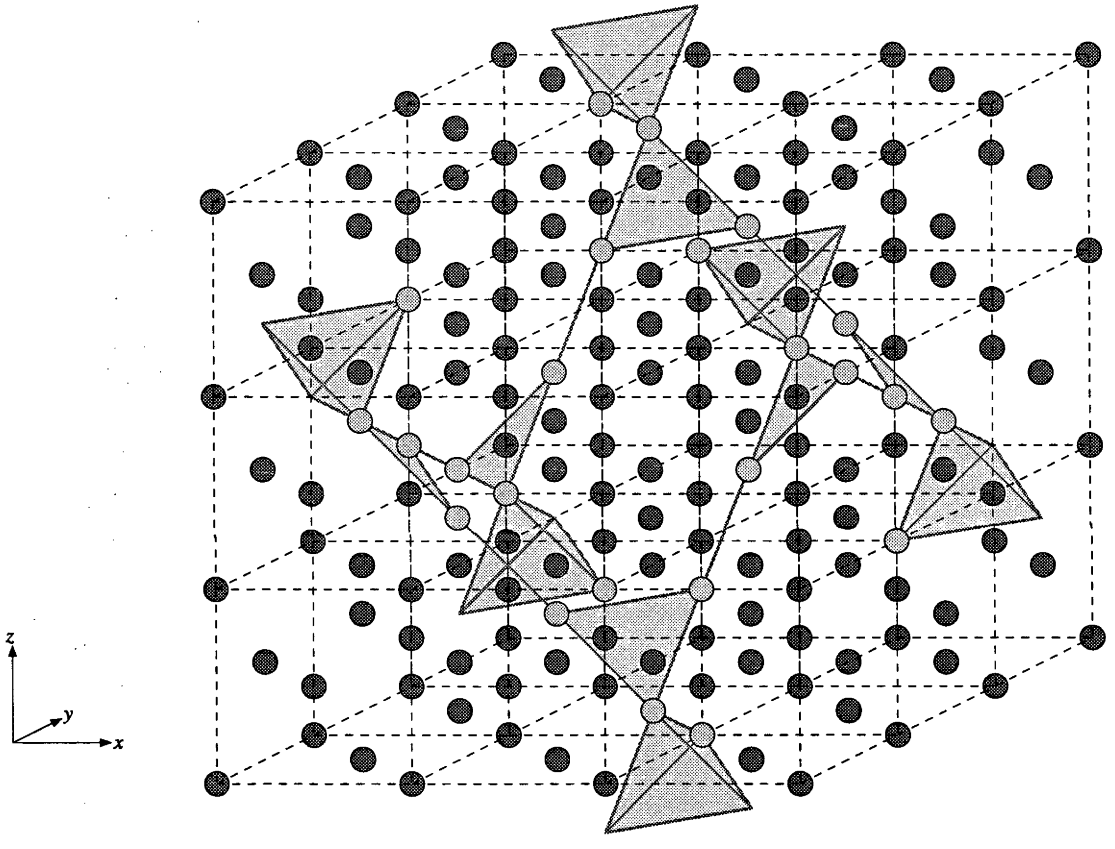

Figure 30. The metal atom array of type II $Bi_8(Nb/Ta)_2O_{17}$ when $\varepsilon = 3/8$ and $\delta_1 = \delta_2 = \delta_3 = 3/16$ mapped onto 3 x 3 x 3 average fluorite-type subcells. Dashed lines indicate the fluorite-type subcell grid. Bismuth atoms are darker than Nb/Ta atoms. Grey lines and shaded triangles and tetrahedra highlight nearest-neighbour Nb/Ta connections along $<1\ 1\ 0>_f$ directions.

4.3 Type III Bi_2O_3-Nb_2O_5: Bi_3NbO_7

As discussed in Section 3.3, Bi_3NbO_7 (the type III phase in the Bi_2O_3-Nb_2O_5 system) is clearly a superstructure of fluorite-type δ-Bi_2O_3. The possibility therefore exists of determining the structure absolutely given sufficient data. Two previous attempts have been made, using different data types and methodologies. Zhou *et al.* (17) used image matching / multi-slice methods with HRTEM and ED data to propose a model based on corner-connected tetrahedral Nb_4 clusters from pyrochlore-type (Figure 2) within a fluorite-type sublattice. The

interaction of the pyrochlore-type units with one another in this model creates some perovskite-type regions, such that the model appears to be a composite of fluorite, pyrochlore and perovskite types. This appeared reasonable given that the parent structure was clearly fluorite-type, that the slightly more bismuth-rich type II phase was thought to contain pyrochlore-type units (15, 18) and that the slightly more bismuth-poor type IV phase was thought to contain perovskite-type units (19, 20). However, in light of the significant re-interpretation in this study (Section 4.2) of the relationship of the type II structure to pyrochlore-type, it is clearly necessary to re-examine this type III model.

More recently, the structure of Bi_3NbO_7 was the subject of a single-crystal X-ray diffraction study by Aguardo *et al.* (26). This study makes no reference to the satellite reflections clearly visible in ED and XRD and makes use only of the subcell reflections. The structure of the subcell is refined in $Fm\bar{3}m$, *i.e.* as fluorite-type, with mixed occupancy on the metal atom site. Only one positional parameter is refined; the x-coordinate of the oxygen site, which was shifted from $x = \frac{1}{4}$ to $x = 0.182$ (*i.e.* ~ 0.4 Å shift) in order to introduce some disorder. It was unclear whether this was a deliberate simplification of the refinement intended to avoid the difficulties of solving the superstructure, or whether the failure to collect and refine satellite reflections was due to their absence in the crystal used. One possibility is that the synthesis of Aguardo *et al.* may have failed to control the stoichiometry adequately; the unit cell reported is cubic (rather than tetragonal) with a cell constant $a = 5.4788(9)$ Å, which from Figure 5 corresponds to the type II phase with a composition of approximately 21 mol% Nb_2O_5 (rather than 25 mol%).

Repetition of the synthetic work of Aguardo *et al.* suggested that the crystals studied could alternatively have been poorly crystallised Bi_3NbO_7. Crystals grown *via* the slow-cooling method reported and examined on a single-crystal diffractometer were found to have poor peak shapes, cubic (rather that tetragonal) subcells and far weaker satellite reflections than expected on the basis of XRD data. It appears that macroscopic crystals do not fully order due, presumably, to repeated twinning of the tetragonal, but pseudo-cubic, subcell. The poor peak shapes and cubic subcell may have been due to overlapping twin reflections, and the poor satellite intensities to their dilution by three-way twinning. Attempts to grow crystals by slow-cooling of two-phase mixtures with either types II or IV failed to produce crystals of higher quality.

In the absence of useful single crystals, neutron powder diffraction data were collected on HRPD and on POLARIS to be used in conjunction with the synchrotron XRD data in attempts to solve the structure of this phase.

In Section 3.4.1.1 it was shown that there was a probable relationship between the primary modulation wave-vector of the type II Bi_2O_3-Nb_2O_5 phase and that of type III

Bi_3NbO_7. The first stage in arriving at a structural model for Bi_3NbO_7 was therefore to consider the adjacent type II structure.

The unit cell of Bi_3NbO_7 can be described as an *F*-centered 3 x 3 x 7 supercell of fluorite-type, or alternatively as a $\frac{3}{2}(\mathbf{a}_f + \mathbf{b}_f)$, $\frac{3}{2}(-\mathbf{a}_f + \mathbf{b}_f)$, $7\mathbf{c}_f$ *I*-centered supercell. Either description is incompatible with a commensurate version of the type II phase, which ought to be cubic. Previous HRTEM work (16), however, indicates the way in which this incompatibility might be resolved; the structure is clearly 'layered', with a repeat of 3.5 fluorite-type unit cells. The observed image contrast implies the presence of a bismuth-rich layer in the metal atom array twice per unit cell perpendicular to the long (*c*) axis. The remaining metal atoms in the unit cell therefore comprise two 3 x 3 x 3 fluorite-type blocks, symmetrically related by the observed *F*-centering of the 3 x 3 x 7 type III supercell.

Modelling of the structure of Bi_3NbO_7 began by treating this 3 x 3 x 3 fluorite-type block analogously to the type II phase described in Section 4.2. In terms of the equations described in Appendix A.2, this corresponds to the choice $\varepsilon = \frac{1}{3}$. The superspace group symmetry of the type II phase $P{:}Fm\bar{3}m{:}Fd\bar{3}m$ can then be reduced to a conventional space group symmetry for certain choices of δ_1, δ_2 and δ_3. The highest possible resultant 3 x 3 x 3 space group symmetry consistent with a tetragonal 3 x 3 x 7 supercell is $F\bar{4}3m$, obtained when $\delta_1 = \delta_2 = -\frac{1}{8}$, $\delta_3 = \frac{3}{8}$. The $\bar{4}3m$ point group symmetry of this space group is essentially that of a tetrahedron.

Incorporating two such $F\bar{4}3m$ blocks into the 3 x 3 x 7 supercell, and taking into consideration the observed centering, the resultant space group symmetry reduces to $F\bar{4}2m$ with respect to the 3 x 3 x 7 supercell, or $I\bar{4}m2$ (# 119) with respect to the $\frac{3}{2}(\mathbf{a}_f + \mathbf{b}_f)$, $\frac{3}{2}(-\mathbf{a}_f + \mathbf{b}_f)$, $7\mathbf{c}_f$ *I*-centered supercell. This symmetry drop can be thought of in terms of 'stretching' a tetrahedron along its $\bar{4}$ axis; its $\bar{4}$ axis, 2-fold axis and mirror plane are preserved but its 3-fold axis is broken. The space group $I\bar{4}m2$ is compatible with the selected area ED observations in Section 3.2.2.1, which suggested a maximum symmetry space group *I4/mmm* (adding an inversion centre to a point group symmetry of $\bar{4}m2$ implies Laue symmetry of 4/*mmm*). The space group symmetry is lowered by breaking the mirror plane perpendicular to *c*, a symmetry element that was not compatible with the 3 x 3 x 3 block concept. The presence or otherwise of an inversion centre is difficult to detect by selected area ED.

This *I*-centered ($\frac{3}{2}(\mathbf{a}_f - \mathbf{b}_f)$, $\frac{3}{2}(\mathbf{a}_f + \mathbf{b}_f)$, $7\mathbf{c}_f$) cell contains 3 x 3 x 7 x 2 = 126 metal atom sites, of which 32 (25.4 %) should be niobium to most closely match the composition determined (Section 3.3.1) from starting materials in synthesis as 25 % and by EDXA as 25.5(2) %. The proposed model calls for two of the 14 metal atom layers perpendicular to the long axis *c*, at $z = 0$ and $z = \frac{1}{2}$, to be pure bismuth. The 3 x 3 x 3 fluorite-type blocks should therefore each contain 32 Nb atoms, *i.e.* 29.63 %.

Low-angle (5 - 45 °2θ) synchrotron XRD data were the most sensitive available to Bi/Nb metal atom compositional ordering, due to the relative insensitivity of X-rays (compared with neutrons) to the presence of oxygen atoms and due to the dominance of compositional information over displacive information at low angle (particularly at < ~15 °2θ). Fourier difference techniques were carefully used with these data in order to find a metal atom compositional ordering pattern that satisfied both the low angle XRD data and the required composition. One solution above all others investigated was found to give a remarkably good fit to the low angle satellite reflections, ignoring any displacive modulation away from the fluorite-type subcell positions. Refining overall isotropic displacement parameters for each metal atom type gave refinement statistics $R_p = 0.0381$, $wR_p = 0.0687$, $R(F^2) = 0.1725$, $\chi^2 = 10.26$. This model is shown in Figure 31 (note that the standard $I\bar{4}m2$ setting is used) and the coordinates listed in Table 8. The corresponding calculated, observed and difference XRD profiles are shown in Figure 32.

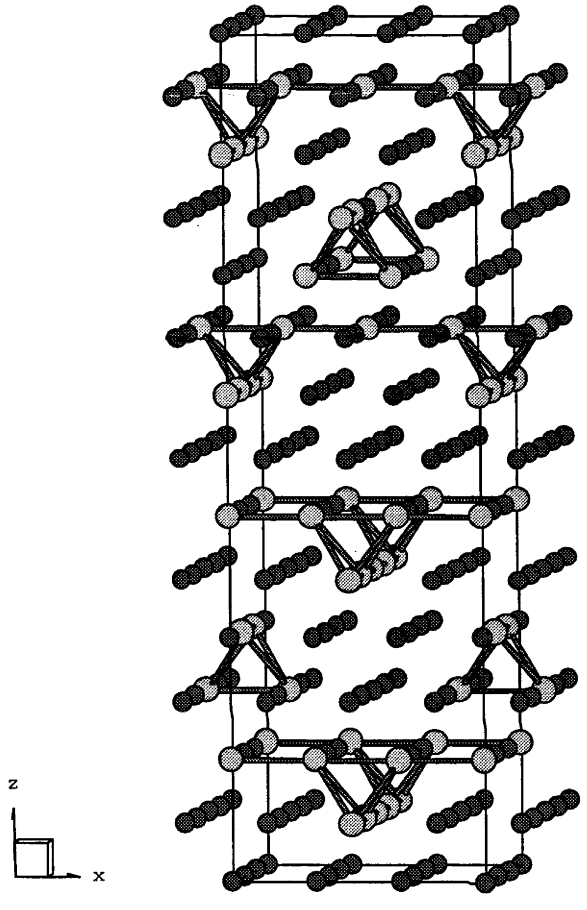

Figure 31. The metal atom compositional ordering model of type III Bi_3NbO_7 viewed close to the [0 1 0] ≡ [1 1 0]$_f$ direction. Nb-Nb nearest neighbour contacts are shown. Bismuth atoms are darker than niobium atoms.

Despite the quality of the fit to observed low-angle XRD data, this model is not immediately or intuitively satisfying. In the case of Bi_2O_3-$(Nb/Ta)_2O_5$ type II (Section 4.2.2), two pyrochlore-type structural motifs could be considered as having been incorporated into the fluorite-type matrix, and while this model possesses both it cannot be fully explained in

terms of either. The first such motif consists of niobium atoms in the form of tetrahedral clusters with nearest neighbour niobium atoms along <1 1 0>$_f$ directions. An oxygen-deficient fluorite-type lattice can fully order around such a unit to create tetrahedra of NbO_6 octahedra, as shown in Figure 2 and Figure 3*(c)*. This approach allows niobium tetrahedra to be corner-connected (as in actual pyrochlore-type) but not edge- or face-connected. The model shown in Figure 31 goes some way towards fulfilling this ideal, with the majority of niobium atoms in 6 isolated tetrahedra. In addition, however, 8 additional niobium sites (Nb3 and Nb5) are located between these tetrahedra.

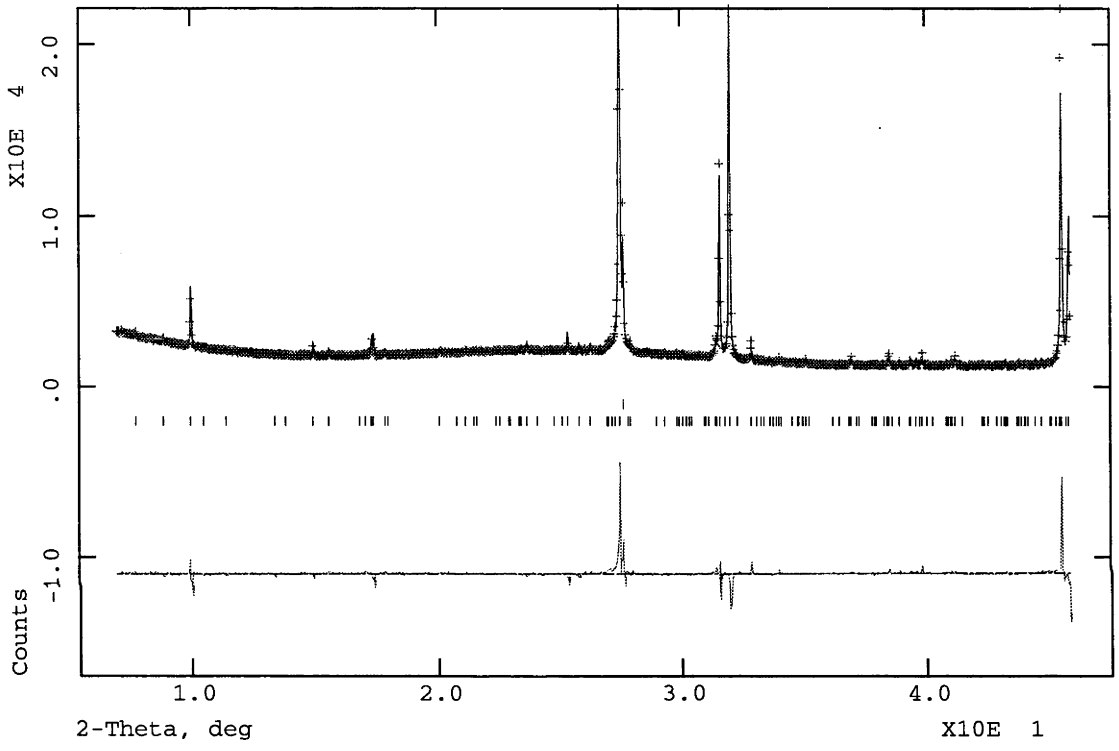

Figure 32. Observed (+), calculated and difference (bottom) low-angle XRD profile for the metal compositional ordering model of type III Bi_3NbO_7. The scale is enlarged in order to highlight the satellite reflections. The top row of reflection markers refers to the Si standard.

On consideration, it is not in fact possible to construct a model of the required composition in this space-group based solely on Nb_4 tetrahedra while retaining the two pure bismuth layers. If all 8 non-tetrahedral niobium atoms were removed, two Nb_4 tetrahedra would be required to restore the correct stoichiometry. These could only be incorporated by destroying the integrity of the pure bismuth layers, therefore more complex units of corner connected tetrahedra must be invoked. The $3\mathbf{a}_f$, $3\mathbf{b}_f$ fluorite-type basal plane of the supercell does not, however, permit continuous strings of corner-connected Nb_4 tetrahedra to be constructed, and therefore the symmetry would have to be lowered to allow any units more complex than isolated tetrahedra. In particular, the $\bar{4}$ element would be destroyed, reducing the cell symmetry from tetragonal to orthorhombic. Given that no orthorhombic distortion is observed, even in high-angle synchrotron XRD data, it is very hard to justify this lowering of

symmetry. The model proposed here therefore incorporates the Nb_4 tetrahedral motif from pyrochlore-type as far as is possible in a tetragonal space group.

The alternative pyrochlore-type structural motif incorporated into the fluorite-type matrix in Bi_2O_3-$(Nb/Ta)_2O_5$ type II is continuous strings of corner-connected NbO_6 octahedra along $<1\ 1\ 0>_f$ directions. In pyrochlore-type itself, these strings can be identified along all six $<1\ 1\ 0>_f$ directions (Figure 3*(a)* and *(c)*); in type II, they are only evident along three of the six (Figure 30). In Figure 31, such strings are only visible along two $<1\ 1\ 0>_f$ directions ([1 0 0] and [0 1 0] of the *I*-centered supercell).

Atom	*x*	*y*	*z*	U_{iso} (Å^2)
Nb1	0.66667	0.00000	0.14286	0.026(7)
Nb2	0.50000	0.16667	0.07143	0.026(7)
Nb3	0.00000	0.00000	0.14286	0.026(7)
Nb4	0.66667	0.00000	0.71429	0.026(7)
Nb5	0.50000	0.50000	0.07143	0.026(7)
Bi1	0.83333	0.16667	0.21429	0.056(2)
Bi2	0.66667	0.00000	0.28571	0.056(2)
Bi3	0.16667	0.00000	0.50000	0.056(2)
Bi4	0.66667	0.00000	0.85714	0.056(2)
Bi5	0.66667	0.00000	0.57143	0.056(2)
Bi6	0.00000	0.00000	0.28571	0.056(2)
Bi7	0.33333	0.00000	0.00000	0.056(2)
Bi8	0.00000	0.00000	0.00000	0.056(2)
Bi9	0.16667	0.16667	0.07143	0.056(2)
Bi10	0.16667	0.16667	0.35714	0.056(2)

Table 8. Fractional atomic coordinates and equivalent isotropic displacement parameters for the metal compositional ordering model of type III Bi_3NbO_7.

Again, however, on consideration it becomes apparent that complete adoption of this $<1\ 1\ 0>_f$ string motif is precluded by the nature of the unit cell. Continuous strings cannot be accommodated in the four $<1\ 1\ 0>_f$ directions which have a component along *c* without some disjunction. Even with the presence of such a disjunction (on the pure bismuth layers), it would still be necessary to break tetragonal symmetry in the *I*-centered cell to accommodate these strings. Furthermore, in the proposed metal atom ordering model, the isolated Nb_4 tetrahedra can be interpreted as continuous strings identical to those containing the other niobium atoms but with only $\frac{2}{3}$ occupancy (Bi6 being a bismuth site rather than a niobium site), an unavoidable consequence of the composition. In this sense, the proposed model incorporates $<1\ 1\ 0>_f$ niobium strings as far as is possible in a tetragonal space group.

Given that the structure of Bi_3NbO_7 is a $\frac{3}{2}(\mathbf{a}_f - \mathbf{b}_f)$, $\frac{3}{2}(\mathbf{a}_f + \mathbf{b}_f)$, $7\mathbf{c}_f$ superstructure of fluorite-type, that the cell is tetragonal and that it contains two pure bismuth layers perpendicular to *c*, the proposed model is clearly more probable than any alternative. It has the most probable symmetry, it incorporates niobium atoms in the most chemically sensible

way (according to the ordering scheme of the archetypal pyrochlore-type) and it fits the low angle XRD data remarkably well without the introduction of any displacive modulations from a fluorite-type parent.

Although Zhou *et al.* (17) give no coordinates, space group or even crystal system for their metal atom ordering model, it is clear from the (incomplete) picture published that its symmetry is lower than tetragonal, possibly even lower than orthorhombic. As discussed above, there is simply no evidence for this symmetry lowering. The picture published by Zhou *et al.* is actually very hard to interpret. It appears to show 8 of the 14 metal atom layers perpendicular to *c* as a continuous network of corner-connected NbO_6 octahedra on $[1\ 1\ 1]_f$ planes, an impossible arrangement given that the 3 x 3 x 7 fluorite-type supercell they use is quite clearly *F*-centered. The model of Agauardo *et al.* (26) only refers to the subcell and therefore cannot usefully be compared with the model proposed in the present study.

Given the above metal atom compositional ordering model, it was hoped that it would be possible to fully solve and refine this structure using only powder data. It was possible to freely refine all metal atom positions (still with two overall isotropic displacement parameters) using synchrotron XRD data to 135 °2θ, giving overall refinement statistics $R_p = 0.0316$, $wR_p = 0.0543$, $\chi^2 = 5.374$. Final metal atom displacements were all very small (≤ 0.1 Å from the fluorite-type parent positions), as expected. It was found, however, when the refinement was repeated with different initial displacement patterns that the final displacement pattern was not reproducible but that the refinement statistics were much the same. It was evidently possible to completely fit the high-angle XRD data simply through an increased number of variables in the refinement, with the refined coordinates merely representing a slight randomisation of the metal atom array. Synchrotron XRD data contained too much reflection overlap at high angle to absolutely determine the subtle displacive modulations of the metal atom array.

A fluorite-type oxygen atom array (with occupancies of 87.7 % to conform to stoichiometry) was then added to the compositionally ordered fluorite-type metal atom array. This model was compared to observed neutron powder diffraction data while refining overall isotropic displacement parameters for each atom type. The results are shown in Figure 33. The refinement statistics for the low *d*-spacing data set shown were $R_p = 0.2239$, $wR_p = 0.2559$, $R(F^2) = 0.2929$ and for the high *d*-spacing data set $R_p = 0.1029$, $wR_p = 0.1411$, $R(F^2) = 0.0631$. It is immediately obvious from Figure 33 that these data contain a vast amount of information about oxygen vacancy ordering (at high *d*-spacing) and displacive relaxation (at low *d*-spacing), suggesting that the oxygen atom array is highly (or possibly fully) ordered.

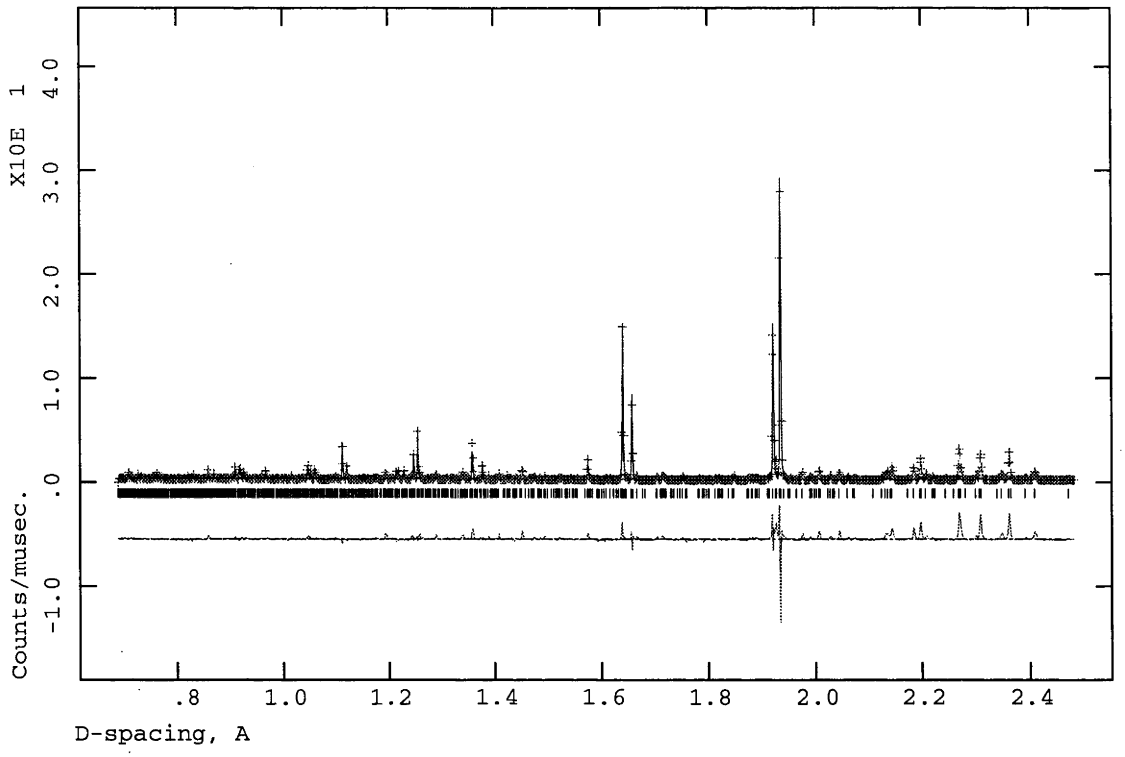

(a)

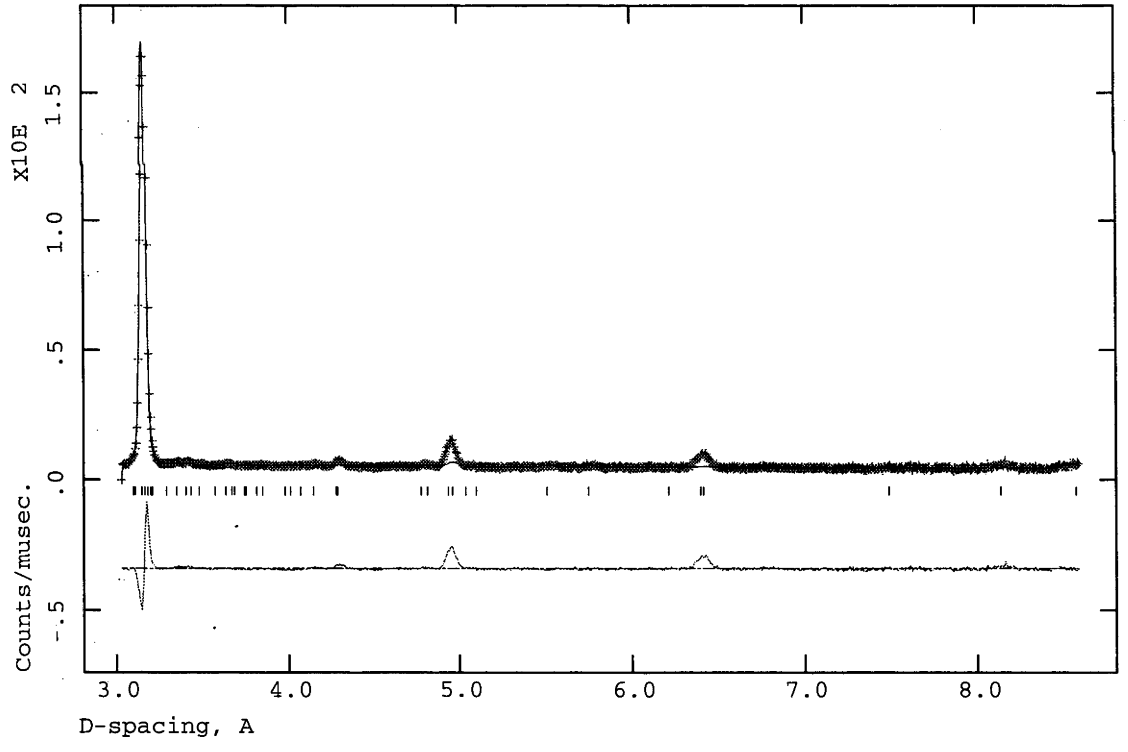

(b)

Figure 33. Observed (+), calculated and difference (bottom) neutron powder diffraction profiles for the metal atom compositional ordering model of type III Bi_3NbO_7 plus a fluorite-type oxygen array (a) using the 30-130 ms TOF window with the backscattering detector of HRPD and (b) at the 35 ° detector bank of POLARIS.

Fourier difference analyses were carefully and systematically used with high *d*-spacing data in an attempt to determine an oxygen vacancy ordering model. In this way, a model was found which gave the desired 6-fold coordination around each niobium site and the 30 oxygen vacancies required to most closely match the required stoichiometry. Displacing oxygen atoms adjacent to the vacancies after the manner shown in Figure 2 gave refinement statistics $R_p = 0.2181$, $wR_p = 0.2505$, $R(F^2) = 0.2563$ for the low *d*-spacing data set and statistics $R_p = 0.0985$, $wR_p = 0.1331$, $R(F^2) = 0.0668$ for the high *d*-spacing data set (Figure 34). This model is shown in Figure 35. Note that oxygen atoms in NbO_6 octahedra were distorted from fluorite-type positions prior to refinement. Careful attempts were then made to refine oxygen atom positional parameters. As with XRD data in the case of metal atoms, however, despite improvements in refinement statistics it eventually became clear that a unique and unambiguous solution for oxygen atom displacive relaxations was not obtainable due to reflection overlap at low *d*-spacing in powder data.

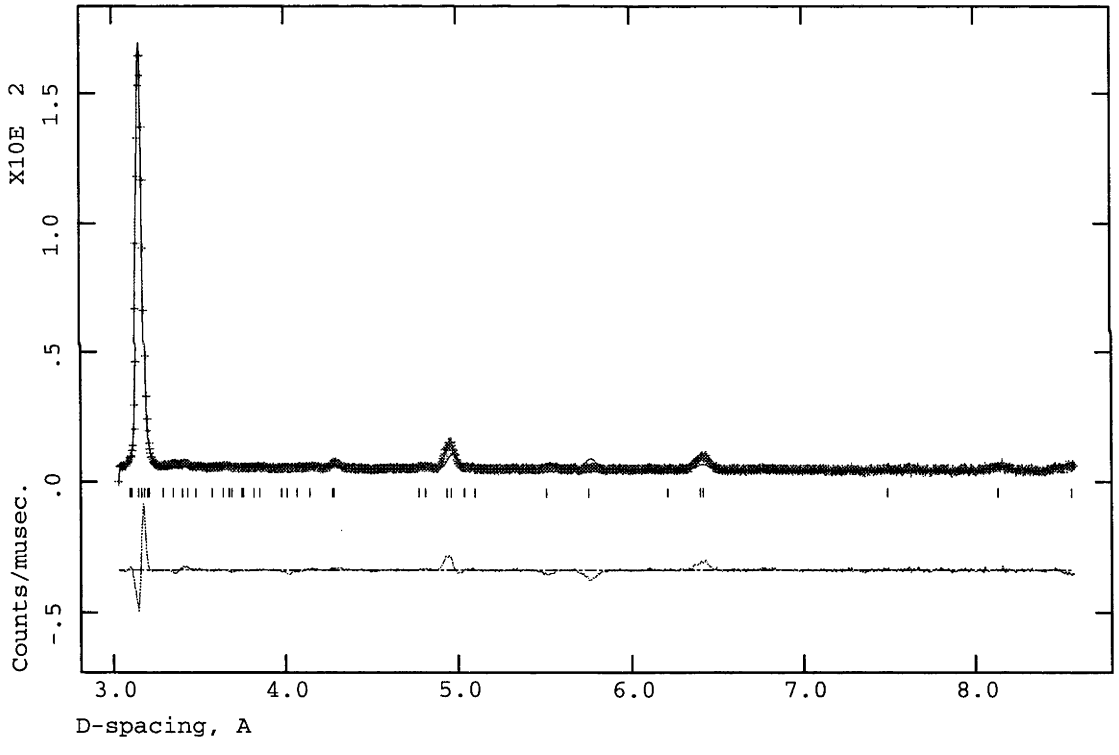

Figure 34. Observed (+), calculated and difference (bottom) neutron powder diffraction profiles for final (unrefined) model of type III Bi_3NbO_7 at the 35 ° detector bank of POLARIS.

The final model for Bi_3NbO_7 is therefore that shown in Figure 35. With full occupancy of all oxygen sites this model has a stoichiometry $Bi_{94}Nb_{32}O_{222}$. Partial occupancy of one or more oxygen atom sites not coordinating niobium atoms would correct the slight oxygen excess in this model (0.5 % overall, *i.e.* one site). Despite the inability to fully refine displacive relaxations in this model from powder data, on the basis of available data this model is qualitatively the most probable solution for the structure of Bi_3NbO_7. A full

refinement will require single crystal X-ray diffraction data, if and when it is possible to grow a useful single crystal for the collection of these data.

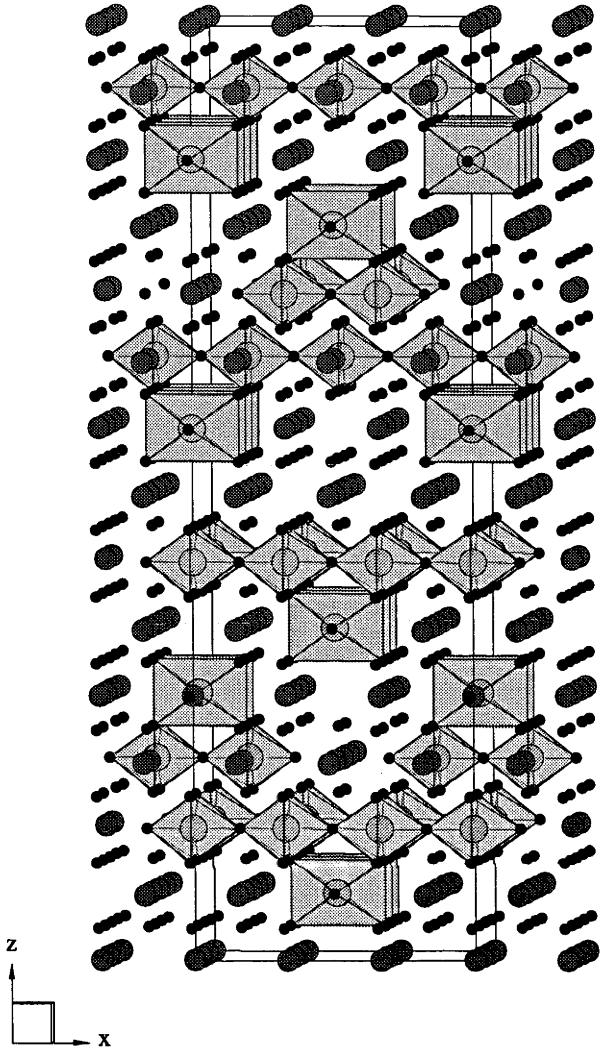

Figure 35. The final (unrefined) model of type III Bi_3NbO_7 viewed close to the [0 1 0] *direction. Bismuth atoms are darker than NbO_6 octahedra, and oxygen atoms are black.*

Figure 36 highlights the nearest-neighbour Nb-Nb connectivity of this model along $<1\ 1\ 0>_f$ directions mapped onto a fluorite-type subcell grid, in order that the 3 x 3 x 3 block derived from Bi_2O_3-$(Nb/Ta)_2O_5$ type II may be directly compared to the type II structure itself (Figure 30). Despite the strong relationship between the phases in reciprocal space, there are clear differences between these real space structures. As discussed above, the relative significance of the string *versus* the cluster structural motifs from pyrochlore-type appears to be equal in this case, whereas the string motif dominated type II. Another important difference is that the number of independent $<1\ 1\ 0>_f$ directions in which continuous Nb strings are observed has not only reduced from three to two, but that the relative orientations of these directions is different. In type II, each of the $<1\ 1\ 0>_f$ three strings is perpendicular to a different $<1\ 0\ 0>_f$ direction, whereas in type III, both strings are perpendicular to the same $<1\ 0\ 0>_f$ direction. Re-examining Figure 2*(d)*, it should be noted that pyrochlore-type itself

can be constructed from either three <1 1 0>$_f$ strings such as are found in type II, or from two <1 1 0>$_f$ strings such as are found in type III. These two structures may therefore represent alternative expansions of pyrochlore-type for incorporation into fluorite-type, both based on a motif of <1 1 0>$_f$ strings of *M* atoms. Both of these possibilities would clearly need to be considered during structural studies of phases with similar compositions.

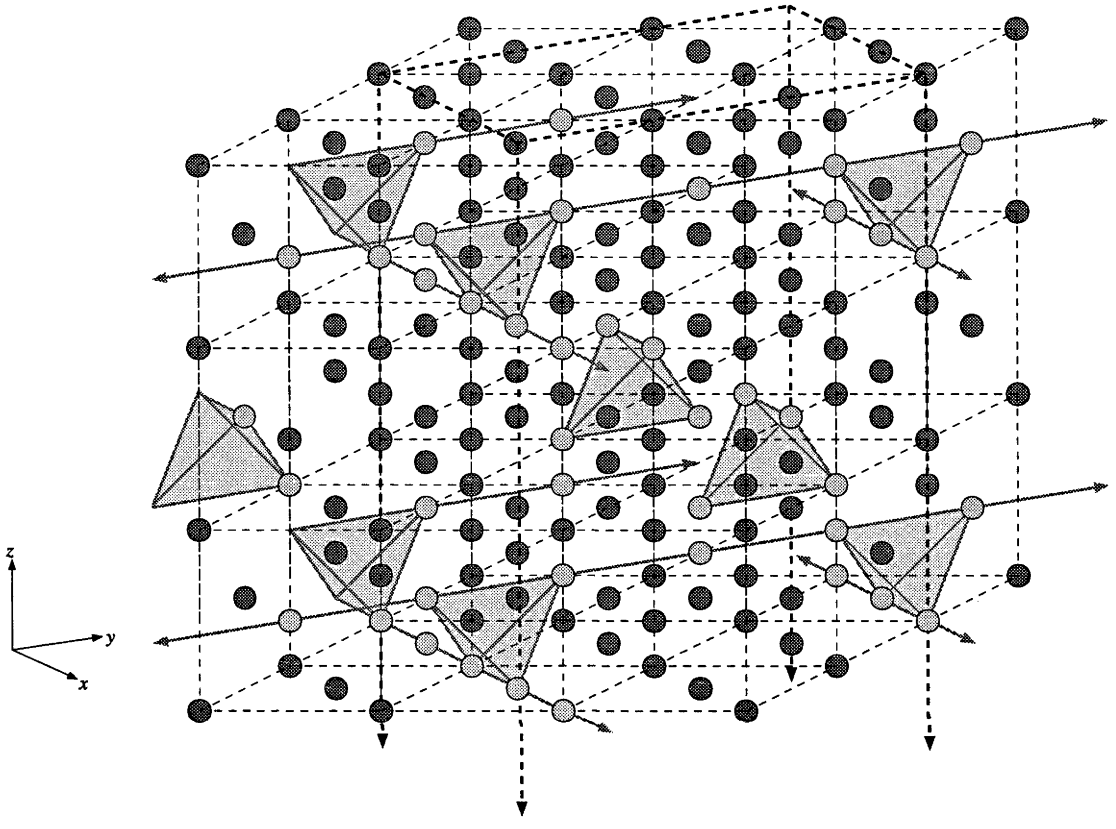

Figure 36. The metal atom array of type III Bi_3NbO_7 mapped onto 3 x 3 x 3 average fluorite-type subcells. Dashed lines indicate the fluorite-type subcell grid, and heavy dashed lines indicate the supercell. Bismuth atoms are darker than Nb atoms. Grey lines and shaded tetrahedra highlight nearest-neighbour Nb connections along <1 1 0>$_f$ directions.

4.4 Type I Bi_2O_3-Ta_2O_5: $Bi_{15}TaO_{25}$

$Bi_{15}TaO_{25}$, the type I phase in the Bi_2O_3-Ta_2O_5 system, is a cubic 2 x 2 x 2, *I*-centered superstructure of fluorite-type (Section 3.4.1.2). There is therefore only one possible (fully ordered) Bi/Ta metal atom compositional ordering scheme, as shown in Figure 37 and as originally proposed by Zhou *et al.* (21). The tantalum atoms in this scheme have the maximum possible separation from one another. This model has *Im3m* space group symmetry. If the assumption is made that the Ta atoms are in octahedral coordination environments, then there are two fluorite-type oxygen vacancies associated with each Ta atom, giving the stoichiometry $Bi_{15}TaO_{30}$. There must therefore be five additional fluorite-type oxygen vacancies associated with bismuth atoms only.

The phase was identified on the basis of ED with the fluorite-type subcell dimensions determined from conventional XRD. XRD satellite reflection intensities were too weak to be used to test the model; an XRD pattern calculated on the basis of the model shown in Figure 37 identified the most intense satellite reflection ((1 1 0)*) as having only 0.1 % the intensity of the strongest reflection, (2 2 2)* ≡ (1 1 1)*$_f$. The weakness of the satellite reflections in XRD requires that there be negligible displacive relaxation of the metal atom array from fluorite-type positions. As neutron powder diffraction data were not collected for this phase, it was not possible to determine whether oxygen vacancy ordering was also occurring. In the absence of any contradictory evidence, it must be concluded that the Bi/Ta metal atom ordering scheme shown in Figure 37 is the simplest, highest symmetry, and most probable solution for the metal atom array of $Bi_{15}TaO_{25}$.

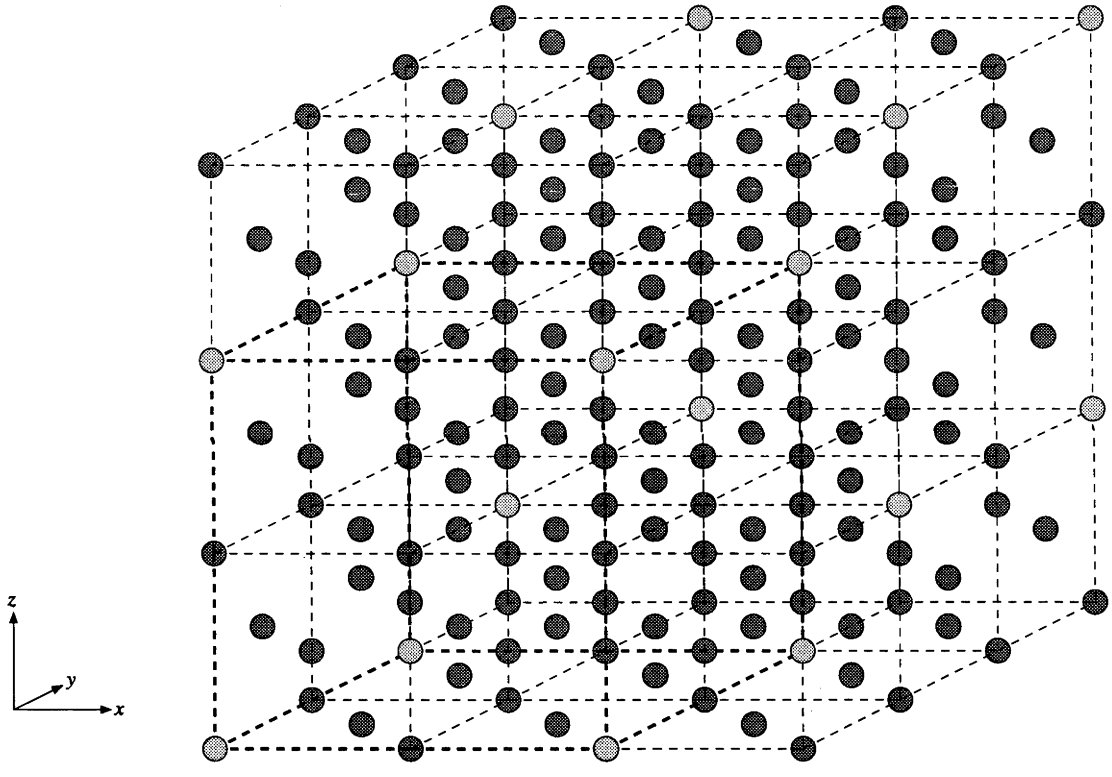

Figure 37. Model of Zhou et al. of the metal atom ordering in type I $Bi_{15}TaO_{25}$ mapped onto 3 x 3 x 3 average fluorite-type subcells. Dashed lines indicate the fluorite-type subcell grid, and heavy dashed lines indicate the supercell. Bismuth atoms are darker than Ta atoms.

In Figure 37, the metal atom array of this model is mapped onto 3 x 3 x 3 average fluorite-type subcells. As for type Ia $Bi_{14}(W/Mo)O_{24}$ (Section 4.1, Figure 24), Ta atoms are isolated from one another within the fluorite-type Bi atom array. It should be remembered, however, that *M* atoms in that phase have (locally) tetrahedral coordination environments, plausible for W^{6+}/Mo^{6+} cations, whereas *M* atoms in type I $Bi_{15}TaO_{25}$ will almost certainly have octahedral coordination environments, as preferred by Ta^{5+} cations. The presence or otherwise of the string or cluster structural motifs from pyrochlore-type found in Bi_2O_3-$(Nb/Ta)_2O_5$ type II (Section 4.2) and Bi_2O_3-Nb_2O_5 type III (Section 4.3) does not, therefore,

automatically follow when octahedrally coordinated *M* atoms are present. (Note that isolated *M* atoms are also found in Bi_2O_3-$(Nb/Ta)_2O_5$ type II; see, *e.g.*, Figure 26.)

4.5 Type Ib Bi_2O_3-WO_3

As discussed in Section 3.3.3, the type Ib phase in the Bi_2O_3-WO_3 system is a solid-solution with metal atom compositions between approximately 12.5 and 16.0 mol% W_2O_6. ED work (Section 3.4.1.3) supported previous descriptions (14, 27) of the phase as a superstructure of fluorite-type (Table 2) and indicated the space group symmetry to be $I4_1$ but pseudo-$I4_1/a$. There was no evidence to indicate that unit cell or space-group symmetry were functions of composition, requiring the presence of some compositional disorder in the structure of the phase to account for the solid-solution range.

Watanabe *et al.* (27) used precession photography of a single-crystal to determine the space group of $Bi_{14}W_2O_{27}$ (at the bismuth-rich end of the solid-solution) to be $I4_1/a$. A model was proposed in that space group in which tungsten atoms were located on 4*a* and 4*b* sites (the former being fully occupied by tungsten and the latter being a mixed-metal site). These sites are isolated from one another such that there can be no W-O-W bonds, *i.e.* the *M* atoms are isolated in a similar fashion to those in type Ia $Bi_{14}(W/Mo)O_{24}$ (Section 4.1) and type I $Bi_{15}TaO_{25}$. The distribution of oxygen atoms was modelled as a partially occupied fluorite-type array. Zhou *et al.* (14) tested this model using image matching / multi-slice techniques with ED and HRTEM data, and found it to be plausible.

The fact that Watanabe *et al.* used only XRD data to test their model implies that the crystal they obtained was somehow of insufficient quality for single-crystal X-ray data collection. Single-crystals at a range of compositions within the solid-solution field (including $Bi_{14}W_2O_{27}$) were grown in this study and examined on a single-crystal X-ray diffractometer using Mo Kα_1 radiation ($\lambda = 0.7107$ Å) from a rotating-anode source. The intensity of the satellite reflections was extremely low, as expected from the XRD pattern (Figure 15). It was only possible to adequately assess the quality of large crystals (edge dimensions ~ 50 - 100 μm) for which a reasonable number of satellite reflections were observable. These crystals, which were too large for data collection due to the massive absorption coefficient of the compound, suffered badly from twinning of the tetragonal (but pseudo-cubic) subcell. Furthermore, the profiles of reflections, even in untwinned crystals, indicated that the composition (hence the cell dimensions) was slightly inhomogeneous, resulting in 'smeared' reflections. As there was no opportunity to examine the smaller crystals using synchrotron X-ray radiation, it remains unclear whether those crystals would be suitable for synchrotron X-ray data collection.

4.5.1 Experimental

Powder samples towards the bismuth-rich ($Bi_{14}W_2O_{27}$) and tungsten-rich ($Bi_{22}W_4O_{45}$) ends of the type Ib solid-solution field were prepared by solid-state reaction of stoichiometric mixtures of Bi_2O_3 (Koch-Light 99.998 %) and WO_3 (Koch-Light 99.9 %) in platinum crucibles in air at 1073 K for 0.5 hours. The samples were then quenched to room temperature, reground, annealed in sealed platinum vessels at 1173 K for 168 hours and again quenched to room temperature. Homogeneous, pale yellow powders were obtained and identified as single-phase by XRD (Guinier-Hägg camera).

Synchrotron XRD data were collected for both samples. TOF powder neutron diffraction data were collected on POLARIS for both samples, and on HRPD for $Bi_{22}W_4O_{45}$.

4.5.2 X-ray Data Analysis

The starting point for modelling the structure was a fluorite-type metal atom array in $I4_1/a$. Synchrotron XRD data, which have very little sensitivity to oxygen atoms due to the presence of strongly scattering bismuth and tungsten atoms, were then used to Rietveld-refine the metal atom positions. All metal atom sites were initially modelled as mixed occupancy with appropriate compositions, and an overall isotropic displacement parameter was refined. This produced a wave-like pattern of small displacements, principally along *c* and of magnitude $< \sim 0.25$ Å, which was qualitatively identical for $Bi_{14}W_2O_{27}$ and $Bi_{22}W_4O_{45}$, and reproducible regardless of the pattern of introduced initial displacements, suggesting it to be a genuine feature of the type Ib phase. The refined pattern in the case of $Bi_{22}W_4O_{45}$ is shown in Figure 38. Note that Figure 38 is presented with origin choice #2 for $I4_1/a$, as used by Watanabe *et al.*, for the purposes of comparison with their model. The coordinates used subsequently in this study are shifted by $(0\ \frac{1}{4}\ \frac{1}{8})$ relative to this model, to origin choice #1.

Refinement of independent isotropic displacement parameters, and of fractional occupancies in conjunction with an overall isotropic displacement parameter, strongly supported the metal atom compositional ordering scheme of Watanabe *et al.* The model involves a mixed metal atom site (labelled in Figure 38), the composition of which is 25 % tungsten for $Bi_{14}W_2O_{27}$ and 54 % tungsten for $Bi_{22}W_4O_{45}$.

Adding a fluorite-type oxygen atom array (with partial occupancies appropriate to the compositions) to the model actually worsened the quality of the fit to the observed data. However, incorporating the sole fluorite-type oxygen atom site not directly in contact with the tungsten or mixed sites improved the fit. This further supported the proposed metal atom ordering scheme, given that an octahedral coordination environment for W^{6+} would require substantial distortion from a fluorite-type array whereas high coordination Bi^{3+} atoms would not. Note that the tetrahedral coordination of W^{6+} found in type Ia $Bi_{14}(W, Mo)O_{24}$ (Section 4.1) cannot be a feature of the type Ib structure due to compositional constraints,

whereby insufficient oxygen vacancies are available to reduce the coordination number of tungsten from 8-fold to 4-fold.

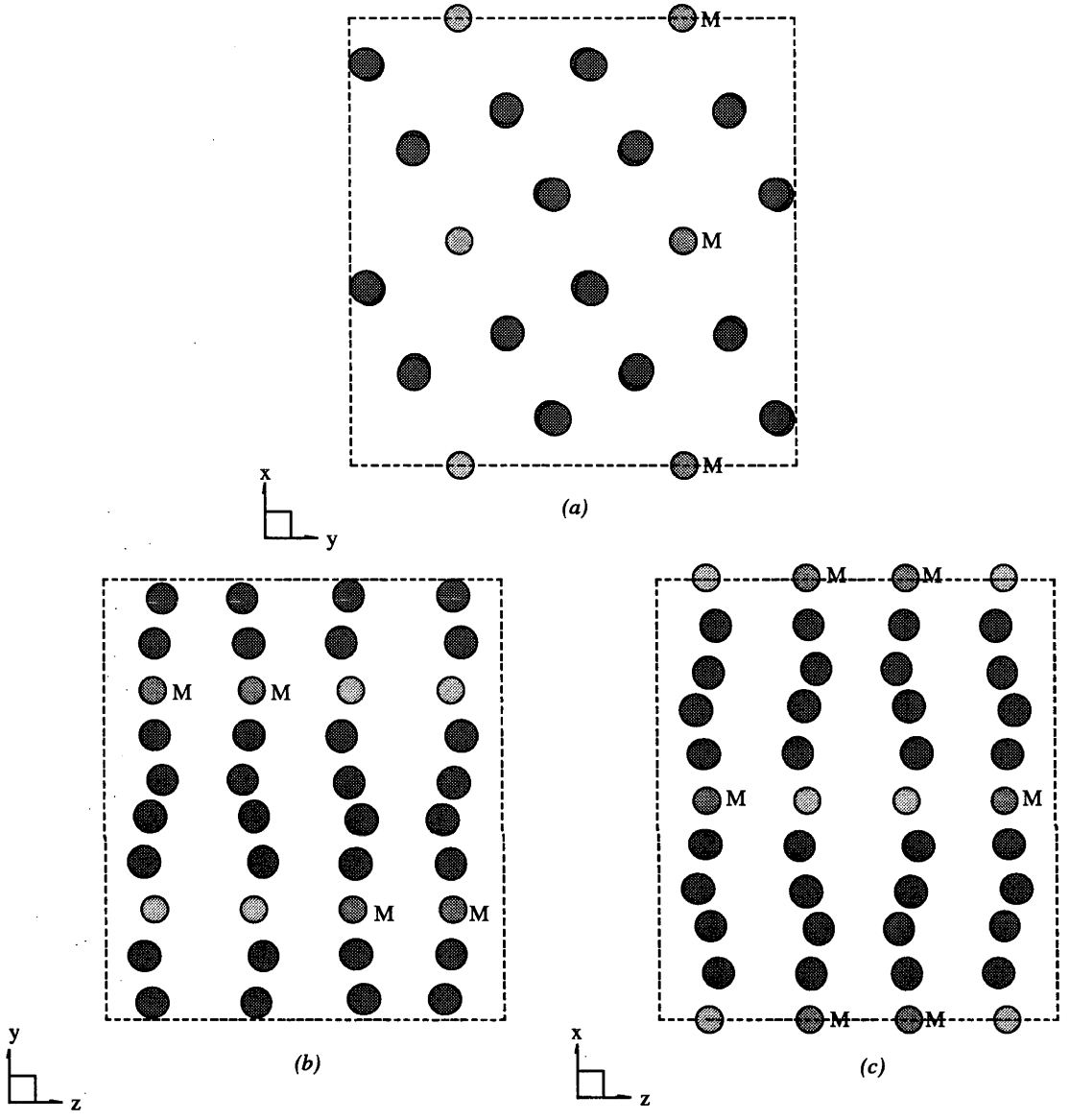

Figure 38. Pattern of metal atom displacements Rietveld-refined from synchrotron XRD data for type Ib $Bi_{22}W_4O_{45}$, viewed down the (a) [0 0 1] ≡ [0 0 1]$_f$, (b) [1 0 0] and (c) [0 1 0] directions. Bismuth atoms are darker than tungsten atoms, and the mixed occupancy site is labelled 'M'.

Reintroducing oxygen atoms at appropriate partial occupancies to the remaining fluorite-type sites (83 % in the case of $Bi_{22}W_4O_{45}$) gave overall statistics $R_p = 0.0461$, $wR_p = 0.0683$, $\chi^2 = 4.553$. The fit to synchrotron XRD data is shown in Figure 39.

Lowering the space group symmetry from $I4_1/a$ to $I4_1$ (in accordance with the ED observations of Section 3.4.1.3) and refining metal atom positions led to a significantly improved fit to synchrotron XRD data. This implied that the symmetry lowering was justified. The pattern of displacements was, however, no longer unambiguous but was dependent on the introduced initial displacements from refined $I4_1/a$ positions. It was not possible to be

confident of a correct or meaningful final refined metal atom array in $I4_1$. Of particular concern was the fact that when the symmetry was lowered, the origin was no longer fixed in *z*, meaning that the fluorite-type oxygen atom array no longer had an unambiguous location relative to the metal atom array.

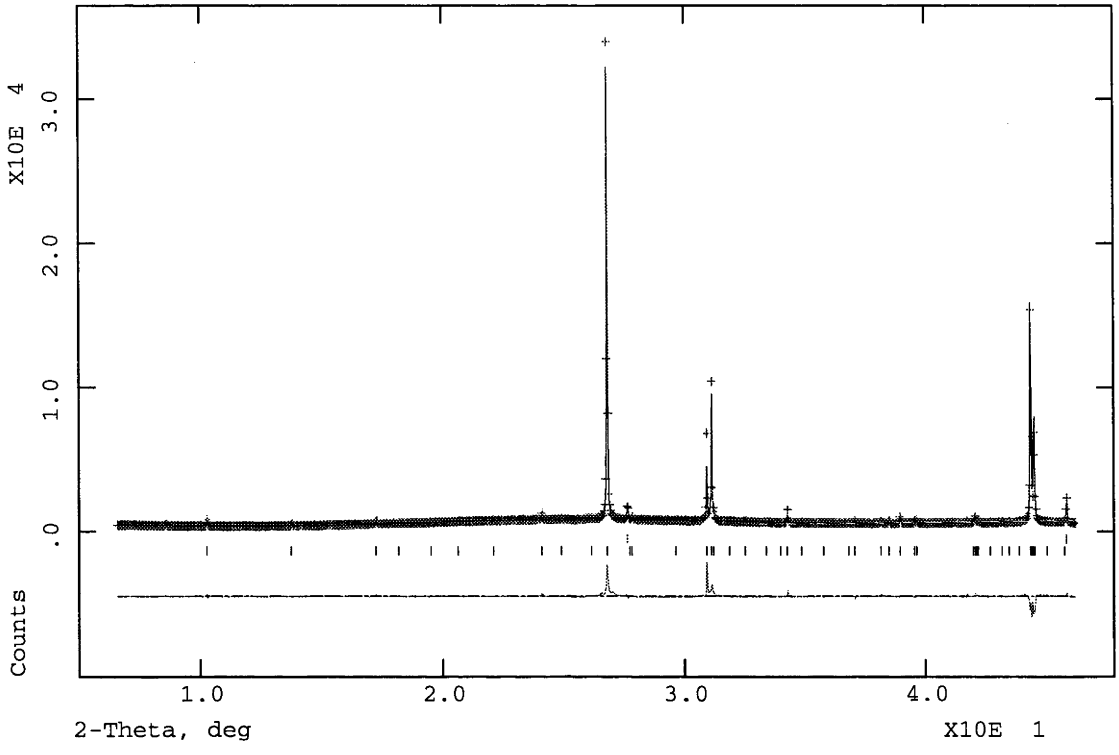

(a)

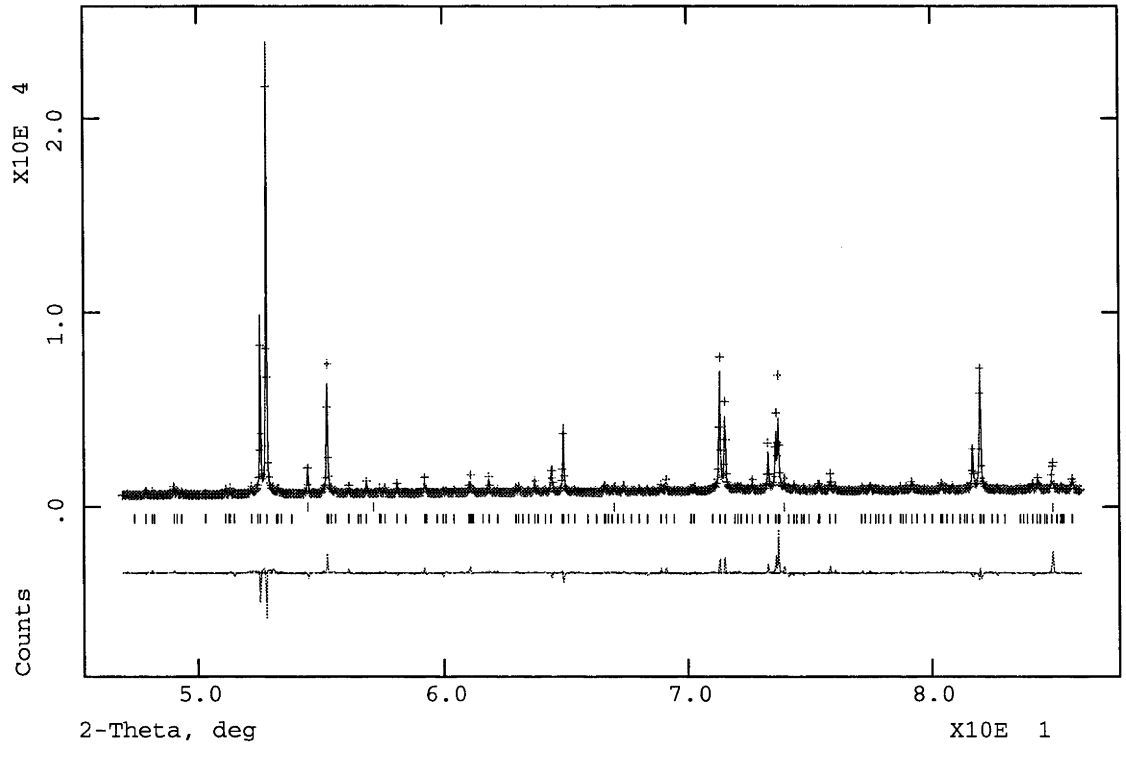

(b)

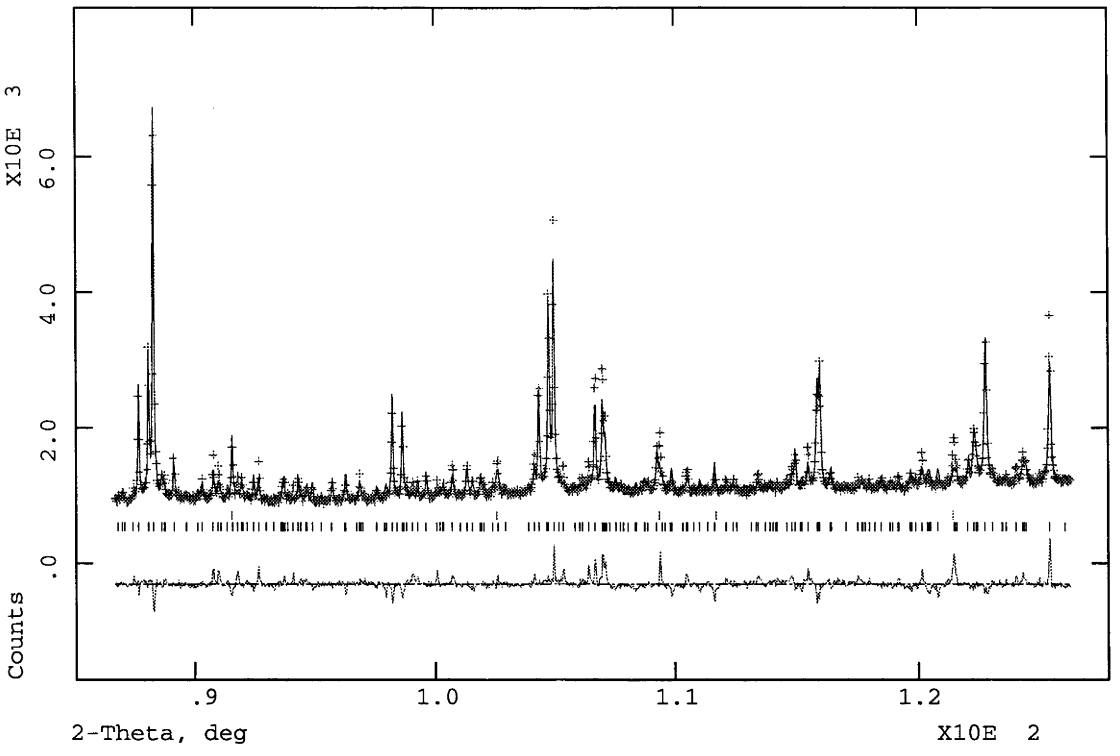

(c)

Figure 39. Observed (+), calculated and difference (bottom) XRD profiles for type Ib $Bi_{22}W_4O_{45}$. The top row of reflection markers refers to the Si standard.

It should be noted that lowering the space group symmetry from $I4_1/a$ to $I4_1$ does not affect the multiplicity of the tungsten and mixed-metal sites. Therefore, if the metal atom distribution shown in Figure 38 is correct for $I4_1/a$, the driving force for symmetry lowering cannot be further metal atom compositional ordering. This observation, in conjunction with the inability to obtain a reliable solution for the metal atom displacements in $I4_1$, suggested that the $I4_1/a$ solution for the metal atom array was the most appropriate starting point for analysis of neutron powder diffraction data.

4.5.3 Neutron Data Analysis

Analysis of neutron powder diffraction data concentrated on the sample of composition $Bi_{22}W_4O_{45}$, for which higher-resolution (HRPD) data were available. These were combined with high *d*-spacing POLARIS data for the same sample.

Starting from the $I4_1/a$ model from the XRD refinement, *i.e.* refined metal atom array and fluorite-type oxygen atom array, it was possible to refine all atomic positions with overall isotropic displacement parameters for metal and oxygen atoms. Refinement of independent isotropic displacement parameters for each metal atom, and of fractional occupancies in conjunction with an overall isotropic displacement parameter, again supported the metal ordering scheme of Watanabe *et al.* Refinement of fractional occupancies for oxygen atoms again supported full occupancy of the one fluorite-type oxygen atom site not in contact with

the tungsten and mixed sites, and variously lower occupancies of the other fluorite-type oxygen atom sites. Refinement of metal atom positions also supported the XRD refinement results.

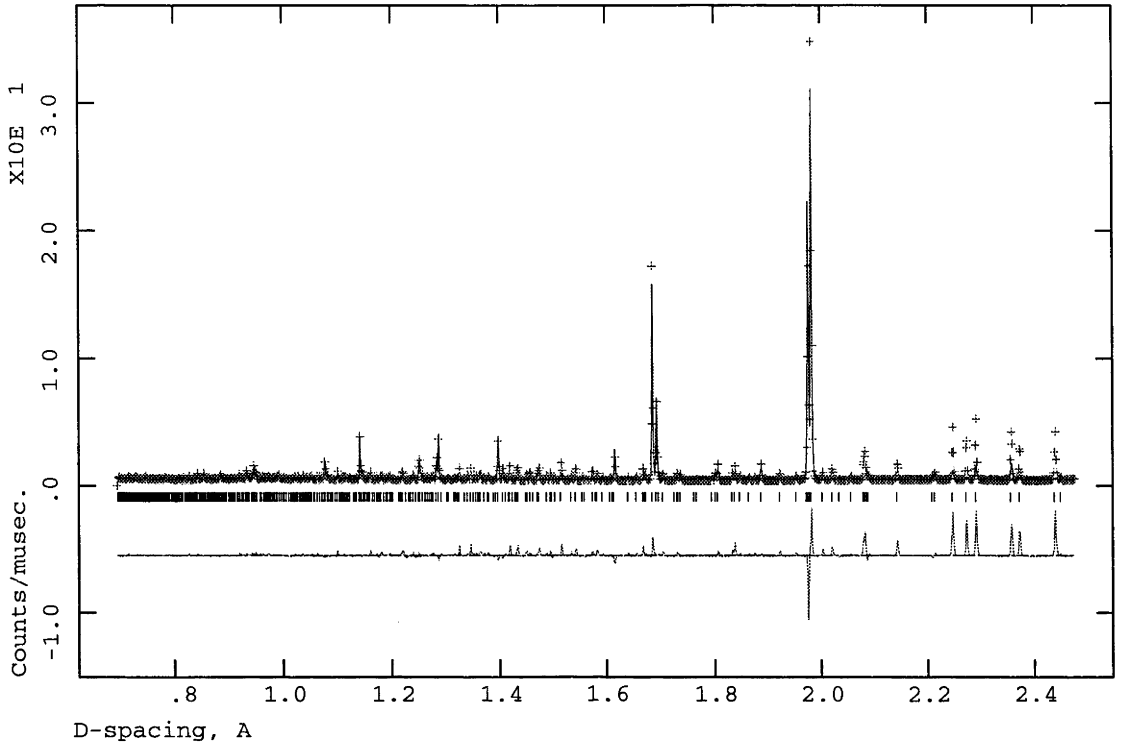

(a)

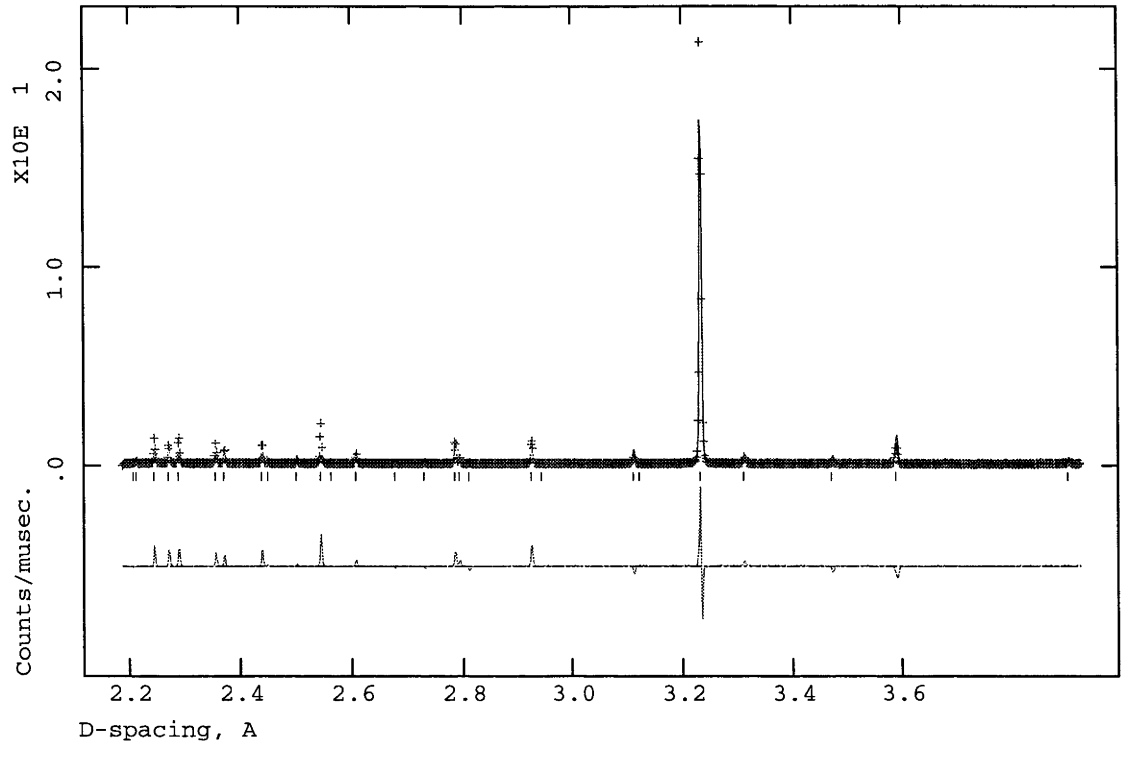

(b)

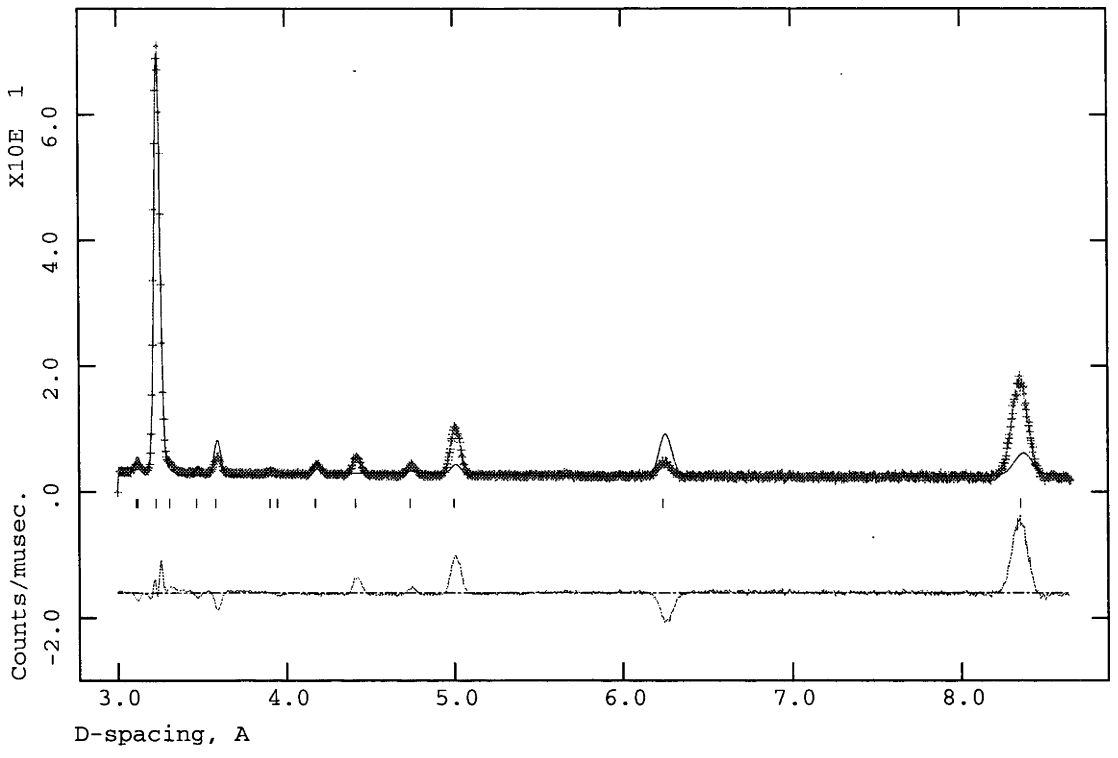

(c)

Figure 40. Observed (+), calculated and difference (bottom) neutron powder diffraction profiles for type Ib $Bi_{22}W_4O_{45}$ using (a) 30-130 ms, (b) 100-200 ms TOF windows with the backscattering detector of HRPD and (c) at the 35 ° detector bank of POLARIS.

Oxygen atom positions refined in a stable manner, preserving the fluorite-type array, albeit in a far more distorted form than the metal atom array. Unfortunately, examination of the low *d*-spacing data showed a very poor fit to the satellite reflections, indicating that the result was almost certainly a false minimum in the refinement and that the improved statistics were due only to the increased number of variables being refined. Repeated attempts to refine oxygen atom positions starting from various introduced initial displacements failed to yield a more convincing result. Attempting to refine fractional occupancies of the oxygen atoms in contact with the tungsten and mixed sites, both before and after their positional refinement, also failed to yield a convincing result in terms of the high *d*-spacing data.

Removing all oxygen atoms from the model and reintroducing them on the basis of Fourier difference map peaks only returned the pseudo-fluorite-type positions and failed to give an improved final result.

Lowering the space group symmetry to $I4_1$ (thereby doubling the number of independent oxygen atoms), it remained impossible to obtain a meaningful answer by refinement of a fluorite-type oxygen array, despite apparently stable refinements. Refinement of fractional occupancies for oxygen atoms only confirmed the results in $I4_1/a$.

As in $I4_1/a$, oxygen atoms were removed from the model and a Fourier difference map approach used to return an approximately fluorite-type oxygen array. In this case, however, a significant new feature was identified; after the assignment of nine of the Fourier difference map peaks as oxygen atoms (in the model), no peak appeared corresponding to the tenth oxygen atom required to complete the fluorite-type array. The missing fluorite-type oxygen atom site coordinated the tungsten site twice, *i.e.* its absence reduces the coordination number of tungsten from 8-fold to 6-fold.

A 6-fold coordination environment for W^{6+} is chemically far more plausible than an 8-fold one. The absence of one out of ten fluorite-type oxygen atoms also goes some way towards correcting the overall stoichiometry, which in $Bi_{22}W_4O_{45}$ would require 8.65 out of the ten fluorite-type oxygen atom sites to be occupied. Furthermore, by locating the remaining required oxygen vacancies on one of the fluorite-type oxygen sites which doubly coordinates the mixed metal site (54 % W in $Bi_{22}W_4O_{45}$), a sensible model can be proposed in which the percentage of tungsten on the mixed metal site corresponds to the percentage of oxygen missing from the adjacent fluorite-type oxygen site. In the case of $Bi_{22}W_4O_{45}$, 35 % oxygen vacancies does not match 54 % tungsten, however, the two values do match (at 42.85%) for the composition Bi_6WO_{12} which falls between the compositions $Bi_{14}W_2O_{27}$ and $Bi_{22}W_4O_{45}$ *i.e.* within the solid-solution range observed in this study. A similar argument was used by Zhou *et al.* to propose a tungsten-rich upper limit on the type Ib composition of Bi_6WO_{12}.

Space group $I4_1$ (no. 80), a = 12.49687(8), c = 11.24558(14) Å					
	x (a)	y (b)	z (c)	Fraction	$100U_{iso}$ (Å^2)
Bi1	0.2959(2)	0.6064(2)	0.10110(12)	1	2.43(8)
Bi2	0.2117(2)	0.8967(2)	0.1309(2)	1	2.43(8)
Bi3	0.7041(2)	0.8936(2)	0.89890(12)	1	2.43(8)
Bi4	0.7883(2)	0.6033(2)	0.8691(2)	1	2.43(8)
W1	0	0.5	0.125	1	2.43(8)
M1	0	0.5	0.625	0.46 W 0.54 Bi	2.43(8)
O1	0.05	0.85	0.25	1	13.8(2)
O2	0.15	0.55	0.125	1	13.8(2)
O3	0.25	0.75	0.25	1	13.8(2)
O4	0.35	0.95	0.25	1	13.8(2)
O5	0.55	0.85	0.75	1	13.8(2)
O6	0.65	0.55	0.75	0.46	13.8(2)
O7	0.75	0.75	0.75	1	13.8(2)
O8	0.85	0.95	0.75	1	13.8(2)
O9	0.95	0.65	0.75	0.46	13.8(2)
O10	0.95	0.65	0.825	0.54	13.8(2)

Table 9. Final disordered model of the type Ib solid-solution phase in the system Bi_2O_3-WO_3, at the composition $Bi_{22}W_4O_{45}$.

This type of model can exist in $I4_1$ but not $I4_1/a$, because the additional a-glide links fluorite-type oxygen sites around the tungsten and mixed metal sites such that ordered 6-fold coordination cannot be achieved in $I4_1/a$. Given the observed weak breaking of the a-glide, it therefore seems likely that this pattern of oxygen vacancies is the driving force behind symmetry lowering. Considering the more reliable behaviour of metal atom positions in XRD refinements using the higher symmetry space group, it was clearly sensible to retain the $I4_1/a$ XRD refined metal atom positions while testing the various possible combinations of oxygen vacancies around the two tungsten-containing sites. Different combinations were tested against high d-spacing neutron powder diffraction data (from POLARIS), which might be expected to have the highest sensitivity to occupancy ordering and the lowest sensitivity to displacive relaxation. Each fluorite-type oxygen site removed corresponded to a face-diagonal pair of oxygen atoms on the cubic (fluorite-type) coordination sphere of the tungsten-containing sites. The adjacent face-diagonal pair of oxygen atoms was then shifted towards the vacancies in order to create a less distorted octahedral coordination environment. The different combinations of oxygen vacancies tested therefore corresponded to different relative orientations of the octahedra coordinating each tungsten-containing site.

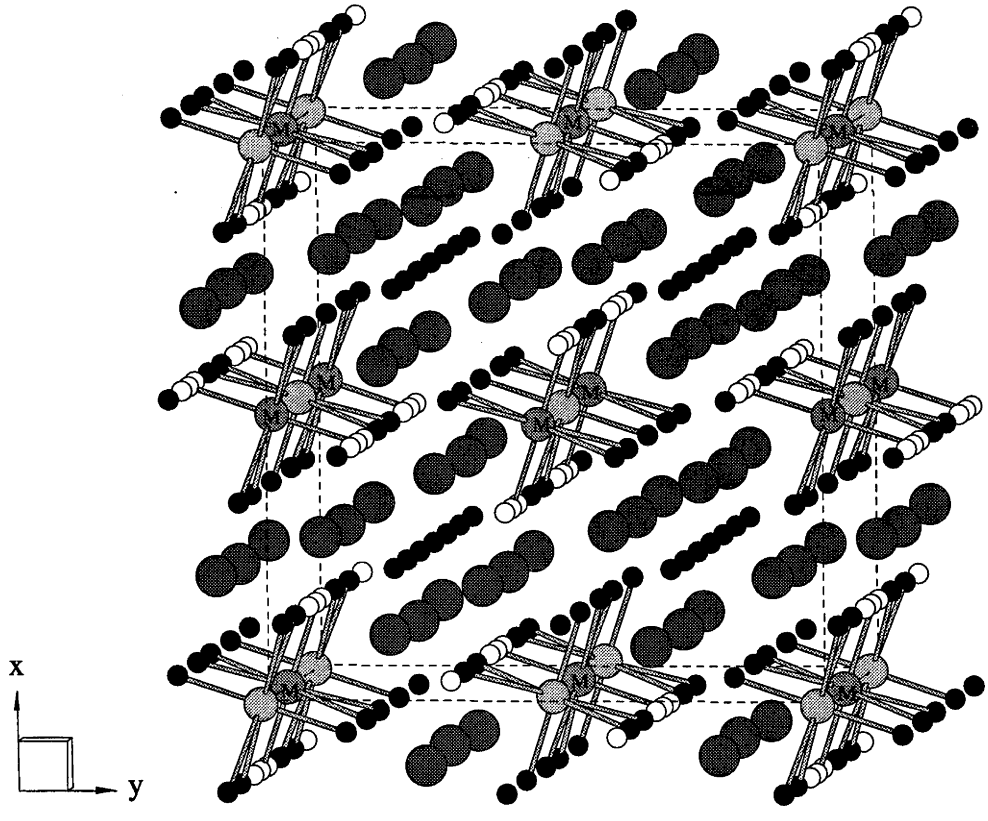

Figure 41. Final disordered model of the type Ib solid-solution phase in the system Bi_2O_3-WO_3. Bismuth atoms are darker than WO_6 octahedra, and oxygen atoms are black. The mixed occupancy metal atom site is labelled 'M', and partially occupied oxygen atom sites are white. Bi-O bonds are omitted for clarity.

One of the eight unique combinations stood out as providing the best fit to high d-spacing neutron data. The fit to the whole of the data set, however, remained far from

satisfying (overall refinement statistics $R_p = 0.1752$, $wR_p = 0.2041$, $\chi^2 = 42.08$). The fit at this stage is shown in Figure 40. The model is shown in Figure 41 and the coordinates given in Table 9, all for the case $Bi_{22}W_4O_{45}$. Note that this model is slightly oxygen deficient (~ 1 %) due to the oxygen atom overcrowding which led Zhou *et al.* (14) to propose tungsten-rich limit on the solid-solution field at the composition Bi_6WO_{12}, for which frac(O6) = frac(O9) = frac(W1) = 43 % in Table 9. It is not clear how additional oxygen atoms would be accommodated at more tungsten-rich compositions. At more bismuth-rich compositions, *e.g.* $Bi_{14}W_2O_{27}$, the fractional occupancies of O1-5 and O7-8 will be less than 100 %.

The extremely poor fit to observed neutron data in Figure 40 contrasts strongly with the fit to observed XRD data in Figure 39. In conjunction with the large refined isotropic displacement parameters of oxygen atoms in Table 9, this indicates that large oxygen atom displacive relaxations needed to be modelled. Attempts to refine oxygen atom displacements from this model were, however, no more successful than previously. Furthermore, it was found that the introduction of small oxygen atom displacements significantly changed the relative qualities of fit for the different oxygen vacancy ordering models, even at high *d*-spacing. It therefore appeared impossible to adequately quarantine the data sensitive to vacancy ordering from the data sensitive to displacements.

The large amount of oxygen atom displacive information remaining in the observed data suggested the possibility of further symmetry lowering. No evidence of peak-splitting was observed, even in high-angle synchrotron XRD data, to suggest that the symmetry was lower than tetragonal, and systematic absences corresponding to a 4_1 screw axis were observed in ED. Any lowering of symmetry would therefore have to be accompanied by repeated twinning on a fine scale (< 1000 Å given the ED evidence) to return the average space group symmetry to $I4_1$. Unfortunately, despite persistent, careful and systematic attempts, a fully ordered solution of this nature could not be found at any composition within the observed solid-solution range.

4.5.4 Discussion

The final model obtained is very much an average solution. It reflects the compositional disorder suggested at the outset by the lack of any apparent correlation between solid-solution composition, unit cell dimensions and space-group symmetry. It is likely that the true structure is of a lower space-group symmetry, disordered through repeated twinning. Importantly, while a sophisticated model such as this could conceivably remove the necessity for a mixed-metal site at certain compositions, it could not remove the necessity for a slight oxygen deficiency at compositions more tungsten-rich than Bi_6WO_{12}. Although Zhou *et al.* (14) reported Bi_6WO_{12} as the upper limit of the solid solution field, slightly more tungsten-rich compositions were found in both this study (Section 3.2.1.3) and that of Watanabe *et al.*

(27). It is possible that the interpretation of compositional data by Zhou *et al.* was influenced by a realisation that their model could not accommodate more tungsten-rich compositions. The problem can, however, be explained by the partial reduction of W^{6+} to W^{5+}; the model described in Table 9 would then actually be approximately $Bi_{22}W^{6+}{}_2W^{5+}{}_2O_{44}$ rather than $Bi_{22}W^{6+}{}_4O_{45}$. This is a quite plausible explanation given that W^{6+} is easily reduced at high temperatures, as indicated by the series WO_{3-x} ($0 \leq x \leq 3$) (75). It must be noted, however, that no darkening in colour was observed as expected for reduced tungsten oxides; this suggests that the extent to which any such reduction occurs must be quite limited.

Ultimately, it appears that while there is a large amount of information in the observed data (particularly HRPD neutron data), the determination of a unique and complete solution with which to model these data is an intractable problem. The extent to which the data are compromised by exact and approximate peak overlap in powder diffraction patterns is at the root of the problem. The success of this study in determining the structure of type Ia $Bi_{14}(W/Mo)O_{24}$ from powder diffraction data (Section 4.1) could not be duplicated in the case of type Ib, for which single-crystal synchrotron X-ray data will probably be necessary. Nonetheless, the model shown in Figure 41 and Table 9 has been carefully and systematically shown to be the most plausible approximate solution obtainable from the data available.

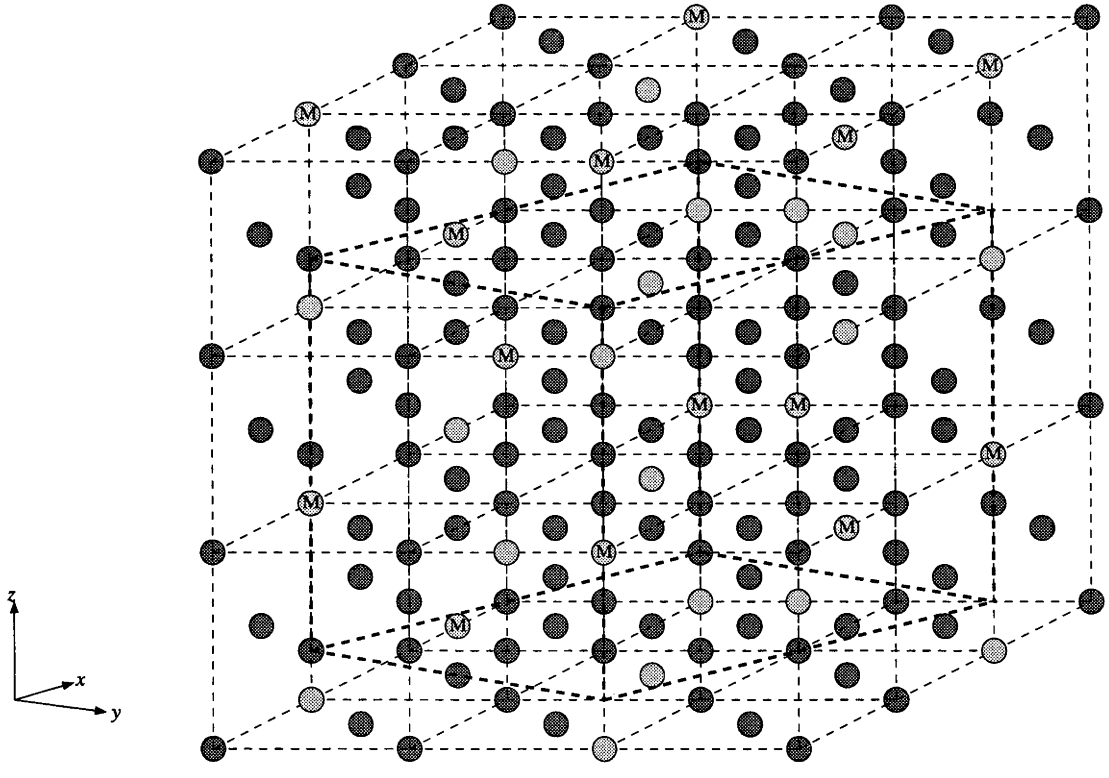

Figure 42. The metal atom array of Bi_2O_3-WO_3 type Ib mapped onto 3 x 3 x 3 average fluorite-type subcells. Dashed lines indicate the fluorite-type subcell grid, and heavy dashed lines indicate the supercell. Bismuth atoms are darker than Ta atoms, and the mixed occupancy metal atom site is labelled 'M'.

The final model of the metal atom array is shown in Figure 42, mapped onto a 3 x 3 x 3 fluorite-type grid. The density of *M* atoms within the metal atom array is much

greater than for type Ia $Bi_{14}(W/Mo)O_{24}$ (Figure 24) and type I $Bi_{15}TaO_{25}$ (Figure 37), yet they remain isolated from one another within the fluorite-type Bi atom array. In fact, *M* atoms could in principle remain isolated from one another within a fluorite-type Bi atom array at densities of up to 50 %. The fact that, on the contrary, this isolation ceases in phases with far lower *M* atom densities than 50 % (Bi_2O_3-$(Nb/Ta)_2O_5$ type II and type III Bi_3NbO_7) is further indication of some crystal-chemical driving force in favour of the string and/or cluster motifs from pyrochlore-type observed for these phases.

4.6 Bi_2O_3-MoO_3: $Bi_{38}Mo_7O_{78}$

The line phase $Bi_{38}Mo_7O_{78}$ reported by Buttrey *et al.* (13) was reproduced in the present study at the same composition (Section 3.3.4). ED analysis (Section 3.4.1.4) was in agreement with the conclusion of that study that the space-group symmetry could be unambiguously identified as orthorhombic *Pccn*.

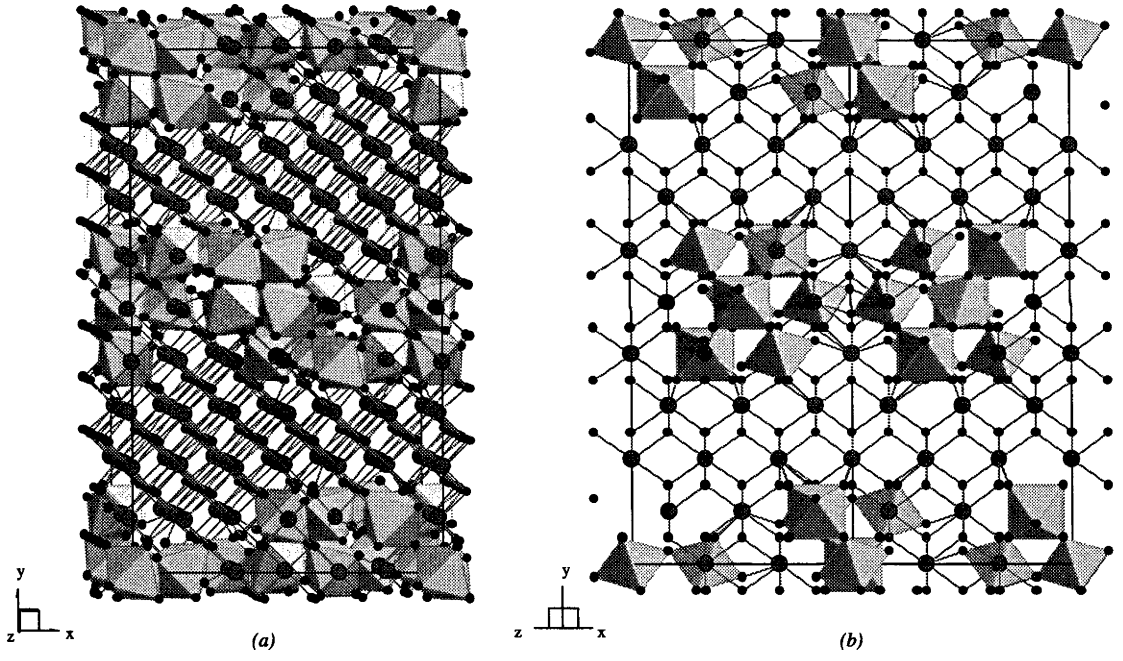

Figure 43. Cluster model for the structure of $Bi_{38}Mo_7O_{78}$ viewed (a) close to the [0 0 1] direction and (b) down the [1 0 1] direction. Bismuth atoms are darker than MoO_6 octahedra, and oxygen atoms are black.

DPs clearly indicated the phase to be a $3\mathbf{a}_f$, $5\mathbf{b}_f$, $3\mathbf{c}_f$ superstructure of fluorite-type. Buttrey *et al.* noted that for a 3 x 5 x 3 fluorite-type metal atom array in *Pccn*, all metal atoms are on general positions with a multiplicity of 8, with the exception of the inversion centre (multiplicity = 4). In order to comply with the stoichiometry $Bi_{38}Mo_7O_{78}$, $z = 4$, this special position must be occupied by a Mo atom. A complete model of the metal atom array then requires a further three (general position) metal atom sites to be occupied by Mo atoms. Buttrey *et al.* noted further that the presence of a Mo atom on an inversion centre implied octahedral, rather than tetrahedral, coordination of Mo atoms by oxygen atoms. They

speculated that the arrangement of the three additional molybdenum sites about the inversion centre would resemble a unit of pyrochlore-type, allowing oxygen vacancies to be accommodated, but did not attempt to determine this arrangement.

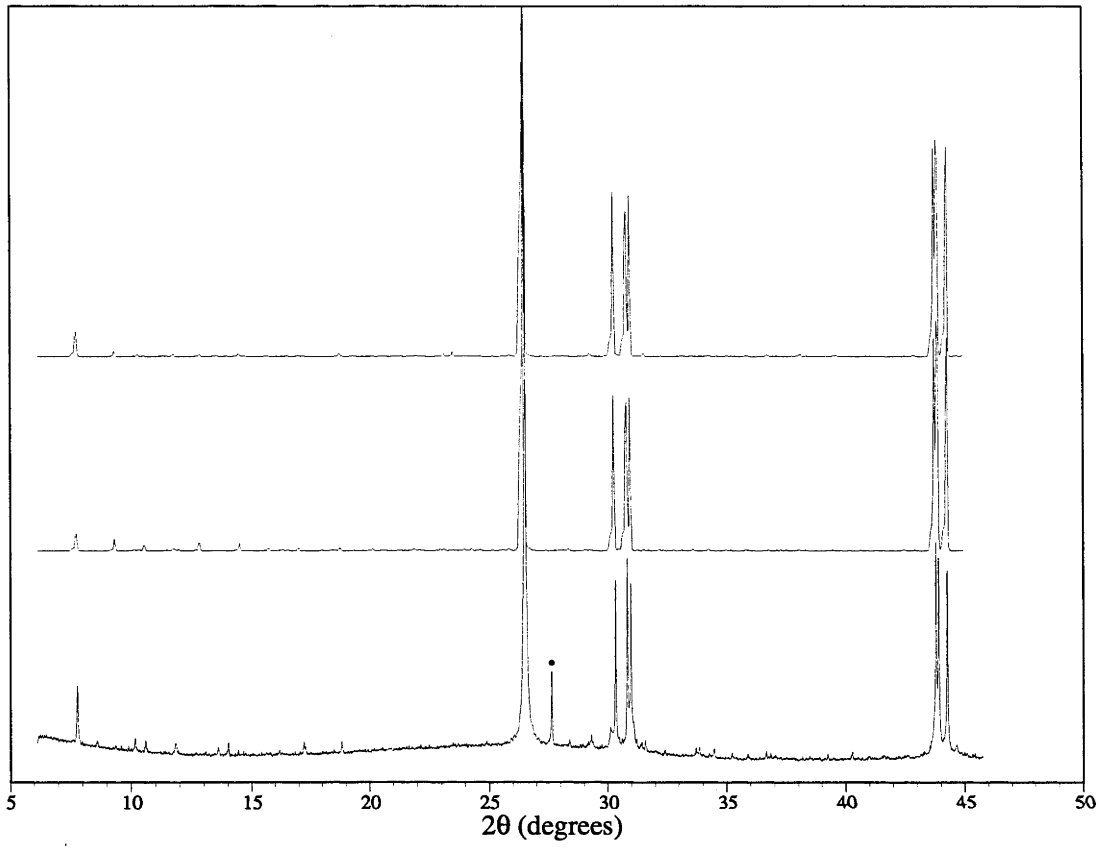

Figure 44. Comparison of XRD patterns calculated from models of $Bi_{38}Mo_7O_{78}$ based on the cluster (top) and string (middle) motifs against synchrotron data (bottom). A silicon standard reflection is marked (•).

Single-phase powder samples of $Bi_{38}Mo_7O_{78}$ grown at stoichiometry in the present study were highly crystalline, and contained large numbers of crystals suitable for single-crystal synchrotron X-ray diffraction. It was hoped that single-crystal data could be collected and used to elucidate the structure of the phase. A large number of crystals were investigated at the Photon Factory, the majority of which displayed good cell dimensions, peak shapes and satellite reflection intensities. In all cases, however, it was found that $\beta = 90.6\,^\circ$ despite the evidence of synchrotron XRD data (Figure 44) that the cell was orthorhombic. This observed monoclinic splitting originates in the pseudo-tetragonal nature of the unit cell, where $a \sim c$ (see Table 2), resulting in endemically twinned crystals in which mismatches occur between **a** and **c**. It can be shown trigonometrically that this leads to the observed 90.6 ° angle between **a*** and **c***. It was not considered worthwhile collecting synchrotron X-ray data from such crystals, and it proved impossible to prepare true single crystals of this phase. An attempt was therefore made to determine the structure of $Bi_{38}Mo_7O_{78}$ using synchrotron XRD and powder neutron diffraction (HRPD and POLARIS) data.

As discussed in relation to the structures of Bi_2O_3-$(Nb/Ta)_2O_5$ type II (Section 4.2) and type III Bi_3NbO_7 (Section 4.3), there are two principal means by which pyrochlore-type structural motifs can be incorporated into fluorite-type; tetrahedral clusters of MoO_6 octahedra, and continuous $<1\ 1\ 0>_f$ strings of MoO_6 octahedra (Figure 3). Building solely from the first of these motifs allows only one possible model for the structure of $Bi_{38}Mo_7O_{78}$, given the restrictions of space group, unit cell and stoichiometry. This cluster model is shown in Figure 43, illustrating the distorted, oxygen-deficient, fluorite-type anion array that would follow from the cation array in the manner shown in Figure 2. This cluster model has stoichiometry $Bi_{38}Mo_7O_{82}$, *i.e.* only a small number of additional oxygen atom vacancies are required in the bismuth-rich regions of the structure to fully comply with stoichiometric requirements.

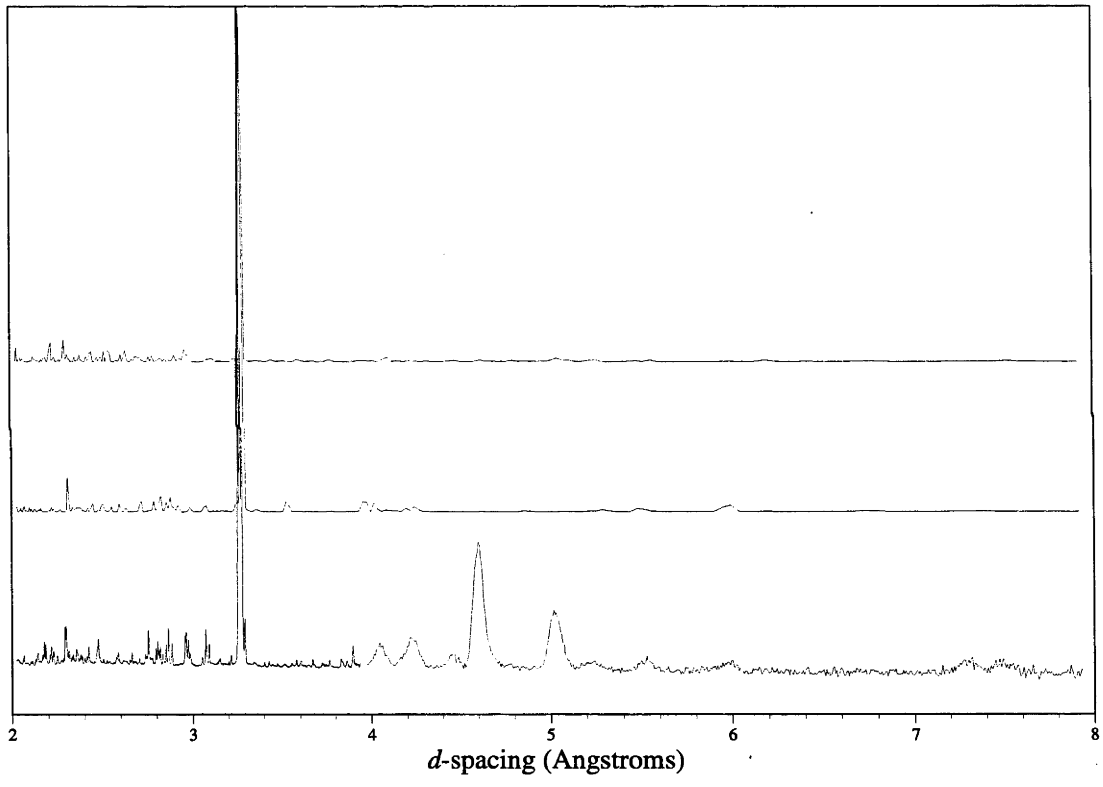

Figure 45. Comparison of neutron powder diffraction patterns calculated from models of $Bi_{38}Mo_7O_{78}$ based on the cluster (top) and string (middle) motifs against observed HRPD and POLARIS data (bottom).

Despite the appealing way in which the cluster approach can be used to build an unambiguous structural model for $Bi_{38}Mo_7O_{78}$, the model itself does not satisfactorily fit observed data. The metal atom ordering scheme does not agree well with low angle synchrotron XRD data (Figure 44), and the fully ordered model shown in Figure 43 gives a poor fit to high *d*-spacing neutron powder diffraction data (Figure 45). Being relatively insensitive to displacive modulation, both these data subsets should be expected to show greater agreement with a correct compositionally ordered model. The model is also at odds with HRTEM images published by Buttrey *et al.* (13). The images clearly show a stepped,

diamond-like contrast pattern in the $[1\ 0\ 1] = [1\ 0\ 1]_f$ projection, but no such distinct contrast pattern in the $[0\ 3\ 5] = [0\ 1\ 1]_f$ projection. The cluster model fails to explain either the diamond-like pattern or the reason behind any significant difference between the contrast patterns in different $<1\ 1\ 0>_f$ projections.

Alternatively, a model can be constructed using the string motif from pyrochlore-type. This motif requires the construction of the longest possible strings of MoO_6 octahedra along $<1\ 1\ 0>_f$ directions. As in the case of the 3 x 3 x 7 fluorite-type superstructure of type III Bi_3NbO_7 (Section 4.3), infinite strings are only possible perpendicular to the long axis of the supercell. Given the space-group symmetry and the presence of one of the Mo atoms on the inversion centre, this would place all Mo atoms in parallel 'cross' patterns at $z = 0$ and $z = \frac{1}{2}$. Such a 'cross' pattern cannot, however, provide the correct stoichiometry, placing 20 Mo atoms in the unit cell where 28 are required. The model also conspicuously fails to account for the HRTEM observations of Buttrey *et al.* A diamond-like contrast pattern would be generated in the $[0\ 3\ 5] = [0\ 1\ 1]_f$ and $[5\ 3\ 0] = [1\ 1\ 0]_f$ projections, but not the $[1\ 0\ 1] = [1\ 0\ 1]_f$ projection where a layered contrast pattern would be generated. Furthermore, the diamond-like pattern would not be 'stepped' as observed.

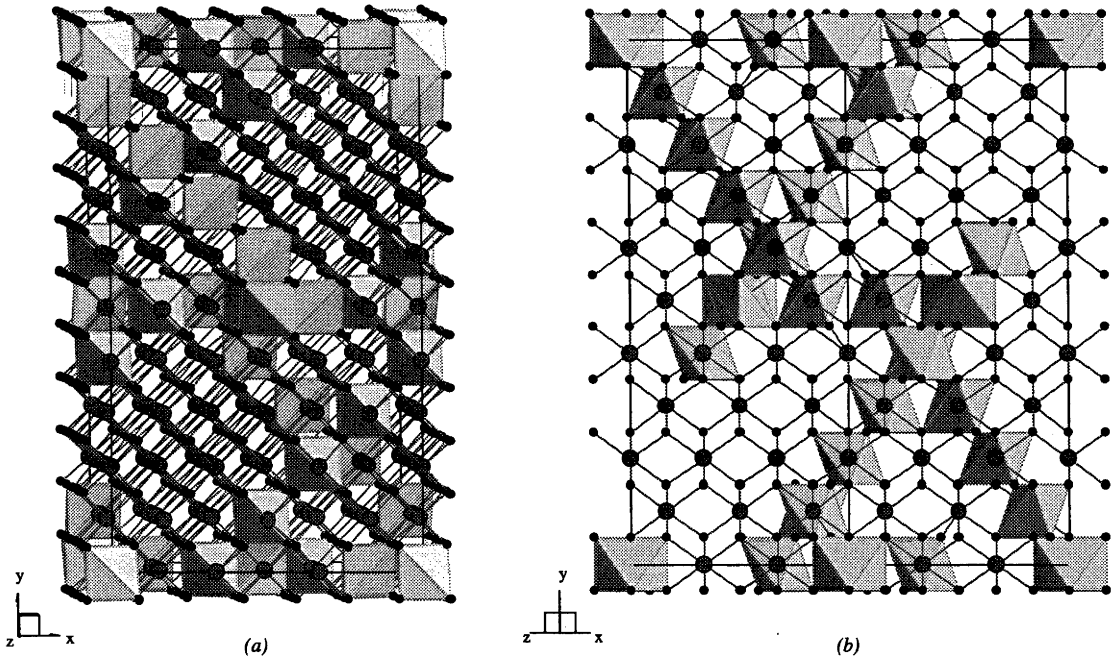

Figure 46. String model for the structure of $Bi_{38}Mo_7O_{78}$ (a) close to the [0 0 1] direction and (b) down the [1 0 1] direction. Bismuth atoms are darker than MoO_6 octahedra, and oxygen atoms are black.

In order for a string model to fit the observed HRTEM contrast pattern, it is necessary to orient the strings perpendicular to the **c** axis of the supercell. Unfortunately, the 5 x 3 fluorite-type cross-section in this direction rules out the possibility of infinite strings of MoO_6 octahedra. The arrangement which gives the longest continuous strings and the desired stoichiometric ratio is shown in Figure 46. This model generates a stepped, diamond-like

contrast pattern in the [1 0 1] projection and no contrast pattern in the [0 3 5] or [5 3 0] projections. Note that the 'steps' in the $<1\ 1\ 0>_f$ strings form triangles of three Mo atoms on $<1\ 1\ 1>_f$ planes, *i.e.* the faces of tetrahedra from the cluster model (Figure 43). The modified fluorite-type oxygen atom array which follows from the metal atom array can therefore be determined in the manner shown in Figure 2. This oxygen atom array is included in Figure 46. The overall stoichiometry is $Bi_{38}Mo_7O_{83}$, *i.e.*, again, a small number of additional oxygen vacancies are required in the bismuth-rich regions of the model.

Diffraction patterns calculated from this model are compared with observed synchrotron XRD and neutron powder diffraction data in Figure 44 and Figure 45 respectively. It is not immediately obvious that the string model offers an improved fit to observed data compared to the cluster model. Rietveld analysis (GSAS) indicates slightly better statistical fits for the string model, however, without refinement the difference is not significant. It can nonetheless be seen qualitatively, particularly for the XRD data (Figure 44), that the string model more effectively places intensity in the low-angle/high *d*-spacing satellite reflections. These data therefore qualitatively support the string model.

Attempts were made to refine metal atom positions from XRD data for both models. Stable refinements could be achieved in both cases, however, in neither case were the results convincing; rather, they appeared to represent a randomisation of the fluorite-type array. Fourier synthesis methods also failed to yield convincing evidence for any particular metal atom compositional distribution. There is apparently insufficient intensity in the satellite reflections, even using synchrotron XRD data, to refine the positions of the 23 independent metal atom sites.

Similarly, attempts to refine the oxygen atom array (or to determine it through Fourier synthesis methods) using neutron powder diffraction data for both models failed to produce meaningful results. In the case of neutron data, such an outcome could reasonably be anticipated; there are 48 independent oxygen atom sites in the fluorite-type subcell, *i.e.* 71 independent atoms (minus a relatively small number of oxygen vacancies) make a significant contribution to the observed diffraction intensity. Such a problem is almost certainly intractable using powder data.

Clearly, resolution of the structure of $Bi_{38}Mo_7O_{78}$ will require the collection of single-crystal X-ray diffraction data. The endemic twinning observed in the crystals will complicate the collection of such data, as it will almost certainly be necessary to collect both twin components as single overlapping reflections, except at very high angle. Nonetheless, on the basis of available evidence, it must be concluded that the string model shown in Figure 46 is a more likely solution than the cluster model.

The final (string) model for the metal atom ordering in $Bi_{38}Mo_7O_{78}$ is shown in Figure 47, mapped onto a 3 x 3 x 3 fluorite-type grid. Lines connecting nearest-neighbour Mo atoms directions highlight the $<1\ 1\ 0>_f$ strings of Mo atoms, which are stepped in a bow-tie pattern. Comparing Figure 47 with the equivalent projections of Bi_2O_3-$(Nb/Ta)_2O_5$ type II (Figure 30) and pyrochlore-type (Figure 2*(d)*), it can be seen that this bow-tie pattern is equivalent to the parallel faces of adjacent corner-connected M_4 tetrahedra. The structure model for $Bi_{38}Mo_7O_{78}$ therefore contains recognisable clusters from pyrochlore-type, and in this sense a relationship to the type II phase can be proposed. The dominant structural motif in this structure is, however, continuous $<1\ 1\ 0>_f$ strings of *M* atoms, and in this sense the structure of $Bi_{38}Mo_7O_{78}$ is much more closely related to that of type III Bi_3NbO_7; the two $<1\ 1\ 0>_f$ directions along which strings are oriented are both perpendicular to the same $<1\ 0\ 0>_f$ direction, as in Bi_3NbO_7 (Figure 36). It is the interactions between the strings that differentiates the structure types. Clearly, $<1\ 1\ 0>_f$ strings of *M* atoms represent a very versatile structural motif by which pyrochlore-type units may be incorporated into fluorite-type.

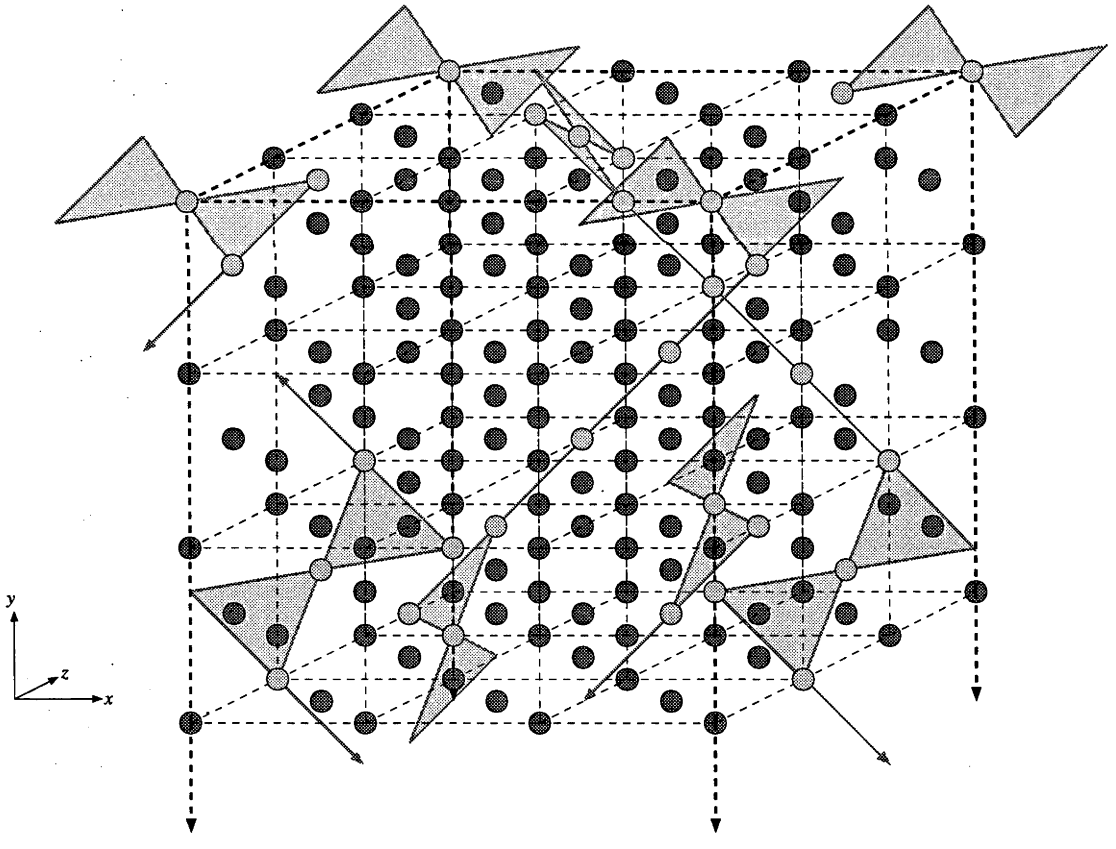

Figure 47. The metal atom array of $Bi_{38}Mo_7O_{78}$ mapped onto 3 x 3 x 3 average fluorite-type subcells. Dashed lines indicate the fluorite-type subcell grid, and heavy dashed lines indicate the supercell. Bismuth atoms are darker than Mo atoms. Grey lines and shaded triangles highlight nearest-neighbour Mo connections along $<1\ 1\ 0>_f$ directions.

4.7 Type II Bi_2O_3-WO_3

As discussed in Section 3.3.3, the type II phase reported by Zhou (14) in the system Bi_2O_3-WO_3 as a solid solution in the range Bi_6WO_{12}-$Bi_{18}W_4O_{39}$ was identified in the present study at approximately 17.5 mol% W_2O_6. The reported, tetragonal, $3\mathbf{a}_f$, $3\mathbf{b}_f$, $3\mathbf{c}_f$ *F*-centered superstructure of fluorite-type was confirmed (Section 3.4.1.3).

Zhou inferred from HRTEM observations that tungsten atoms were arranged on the $<1\ 1\ 1> \equiv <1\ 1\ 1>_f$ planes of this fluorite-type superstructure. In the context of the present study, this observation suggests that the structure may be related to those of type II Bi_2O_3-$(Nb/Ta)_2O_5$ (Section 4.2), type III Bi_3NbO_7 (Section 4.3) and $Bi_{38}Mo_7O_{78}$ (Section 4.6). These phases share a pyrochlore-type structural motif in the form of strings of MO_6 octahedra along $<1\ 1\ 0>_f$ directions (Figure 3*(d)*). (The structure of Bi_2O_3-WO_3 type II might, for example, be considered as a variant of type II Bi_2O_3-$(Nb/Ta)_2O_5$ in which $\varepsilon = \frac{1}{3}$.) Given the different expressions of the $<1\ 1\ 0>_f$ string motif in these structures, however, (Figure 30, Figure 36 and Figure 47) there are many possible models which can be proposed.

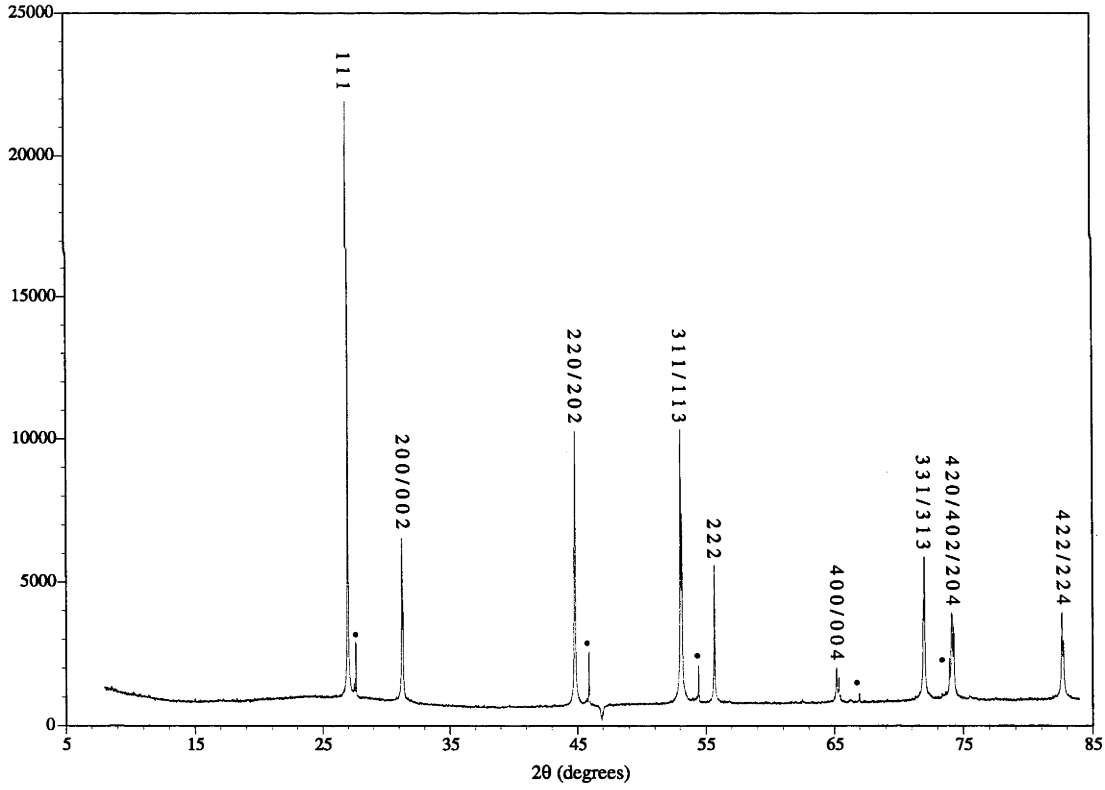

Figure 48. XRD pattern collected using a synchrotron source (λ = 1.4986 (4) Å) of type II Bi_2O_3-WO_3 indexed onto a tetragonal fluorite-type subcell. Silicon standard reflections are marked (•).

Any such proposals would need to be tested against observed diffraction data. Unfortunately, however, it was not possible to obtain single crystals of this phase, nor was there any opportunity to collect neutron powder diffraction data. The best available data were the synchrotron XRD data shown in Figure 48. While these data display the fine tetragonal

splitting expected in the fluorite-type subcell, there is clearly no significant intensity in the satellite reflections. This indicates that there are no significant displacive relaxations of the metal atoms from their positions in the fluorite-type subcell, and gives no information about compositional ordering; the extremely small difference between the X-ray scattering powers of tungsten and bismuth mean that even with complete compositional ordering, the strongest modulation peaks would be less than 0.1 % the intensity of the $(1\ 1\ 1)_f$ peak. Therefore, given the available data, and in the absence of a definitive space-group determination from ED, a definitive structural model for this phase could not be proposed.

A structural model was proposed for this phase by Zhou (14) based on the cluster motif for the inclusion of pyrochlore-type into fluorite-type (Figure 2), and simulated HRTEM images and DPs were shown to agree with observations. The string motif, which has so far been more successful in the present study, might have had a number of advantages in this case, such as allowing a higher symmetry (Zhou's model being monoclinic despite the metrically tetragonal cell) and a more flexible composition (Zhou's model having the composition $Bi_{46}W_8O_{93}$ *i.e.* 14.8 mol% W_2O_6). Ultimately, however, given the available data it was not possible to meaningfully propose such a model. It could only be concluded that Bi_2O_3-WO_3 type II was a superstructure of fluorite-type δ-Bi_2O_3, with very little displacive relaxation in the metal atom array.

4.8 Type II* Bi_2O_3-Ta_2O_5: $Bi_7Ta_3O_{18}$ (59)

In Section 3.4.1.2 (8), ED patterns reported for type II* $Bi_7Ta_3O_{18}$ were reproduced, but a unit cell was derived apparently unrelated to that reported by Zhou (21). There was no unambiguous fluorite-type subcell underlying this unit cell, despite observation of a number of ostensibly fluorite-like projections of the reciprocal sub-lattice. Synchrotron XRD data also showed a pseudo-fluorite-type reciprocal lattice which could not be unambiguously indexed as fluorite-type. It was concluded that while $Bi_7Ta_3O_{18}$ might contain structural elements of fluorite-type δ-Bi_2O_3, it must be too far removed from that prototype to be usefully described as a modulated variant thereof.

It proved possible to grow crystals of $Bi_7Ta_3O_{18}$, of sufficient size for collection of X-ray diffraction data at a synchrotron source. $Bi_7Ta_3O_{18}$ has also been synthesised as a single phase powder in sufficient quantities for collection of neutron powder diffraction data. The greater relative contribution of oxygen atoms to neutron scattering (compared to their contribution to X-ray scattering) provides an important independent check on refined oxygen atom parameters. In this Section, the structure of $Bi_7Ta_3O_{18}$ is reported and discussed.

4.8.1 Experimental

4.8.1.1 Single Crystal X-ray Diffraction

Crystals of $Bi_7Ta_3O_{18}$ were grown by solid-state reaction of a mixture of Bi_2O_3 (Koch-Light 99.998 %) and Ta_2O_5 (Aldrich 99.99 %) at mole ratio 17:8. The mixture was heated in a platinum crucible to 1473 K then cooled to 1123 K over 160 hours before quenching to room temperature. Small, transparent yellow, plate-like crystals were formed on the surface.

Crystal data	
Chemical formula	$Bi_7Ta_3O_{18}$
Chemical formula weight	2293.71
Cell setting	Triclinic
Space group	*C*1
a (Å)	34.005(3)
b (Å)	7.6024(4)
c (Å)	6.6358(5)
α (°)	90.086(6)
β (°)	109.127(6)
γ (°)	90.043(6)
V (Å^3)	1620.8(2)
Z	4
D_x (Mg m^{-3})	9.4
Radiation type	Synchrotron X-ray
Wavelength (Å)	0.9580(4)
No. of reflections for cell parameters	25
θ range (°)	22.76-37.98
μ (mm^{-1})	85.4
Temperature (K)	293
Crystal form	Plate
Crystal size (mm)	0.02 x 0.02 x 0.002
Crystal colour	Yellow
Data collection	
Diffractometer	Tsukuba BL14a
Data collection method	ω scans
Absorption correction	Gaussian
T_{min} - T_{max}	0.277 - 0.844
No. of measured reflections	17604
No. of independent reflections	13798
No. of observed reflections	11796
Criterion for observed reflections	$F^2 > 3\sigma(F^2)$
R_{int}	0.023
θ_{max} (°)	50
Range of *h*, *k*, *l*	$-54 \rightarrow h \rightarrow 54$, $-12 \rightarrow k \rightarrow 12$, $-10 \rightarrow l \rightarrow 10$
No. of standard reflections	6
Frequency of standard reflections	Every 200 reflections

Refinement	
Refinement on	F^2
$R[F^2 > 2\sigma(F^2)]$	0.0386
$wR(F^2)$	0.0337
S	1.2490
No. of reflections used in refinement	11796
No. of parameters used	327
Weighting scheme	$1/\sigma^2(F)$
$(\Delta/\sigma)_{max}$	0.00118
$\Delta\rho_{max}$ (e Å^{-3})	5.80
$\Delta\rho_{min}$ (e Å^{-3})	-5.61
Extinction method	Zachariasen (60)
Extinction coefficient	1828 (30)
Source of atomic scattering factors	Int. Tables Vol. IV Tables 2.2B and 2.3.1

Table 10. Experimental details: single crystal X-ray diffraction.

Single-crystal X-ray diffraction data were collected at the Photon Factory in order that the smallest possible crystals could be used, minimising absorption and reducing the probability of twinning. Experimental details for the diffraction experiment are summarised in Table 10. *Xtal3.2* (61) was used for all calculations.

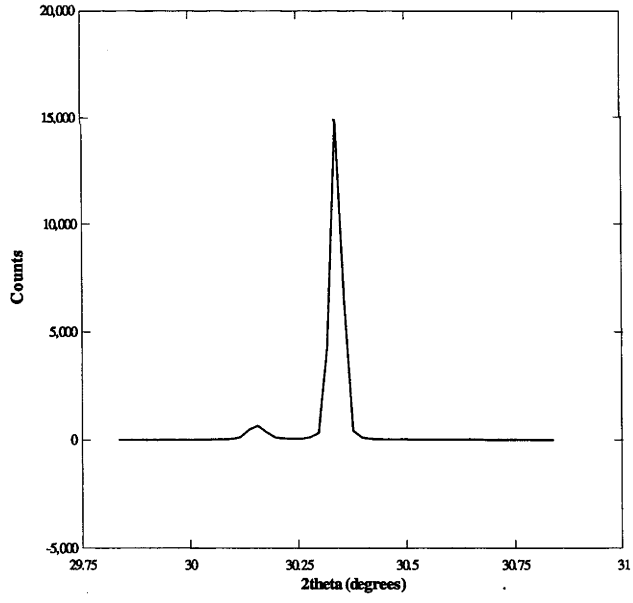

Figure 49. An example of a split peak, (0 8 0), observed in single-crystal X-ray diffraction due to twinning of the triclinic cell.

ED and XRD indicated the probable symmetry to be monoclinic *C2/m* (8). Strong twinning was observed against the monoclinic *b* axis in this setting, and some difficulty was experienced in finding an untwinned crystal. Very small plates (~ 20 μm across and 1-2 μm thick) were found to be relatively twin-free. When ostensibly untwinned crystals were found, however, it was noted that the angles α and γ, constrained to 90 ° in *C2/m*, in fact

reproducibly deviated from 90 ° by approximately 0.08 ° and 0.05 °, respectively. Furthermore, peak splitting was observed in high-angle ω-scans (principally along the *b* axis) corresponding to twinning against these slightly non-90 ° angles. On this basis it was concluded that the symmetry was in fact triclinic ($C\bar{1}$ or $C1$).

Although this twinning was never eliminated, the major twin component of the crystal ultimately chosen for data collection contributed approximately 95 % of the total intensity. An example of a split reflection in this crystal is shown in Figure 49. Because the majority of peaks were not split sufficiently for separate data collection, data were collected using 1 ° wide ω-scans in order that the full intensity from both components would be collected for all reflections.

An absorption correction was applied with the crystal approximated to a circular plate 20 μm in diameter and 2 μm thick (normal to the long axis *a*).

Crystal data	
Chemical formula	$Bi_7Ta_3O_{18}$
Chemical formula weight	2293.71
Cell setting	Mononclinic
Space group	*C2/m*
a (Å)	34.0084(9)
b (Å)	7.6069(2)
c (Å)	6.6364(2)
β (°)	109.237(1)
V (Å^3)	1620.94(7)
Z	4
Radiation type	Neutron
Temperature (K)	293
Specimen shape	Cylinder
Dimensions (mm)	25 x 8
Particle morphology	Plate
Preparation conditions	Sealed platinum tube, 101.3 kPa, 1173 K
Colour	Yellow
Data collection	
Diffractometer	POLARIS
Detectors	^{3}He gas and ZnS scintillation counters
Data collection method	Time-of-flight scans
Specimen mounting	Vanadium can
Refinement	
R_p	0.0455
wR_p	0.0342
S	5.41
Profile function	Exponential pseudo-Voigt convolution
No. of parameters used	116

Table 11. Experimental details: neutron powder diffraction.

4.8.1.2 Neutron Powder Diffraction

A powder sample of $Bi_7Ta_3O_{18}$ was prepared by solid-state reaction of a mixture of Bi_2O_3 (Koch-Lite 99.998 %) and Ta_2O_5 (Aldrich 99.99 %) at mole ratio 7:3 in a platinum crucible at 1173 K for 0.5 hours. The sample was quenched to room temperature, reground, annealed in a sealed platinum vessel at 1173 K for 168 hours and again quenched to room temperature. A homogeneous, pale yellow powder was obtained and identified as single-phase $Bi_7Ta_3O_{18}$ by XRD (Guinier-Hägg camera) (8).

Neutron powder diffraction data were collected on POLARIS (6). The high flux instrument was sought in order that a small sample could be used; difficulties were experienced in obtaining a large, homogenous sample via the method described above. Experimental details for the diffraction experiment are summarised in Table 11. The resolution was not sufficient to observe the small triclinic splitting described above. Calculations were carried out using *GSAS* (34).

4.8.2 Refinement

An initial model for the structure of the metal atom array was obtained using direct methods on the single-crystal data set in the high symmetry, *C*2/*m*, setting. Occupational and positional parameters were refined, and the metal atom populations appeared to be fully ordered. Using Fourier difference syntheses to determine oxygen atom positions, it became clear that many peaks in the difference map were at plausible distances from metal atoms, but implausibly close to each other. It was possible to choose and refine a complete set of plausible oxygen sites, yet the refinement statistics remained poor ($R = 0.195$) and the Fourier difference map retained many extraneous (plausible oxygen) peaks.

This *C*2/*m* model was subsequently tested against the powder neutron diffraction profile by the Rietveld method using GSAS (34), in order to corroborate the refined oxygen atom positions. It was possible to refine all positional and isotropic displacement parameters without any significant atomic shifts developing. The difference between observed and calculated patterns at this point (Figure 50) appeared sufficiently small that meaningful refinement of further parameters (*i.e.* in lower symmetries) was considered unlikely.

Using this neutron-diffraction refined *C*2/*m* model as a starting point for further single-crystal refinement, the symmetry was lowered to each of the three maximal non-isomorphic subgroups; $C\bar{1}$, *C*2 and *Cm*. The refinement statistics, however, improved only slightly, to $R = 0.178$, 0.175 and 0.147 respectively. These improvements were considered insufficient to justify the increased number of refined variables. It was necessary to lower the symmetry to *C*1 before the statistics dramatically improved, to $R = 0.047$, and the extraneous oxygen peaks in the Fourier difference map disappeared (equivalent positions: x, y, z; $\frac{1}{2} + x$, $\frac{1}{2} + y, z$). See Section 4.8.4 for a discussion of the use of the non-standard space group *C*1.

The refinement was further improved ($R = 0.045$) by modelling the ~ 5 % twin component observed during data collection as a mirror-related twin perpendicular to **b**. The volume of this twin component was refined to 5.8(2) % of the total volume. Comparative refinement statistics for the various stages of the refinement described above are given in Table 12. Refinement of anisotropic displacement parameters on metal atom sites gave $R = 0.039$.

Space Group	*R*	*wR*	*S*
*C*2/*m*	0.1951	0.1791	5.1254
$C\bar{1}$	0.1776	0.1639	4.7027
*C*2	0.1749	0.1634	4.8541
Cm	0.1473	0.1416	4.4260
*C*1	0.0474	0.0410	1.4968
*C*1 (*Cm* twin)	0.0447	0.0384	1.4301

Table 12. Comparative refinement statistics for the single-crystal X-ray refinement of type II $Bi_7Ta_3O_{18}$ (all atoms refined with isotropic displacement parameters).*

The final (*C*1) refined model, when tested against the powder neutron data, gave a slightly improved fit ($R_p = 0.0426$, $wR_p = 0.0321$, $\chi^2 = 25.66$ *vs.* $R_p = 0.0455$, $wR_p = 0.0342$, $\chi^2 = 29.23$). The large number of atomic variables involved in the *C*1 model (including 165 displacive parameters), however, made refinement impractical.

4.8.3 Results

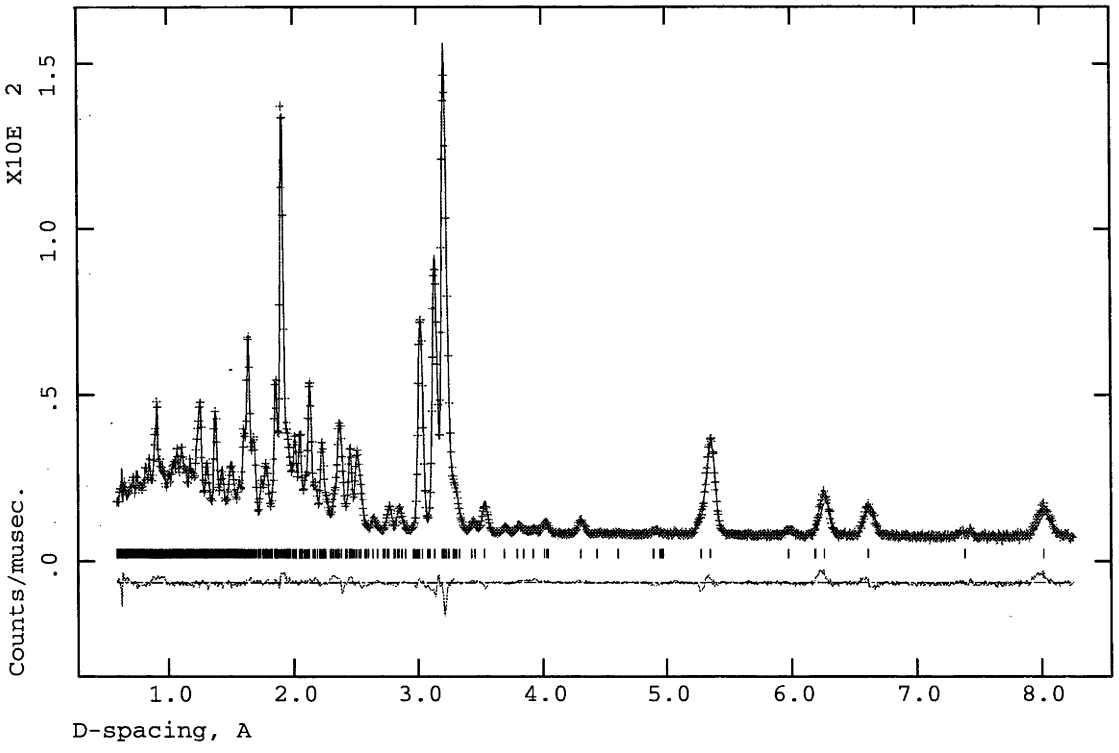

(a)

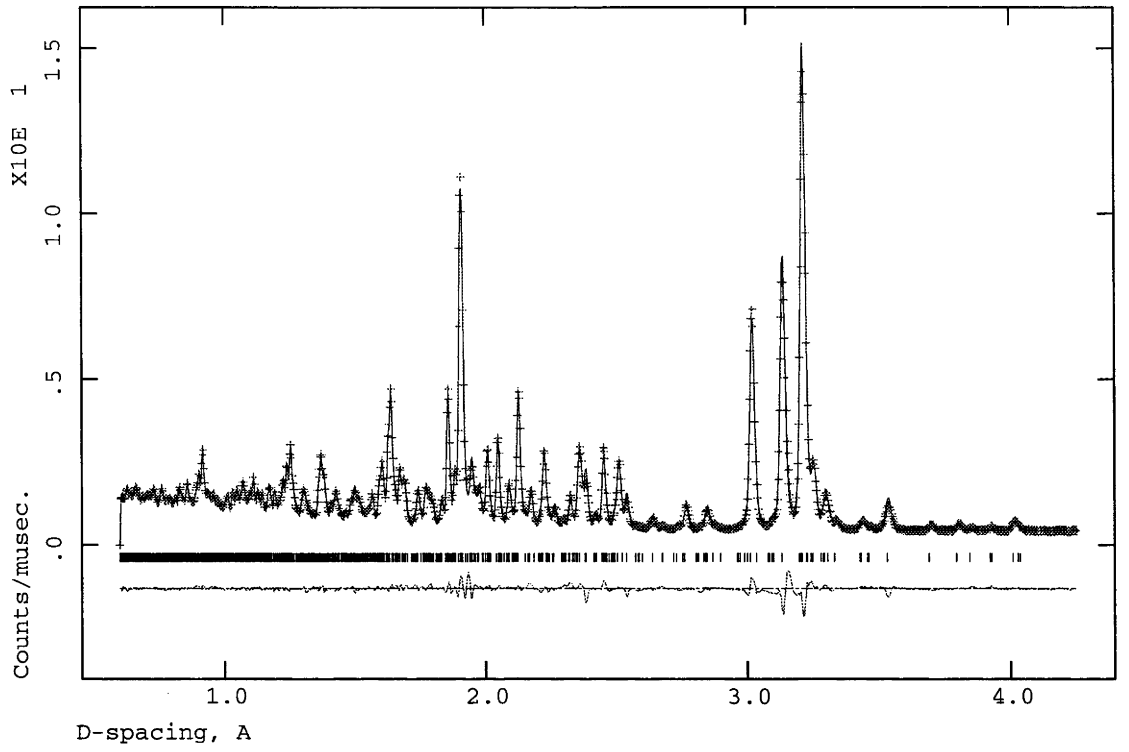

(b)

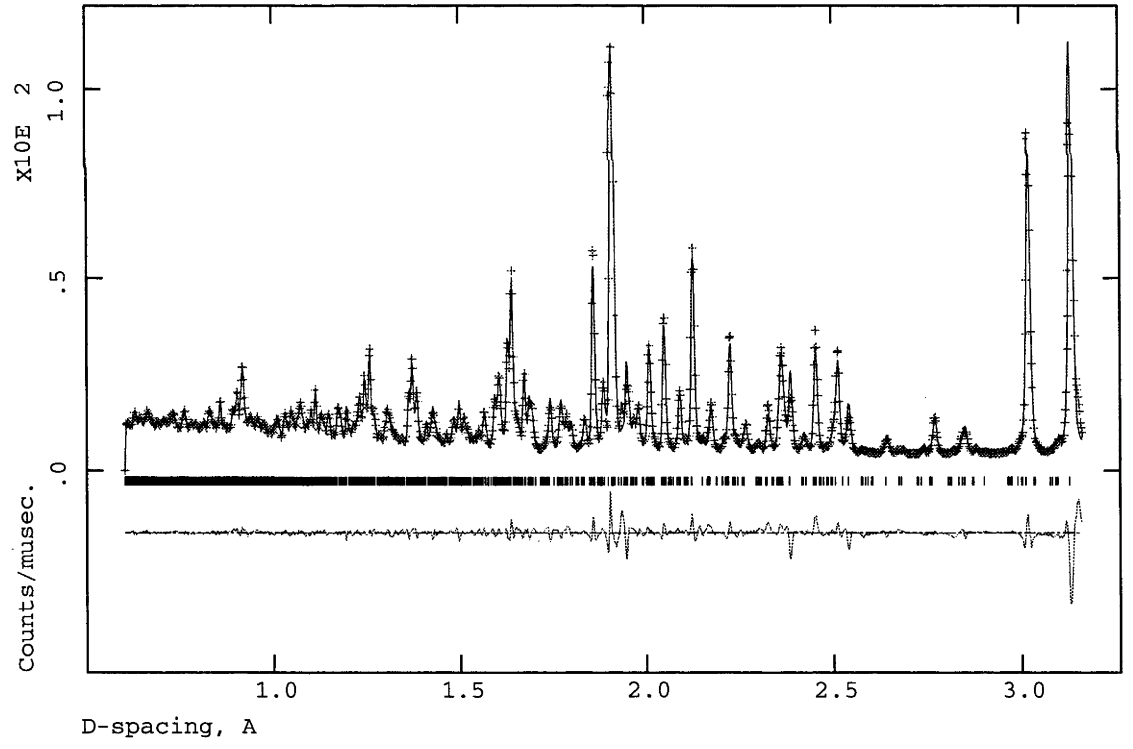

(c)

Figure 50. Observed (+), calculated and difference (bottom) neutron powder diffraction profiles for type II $Bi_7Ta_3O_{18}$ at the (a) 35 °, (b) 90 ° and (c) 145 ° detector banks.*

Final refined values for the fractional coordinates and $U_{eq} = \frac{1}{3}\Sigma_i\Sigma_j U_{ij} a_i^* b_j^* \mathbf{a}_i.\mathbf{a}_j$ / U_{iso} values of $Bi_7Ta_3O_{18}$ are given in Table 13, for both the single-crystal X-ray (*C*1) and the

powder neutron (*C*2/*m*) refinements. The *C*1 setting is used in order to emphasise the relationship to the *C*2/*m* parent structure; it may be transformed to the standard reduced, *P*1, setting *via* the real space transform $\mathbf{a}' = \mathbf{c}$, $\mathbf{b}' = \mathbf{b}$, $\mathbf{c}' = -\frac{1}{2}\mathbf{a} - \frac{1}{2}\mathbf{b} - \mathbf{c}$. Bond lengths for the refined *C*1 structure are given in Table 14 and anisotropic atomic displacement parameters in Table 15. The final observed, calculated and difference powder neutron diffraction profiles for the Rietveld-refinement in *C*2/*m* are shown in Figure 50.

Atom	*x*	*y*	*z*	U_{eq}/U_{iso} (Å^2)
Single crystal refinement				
Bi1	0.34035(3)	0.23954(9)	0.48808(13)	0.0175(4)
Bi2	0.338481(19)	0.50059(8)	0.96705(9)	0.0077(3)
Bi3	0.352745(18)	0.00191(8)	0.00818(8)	0.0078(3)
Ta4	0.439500(19)	0.25362(8)	0.97483(10)	0.0053(2)
Bi5	0.13920(2)	0.25045(8)	0.42381(9)	0.0084(3)
Ta6	0.44073(2)	0.75159(8)	0.98212(10)	0.0052(3)
Bi7	0.145987(18)	0.50095(7)	0.96509(8)	0.0074(3)
Ta8	0.25045(2)	0.74852(9)	0.00335(10)	0.0055(2)
Bi9	0.13846(2)	0.74789(8)	0.42799(10)	0.0106(3)
Bi10	0.35341(2)	0.74841(9)	0.50671(11)	0.0149(4)
Bi11	0.44582(2)	0.01013(9)	0.52880(9)	0.0108(3)
Ta12	0.051995(18)	0.74855(7)	0.96806(9)	0.0052(3)
Bi13	0.249612(19)	0.99561(8)	0.52358(9)	0.0076(3)
Bi14	0.05081(2)	0.00216(9)	0.49021(10)	0.0095(3)
Ta15	0.24956(2)	0.25148(9)	0.99665(11)	0.0059(2)
Bi16	0.246719(19)	0.50346(9)	0.46346(9)	0.0090(3)
Bi17	0.045577(19)	0.50016(8)	0.42758(9)	0.0097(3)
Ta18	0.052326(18)	0.25109(7)	0.99677(9)	0.0049(3)
Bi19	0.158172(19)	0.99860(8)	0.99300(8)	0.0088(3)
Bi20	0.44170(2)	0.49876(8)	0.46484(9)	0.0079(3)
O1	0.4279(3)	0.0028(12)	0.8918(13)	0.0066(14)
O2	0.3787(3)	0.7102(13)	0.8888(15)	0.0104(16)
O3	0.1165(3)	0.7870(12)	0.0673(14)	0.0084(15)
O4	0.3789(3)	0.2971(13)	0.8917(15)	0.0117(17)
O5	0.1162(3)	0.2103(11)	0.0686(13)	0.0053(14)
O6	0.0674(3)	0.2152(12)	0.2988(14)	0.0068(15)
O7	0.4455(3)	0.2042(13)	0.2681(15)	0.0127(17)
O8	0.4476(3)	0.8047(13)	0.2686(16)	0.0137(18)
O9	0.4247(3)	0.7119(12)	0.6500(14)	0.0096(16)
O10	0.4971(3)	0.7834(12)	0.9688(14)	0.0087(15)
O11	0.2356(3)	0.0006(13)	0.9354(15)	0.0124(16)
O12	0.3814(3)	0.9934(13)	0.4020(14)	0.0095(15)
O13	0.2581(3)	0.7938(13)	0.3109(15)	0.0129(17)
O14	0.4506(3)	0.5032(13)	0.0500(15)	0.0119(17)
O15	0.2662(3)	0.2029(11)	0.3241(13)	0.0085(14)
O16	0.1632(3)	0.5022(13)	0.3090(14)	0.0100(15)

O17	0.3246(3)	0.0028(14)	0.6498(15)	0.0146(17)
O18	0.0456(3)	0.9970(13)	0.8942(14)	0.0110(16)
O19	0.3779(3)	0.5098(14)	0.3089(15)	0.0144(17)
O20	0.1917(3)	0.2938(12)	0.9800(14)	0.0117(16)
O21	0.1131(3)	0.0024(14)	0.6343(15)	0.0144(17)
O22	0.1907(3)	0.7023(14)	0.9537(16)	0.0158(18)
O23	0.0671(3)	0.4998(13)	0.0475(13)	0.0083(15)
O24	0.1805(3)	0.0085(14)	0.3466(16)	0.0142(18)
O25	0.1098(3)	0.5058(14)	0.5408(16)	0.0136(17)
O26	0.0476(3)	0.2990(12)	0.6789(14)	0.0094(16)
O27	0.0687(3)	0.7908(13)	0.2996(15)	0.0106(16)
O28	0.2646(3)	0.5027(12)	0.0867(14)	0.0105(15)
O29	0.4278(3)	0.2940(13)	0.6522(15)	0.0107(16)
O30	0.0448(3)	0.7037(14)	0.6775(16)	0.0148(18)
O31	0.3110(3)	0.2065(13)	0.0623(15)	0.0151(18)
O32	0.3111(3)	0.8029(14)	0.0691(17)	0.019(2)
O33	0.2428(3)	0.3012(15)	0.7091(17)	0.022(2)
O34	0.3141(3)	0.4929(14)	0.5909(16)	0.0153(18)
O35	0.2463(3)	0.6994(14)	0.7057(17)	0.019(2)
O36	0.4982(3)	0.2185(13)	0.9810(14)	0.0095(16)
Rietveld refinement				
Bi1	0.24592(12)	0.5	0.4693(6)	0.0114(7)
Bi2	0.14509(7)	0.2522(4)	0.4641(3)	0.0154(5)
Bi3	0.14788(9)	0.5	0.9794(5)	0.0019(6)
Ta4	0.05535(7)	0.2490(3)	0.9919(4)	0.0011(4)
Bi5	0.04985(10)	0.5	0.4544(6)	0.0234(11)
Ta6	0.25	0.25	0	0.0032(8)
Bi7	0.16126(10)	0	0.0205(5)	0.0119(6)
Bi8	0.05314(9)	0	0.5117(5)	0.0043(6)
O9	0.07053(12)	0.5	0.0872(5)	0.0016(8)
O10	0.11913(9)	0.2017(4)	0.0979(5)	0.0085(7)
O11	0.04957(9)	0.2973(4)	0.7019(4)	0.0064(6)
O12	0.07096(9)	0.2109(5)	0.3232(5)	0.0106(7)
O13	0.04746(14)	0	0.9260(7)	0.0098(10)
O14	0	0.2889(5)	0	0.0026(7)
O15	0.23936(13)	0.2937(7)	0.6883(7)	0.0436(13)
O16	0.23930(15)	0	0.9454(8)	0.0140(10)
O17	0.16979(15)	0.5	0.3363(8)	0.0131(10)
O18	0.18926(11)	0.2898(5)	0.9466(6)	0.0223(9)
O19	0.11791(16)	0	0.6697(8)	0.0206(12)
O20	0.11376(13)	0.5	0.5550(7)	0.0035(8)
O21	0.18336(13)	0	0.3733(7)	0.0086(8)

Table 13. Fractional atomic coordinates and equivalent isotropic thermal displacement parameters ($Å^2$) for the single-crystal X-ray and Rietveld-refined structures of type II $Bi_7Ta_3O_{18}$.*

Bi1-O17	2.249(11)	Bi11-O12^{v}	2.076(9)
Bi1-O34^{i}	2.317(11)	Bi11-O7^{v}	2.273(11)
Bi1-O15	2.413(8)	Bi11-O8^{v}	2.341(11)
Bi2-O19	2.226(9)	Bi11-O29	2.456(10)
Bi2-O4^{iii}	2.233(11)	Ta12-O36^{vi}	1.873(10)
Bi2-O2	2.268(11)	Ta12-O30	1.893(11)
Bi2-O34	2.359(10)	Ta12-O18	1.947(10)
Bi3-O32	2.198(12)	Ta12-O23	1.986(9)
Bi3-O31	2.213(11)	Ta12-O3	2.092(9)
Bi3-O17	2.254(9)	Ta12-O27	2.108(10)
Ta4-O7	1.927(10)	Bi13-O13^{v}	2.166(10)
Ta4-O14^{iv}	1.966(10)	Bi13-O15^{v}	2.246(9)
Ta4-O4	1.978(10)	Bi13-O24^{v}	2.259(10)
Ta4-O1	1.987(9)	Bi13-O17	2.409(10)
Ta4-O36	2.001(10)	Bi14-O21	2.018(9)
Ta4-O29	2.069(10)	Bi14-O6^{v}	2.243(10)
Bi5-O5	2.247(8)	Bi14-O27^{v}	2.247(10)
Bi5-O16^{iv}	2.306(10)	Ta15-O33	1.885(12)
Bi5-O6	2.322(9)	Ta15-O20	1.962(10)
Bi5-O25^{ii}	2.424(11)	Ta15-O11	1.975(10)
Ta6-O8	1.881(11)	Ta15-O28^{iv}	2.015(9)
Ta6-O14	1.945(10)	Ta15-O31	2.020(10)
Ta6-O10	1.962(10)	Ta15-O15	2.092(9)
Ta6-O1	2.008(9)	Bi16-O34^{i}	2.169(10)
Ta6-O2	2.019(10)	Bi16-O35^{i}	2.194(11)
Ta6-O9	2.111(9)	Bi16-O33^{vii}	2.277(12)
Bi7-O16	2.162(9)	Bi17-O25^{i}	2.064(10)
Bi7-O22	2.175(11)	Bi17-O26^{vii}	2.249(10)
Bi7-O20	2.193(10)	Bi17-O30^{i}	2.273(11)
Ta8-O28	1.965(9)	Ta18-O10^{viii}	1.899(10)
Ta8-O35	1.969(11)	Ta18-O26	1.900(10)
Ta8-O22	1.981(11)	Ta18-O23^{iv}	1.984(9)
Ta8-O11	1.996(10)	Ta18-O18	1.985(10)
Ta8-O13	2.000(10)	Ta18-O5	2.077(9)
Ta8-O32	2.006(11)	Ta18-O6	2.110(9)
Bi9-O27	2.268(9)	Bi19-O24	2.218(10)
Bi9-O3	2.282(9)	Bi19-O3	2.302(10)
Bi9-O16	2.292(10)	Bi19-O5	2.313(9)
Bi9-O25^{i}	2.319(11)	Bi19-O21	2.372(9)
Bi10-O12^{v}	2.303(10)	Bi20-O19	2.078(9)
Bi10-O9	2.313(9)	Bi20-O29^{vii}	2.141(10)
Bi10-O2	2.414(9)	Bi20-O9^{i}	2.220(10)

Symmetry codes: (i) $x, y, 1 + z$; (ii) $x, 1 + y, 1 + z$; (iii) $x, y - 1, z$; (iv) $x, 1 + y, z$; (v) $x, y, z - 1$; (vi) $x - \frac{1}{2}, y - \frac{1}{2}, z$; (vii) $x, y - 1, 1 + z$; (viii) $x - \frac{1}{2}, \frac{1}{2} + y, z$.

Table 14. Bond lengths (Å) for the refined single-crystal X-ray structure of type II $Bi_7Ta_3O_{18}$.*

Atom	U_{11}	U_{22}	U_{33}	U_{12}	U_{13}	U_{23}
Bi1	0.0304(4)	0.0088(3)	0.0224(3)	0.0040(3)	0.0180(3)	0.0028(2)
Bi2	0.0076(2)	0.0087(2)	0.0075(2)	-0.0001(2)	0.00230(19)	-0.0002(2)
Bi3	0.0068(2)	0.0082(2)	0.0083(2)	0.0004(2)	0.00184(18)	-0.0001(2)
Ta4	0.0058(2)	0.0051(2)	0.0056(2)	-0.00038(16)	0.00254(16)	-0.00041(15)
Bi5	0.0111(2)	0.0093(2)	0.0085(2)	-0.00057(19)	0.00229(18)	-0.00022(18)
Ta6	0.0058(2)	0.0053(2)	0.0059(2)	0.00013(16)	0.00278(16)	0.00015(15)
Bi7	0.0073(2)	0.0080(2)	0.0074(2)	-0.0010(2)	0.0023(2)	-0.0004(2)
Ta8	0.0069(2)	0.00494(17)	0.0064(2)	-0.00009(16)	0.00363(18)	-0.00014(16)
Bi9	0.0107(2)	0.0099(3)	0.0100(2)	-0.0000(2)	0.0031(2)	0.0000(2)
Bi10	0.0180(3)	0.0112(3)	0.0174(3)	-0.0040(3)	0.0070(3)	-0.0006(2)
Bi11	0.0073(2)	0.0139(3)	0.0099(2)	0.0003(2)	0.0017(2)	0.0002(2)
Ta12	0.0047(2)	0.0049(2)	0.0059(2)	-0.00043(17)	0.00177(17)	-0.00029(16)
Bi13	0.0071(2)	0.0086(2)	0.0071(2)	0.0006(2)	0.00201(18)	-0.00056(19)
Bi14	0.0075(2)	0.0119(3)	0.0098(2)	-0.0001(2)	0.00397(18)	-0.0000(2)
Ta15	0.0073(2)	0.00481(16)	0.0070(2)	-0.00018(15)	0.00411(17)	0.00023(15)
Bi16	0.0077(3)	0.0103(2)	0.0076(2)	0.0001(2)	0.0013(2)	-0.0005(2)
Bi17	0.0081(2)	0.0118(3)	0.0094(2)	-0.0001(2)	0.00276(19)	-0.0003(2)
Ta18	0.0054(2)	0.0049(2)	0.0060(2)	-0.00068(17)	0.00248(17)	-0.00049(16)
Bi19	0.0085(2)	0.0101(2)	0.0069(2)	-0.0005(2)	0.00247(19)	-0.0000(2)
Bi20	0.0064(2)	0.0103(2)	0.0082(2)	-0.0003(2)	0.00202(19)	0.0004(2)

Table 15. U_{ij} displacement parameters (10^{-3} Å^2) for metal atoms in the refined single-crystal X-ray structure of type II $Bi_7Ta_3O_{18}$.*

4.8.4 Discussion

The final refined model (*C*1) from single-crystal X-ray data is shown in Figure 51. The *C*2/*m* structure derived from X-ray and neutron diffraction data is topologically equivalent to this *C*1 model, with atom positions differing by less than 0.25 Å. The structure is essentially layered perpendicular to the long (*a*) axis, as can be seen in these projections. Tantalum atoms are coordinated in regular TaO_6 octahedra, which form columns along the [0 1 0] direction (Figure 51*(b)*). Octahedra within these columns are rotated through ~ 10 ° about the [0 0 1] direction (Figure 51*(b)*). The coordination environments of bismuth atoms appear to be related to the cubic (8-fold) coordination found in fluorite-type, distorted by the presence of TaO_6 octahedra such that Bi-O bond lengths vary between 2.0 and 3.0 Å. Setting the maximum Bi-O bond length at 2.75 Å allows three distinct classes of site to be identified: *(a)* Bi2, Bi3, Bi7, Bi13, Bi16 and Bi19 have distorted octahedral coordination; *(b)* Bi11, Bi14, Bi17 and Bi20 are located on the basal planes of square (Bi11, Bi14) or pentagonal (Bi17, Bi20) pyramids; and *(c)* Bi1, Bi5, Bi9 and Bi10 are offset from the centre of trigonal prisms. Examples of each of these coordination polyhedra are shown in Figure 52.

Pyramidal and trigonal prismatic coordination environments are typically observed around cations with stereochemically active electron lone pairs, such as Bi^{3+}. The archetypes

are α-PbO and $SbCl_3$ (or XeO_3) respectively (62). The distorted octahedral sites also reflect the stereochemical influence of the lone pair.

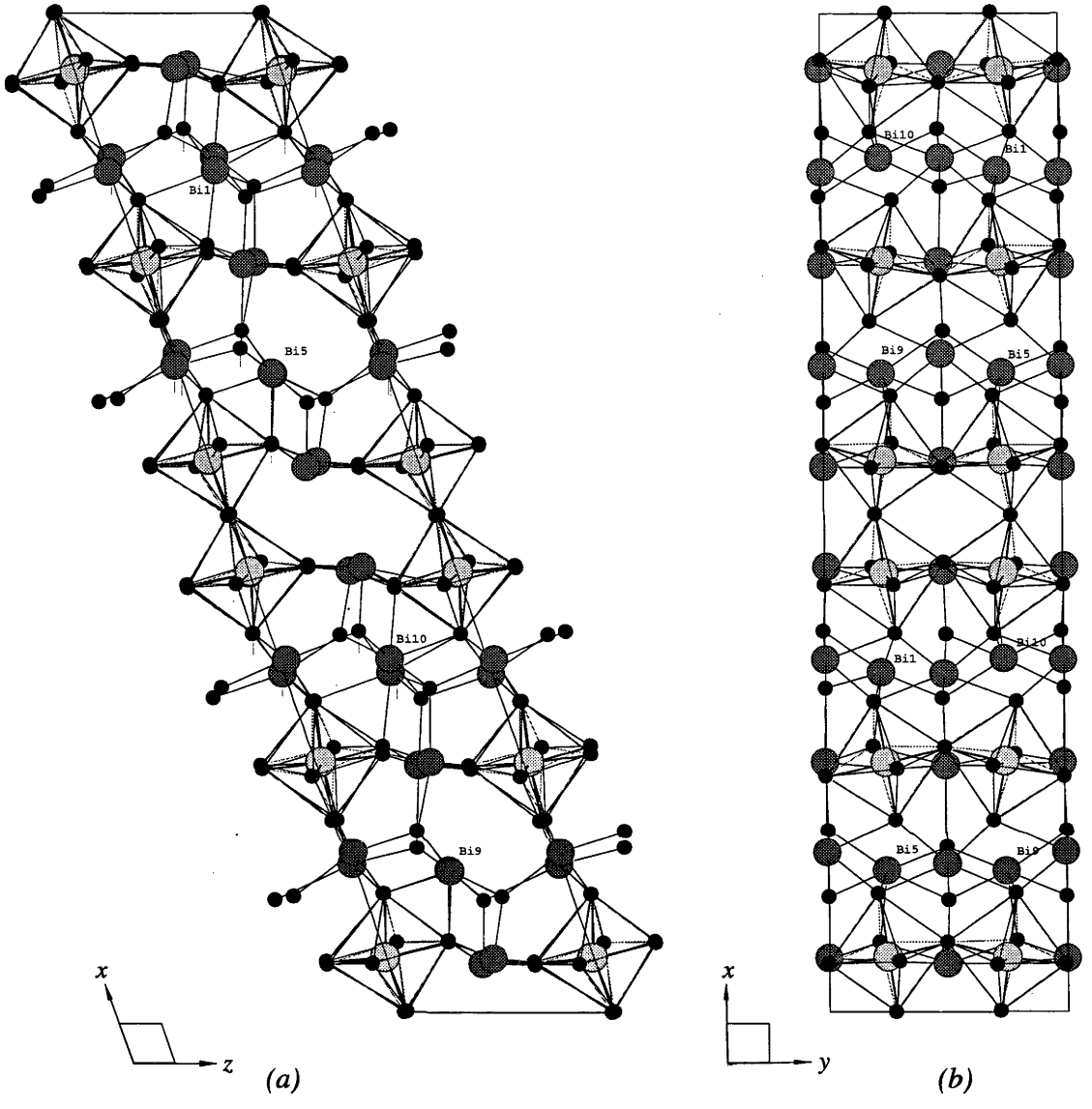

Figure 51. The final refined C1 structure of type II $Bi_7Ta_3O_{18}$ viewed down the (a) [0 1 0] and (b) [0 0 1] axes. Bismuth atoms are darker than TaO_6 atoms and octahedra, and oxygen atoms are black.*

Bond valence sums (52) are given in Table 16 for both the *C*2/*m* and *C*1 refined models. The results are of a similar standard in both space groups, and do not immediately indicate the driving force behind symmetry lowering. It is significant, however, that for both models bismuth atoms in trigonal prismatic sites have bond valence sums furthest from the expected value of 3.0. In *C*2/*m*, these four atoms are equivalent. Figure 51*(b)* shows that in *C*1, Bi1 and Bi10 have broken the mirror plane perpendicular to **b**, and Figure 51*(a)* shows that the 2-fold rotation axis about **b** now no longer maps the Bi1/Bi10 pair into the Bi5/Bi9 pair. This is by far the most significant deviation from *C*2/*m* symmetry in the final refined *C*1 structure. The subsequent improvement in bond valence sums is small, and the breaking of symmetry may be more an indication of the instability of the coordination environment than

the inherent stability of the lower symmetry configuration. Note that the mirror twin modelled in the refinement is accomplished by simply exchanging the x coordinates of Bi1 and Bi10, whereas a twin against the 2-fold axis would involve a split of the Bi5/Bi9 pair rather than the Bi1/Bi10 pair. That the structure is closer to *Cm* than to *C*2 is also supported by the comparative refinement statistics presented in Table 12.

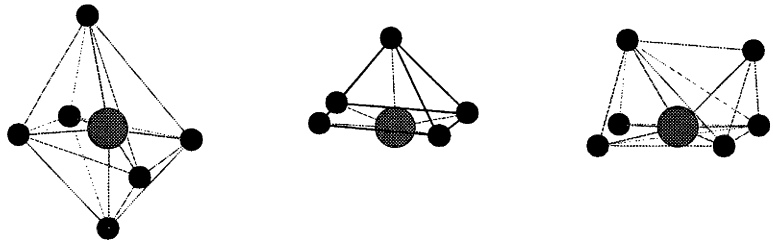

(a) *(b)* *(c)*

Figure 52. The coordination environments of (a) Bi2, (b) Bi11 and (c) Bi1.

No other reasons for symmetry lowering could be found; there is no evidence of unfavourably short metal-oxygen or oxygen-oxygen contacts in the higher symmetry, nor does the regularity of the TaO_6 octahedra, in terms of either O-Ta-O angles and Ta-O distances, appear to be compromised.

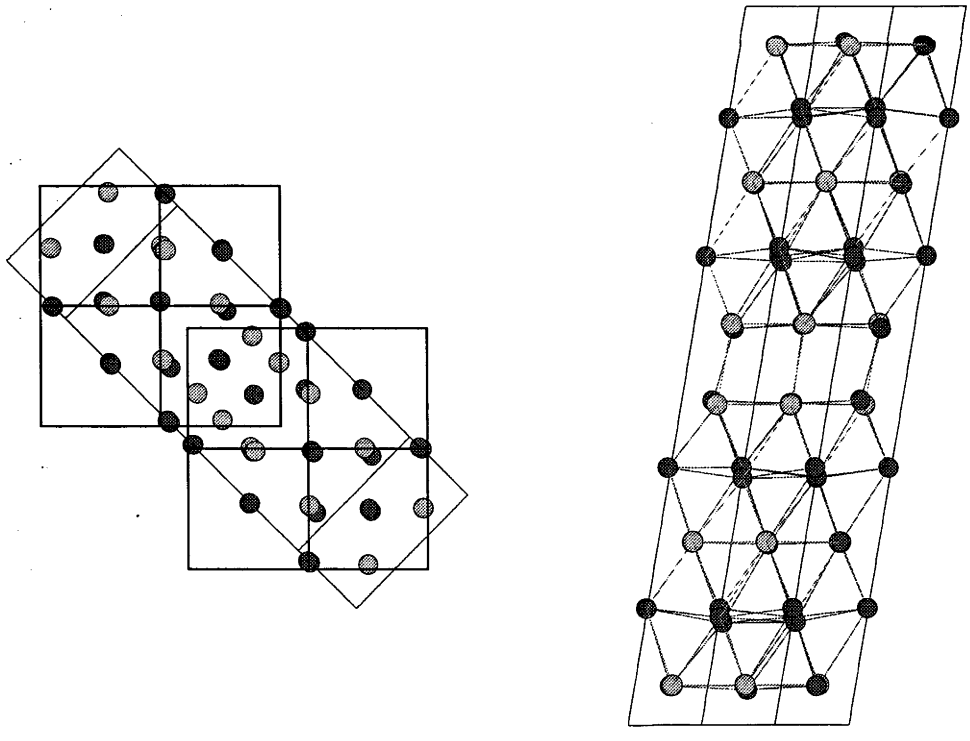

(a) *(b)*

Figure 53. The final refined C1 structure of type II $Bi_7Ta_3O_{18}$ viewed down the (a) [$\bar{1}$ 0 5] ≡ <1 0 0>$_f$ and (b) [0 $\bar{1}$ 2] ≡ <1 1 0>$_f$ axes. Dashed lines indicate a fluorite-type subcell grid. Nearest-neighbour metal atom connections are drawn in (b). Bismuth atoms are darker than tantalum atoms, and oxygen atoms are black.*

Although there is no unambiguous fluorite-type subcell in the diffraction patterns of type II* $Bi_7Ta_3O_{18}$, a number of fluorite-like patterns were obtained in ED (8). The origin of these patterns can be seen in the final refined structure. Figure 53*(a)* and *(b)* show only the metal atom array and clearly demonstrate the layered nature of the structure. Metal atoms between the layers have an fcc arrangement, highlighted by laying a fluorite-type grid over the metal atoms on either side (Figure 53*(a)*). Fluorite-type slabs therefore exist continuously throughout the structure, except on the layers at $x = 0$ and $x = \frac{1}{2}$. Fluorite-type slabs are stepped on these planes, perpendicular to $[1\ 1\ 1]_f$ within the slabs, making it meaningless (and effectively impossible) to relate a unique, average fluorite-type subcell to the unit cell of $Bi_7Ta_3O_{18}$ in diffraction space. In terms of these slabs, the major projections shown in Figure 51 are equivalent to *(a)* $<1\ 1\ 0>_f$ and *(b)* $<1\ 1\ 2>_f$.

Atom	*C2/m*	*C*1	Atom	*C2/m*	*C*1
Bi1	2.688	2.655	Bi2	3.290	3.101
Bi3	2.958	3.069	Ta4	4.996	5.025
Bi5	2.688	2.741	Ta6	4.996	5.064
Bi7	2.958	3.241	Ta8	5.041	5.003
Bi9	2.688	2.839	Bi10	2.688	2.699
Bi11	3.229	3.103	Ta12	4.996	5.177
Bi13	3.109	3.133	Bi14	2.941	3.218
Ta15	5.041	5.002	Bi16	3.109	3.111
Bi17	3.229	3.147	Ta18	4.996	5.044
Bi19	3.290	3.042	Bi20	2.941	3.197
O1	1.788	1.945	O2	2.011	2.055
O3	2.011	2.064	O4	2.011	2.032
O5	2.011	2.108	O6	1.999	2.111
O7	1.946	1.832	O8	1.946	1.803
O9	1.999	2.120	O10	2.036	2.011
O11	2.072	1.936	O12	2.358	2.300
O13	1.876	2.009	O14	2.022	1.939
O15	1.876	1.941	O16	2.136	2.179
O17	2.136	2.065	O18	2.022	1.940
O19	1.926	2.177	O20	1.973	1.963
O21	1.926	2.121	O22	1.973	1.964
O23	1.788	1.920	O24	1.988	1.968
O25	2.358	2.255	O26	1.946	1.959
O27	1.999	2.147	O28	2.072	1.945
O29	1.999	2.045	O30	1.946	1.922
O31	1.973	1.956	O32	1.973	1.907
O33	1.876	1.911	O34	1.988	2.167
O35	1.876	1.899	O36	2.036	2.000

Table 16. Bond valence sums for the single-crystal X-ray and Rietveld-refined structures of type II $Bi_7Ta_3O_{18}$.*

The nature of the [1 0 0] ≡ <1 1 1>$_f$ step itself can be seen in Figure 53*(b)*. One of the metal atom layers perpendicular to [1 0 0] ≡ <1 1 1>$_f$ is repeated in the fcc stacking sequence along **a**, creating an approximately identical layer shifted by $\frac{1}{10}$**a**, *i.e.* $\frac{1}{4}(\mathbf{a}_f + \mathbf{b}_f + \mathbf{c}_f)$. This introduces a primitive hexagonal double-layer into the stacking sequence of fluorite-type metal atom layers. This introduction of a primitive hexagonal double-layer is induced by corner-connection of TaO_6 octahedra perpendicular to the hexagonal close-packed metal atom layer (see Figure 51 and Figure 53*(b)*). Connection of TaO_6 octahedra in such a manner is incompatible with the maintenance of an fcc metal atom array. The fcc stacking sequence – *ABC*– of hexagonal layers is thereby expanded to –*ABCABBCABCCABCA*–. (Note that since the layers are shifted along **a**, the primitive double-layer is distorted slightly by the (pseudo)-monoclinic angle $\beta \sim 109$ °.)

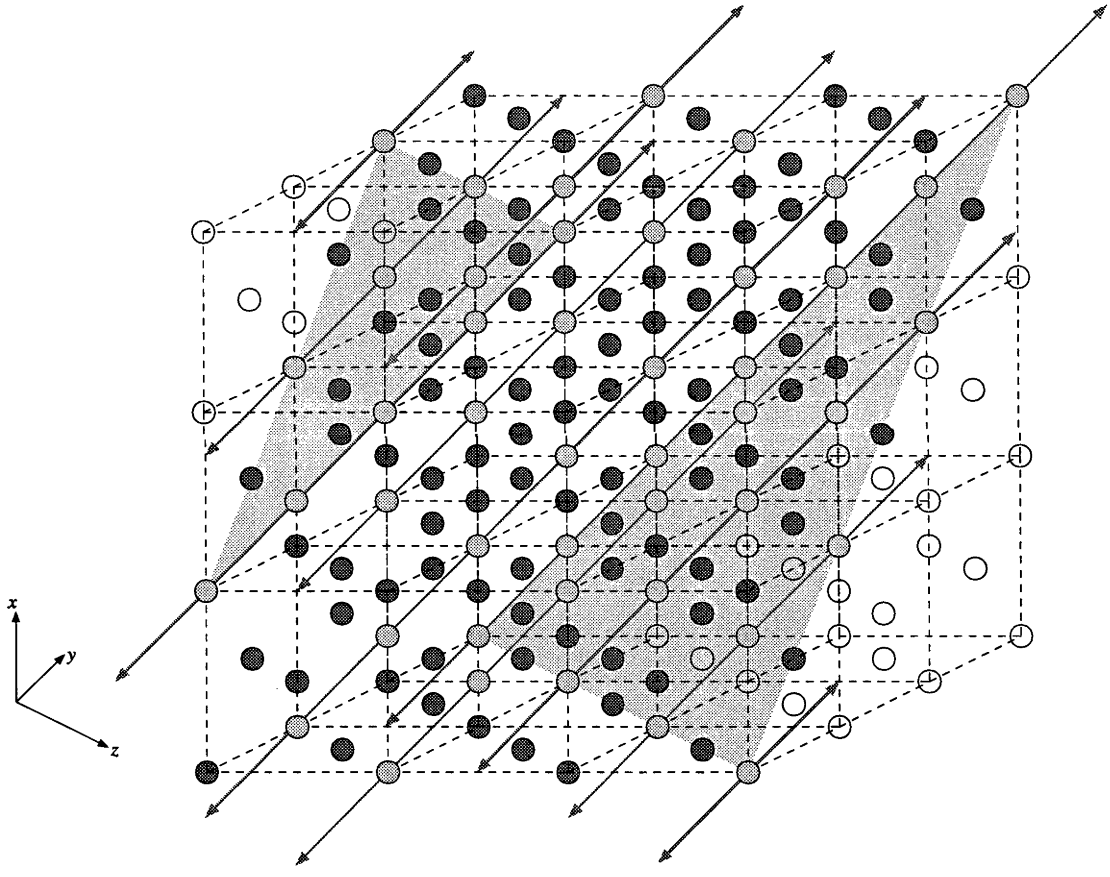

Figure 54. The metal atom array of a fluorite-type slab in type II $Bi_7Ta_3O_{18}$ mapped onto 3 x 3 x 3 average fluorite-type subcells. Dashed lines indicate the fluorite-type subcell grid. Shaded planes indicate the boundaries of the fluorite-type block, and empty circles indicate fluorite-type metal atom positions outside the block. Bismuth atoms are darker than Ta atoms. Grey lines highlight nearest-neighbour Ta connections along <1 1 0>$_f$ directions.*

Figure 54 shows the metal atom array within one of the fluorite-type slabs, mapped onto a 3 x 3 x 3 fluorite-type grid. The presence of continuous <1 1 0>$_f$ strings of Ta atoms, a structural motif from pyrochlore-type (Figure 3*(d)*) which has featured prominently in many of other structures investigated in this study (see Figure 30, Figure 36 and Figure 47), is immediately obvious. In this structure, strings are only found along one of the six <1 1 0>$_f$

directions, and do not interact with each other within the fluorite-type slabs. In the real structure (Figure 51), the $<1\ 1\ 0>_f$ strings corner-connect across the primitive hexagonal step, but isolated strings do exist within the slabs. This robustness of the $<1\ 1\ 0>_f$ string structural motif across such different structures is a strong indication of its value in describing the structures of phases investigated in this study.

4.9 Type III Bi_2O_3-Ta_2O_5: $Bi_4Ta_2O_{11}$ (63)

Strong similarities between the unit cells and DPs of type II* $Bi_7Ta_3O_{18}$ and type III $Bi_4Ta_2O_{11}$ (Section 3.4.1.2) indicated structural similarities between the two phases. In this Section, a model was developed for the structure of $Bi_4Ta_2O_{11}$ based on the structure of $Bi_7Ta_3O_{18}$, and Rietveld-refined using synchrotron XRD and neutron powder diffraction data.

4.9.1 Experimental

A powder sample of $Bi_4Ta_2O_{11}$ was prepared by solid-state reaction of a mixture of Bi_2O_3 (Koch-Light 99.998 %) and Ta_2O_5 (Aldrich 99.99 %) at mole ratio 2:1 in a platinum crucible at 1103 K for 0.5 hours. The sample was quenched to room temperature, reground, annealed in a sealed platinum vessel at 1173 K for 192 hours and again quenched to room temperature. A homogeneous, pale yellow powder was obtained and identified as single-phase $Bi_4Ta_2O_{11}$ by XRD (Guinier-Hägg camera) (8).

Synchrotron XRD data were collected at the Photon Factory. Powder neutron diffraction data were collected on POLARIS (6). The high flux of POLARIS was sought due to difficulties encountered in obtaining a large, homogenous sample via the method described above.

4.9.2 Modelling

The first consideration in proposing a model for the structure of type III $Bi_4Ta_2O_{11}$ was the relationship of its unit cell to that of type II* $Bi_7Ta_3O_{18}$ (Section 4.8). To this end, the unit cells of both phases were reduced to their primitive settings. The pseudo-monoclinic *C*-centered cell of $Bi_7Ta_3O_{18}$ is related to its primitive setting by $\mathbf{a} = \mathbf{c}_C$, $\mathbf{b} = \mathbf{b}_C$, $\mathbf{c} = -\frac{1}{2}\mathbf{a}_C - \frac{1}{2}\mathbf{b}_C - \mathbf{c}_C$. The pseudo-monoclinic *B*-centered cell of $Bi_4Ta_2O_{11}$ (Section 3.4.1.2) is related to its primitive setting by $\mathbf{a} = \mathbf{b}_B$, $\mathbf{b} = \mathbf{a}_B$, $\mathbf{c} = -\frac{1}{2}\mathbf{b}_B - \frac{1}{2}\mathbf{c}_B$. The XRD-refined parameters of these reduced cells (converted from the values in Table 2) are compared in Table 17.

The most significant difference between the two cells was clearly the length of the long *c*-axis. $Bi_7Ta_3O_{18}$ is essentially composed of five layers of metal atoms layered perpendicular to **c** (see Figure 51 and Figure 53*(b)* of Section 4.8). Given that $c(Bi_4Ta_2O_{11}) \approx \frac{3}{5}c(Bi_7Ta_3O_{18})$, it seemed very likely that $Bi_4Ta_2O_{11}$ was composed of three layers in the same manner.

	$Bi_7Ta_3O_{18}$	$Bi_4Ta_2O_{11}$
a (Å)	6.6358(7)	6.6112(7)
b (Å)	7.6024(8)	7.6607(8)
c (Å)	16.5364(17)	9.8899(10)
α (°)	103.208(10)	101.280(10)
β (°)	93.672(9)	90.201(9)
γ (°)	90.086(9)	90.020(9)

Table 17. Comparison of the unit cells of type II $Bi_7Ta_3O_{18}$ and type III $Bi_4Ta_2O_{11}$.*

The second consideration in proposing a model was the compositions of the respective phases. The average populations of the five metal atom layers in $Bi_7Ta_3O_{18}$ follow the sequence $Bi_{½}Ta_{½}$ - Bi - $Bi_{½}Ta_{½}$ - Bi - $Bi_{½}Ta_{½}$ (Figure 51). The only way to change the overall composition to $Bi_4Ta_2O_{11}$ while maintaining the same inter-layer connectivity was to collapse this sequence to $Bi_{½}Ta_{½}$ - Bi - $Bi_{½}Ta_{½}$.

The final aspect of the model to be considered was the possible presence of symmetry elements not previously determinable by systematically absent diffraction peaks. It was found that the presence of any mirror plane or rotation axis was incompatible with maintenance of the inter-layer connectivity found in $Bi_7Ta_3O_{18}$. The presence of an inversion centre did not, however, disrupt this connectivity, and was therefore incorporated into the initial model ($P\bar{1}$) in order to reduce the number of refined variables. Note that there is no inversion centre in the refined structure of $Bi_7Ta_3O_{18}$ ($P1$). For further consideration of the symmetry of these phases see Section 4.9.4.

Fractional atomic coordinates for $Bi_4Ta_2O_{11}$ were obtained from those of the final refined structure of $Bi_7Ta_3O_{18}$ (Section 4.8) by selecting atoms from the first two layers and introducing an inversion centre. Atoms in the middle layer had their coordinates averaged about the inversion centre. Fractional z coordinates were multiplied by $\frac{5}{3}$ to account for the shorter cell of $Bi_4Ta_2O_{11}$.

4.9.3 Refinement

The relatively small contribution of oxygen atoms to the X-ray scattering of $Bi_4Ta_2O_{11}$ allowed unconstrained refinement of metal atom parameters (positional and isotropic displacement) from the initial model while fixing the oxygen atoms at their starting positions. Rietveld refinements were carried out using GSAS (34). The success of this initial refinement ($R_p = 0.0360$, $wR_p = 0.0549$, $\chi^2 = 2.703$) indicated that the metal atom array was essentially correct.

Oxygen atom parameters (positional and overall isotropic displacement) in this model were then refined using neutron powder diffraction data, converging rapidly ($R_p = 0.0543$,

$wR_p = 0.0473$, $\chi^2 = 23.99$) and indicating that the oxygen atom array was also essentially correct.

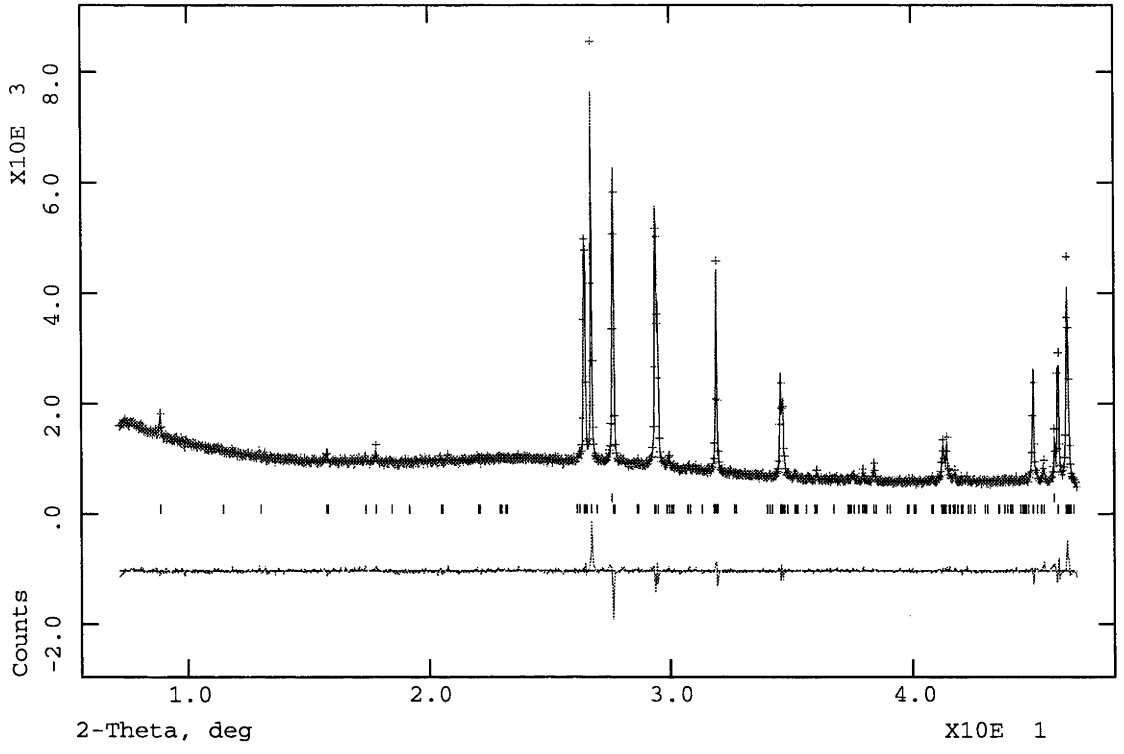

(a)

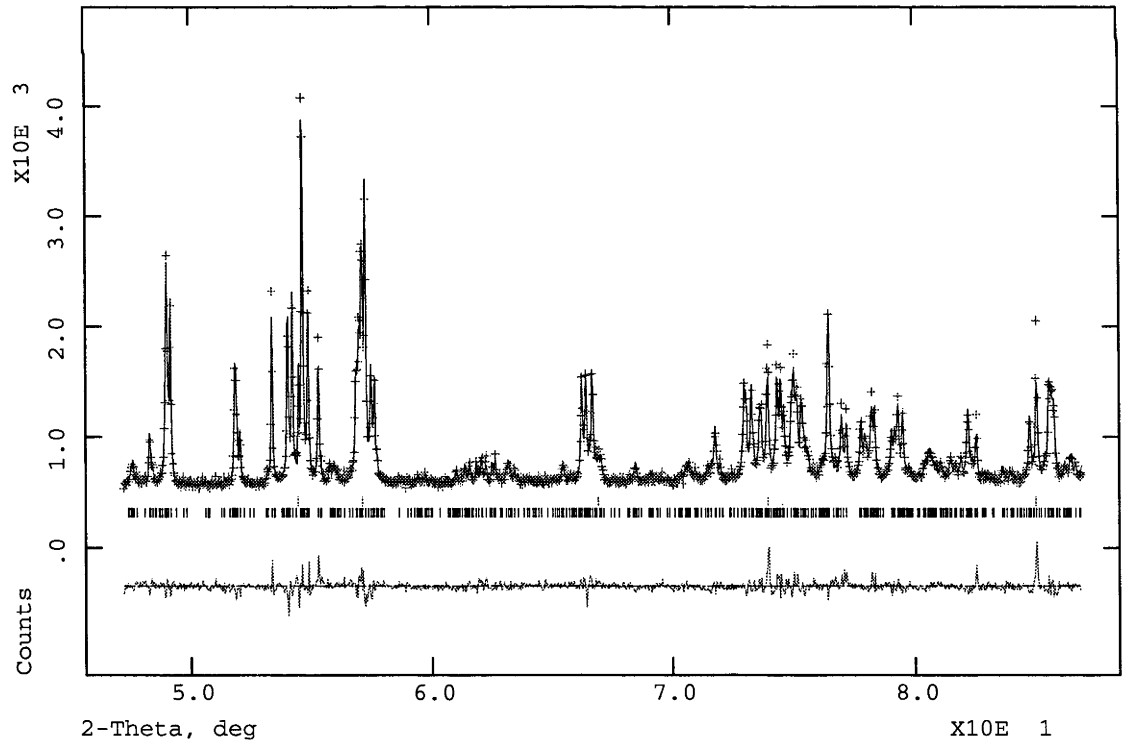

(b)

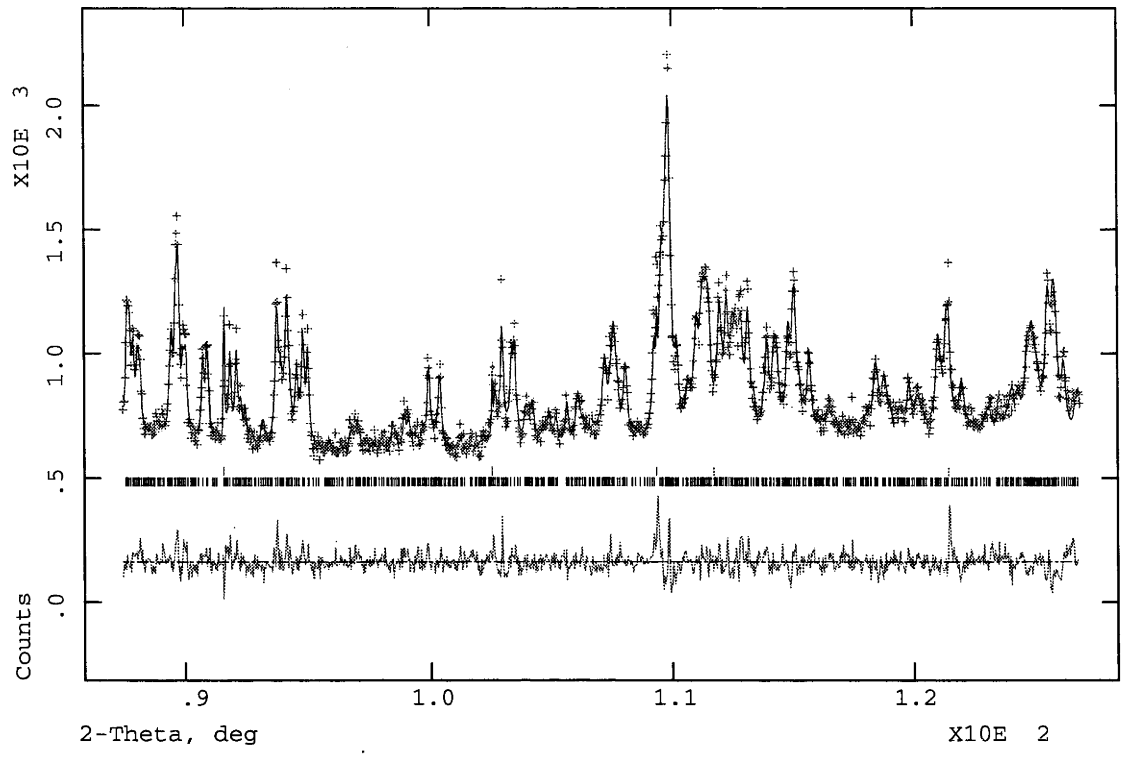

(c)

Figure 55. Observed (+), calculated and difference (bottom) XRD profiles for type III $Bi_4Ta_2O_{11}$. The top row of reflection markers refers to the Si standard.

Repeating the X-ray refinement of metal parameters using these refined oxygen parameters improved the result ($R_p = 0.0328$, $wR_p = 0.0439$, $\chi^2 = 1.691$). The observed, calculated and difference XRD profiles at this stage are shown in Figure 55. Note that the most significant features in the difference profiles correspond to diffraction peaks of the silicon standard, which were too weak (and too sharp) for adequate profile and phase fraction refinement. Refinement statistics for individual histograms are presented in Table 18.

		R_p	wR_p	$R(F^2)$	χ^2
X-rays	$5 - 45\ ^\circ 2\theta$	0.0296	0.0407	0.0841	
	$45 - 85\ ^\circ 2\theta$	0.0358	0.0474	0.0681	
	$85 - 125\ ^\circ 2\theta$	0.0339	0.0440	0.0539	
	Overall	0.0328	0.0439		1.691
Neutrons	$35\ ^\circ 2\theta$	0.0414	0.0406	0.0267	
	$90\ ^\circ 2\theta$	0.0448	0.0379	0.0288	
	$145\ ^\circ 2\theta$	0.0604	0.0391	0.0210	
	Overall	0.0487	0.0388		16.16

Table 18. Rietveld refinement statistics for type III $Bi_4Ta_2O_{11}$.

Subsequently, unconstrained refinement of all positional parameters, as well as overall isotropic displacement parameters for metal and oxygen atoms, using powder neutron diffraction data gave $R_p = 0.0487$, $wR_p = 0.0388$ and $\chi^2 = 16.16$. Refinement of independent

isotropic displacement parameters for all atoms reduced this to $R_p = 0.0486$, $wR_p = 0.0381$ and $\chi^2 = 11.48$, however, this final improvement in statistics was not considered significant given the number of new variables introduced. In addition, the use of independent displacement parameters resulted in slightly negative values for Ta1, Ta2, O4 and O11. The final model described below refers to the previous refinement, using two isotropic displacement parameters, one for metal atoms and one for oxygen atoms.

Atom	x	y	z	$100U_{iso}$
Bi1	0.6057(4)	0.5414(6)	0.1665(3)	0.236(15)
Bi2	0.5713(4)	0.0448(5)	0.1808(3)	0.236(15)
Bi3	0.2499(4)	0.1328(5)	0.5225(3)	0.236(15)
Bi4	0.2386(4)	0.6388(5)	0.5139(3)	0.236(15)
Ta1	0.0902(5)	0.7955(7)	0.1911(4)	0.236(15)
Ta2	0.0850(6)	0.2929(7)	0.1875(4)	0.236(15)
O1	0.0234(5)	0.5476(11)	0.1858(4)	0.90(2)
O2	0.9973(10)	0.7795(5)	0.9999(7)	0.90(2)
O3	0.5933(7)	0.6166(7)	0.3789(5)	0.90(2)
O4	0.1597(6)	0.0533(10)	0.2132(4)	0.90(2)
O5	0.5416(6)	0.0976(9)	0.3949(4)	0.90(2)
O6	0.0911(7)	0.3713(8)	0.4013(5)	0.90(2)
O7	0.7836(8)	0.8546(7)	0.2409(6)	0.90(2)
O8	0.1100(7)	0.8264(7)	0.3957(5)	0.90(2)
O9	0.3751(8)	0.7468(8)	0.1576(5)	0.90(2)
O10	0.3752(9)	0.3468(7)	0.1692(6)	0.90(2)
O11	0.7843(8)	0.2682(6)	0.2326(5)	0.90(2)

Table 19. Final refined fractional coordinates and U_{iso} values for type III $Bi_4Ta_2O_{11}$.

The observed, calculated and difference powder neutron diffraction profiles for the final refined $P\bar{1}$ structure of type III $Bi_4Ta_2O_{11}$ are shown in Figure 56. Refinement statistics for individual histograms are presented in Table 18. Final refined values for the fractional coordinates and U_{iso} values are given in Table 19. The final refined unit cell parameters were $a = 6.60890(8)$, $b = 7.65686(10)$, $c = 9.88280(13)$ Å, $\alpha = 101.3445(19)$, $\beta = 90.1829(15)$, $\gamma = 90.029(3)$ °, $V = 490.329(11)$ Å^3.

Bond valence sums (52) for the initial model and the final refined structure of $Bi_4Ta_2O_{11}$ are presented in Table 20. Note that those atoms in the initial model for which the bond valence sums are furthest from expected values are those closest to the $z = \frac{1}{2}$ plane, where average coordinates about the inversion centre were used. In this context, the initial model is chemically reasonable. Nonetheless, the refined structure clearly represents a significant improvement and therefore strongly supports the validity of the refinement.

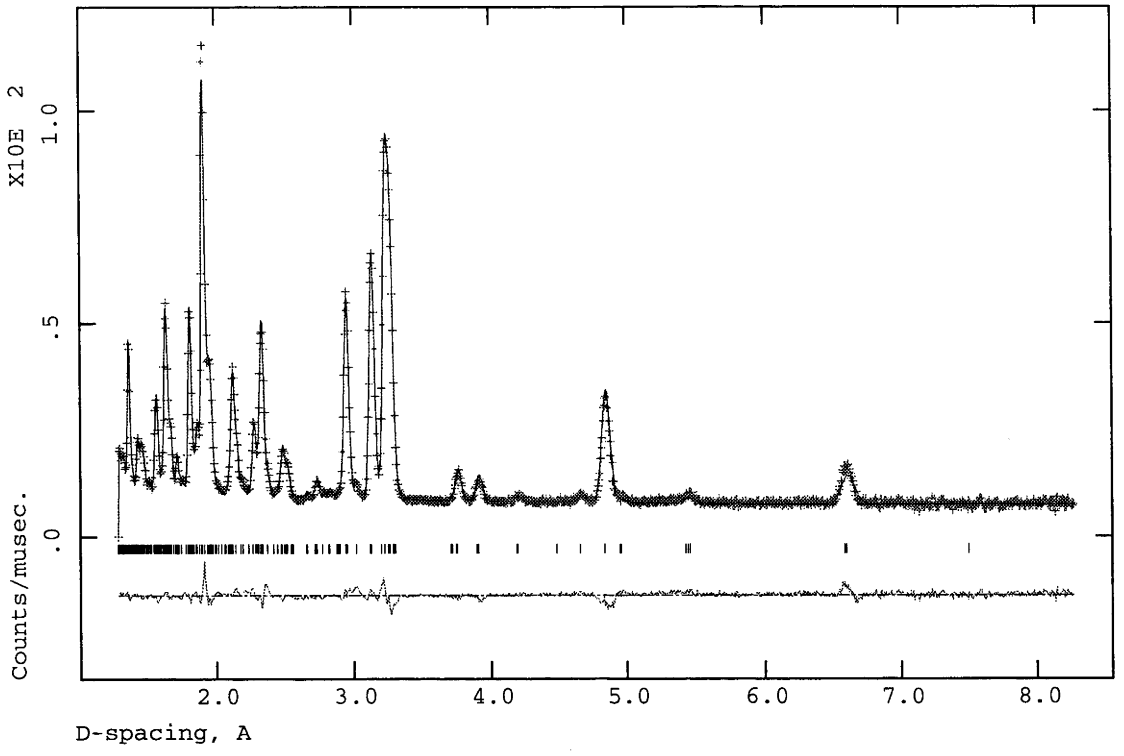
X10E 2
1.0
.5
.0
Counts/musec.
2.0
3.0
4.0
5.0
6.0
7.0
8.0
D-spacing, A

(a)

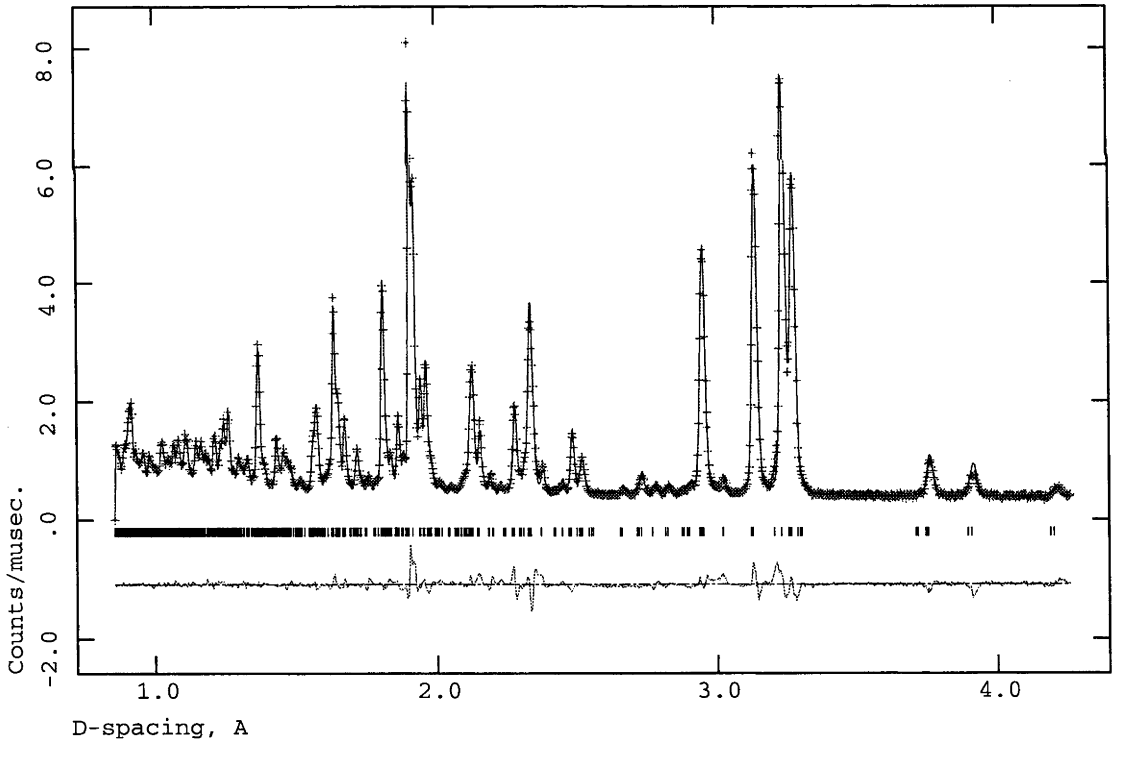
8.0
6.0
4.0
2.0
.0
-2.0
Counts/musec.
1.0
2.0
3.0
4.0
D-spacing, A

(b)

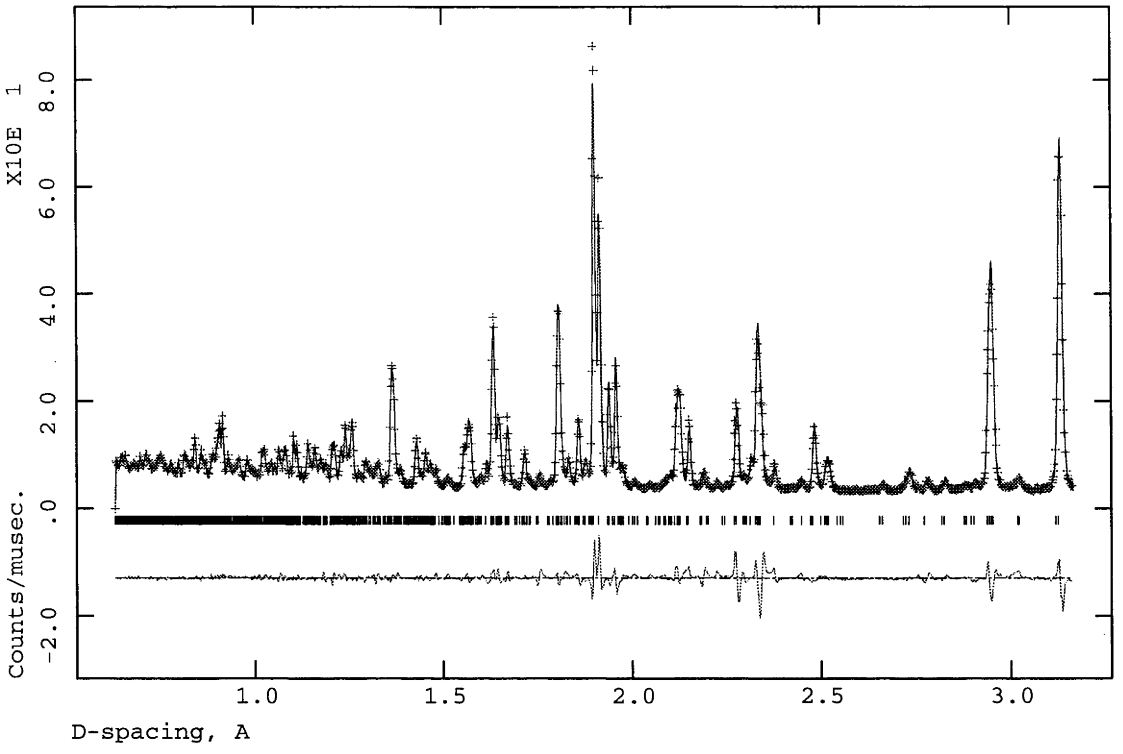

(c)

Figure 56. Observed (+), calculated and difference (bottom) neutron powder diffraction profiles for type III $Bi_4Ta_2O_{11}$ at the (a) 35 °, (b) 90 ° and (c) 145 ° detector banks of POLARIS.

Atom	Initial	Refined	Expected
Bi1	3.031	3.353	3.000
Bi2	3.115	3.198	3.000
Bi3	4.573	3.038	3.000
Bi4	2.303	2.897	3.000
Ta1	5.107	5.000	5.000
Ta2	5.002	4.932	5.000
O1	1.891	1.922	2.000
O2	1.647	1.922	2.000
O3	2.405	2.190	2.000
O4	2.021	1.946	2.000
O5	2.277	2.265	2.000
O6	2.396	1.922	2.000
O7	2.135	2.117	2.000
O8	2.798	2.157	2.000
O9	1.873	1.952	2.000
O10	1.857	1.956	2.000
O11	1.832	2.068	2.000

Table 20. Bond valence sums for the initial and final refined models of type III $Bi_4Ta_2O_{11}$.

4.9.4 Discussion

The final refined $P\bar{1}$ structure of $Bi_4Ta_2O_{11}$ is shown in Figure 57*(a)* and *(b)*, compared to the $P1$ structure of $Bi_7Ta_3O_{18}$ in Figure 57*(c)* and *(d)*. The relationship between the two phases, as members of a homologous series of layered structures, is obvious from Figure 57. For all types of atoms, the same connectivity and coordination environments are observed in both structures. The only significant difference is in the relationship between the distribution and orientation of TaO_6 octahedra in mixed metal atoms layers (perpendicular to **c**) separated by Bi-only layers. In $Bi_7Ta_3O_{18}$, this relationship (approximately) incorporates both a mirror plane and a 2-fold rotation axis (indicated in Figure 57*(c)* and *(d)*) lending the structure pseudo-*C2/m* symmetry (in an alternative setting). The breaking of both symmetry elements lowers the symmetry to $P1$ rather than $P\bar{1}$. In $Bi_4Ta_2O_{11}$, Figure 57*(a)* shows that these symmetry elements are forbidden; the 2-fold rotation axis by the Ta distribution within the metal atom layers, and the mirror plane by the rotation of TaO_6 octahedra. An inversion centre is allowed, and appears to hold. It should be noted, however, that the refinement of $Bi_7Ta_3O_{18}$ using powder neutron diffraction data (Section 4.8.2) could not effectively refine the symmetry lowering from *C2/m* to $P1$. The possibility therefore exists that using single crystal X-ray data, particularly with the benefit of anomalous scattering, a $P1$ model for the structure of type III $Bi_4Ta_2O_{11}$ might lead to a more satisfactory solution. At this stage it has not been possible to grow single crystals of $Bi_4Ta_2O_{11}$.

It was earlier demonstrated (Section 3.4.1.2) that neither $Bi_7Ta_3O_{18}$ nor $Bi_4Ta_2O_{11}$ possess unambiguous fluorite-type subcells such as those described by Zhou (21). Nonetheless, DPs of both phases did display some distinctly fluorite-like projections. These patterns were explained in the case of $Bi_7Ta_3O_{18}$ by describing the structure as consisting of layers of pseudo-fluorite-type which were stepped on the $z = 0$ planes of the primitive cell (perpendicular to a $<1\ 1\ 1>_f$ direction). On these planes, two adjacent metal layers form a primitive hexagonal (rather than fcc) array. The same phenomenon underlies the fluorite-like projections observed for $Bi_4Ta_2O_{11}$.

As in the case of $Bi_7Ta_3O_{18}$, the coordination environments of tantalum atoms in $Bi_4Ta_2O_{11}$ consist of regular octahedra forming columns along the [0 1 0] direction. Octahedral rotations in the order of ~ 10 ° about the [1 0 0] direction are observed. Also as for $Bi_7Ta_3O_{18}$, the coordination environments of bismuth atoms are difficult to define; they appear to be related to the cubic (8-fold) coordination found in fluorite-type δ-Bi_2O_3, distorted by the presence of TaO_6 octahedra such that Bi-O bond lengths vary between 2.0 and 3.0 Å. Setting the maximum Bi-O bond length at 2.7 Å differentiates the environments of Bi1 and Bi2 from those of Bi3 and Bi4. Bi1 and Bi2 are located on the basal planes of square pyramids, a coordination observed in $Bi_7Ta_3O_{18}$ and typical of cations with stereochemically active electron lone pairs such as Bi^{3+}, the archetype being α-PbO (62). Bi3 and Bi4 occupy

sites not observed in $Bi_7Ta_3O_{18}$, and shown in Figure 58. These 7-fold sites are clearly oxygen-deficient variations on the 8-fold cubic sites of fluorite-type δ-Bi_2O_3.

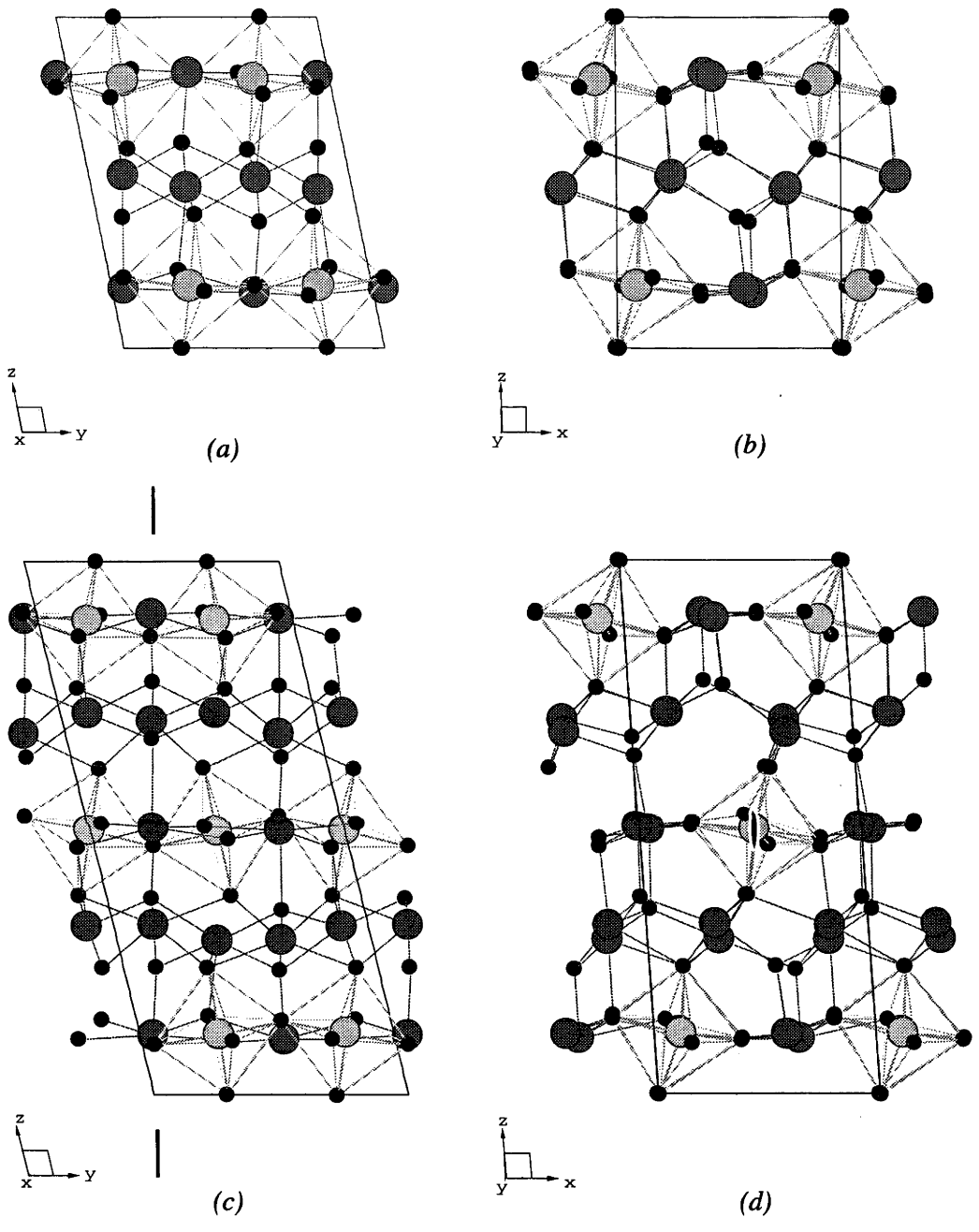

Figure 57. The final refined $P\bar{1}$ structure of type III $Bi_4Ta_2O_{11}$ viewed down the (a) [1 0 0] and (b) [0 1 0] directions. (c) and (d) Show corresponding views of the P1 structure of type II $Bi_7Ta_3O_{18}$, with pseudo-symmetry elements indicated. Bismuth atoms are darker than TaO_6 atoms, and oxygen atoms are black.*

Figure 59 shows the metal atom array within one of the fluorite-type slabs of type III $Bi_4Ta_2O_{11}$, mapped onto a 3 x 3 x 3 fluorite-type grid, corresponding to the representation of type II* $Bi_7Ta_3O_{18}$ shown in Figure 54. The same continuous $<1\ 1\ 0>_f$ strings of Ta atoms, aligned along only one of the six $<1\ 1\ 0>_f$ directions, are in evidence. The fcc stacking sequence *–ABC–* of hexagonal layers is expanded by the interface modulation in much the same manner as that of type II* $Bi_7Ta_3O_{18}$; in this case, to *–ABCCABBCA–*. In terms of this

pyrochlore-type structural motif, an important distinction between the two structures is the absence of any truly isolated strings in type III $Bi_4Ta_2O_{11}$; all are paired across primitive hexagonal steps. Consequently, any connection between type III and a fluorite-type parent structure *via* a pyrochlore-type string motif, as discussed for type II* $Bi_7Ta_3O_{18}$ and many other phases investigated in this study, is highly tenuous. Nonetheless, the obvious relationship between Bi_2O_3-Ta_2O_5 types II* and III suggests that such a connection may have some (limited) meaning even for type III $Bi_4Ta_2O_{11}$.

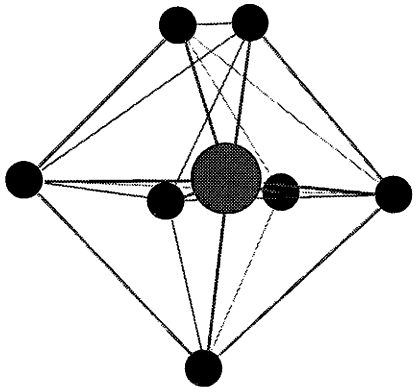

Figure 58. The coordination environment of Bi4. Oxygen atoms are black.

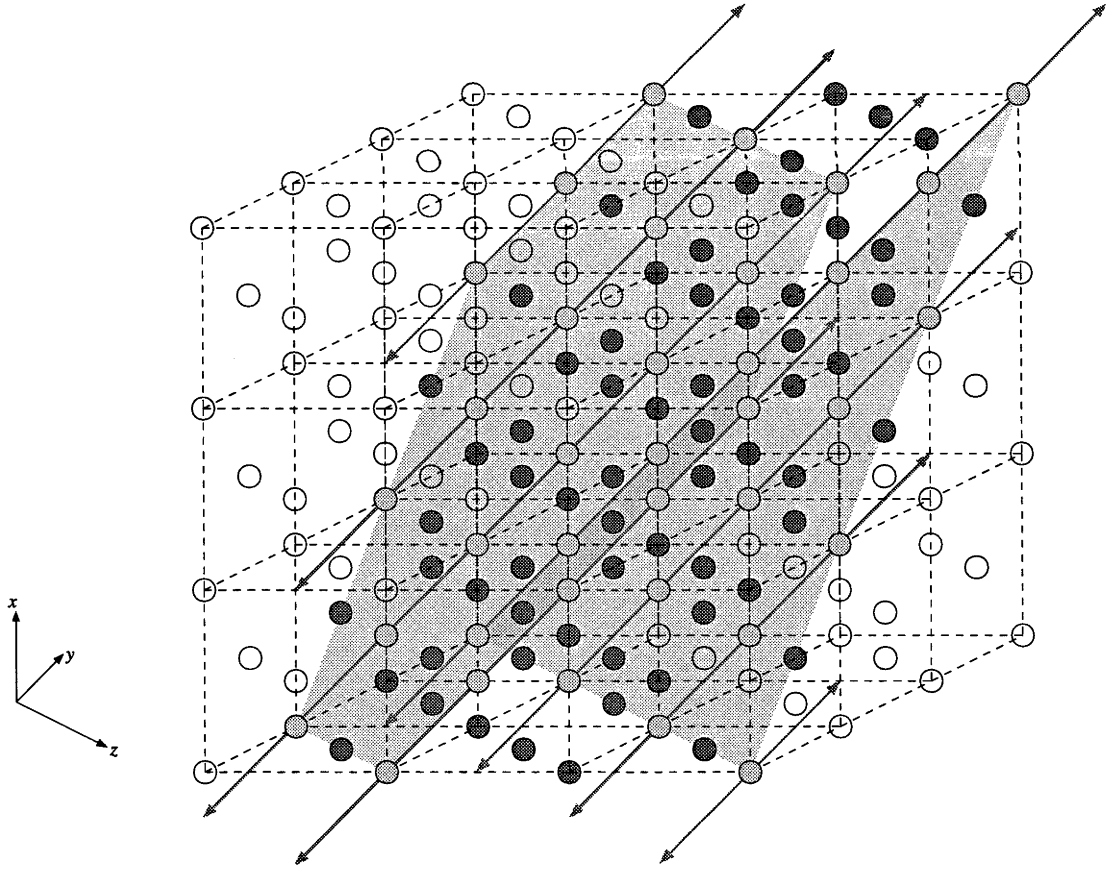

Figure 59. The metal atom array of a fluorite-type slab in type III $Bi_4Ta_2O_{11}$ mapped onto 3 x 3 x 3 average fluorite-type subcells. Dashed lines indicate the fluorite-type subcell grid. Shaded planes indicate the boundaries of the fluorite-type block, and empty circles indicate fluorite-type metal atom positions outside the block. Bismuth atoms are darker than Ta atoms. Grey lines highlight nearest-neighbour Ta connections along <1 1 0>$_f$ directions.

4.10 Type IV Bi_2O_3-Nb_2O_5 and Bi_2O_3-Ta_2O_5

As discussed in Section 3.3.1, the prototype parent structure of type IV $Bi_5Nb_3O_{17}$ is more akin to perovskite-type than to fluorite-type δ-Bi_2O_3. Although a modulated structure description was used in this study, and a greater degree of incommensurability observed, the ED results in Section 3.4.1.1 were essentially in agreement with those of Zhou *et al.* (19).

Gopalakrishnan *et al.* (20) proposed a model for the structure of type IV $Bi_5Nb_3O_{17}$ based on an intergrowth between $n = 1$ and $n = 2$ members of the perovskite-related Aurivillius family of phases (64). In this model, the primary modulation wave-vector **q** (described in Section 3.4.1.1) is ignored and only the parent structure modelled. Gopalakrishnan *et al.* reported the long axis $c \sim 21$ Å, *i.e.* half the length observed by Zhou *et al.* and in this study. Such an idealised $n = 1 + 2$ Aurivillius-type intergrowth model was easily constructed, as shown in Figure 60. This model was constructed in the space group *Cmmm*, in accordance with the *Fmmm* symmetry of Aurivillius-type parent structures.

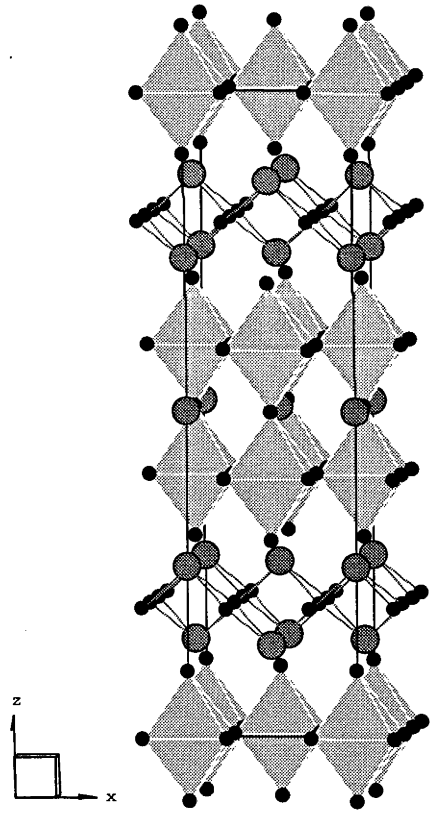

Figure 60. Gopalakrishnan et al.'s (20) idealised n = 1 + 2 Aurivillius-type intergrowth model of type IV $Bi_5Nb_3O_{15}$. Bismuth atoms are darker than niobium octahedra, and oxygen atoms are black.

Zhou *et al.* proposed a more sophisticated model based on the $n = 1 + 2$ Aurivillius-type intergrowth concept. This model doubled the length of the long axis *c*, and also incorporated step-like dislocations observed in HRTEM as responsible for the **a*** component of **q** and approximated by Zhou *et al.* to a 6-times supercell along **a**. It was possible to construct this model in the space group $B1m1$ from blocks of the *Cmmm* model (Figure 61).

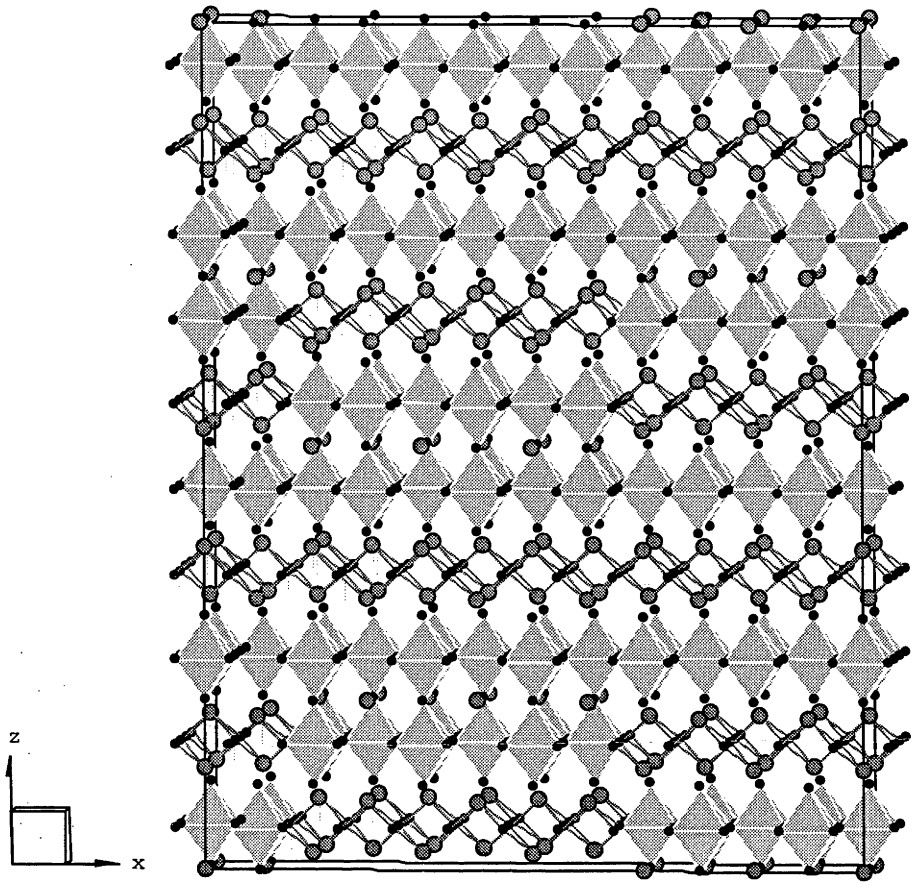

Figure 61. Zhou et al.'s (19) idealised n = 1 + 2 Aurivillius-type intergrowth model of type IV $Bi_5Nb_3O_{15}$. Bismuth atoms are darker than niobium octahedra, and oxygen atoms are black.

Patterns calculated for both these models were tested against observed XRD (Figure 62) and neutron powder diffraction (Figure 63) data. In each case, both models offer reasonable matches to observed data at low angle / high *d*-spacing. This indicates that the smaller structural building blocks, *i.e.* $n = 1$ and $n = 2$ Aurivillius-type units, are probably correct. At higher angle / lower *d*-spacing, the more sophisticated model of Zhou *et al.* clearly provides a far better fit to observed data, particularly to the observed decay in reflection intensity. The step in the model of Zhou *et al.* is responsible for this decay, and its presence is therefore strongly supported; *cf.* the way in which an interface modulation of fluorite-type affects the diffraction patterns of type III $Bi_4Ta_2O_{11}$ (Section 3.4.1.2 and Figure 17).

The failure of either model to provide a precise fit to observed data, particularly at high angle / low *d*-spacing, is unsurprising given their high symmetry. Real Aurivillius-type phases are known to distort from idealised *Fmmm* parent structures *via* a series of rotational and displacive modes (65). The rotation of NbO_6 octahedra ought particularly to effect the neutron data, which is far more sensitive to oxygen atom displacements. Furthermore, even the large unit cell of Zhou's model is only an approximation to the incommensurate cell described in this study (Section 3.4.1.1).

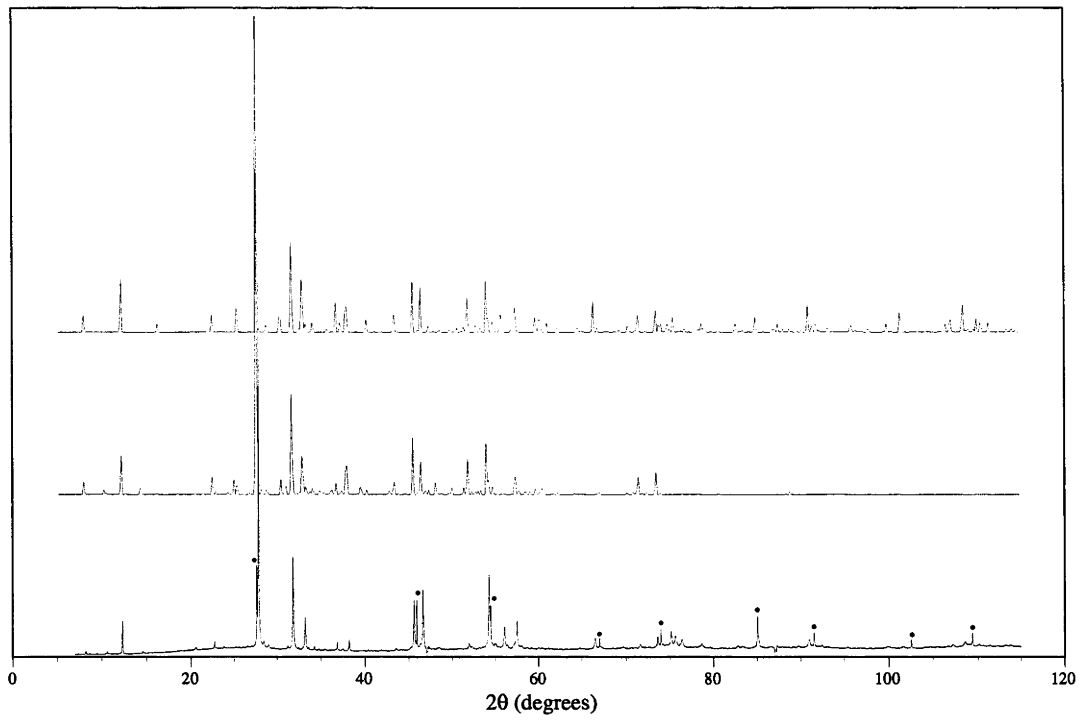

Figure 62. Comparison of XRD patterns calculated from models of type IV $Bi_5Nb_3O_{15}$ proposed by Gopalakrishnan et al. (top) and Zhou et al. (middle) against observed synchrotron XRD data (bottom). Silicon standard reflections are marked (•).

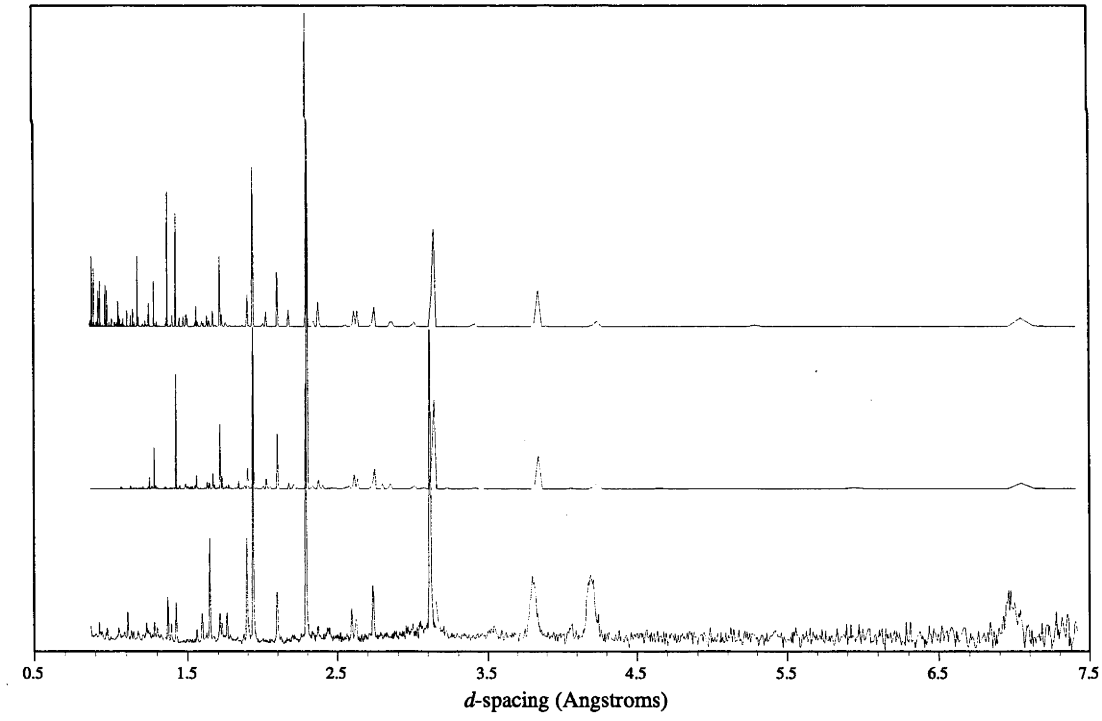

Figure 63. Comparison of neutron powder diffraction patterns calculated from models of type IV $Bi_5Nb_3O_{15}$ proposed by Gopalakrishnan et al. (top) and Zhou et al. (middle) against observed POLARIS data (bottom).

Although this model appeared to have much in common with the true structure, Rietveld-refinements were unfortunately not feasible due to the large number of variables (216 independent atoms in *B*1), the relatively poor quality data and the truly incommensurate

nature of the unit cell. Given the high possibility of stacking faults in such a complex structure, and Zhou's observation (19) of a type IV* variant on the same theme, it seems likely that the complexity of the true structure is such that a solution from powder diffraction data would be extremely difficult. At the same time, growth of single crystals of this phase remains elusive. HRTEM, used in the studies that proposed these models, is clearly a more appropriate technique, and the results presented here seem to vindicate their conclusion that the type IV phase does not have a fluorite-type δ-Bi_2O_3-related parent structure in any meaningful sense.

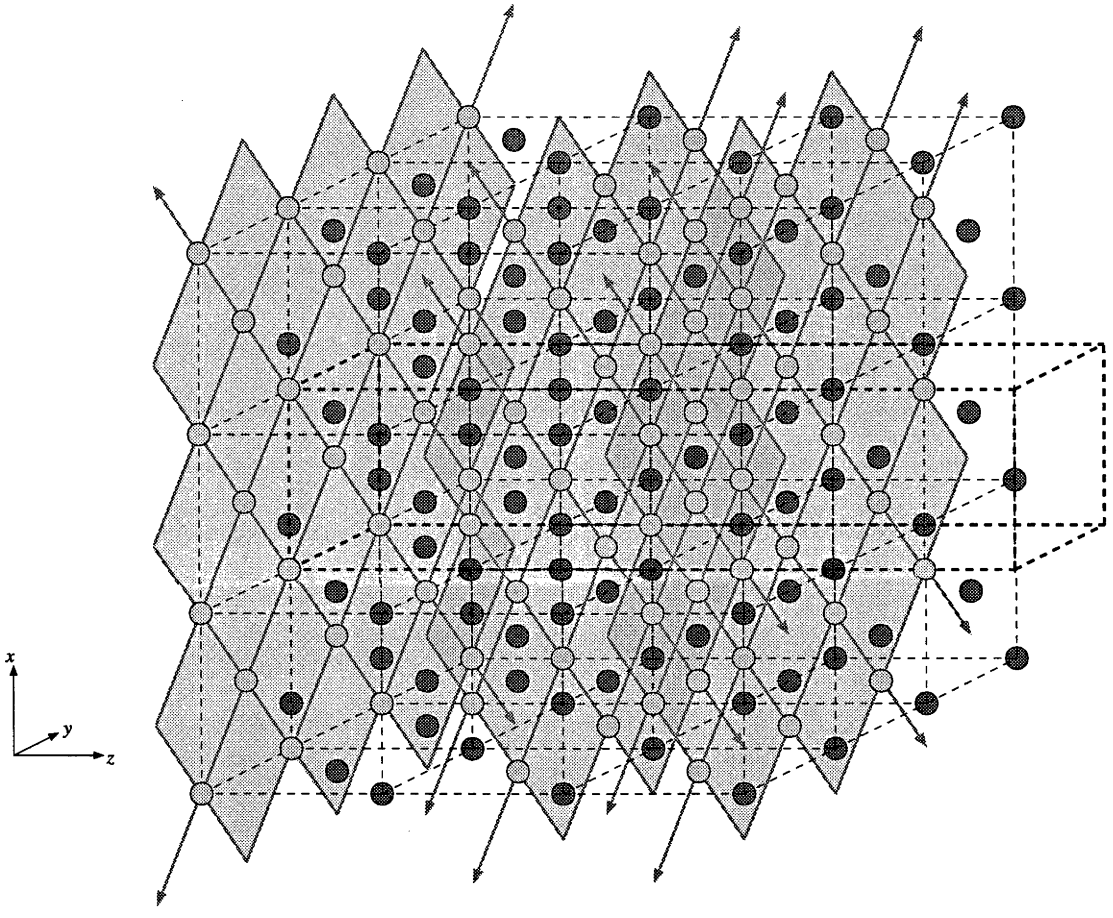

Figure 64. The metal atom array in the model of Gopalakrishnan et al. for type IV $Bi_5Nb_3O_{17}$ mapped onto 3 x 3 x 3 average fluorite-type subcells. Dashed lines indicate the fluorite-type subcell grid, and heavy dashed lines indicate the supercell. Bismuth atoms are darker than Nb atoms. Grey lines and shaded planes highlight nearest-neighbour Nb connections along $<1\ 1\ 0>_f$ directions.

Neither synchrotron XRD nor neutron powder diffraction data were obtained for the corresponding type IV phase in the Bi_2O_3-Ta_2O_5 system, $Bi_{31}Ta_{17}O_{89}$. Zhou *et al.* (19) modelled this phase in essentially the same way as for $Bi_5Nb_3O_{17}$, based on an intergrowth between $n = 1$ and $n = 2$ Aurivillius phases, but with the step oriented in a different direction; this is in agreement with the different orientation of the primary modulation wave-vector **q** described in Section 3.4.1.2. The underlying similarity between these two phases is seen most clearly in Table 2. In light of these similarities, the type IV model of Zhou *et al.* for $Bi_{31}Ta_{17}O_{89}$ seems equally plausible as that proposed for $Bi_5Nb_3O_{17}$.

The metal atom array of Gopalakrishnan *et al.*'s model for type IV $Bi_5Nb_3O_{17}$ is shown in Figure 64, mapped onto a 3 x 3 x 3 fluorite-type grid. Comparing the nearest-neighbour Nb connectivity along $<1\ 1\ 0>_f$ directions to Figure 60, it can be seen that the connectivities are different; Nb atoms in Figure 60 interact between layers in the same way as within layers, whereas in Figure 64, Nb atoms in separate layers are not nearest neighbours. This change in connectivity throughout the whole structure clearly indicates that Bi_2O_3-$(Nb/Ta)_2O_5$ type IV phases cannot be meaningfully be described in terms of a fluorite-type parent structure.

4.11 Bi_2O_3-MoO_3: $Bi_{26}Mo_{10}O_{69}$

The structure of $Bi_{26}Mo_{10}O_{69}$, as solved and refined in a single crystal X-ray study by Vannier *et al.* (28), was discussed in Section 3.3.4. Since publication of the work in Chapter 3 (8), this structure has been confirmed by Enjalbert *et al.* (66), however, these authors criticised the chemistry of Vannier *et al.* Enjalbert *et al.* disputed the existence of a phase with the reported structure type (isostructural with $Bi_{26}Mo_6V_4O_{67}$, also reported by Vannier *et al.* (28)) in the Bi_2O_3-MoO_3 system, suggesting that a small amount of alumina from the reaction vessel may have been responsible for stabilising the structure by substituting for MoO_3. Vannier *et al.* subsequently reiterated their own conclusions (67), following a refinement of the structure of $Bi_{26}Mo_{10}O_{69}$ from neutron powder diffraction data (68), and noting the synthesis in the present study (8) of $Bi_{26}Mo_{10}O_{69}$ using sealed platinum tubing to remove the possibility of doping by impurities such as alumina. It should be noted in this context that in addition to indexing synchrotron XRD data to the cell of Vannier *et al.* as reported in Chapter 3 (8) (Figure 18), the structure of Vannier *et al.* was successfully fitted to these synchrotron XRD data using the Rietveld method, further supporting their claim that the reported structure type does indeed exist in the pure Bi_2O_3-MoO_3 system.

The somewhat controversial chemistry of the phase has corresponded to slightly different interpretations of the details of the structure, in particular the location of the final oxygen atom. (Vannier *et al.*'s original structure was for $Bi_{26}Mo_{10}O_{68}$; the apparent excess of oxygen was the source of Enjalbert *et al.*'s original criticisms.) Nonetheless, all reports are in agreement about the fundamental features of the structure, whereby $[Bi_{12}O_{14}]_\infty$ columns are surrounded by 10 MoO_4 tetrahedra organised in layers perpendicular to [0 1 0], the layers being separated by an additional Bi atom between two tetrahedra. As stated in Section 3.4.1.4, there appears to be little to gain from an interpretation of this structure type in terms of fluorite-type, despite the determination in the present study (Section 3.4.1.4) (8) of a relationship to a fluorite-type subcell. Interestingly, however, in their second paper on the subject, Vannier *et al.* (67) used this relationship, in conjunction with the structural approach of Buttrey *et al.* (68), to propose the location of the final contentious oxygen atom. They felt

that despite the massive distortion from fluorite-type of the oxygen atom array, it was possible to identify a fluorite-type oxygen atom site that was distinctly unoccupied. By introducing an oxygen atom on this site at 10 % occupancy, the chemically correct composition $Bi_{26}Mo_{10}O_{69}$ was achieved. Although it was necessary to constrain contact distances in the neighbourhood of this oxygen atom in order to obtain sensible bond valence sums, a stable Rietveld-refinement using neutron powder diffraction data was achieved. The refinement statistics were not significantly different to those for the oxygen-deficient $Bi_{26}Mo_{10}O_{68}$ model. Despite using a fluorite-type parent structure as the basis for this aspect of their model, Vannier *et al.* nonetheless agree with the conclusions of the present study (8) that $Bi_{26}Mo_{10}O_{69}$ cannot usefully be described as a fluorite-type δ-Bi_2O_3-related phase.

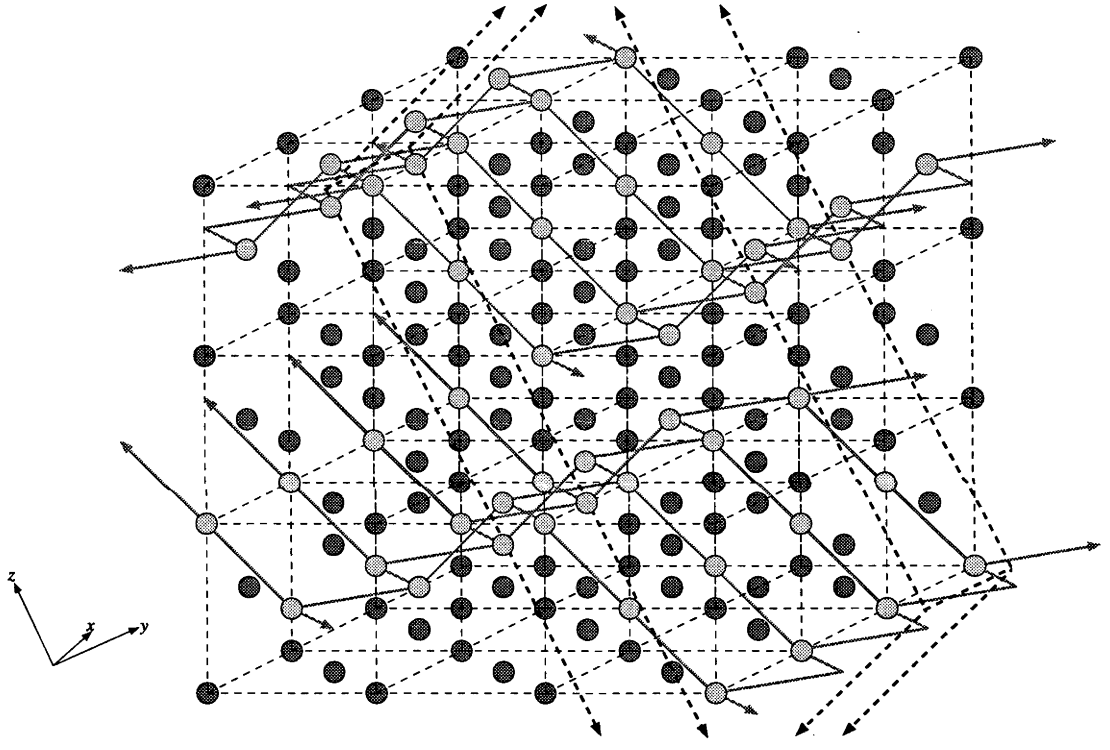

Figure 65. The metal atom array of $Bi_{26}Mo_{10}O_{69}$ mapped onto 3 x 3 x 3 average fluorite-type subcells. Dashed lines indicate the fluorite-type subcell grid, and heavy dashed lines indicate the supercell. Bismuth atoms are darker than Mo atoms. Grey lines highlight nearest-neighbour Nb connections along <1 1 0>$_f$ directions.

The principal reason for placing this structure type in a different category to others discussed in the present study, despite the fcc metal atom array, is the distribution and coordination environments of Mo atoms. Although isolated tetrahedral coordination environments were observed for Mo and W atoms in type Ia $Bi_{14}(W/Mo)O_{24}$ (Section 4.1), in that case the density of non-Bi atoms was too low to allow for extended connectivity between their coordination polyhedra. This is no longer so in the case of $BI_{26}Mo_{10}O_{69}$. In other structures considered in this study, higher densities of non-Bi atoms has led to increasingly extensive connectivity between octahedral coordination environments, oriented along <1 1 0>$_f$ directions.

Figure 65 shows the metal atom distribution in $Bi_{26}Mo_{10}O_{69}$ mapped onto a 3 x 3 x 3 fluorite-type subcell grid. Examining Mo-Mo nearest-neighbour connectivity, it can be seen that it is possible to interpret the Mo distribution in terms of $<1\ 1\ 0>_f$ strings. In this structure, however, no continuous string extends further than one fluorite-type subcell, making comparisons with the continuous strings of pyrochlore-type (Figure 2) highly tenuous. At the same time, the Mo_x clusters connecting these short strings bear no relationship to any clusters found in pyrochlore-type, rendering the alternative pyrochlore-type cluster motif equally irrelevant to this structure. Any interpretation of the Mo distribution in $Bi_{26}Mo_{10}O_{69}$ in terms of pyrochlore-type structural motifs is therefore too contrived to be meaningful.

Chapter 5

Crystal Chemistry

The crystallographic work described in Chapter 4 forms a large pool of data from which it ought to be possible to draw some general principles. A crystal-chemical scheme could thereby be constructed, fulfilling the ultimate aim of this study discussed in Chapter 1. Such a scheme should incorporate the compositional, symmetrical and structural relationships between phases, and it should ideally be predictive, *i.e.* given the position of a new phase with respect to two of these variables it ought to be possible to locate it with respect to the third. This Chapter attempts to construct such a crystal-chemical scheme.

5.1 Framework

The success or otherwise of this aim depends critically on the accumulation of sufficient data. Partial results from Chapter 4 will therefore be considered in terms of the most probable structure for each phase. This will allow the tentative inclusion of the minority of relatively poorly resolved structures alongside well resolved structures, and can be justified on the basis that any possibly incorrect structural models will be diluted by the majority of reliable structures. Given their demonstrated relationship to the type IV phases (Section 4.10), the $n = 1$ Aurivillius phases Bi_2WO_6 and γ-Bi_2MoO_6 (11) have also been added to the data pool for consideration. Finally, phases whose space groups and unit cells approximate higher symmetry space groups and unit cells will be considered in terms of those high-symmetry approximates. This is in order to focus attention on the large-scale structural principles that certain phases have in common, rather than on the small-scale perturbations which differentiate them.

5.2 Classification of Phases

As discussed in Chapter 1, due to the disordered nature of the oxygen atom array in fluorite-type δ-Bi_2O_3, phases will be primarily classified into structural types on the basis of metal atom compositional ordering. Three general structural types emerged in Chapter 4; those containing isolated *M* atoms, strings of *M* atoms along $<1\ 1\ 0>_f$ directions, and planes of *M* atoms perpendicular to $<1\ 0\ 0>_f$ directions. The relationship between these motifs needs to be elucidated in any successful unifying crystal-chemical scheme.

Relationships between structure type and composition for the phases considered in Chapter 4 are illustrated in Figure 66. Individual phases are summarised in point form below, and graphically in Figure 67.

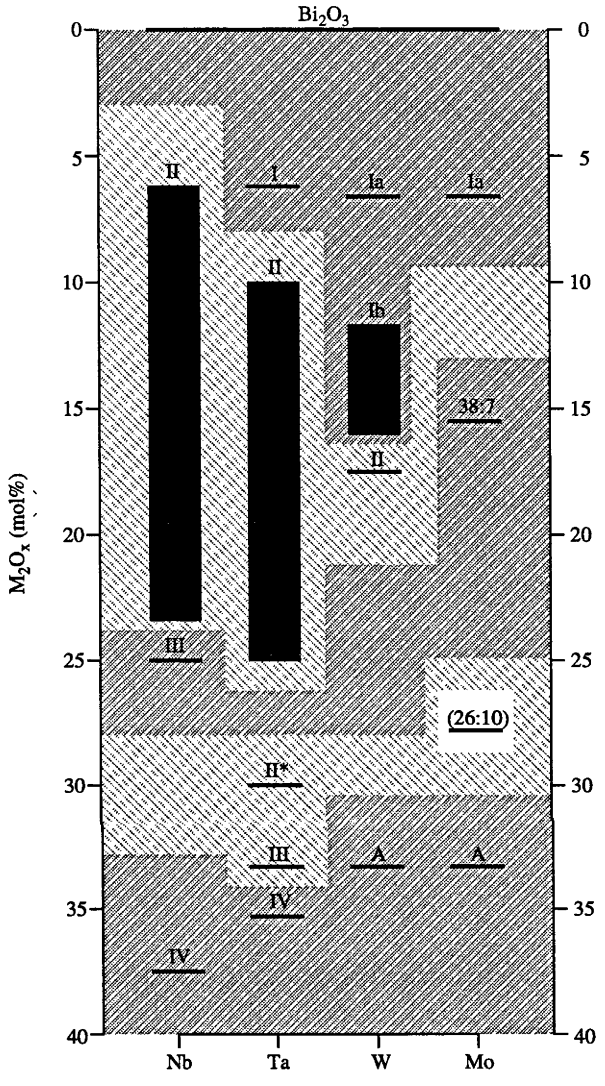

Figure 66. Phases investigated in this study, with respect to composition. Background shadings group phases with similar structural relationships to fluorite-type δ-Bi_2O_3.

- Bi_2O_3-Ta_2O_5 type I (Section 4.4) has isolated Ta atoms in a fluorite-type metal atom array. The composition (15Bi:Ta) allows a cubic distribution of Ta atoms which, combined with the octahedral coordination environment of Ta atoms, leads to a cubic unit cell.

- Bi_2O_3-WO_3 and Bi_2O_3-MoO_3 type Ia (Section 4.1) have isolated Mo/W atoms in a fluorite-type metal atom array. Mo/W atoms have (disordered) tetrahedral coordination environments, lowering the symmetry to tetragonal.

- Bi_2O_3-WO_3 type Ib (Section 4.5) has isolated W atoms in a fluorite-type metal atom array, with a partially disordered distribution allowing some compositional flexibility within the

solid-solution range. W atoms have octahedral coordination environments, but the composition does not allow a cubic distribution of W atoms and a tetragonal unit cell results.

- Bi_2O_3-Nb_2O_5 and Bi_2O_3-Ta_2O_5 type II (Section 4.2) have strings of Nb/Ta atoms in a fluorite-type metal atom array, arranged along three of the six possible $<1\ 1\ 0>_f$ directions, *e.g.* $[1\ 1\ 0]_f$, $[1\ 0\ 1]_f$ and $[0\ 1\ 1]_f$, *i.e.* no two of the string directions are coplanar perpendicular to a $<1\ 0\ 0>_f$ direction and all the strings are at 60 ° to one other. This combination of string directions, with the octahedral coordination environments of Nb/Ta atoms, allows the unit cell to remain cubic. Incommensurate variability in both the spacing and the continuity of the strings permits a wide compositional solid solution.

- Bi_2O_3-WO_3 type II (Section 4.7) appears to be a commensurate version of Bi_2O_3-Nb_2O_5 and Bi_2O_3-Ta_2O_5 type II, *i.e.* it has strings of W atoms along $[1\ 1\ 0]_f$, $[1\ 0\ 1]_f$ and $[0\ 1\ 1]_f$. W atoms have octahedral coordination environments, so the unit cell remains (approximately) cubic.

- Bi_2O_3-MoO_3 38:7 (Section 4.6) has strings of Mo atoms in a fluorite-type metal atom array, arranged along two of the six possible $<1\ 1\ 0>_f$ directions, $[1\ 1\ 0]_f$ and $[1\ \bar{1}\ 0]_f$, *i.e.* both string directions are perpendicular to $[0\ 0\ 1]_f$. Note that strings in alternate $<1\ 1\ 0>_f$ directions are never actually coplanar perpendicular to $[0\ 0\ 1]_f$. Strings are occasionally stepped along the $[1\ 0\ 1]_f$ and $[1\ 0\ \bar{1}\ ]_f$ directions. Mo atoms have octahedral coordination environments, and the unit cell is (pseudo-) tetragonal reflecting the uniqueness of $[1\ 0\ 0]_f$.

- Bi_2O_3-Nb_2O_5 type III (Section 4.3) has strings of Nb atoms in a fluorite-type metal atom array, arranged along two of the six possible $<1\ 1\ 0>_f$ directions, $[1\ 1\ 0]_f$ and $[1\ \bar{1}\ 0]_f$, *i.e.* both string directions are parallel to the $[0\ 0\ 1]_f$ plane. Note that strings in alternate $<1\ 1\ 0>_f$ directions are never actually coplanar perpendicular to $[0\ 0\ 1]_f$, although they are in occasional contact along the other $<1\ 1\ 0>_f$ directions. Half the strings are one-third incomplete. Nb atoms have octahedral coordination environments, and the unit cell is tetragonal reflecting the uniqueness of $[1\ 0\ 0]_f$.

- Bi_2O_3-MoO_3 26:10 (Section 4.11) can be interpreted as having short strings of Mo atoms in a fluorite-type metal atom array along only one $<1\ 1\ 0>_f$ direction. As discussed in Section 4.11, however, such an interpretation provides only a tenuous link to the other phases investigated in this study. The isolated tetrahedral coordination environments of Mo atoms cast further doubt on the validity of a string-type interpretation. The unit cell is monoclinic.

- Bi_2O_3-Ta_2O_5 type II* (Section 4.8) has strings of Ta atoms in an interface-modulated fluorite-type metal atom array, arranged along only one of the six possible $<1\ 1\ 0>_f$

directions within the fluorite-type slabs. The interface-modulation layers, perpendicular to $[1\ 1\ 1]_f$, allow two-thirds of these strings to link together, forming primitive hexagonal metal atom arrays, *i.e.* these units are not related to either fluorite-type or pyrochlore-type. They reduce the unit cell symmetry to (approximately) monoclinic. Ta atoms have octahedral coordination environments.

- Bi_2O_3-Ta_2O_5 type III (Section 4.9) is a close relative of the type II* phase, in which all the parallel pseudo-$<1\ 1\ 0>_f$ strings are paired. Unit cell symmetry is again monoclinic.

- The $n = 1$ Aurivillius phases Bi_2WO_6 and γ-Bi_2MoO_6 (11) can be thought of as having planes of W/Mo atoms in a fluorite-type metal atom array perpendicular to $[0\ 0\ 1]_f$. W/Mo atoms have octahedral coordination environments, therefore the planes can be thought of as $1 \times \infty \times \infty$ octahedra units of perovskite-type. The location of the planes perpendicular to $[1\ 0\ 0]_f$ allows the unit cell to retain (approximately) tetragonal symmetry.

- Bi_2O_3-Nb_2O_5 and Bi_2O_3-Ta_2O_5 type IV (Section 4.10) have planes of Nb/Ta atoms in a fluorite-type metal atom array, arranged perpendicular to $[0\ 0\ 1]_f$ to create units of perovskite-type as for the $n = 1$ Aurivillius phases. Half of these planes interact with parallel planes to create $2 \times \infty \times \infty$ octahedra units of perovskite-type as for $n = 2$ Aurivillius phases. This $n = 1, 2$ Aurivillius intergrowth is then stepped perpendicular to $[1\ 1\ 0]_f$ (Bi_2O_3-Nb_2O_5 type IV) or $[1\ 0\ 0]_f$ (Bi_2O_3-Ta_2O_5 type IV), lowering the unit cell symmetry to (approximately) monoclinic.

5.3 Scheme

The above summary demonstrates the presence of three general structural types (involving isolated *M* atoms, strings and planes thereof) encompassing all the phases investigated in the present study (with the exception of $Bi_{26}Mo_{10}O_{69}$). Phases can then more specifically be grouped into those containing isolated *M* atoms (Bi_2O_3-Ta_2O_5 type I; Bi_2O_3-MoO_3 type Ia; Bi_2O_3-WO_3 types Ia and Ib), $<1\ 1\ 0>_f$ strings of *M* atoms in three dimensions (Bi_2O_3-Nb_2O_5, -Ta_2O_5 and -WO_3 type II), $<1\ 1\ 0>_f$ strings of *M* atoms in two dimensions (Bi_2O_3-Nb_2O_5 type III; Bi_2O_3-MoO_3 38:7), $<1\ 1\ 0>_f$ strings of *M* atoms in one dimension (Bi_2O_3-Ta_2O_5 types II* and III) and $<1\ 1\ 1>_f$ planes of *M* atoms (Bi_2O_3-Nb_2O_5 and -Ta_2O_5 type IV; $n = 1$ Aurivillius).

Grouping phases according to these five categories and plotting them against composition (Figure 66) it can be seen that there is a sequence of types with increasing *M* presence in the metal atom array. Although the sequence is only truly valid within individual systems, and not all systems have a phase in each category, these variations are attributable to the different chemical characters of the *M* atoms *i.e.* different preferred coordination environments for individual or groups of *M* atoms depending on *M*. Attention can then be

focussed on understanding, rather than simply tabulating, the relationship between composition and structure type; *i.e.* the crystal-chemical relationship between these categories.

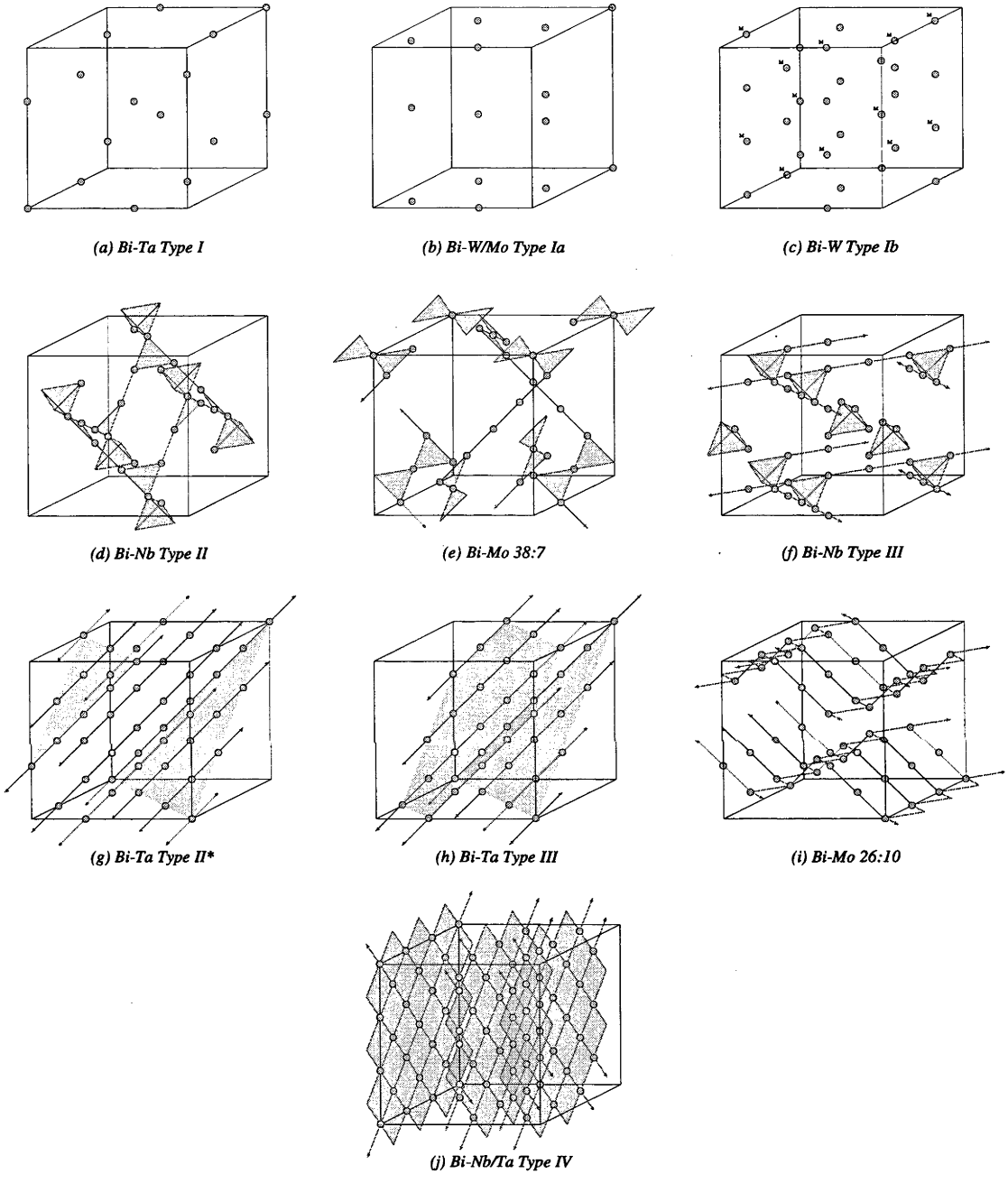

Figure 67. Simplified representations of the various structure types determined in Chapter 4, showing M atoms mapped onto 3 x 3 x 3 fluorite-type subcells and their nearest-neighbour connectivity as grey lines, triangles and tetrahedra. Shaded planes represent the boundaries of fluorite-type slabs in (g) and (h), and highlight planes of M atoms in (j). The figures are simplified versions of (a) Figure 37, (b) Figure 24, (c) Figure 42, (d) Figure 30, (e) Figure 47, (f) Figure 36, (g) Figure 54, (h) Figure 59, (i) Figure 65 and (j) Figure 64.

Figure 67 illustrates the observed patterns of *M* atom distribution within 3 x 3 x 3 fluorite-type subcell arrays, simplified with respect to the relevant Figures from Chapter 4 by the omission of Bi atoms and fluorite-type subcell grids. (Note that the *M* ordering schemes shown for some of these structures, particularly Figure 67*(a, c-f)*, represent the preferred

structural models but remain to be fully determined.) Isolated *M* atoms are seen in *(a-c)*, strings of *M* atoms in three dimensions are seen in *(d)*, strings of *M* atoms in two dimensions are seen in *(e-f)* and strings of *M* atoms in one dimension are seen in *(g-h)*.

5.3.1 Isolated M Atoms

Isolated *M* atoms are illustrated for the phases shown in Figure 67*(a-c)*. This is the simplest possible arrangement, and clearly can accommodate the lowest *M* atom densities of any of the five structure types being discussed. As the *M* atoms are isolated from one another within the flexible oxygen atom array of fluorite-type δ-Bi_2O_3, they can adopt either octahedral (Bi_2O_3-Ta_2O_5 type I; Bi_2O_3-WO_3 type Ib) or tetrahedral (Bi_2O_3-(W/Mo)O_3 and type Ia) coordination environments. Octahedral coordination is strongly favoured by Ta^{5+} ions, but Mo^{6+} and W^{6+} ions can accommodate either coordination. The adoption of tetrahedral coordination environments in type Ia allows the maximum number of disordered oxygen atom vacancies (25 % of fluorite-type sites for pure δ-Bi_2O_3) to be constrained (in ordered positions) about W/Mo atoms. An isolated, tetrahedrally coordinated *M* atom constrains four fluorite-type oxygen vacancies (Figure 68*(b)*). In the more WO_3-rich type Ib, however, a shortage of oxygen atom vacancies forces W atoms to adopt octahedral coordination environments.

Interestingly, further increasing the concentration of *M* atoms in the metal atom array rapidly reduces the number of available oxygen vacancies, such that this structure type becomes unstable well before the theoretical maximum density of isolated *M* atoms within a fluorite-type Bi atom array (25 %) is reached. *M* atoms begin to accumulate in $<1\ 1\ 0>_f$ strings in order to reduce crowding in the oxygen atom array; assuming octahedral coordination environments, an isolated *M* atom constrains two fluorite-type oxygen vacancies (Figure 68*(c)*), whereas an *M* atom in a $<1\ 1\ 0>_f$ string constrains only one (Figure 68*(d)*).

5.3.2 Strings of M Atoms in Three Dimensions

Figure 67*(d)* shows *M* atoms aligned in three $<1\ 1\ 0>_f$ strings at 60 ° to one another. The wide solid-solution ranges observed for this structure type in the Bi_2O_3-Nb_2O_5 and Bi_2O_3-Ta_2O_5 systems indicate that it is a particularly favourable configuration, due to the ability of the oxygen atom array to form strings of corner-connected MO_6 octahedra with only minor distortion from fluorite-type.

The maximum *M* atom density for this structure type is 50 %, corresponding to a hypothetical pyrochlore-type $Bi_2M_2O_7$. Note that no such phase exists for *M* = Nb, Ta, W or Mo, because charge balance would require M^{4+} ions; Nb^{5+}, Ta^{5+}, W^{6+} and Mo^{6+} cations require more O^{2-} anions than can fit into ideal pyrochlore-type. The fact that this structure type is far more stable in the Bi_2O_3-Nb_2O_5 and Bi_2O_3-Ta_2O_5 systems than the Bi_2O_3-WO_3 and

Bi_2O_3-MoO_3 systems can be explained in terms of M^{5+} ions causing less crowding in the oxygen atom array than M^{6+} ions. Similarly, charge-balance explains why this structure type ceases to be the most stable option well before reaching the hypothetical maximum M atom density of 50 %, *i.e.* pyrochlore-type $Bi_2M_2O_7$.

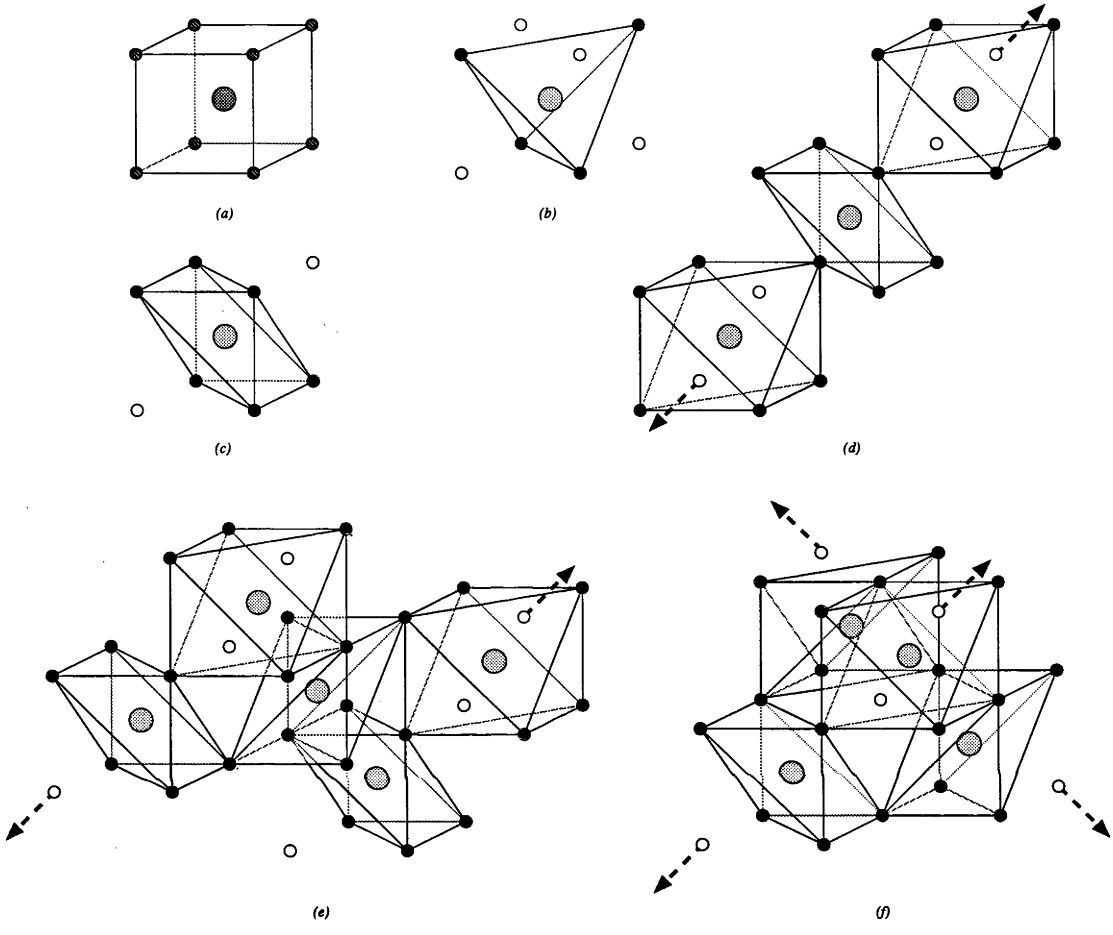

Figure 68. (a) The disordered fluorite-type oxygen atom array of δ-Bi_2O_3. This is compared to the fluorite-type oxygen vacancy ordering patterns which follow from isolated, tetrahedrally coordinated M atoms (b) and octahedrally coordinated M atoms when (c) isolated, (d) in <1 1 0>$_f$ strings, (e) in M_5 triangular clusters on stepped <1 1 0>$_f$ strings and (f) in tetrahedral clusters where perpendicular <1 1 0>$_f$ strings interact. Bi atoms are darker than M atoms, oxygen atoms are black, oxygen vacancies are white and 75 % occupied oxygen sites are striped. Dashed arrows indicate that the <1 1 0>$_f$ string continues, i.e. the oxygen vacancy is shared with an adjacent M atom. Oxygen atom displacements from fluorite-type are not shown.

5.3.3 Strings of M Atoms in Two Dimensions

The structures shown in Figure 67*(e-f)* contain M atoms aligned in two perpendicular <1 1 0>$_f$ strings, which can interact (as in type III Bi_3NbO_7) and may be stepped (as in $Bi_{38}Mo_7O_{78}$). As for the type II structures, this has the effect of reducing the M:Bi ratio in hypothetical $Bi_2M_2O_7$ pyrochlore to the point at which charge-balance considerations allow it to exist. In pyrochlore-type, all six <1 1 0>$_f$ strings of M atoms are present. In the type II phases (Figure 67*(d)*), the network of strings is expanded around an M atom, leaving a set of three strings at 60 ° to one another, each perpendicular to a different <1 0 0>$_f$ direction (*e.g.* [1 1 0]$_f$, [1 0 1]$_f$ and [0 1 1]$_f$). In the structures shown in Figure 67*(e-f)*, the network of strings

is expanded around the centre of an MO_4 tetrahedron, leaving a pair of strings at 90 ° to one another, perpendicular to the same $<1\ 0\ 0>_f$ direction. These general structure types are nonetheless closely related, the transition between Bi_2O_3-Nb_2O_5 types II and III being discussed in Section 4.3 in terms of their relationships on the level of space group symmetry and DPs.

The fact that this structure type (III) is more Nb-rich than type II in the Bi_2O_3-Nb_2O_5 system, and that it is observed in the Bi_2O_3-MoO_3 system whereas a type II phase is not, suggests that it is a more successful adaptation of pyrochlore-type in terms of overcoming charge-balance problems. This is due to the increased concentration of *M* atoms in Nb_4 tetrahedral clusters where perpendicular strings come into contact (type III Bi_3NbO_7) and the triangular pattern of Mo_5 clusters where the strings are stepped ($Bi_{38}Mo_7O_{78}$). With fewer independent string directions, there are more of these clusters for a given length of string. The former construction reduces oxygen crowding more effectively than strings (one fluorite-type oxygen vacancy constrained per *M* atom); each *M* atom in an M_4 tetrahedral cluster on a string (Figure 68*(f)*), is associated with $\frac{3}{4}$ fluorite-type oxygen vacancies. The driving force behind the formation of type III Bi_3NbO_7 is therefore charge balance. Each *M* atom in the latter construction, an M_5 triangular cluster on a string (Figure 68*(e)*), is associated with one fluorite-type oxygen vacancy. Consequently, the driving force behind the formation of $Bi_{38}Mo_7O_{78}$ is less clear, and may simply reflect an inherent stability in these clusters.

5.3.4 Strings of M Atoms in One Dimension

M atoms in the Bi_2O_3-Ta_2O_5 types II* and III structures shown in Figure 67*(g-h)* are aligned in strings along a single $<1\ 1\ 0>_f$ direction. In this sense, the structure type is a logical progression, and the structural relationship to the previous general types seems clear. The crystal chemical progression in terms of oxygen crowding also seems obvious; aligned in strings parallel and adjacent to other strings, each *M* atom constrains only $\frac{1}{2}$ fluorite-type oxygen vacancies. On closer examination of the structures, however, it emerges that these units are not in fact pairs of adjacent $<1\ 1\ 0>_f$ strings. In terms of a fluorite-type metal atom array, the strings are moved within contact distance *via* an interface modulation layer perpendicular to $<1\ 1\ 1>_f$. The fcc stacking sequence of hexagonal layers *–ABC–* is thereby stepped between layers, creating primitive hexagonal double-layers, and hence the overall sequences *–ABCABBCABCCABCA–* (type II* $Bi_7Ta_3O_{18}$) or *–ABCCABBCA–* (type III $Bi_7Ta_3O_{18}$).

This structure type therefore represents the abandonment of (fcc) pyrochlore-type structural motifs alone to accommodate *M* atoms into the fluorite-type metal atom array. This significant change in structure type is driven by charge balance, *i.e.* the shortage of oxygen vacancies in the pure fluorite-type array at these compositions.

5.3.5 Planes of M Atoms

Figure 67*(i-j)* show structure types that are clearly unrelated to pyrochlore-type despite the fact that they can be mapped onto fcc metal atom arrays. In Figure 67*(j)*, the $<1\ 0\ 0>_f$ planes of *M* atoms could be interpreted as an infinite series of adjacent parallel (or criss-crossing) $<1\ 1\ 0>_f$ strings, however, the fact that $<1\ 1\ 0>_f$ strings are never adjacent and never cross one another in pyrochlore-type (Figure 2) means that no useful analogy can be made. The planes highlighted in Figure 67*(j)* are in fact of perovskite-type, separated by Bi-only layers as in Aurivillius-type structures. The oxygen atom array accompanying this metal atom array no longer bears any relationship to fluorite-type. The driving force behind the adoption of this general structure-type at M_2O_x-rich compositions in all the systems studied (Bi_2O_3-$(Nb/Ta)_2O_5$ type IV and $Bi_2(W/Mo)O_6$ Aurivillius) is the insufficient vacancies available in a fluorite-type oxygen atom array for the accommodation of octahedrally coordinated *M* atoms, regardless of *M* atom configuration.

It is important to realise that this general structure type is not a progression from the previous one (Section 5.3.4), either structurally or crystal-chemically. The crystal-chemical scheme used to unify the structural types discussed so far breaks down at these M_2O_x-rich compositions, descriptions of which are therefore beyond the scope of the present study. None of the phases investigated in this study with greater than 25 % M_2O_x really fit this crystal-chemical scheme any better than the $Bi_{26}Mo_{10}O_{69}$ (Figure 67*(i)*), dismissed at the outset of this discussion.

5.4 Discussion

The general crystal-chemical scheme describing the phases investigated in this study can be summarised as follows. Starting with fluorite-type δ-Bi_2O_3, which has 25 % fluorite-type oxygen vacancies and highly flexible coordination environments for all metal atoms, 5+ and 6+ valent cations are substituted for Bi^{3+}. The number of available fluorite-type oxygen vacancies subsequently decreases, while at the same time, the need for these vacancies to satisfy the increasingly rigid coordination environments of *M* atoms increases. The interaction between these competing structural influences is the driving force behind the general structure type adopted. Up to approximately 25 % M_2O_x, it is possible to accommodate the *M* atoms and associated change in vacancy concentration with pyrochlore-type structural motifs while preserving the fcc metal atom array of fluorite-type. At more M_2O_x-rich compositions, however, pyrochlore-type motifs alone are no longer feasible and it is necessary to abandon the fluorite-type δ-Bi_2O_3-related average subcell in favour of a variety of different structural types.

The key observation arising from this is the fact that, although structural types are defined by compositional ordering in the fluorite-type metal atom array (Figure 67), the

driving force behind the adoption of one or another type at a given stoichiometry is the compositional (*i.e.* vacancy) ordering within the fluorite-type oxygen atom array (Figure 68).

The importance of satisfying the oxygen atom array also guides many of the models proposed by Zhou *et al.* (14-18, 21). These authors also use the transition from fluorite-type to pyrochlore-type as a means of preserving a fluorite-type δ-Bi_2O_3-related subcell in Bi_2O_3-rich phases, and abandon it at more M_2O_x-rich compositions (although, due to some misinterpreted DPs in the Bi_2O_3-Ta_2O_5 system (Section 3.4.1.2), they abandon it at slightly more M_2O_x-rich compositions). The important distinction between the approach of Zhou *et al.* and that of the present study is the concentration of the former on tetrahedral clusters of MO_6 octahedra, and of the latter on $<1\ 1\ 0>_f$ strings of MO_6 octahedra, as the key structural motif from pyrochlore-type. Although there is some crossover between these motifs, the different approaches have led to different structural models or solutions for all but the most Bi_2O_3-rich of the fluorite-type δ-Bi_2O_3-related phases (those with isolated M atoms).

In addition to the extensive structural evidence accumulated and discussed in Chapter 4, a further argument against the scheme of Zhou *et al.* is found in the driving forces behind transitions between structure types, as discussed above. Each M atom in an isolated M_4 tetrahedral cluster (Figure 68*(f)* without the arrows) constrains $\frac{5}{4}$ fluorite-type oxygen vacancies, more than an M atom in a $<1\ 1\ 0>_f$ string (which constrains only one). Isolated clusters such as this are therefore a less effective means of incorporating MO_6 octahedra into fluorite-type in the face of the competing charge-balance interaction. Each M_4 tetrahedral cluster would have to be connected to at least two others in order to achieve one fluorite-type oxygen vacancy per M atom.

Throughout this study the notation of Zhou *et al.* with regard to general structural types has been employed for the sake of clarity. From Figure 66, it can be seen that this notation is largely, but not entirely, in agreement with the results of the present study. Certainly the phases labelled type I/Ia/Ib and type II are grouped in agreement with the present study. Present results also agree that Bi_2O_3-Nb_2O_5 type III is a separate general type, and suggest that $Bi_{38}Mo_7O_{78}$ could reasonably be referred to as type III*. The labelling of Bi_2O_3-Ta_2O_5 types II* and III is, however, quite inappropriate. Given that type IV refers to a further, independent, general structure type, it might be more appropriate to refer to these phases ($Bi_7Ta_3O_{18}$ and $Bi_4Ta_2O_{11}$) as type V. However, since the phases in question have been demonstrated to have fully ordered structures largely independent of fluorite-type, it seems unlikely that they will henceforth be referred to in terms of an average fluorite-type parent structure.

Figure 66 indicates that despite the existence of parallel trends in each system, the individual chemical characters of the M cations play a significant role in determining the structure type adopted. Clearly the difference between the pairs W^{6+}/Mo^{6+} and Nb^{5+}/Ta^{5+} are

the greatest, therefore valence state is far more significant than atomic weight (*i.e.* cation size). This reflects the importance of charge balance in the crystal-chemistry of these phases, as discussed above. As expected, pyrochlore-type structural motifs can be incorporated into a fluorite-type average structure at much higher M^{5+} than M^{6+} concentrations. The role of cation size in determining structure type is more subtle, and cannot be explained in terms of the general crystal-chemistry of these systems.

An important test of the proposed crystal-chemical scheme is to relate it to the bismuth-rich regions of the phase diagrams of other Bi_2O_3-M_2O_x systems. Firstly, it is expected that the valence of *M* will play an important role. In particular, systems where the valence is 3+ or less will not be subject to the charge balance considerations which comprise one of the two competing interactions described in this study; such systems would therefore be expected to exhibit quite different behaviour, potentially preserving a fluorite-type δ-Bi_2O_3-related structure at much higher MO_x concentrations. This is borne out in, *e.g.*, the system Bi_2O_3-Y_2O_3, in which one fcc superstructure phase is reported to be stable from 25 ~ 43 mol% Y_2O_3 (72) and another from 47.5 - 49 mol% Y_2O_3 (73).

Bi_2O_3-M_2O_x systems where *M* has a 5+ or 6+ valence would be expected to exhibit similar behaviour to those investigated in the present study. Perhaps the most interesting case in point is the Bi_2O_3-V_2O_5 system, which was investigated in the early part of the present study (Sections 3.3.5 and 3.4.1.5) and extensively in other studies (22-24, 29, 30). The behaviour of the system, while not comprehensively documented due to problems controlling the valence of V, appears consistent with that of the other systems described in this study. Phases labelled types I and II(a-f) by Zhou (23, 24) clearly possess comparable modulations of fluorite-type δ-Bi_2O_3 (Table 2) in comparable compositional ranges.

If sufficient control could be achieved over the apparent reduction of V^{5+} (discussed in Section 3.3.5), it would be interesting to reinvestigate the bismuth-rich part of the Bi_2O_3-V_2O_5 system in the context of the crystal-chemical scheme proposed in this study. Models proposed by Zhou for the types II(a-f) phases are of particular interest, as they use the alternative crystal-chemical scheme based on tetrahedral clusters, rather than $<1\ 1\ 0>_f$ strings, of V atoms in a fluorite-type metal atom array. The reduction of V^{5+} would make the system even more interesting in terms of the proposed crystal-chemical importance of the valence of *M*. With mixed valence as an option, the valence states presumably would be stabilised by the structure, *i.e.* there would be an additional variable that would allow more complex metal atom arrangements, *e.g.* $Bi^{3+}/V^{5+}/V^{4+}$ ordering, potentially stabilising a fluorite-type δ-Bi_2O_3-related average structure at higher V_2O_5 concentrations.

Chapter 6

Conclusions

As discussed in the Introduction (Chapter 1), the goal of this study has been to achieve an understanding of the crystal-chemistry of fluorite-type δ-Bi_2O_3-related phases containing small amounts of certain transition metal oxides. By employing a range of experimental techniques (Chapter 2), the formidable challenges posed by the difficult chemistry (Chapter 3) and crystallography (Chapter 4) of these phases have now been met, and a general crystal-chemical scheme proposed and used to rationalise experimental observations (Chapter 5). At each stage, previous work on the studied systems has been variously reiterated, completed, corrected or contradicted. The result is a thorough, comprehensive investigation.

The pseudo-binary systems Bi_2O_3-Nb_2O_5, Bi_2O_3-Ta_2O_5, Bi_2O_3-WO_3 and Bi_2O_3-MoO_3 have been fully investigated in this way. The Bi_2O_3-V_2O_5 system has been only partially investigated due to the lack of appropriate experimental apparatus for dealing with the tendency of V^{5+} to reduce. Across the four major systems, thirteen distinct phases with unknown or highly tentative structures have been characterized by XRD and ED. Synchrotron XRD data were collected for all thirteen, neutron powder diffraction data for nine, and single-crystal synchrotron X-ray data for one. Despite the complexity of these phases, and the lack of single-crystal data, a large amount of structural information has been extracted from available data. This has been achieved through the use of various complementary experimental techniques, and through careful consideration of the relationships between well-characterized, partly-characterized and poorly-characterized phases. Consequently, the structures of all phases investigated have been determined as accurately and precisely as possible given available data.

Two central questions were posed in Chapter 1 concerning individual phases. Firstly, to what extent can the metal atom array of each phase be described as a modulated variant of fluorite-type δ-Bi_2O_3 average structure? Secondly, to what extent does the oxygen atom array deviate from fluorite-type δ-Bi_2O_3 in order to accommodate the preferred coordination environments of *M* atoms? The answers to these questions can be found in the detailed structural investigations of Chapter 4. The disparate nature of these phases is evident in the range of answers provided; metal atom arrays vary from disordered fluorite-type to ordered

non-fluorite-types, and the extent to which oxygen atom arrays follow metal atom ordering likewise varies enormously.

Answering these questions was critical to achieving the ultimate goal of this study; an understanding of the crystal-chemistry unifying the fundamental structural features of the phases investigated. At the same time, the answers can only really be understood in the context of a crystal-chemical scheme. The scheme proposed in Chapter 5 is based around the transformation of a fluorite-type structure *via* the incorporation of a pyrochlore-type structural motif of strings of *M* atoms along $<1\ 1\ 0>_f$ directions. The orientations of these strings and the way they interact is driven by the competing requirements of overall charge-balance (hence composition) and local coordination environment within a modulated fluorite-type oxygen atom array. These interactions link the oxygen atom array to the metal atom array, and both to composition. At very Bi_2O_3-rich compositions, where insufficient *M* atoms are available to form viable strings, the coordination environments of isolated *M* atoms are likewise determined by the interplay between charge balance and preferred coordination environment. At more M_2O_x-rich compositions, it is this interaction between composition, oxygen atom array and metal atom array which forces the eventual abandonment of this pyrochlore-type motif, and hence of any meaningful relationship to a fluorite-type δ-Bi_2O_3-related parent structure.

It is interesting to note that the reason such a wide variety of structure types are observed in these systems is the same reason for which these systems have come to the attention of researchers; the inherent flexibility of the coordination environment for Bi atoms in δ-Bi_2O_3. This flexibility is the source of the very high anionic conductivity observed in δ-Bi_2O_3 itself and in fluorite-type δ-Bi_2O_3-related phases, and it allows the more rigid coordination environments preferred by certain transition metals to be accommodated within the fluorite-type lattice. The results of the structure determinations in Chapter 4 (particularly the more complete solutions) provide further evidence that the bond valence requirement of Bi^{3+} is capable of being satisfied by 5-, 6-, 7- or 8-fold oxygen coordinations.

At the outset of this study, it was hoped that more structures could be determined from single-crystal X-ray data than was ultimately possible. Had this been the case, obtaining many of the structural models and solutions arrived at through careful consideration of crystal-chemical systematics (and tested against available data) might have been somewhat easier. While reducing the crystallographic challenges of the study, however, this may in fact have also reduced the likelihood of arriving at a general crystal-chemical scheme. The necessity to consider structural principles, and the relationships between phases, and to propose general schematic models rather than exact solutions, has led to a greater understanding of the crystal-chemistry than could easily have been achieved by examining a collection of ostensibly very different crystal structures.

Building on the research described in this study, further work will be necessary to confirm the proposed crystal-chemical scheme. To this end, more crystal structure information will be needed from the systems studied. This may be achieved by growing single crystals from phases that defied all attempts in the present study by using more exotic crystal growth techniques, *e.g.* fluxes, to allow very low temperature growth of crystals below possible displacive phase transitions and thereby obtain useable single domain crystals. The use of high pressure could also be explored. Where growth of single crystals continues to prove impossible, emerging *ab initio* structural modelling techniques using powder diffraction data may eventually be able to extend the achievements of the present study.

This study could also be extended in terms of the range of systems covered. Bi_2O_3-M_2O_x systems have been subject to a large number of investigations for a large range of M (and of x). As discussed in Section 5.4, now that a general crystal-chemical scheme has been proposed to describe the structural behavior of bismuth-rich phases when M = Nb, Ta, Mo and W, it is necessary to test the generality of this scheme against other, possibly analogous, systems. Preliminary investigations into the most obvious such system, Bi_2O_3-V_2O_5, indicated the need for more exotic synthetic techniques (beyond the scope of this study) to control the suspected reduction of V^{5+}. Many other systems, too numerous to cover in this study, are reported to possess bismuth-rich phases with underlying average fcc (*i.e.* fluorite-type) metal atom arrays. The ability or otherwise of the crystal-chemical scheme proposed in Chapter 5 to be adapted or extended to these systems, as the structures of relevant phases are more accurately determined, will be a crucial test of the usefulness of the conclusions of this study.

Appendix (53)

Atomic Modulation Functions, Periodic Nodal Surfaces and the Three-dimensional Incommensurately Modulated $(1 - x)Bi_2O_3.xNb_2O_5$ $(0.06 < x < 0.23)$ Solid Solution

Note: the work in this Appendix was carried out principally by Dr Ray L. Withers.

A.1 Fluorite-Related Average Structure and AMFs

The underlying average structure of the $(1 - x)Bi_2O_3.xNb_2O_5$ $(0.06 < x < 0.23)$ type II phase is of fluorite-type (26), space group symmetry $Fm3m$ ($\mathbf{a}_f$, $\mathbf{b}_f$, $\mathbf{c}_f$,). There are three average ions per primitive unit cell: a fully occupied metal atom M at (0 0 0) (average atomic scattering factor $f_M^{av} = (1 - x)f_{Bi} + xf_{Nb}$) and two partially occupied oxygen atoms, O1 at $(\frac{1}{4}\ \frac{1}{4}\ \frac{1}{4})$ and the inversion symmetry related O2 at $(-\frac{1}{4}\ -\frac{1}{4}\ -\frac{1}{4})$ respectively (average scattering factors $f_O^{av} = \frac{1}{4}(3 + 2x)f_O$).

The three-dimensional compositional and displacive AMFs describing the perturbations away from these average occupancies and positions depend upon $(\mathbf{r}_\mu + \mathbf{T})$, *i.e.* the position of the μth ion (μ = M, O1 or O2) in the Tth ($\mathbf{T} = u\mathbf{a}_f + v\mathbf{b}_f + w\mathbf{c}_f$; u, v, w integers) unit cell of the average structure (43, 57), and can be written as:

$$\delta f_\mu(\mathbf{r}_\mu + \mathbf{T}) = f_\mu^{av}\Sigma_{mnp}a_\mu(m\ n\ p)\cos\{2\pi(m\varepsilon\mathbf{a}^* + n\varepsilon\mathbf{b}^* + p\varepsilon\mathbf{c}^*).(\mathbf{r}_\mu + \mathbf{T}) + \theta_\mu(m\ n\ p)\} \quad ...(1)$$

and

$$\mathbf{u}_\mu(\mathbf{r}_\mu + \mathbf{T}) = \Sigma_{\alpha=a,b,c}\Sigma_{mnp}\alpha\varepsilon_{\mu\alpha}(m\ n\ p)\cos\{2\pi(m\varepsilon\mathbf{a}^* + n\varepsilon\mathbf{b}^* + p\varepsilon\mathbf{c}^*).(\mathbf{r}_\mu + \mathbf{T}) + \theta_{\mu\alpha}(m\ n\ p)\} \quad ...(2)$$

respectively, where m, n and p are integers and label the particular modulation wave harmonic. Note that $a_\mu(-m\ -n\ -p) = a_\mu(m\ n\ p)$, $\theta_\mu(-m\ -n\ -p) = -\theta_\mu(m\ n\ p)$, $\varepsilon_{\mu\alpha}(-m\ -n\ -p) = \varepsilon_{\mu\alpha}(m\ n\ p)$, $\theta_{\mu\alpha}(-m\ -n\ -p) = -\theta_{\mu\alpha}(m\ n\ p)$ *etc.* Determination of the above modulation wave amplitudes and phases essentially constitutes structure refinement.

In the language of superspace (44), the desired resultant fractional coordinates in real space, *i.e.* the x, y, z components of $(\mathbf{r}_\mu + \mathbf{T} + \mathbf{u}_\mu(\mathbf{r}_\mu + \mathbf{T}))$, are labelled x_1, x_2 and x_3 respectively. The corresponding reciprocal space fractional coordinates are given by $x_4 = \varepsilon\mathbf{a}^*.(\mathbf{r}_\mu + \mathbf{T} + \mathbf{u}_\mu(\mathbf{r}_\mu + \mathbf{T}))$, $x_5 = \varepsilon\mathbf{b}^*.(\mathbf{r}_\mu + \mathbf{T} + \mathbf{u}_\mu(\mathbf{r}_\mu + \mathbf{T}))$, $x_6 = \varepsilon\mathbf{c}^*.(\mathbf{r}_\mu + \mathbf{T} + \mathbf{u}_\mu(\mathbf{r}_\mu + \mathbf{T}))$ respectively. (Note that the compositional and displacive AMFs of Eqn. 1 and Eqn. 2 are direct functions of $\bar{x}_4 = \mathbf{q}_1.(\mathbf{r}_\mu + \mathbf{T}) \equiv t_1 = \varepsilon\mathbf{a}^*.(\mathbf{r}_\mu + \mathbf{T})$, $\bar{x}_5 = \mathbf{q}_2.(\mathbf{r}_\mu + \mathbf{T}) \equiv t_2 = \varepsilon\mathbf{b}^*.(\mathbf{r}_\mu + \mathbf{T})$ and $\bar{x}_6 = \mathbf{q}_3.(\mathbf{r}_\mu + \mathbf{T}) \equiv t_3 = \varepsilon\mathbf{c}^*.(\mathbf{r}_\mu + \mathbf{T})$ respectively. Superspace symmetry is expressed in terms of the effect of the particular symmetry operation upon the fractional co-ordinates $\{x_1, ..., x_6\}$ (44, 74).

A.2 Extinction Conditions and Superspace Symmetry

As discussed in Section 3.4.1.1, the $(1 - x)Bi_2O_3.xNb_2O_5$ ($0.06 < x < 0.23$) type II solid solution has superspace group symmetry $P{:}Fm\bar{3}m{:}Fd\bar{3}m$. The generating elements of this superspace group can be taken to be $\{x_1 + \frac{1}{2}, x_2 + \frac{1}{2}, x_3, x_4, x_5, x_6\}$, $\{x_1, x_2 + \frac{1}{2}, x_3 + \frac{1}{2}, x_4, x_5, x_6\}$,$\{x_1, x_2, x_3, x_4 + \frac{1}{2}, x_5 + \frac{1}{2}, x_6\}$ and $\{x_1, x_2, x_3, x_4, x_5 + \frac{1}{2}, x_6 + \frac{1}{2}\}$ for the lattice centring operations and $\{-x_1, x_2, x_3, -x_4 + 2\delta_1, x_5 + \frac{1}{4}, x_6 + \frac{1}{4}\}$, $\{x_1, x_2, -x_3, x_4 + \frac{1}{4}, x_5 + \frac{1}{4}, -x_6 + 2\delta_3\}$, $\{-x_1, -x_2, -x_3, -x_4 + 2\delta_1, -x_5 + 2\delta_2, -x_6 + 2\delta_3\}$, $\{x_2, x_1, x_3, x_5 + (\delta_1 - \delta_2), x_4 - (\delta_1 - \delta_2), x_6\}$ and $\{x_3, x_1, x_2, x_6 + (\delta_1 - \delta_3), x_4 + (\delta_2 - \delta_1), x_5 + (\delta_3 - \delta_2)\}$ for the rotational symmetry operations.

For a truly irrational ε, the global phase parameters δ_1, δ_2 and δ_3 defining the initial phases of the AMFs (see below) can be freely chosen. If ε 'locks in' to a rational value, however, δ_1, δ_2 and δ_3 become structurally significant in that they determine the conventional resultant three-dimensional space group symmetry (44, 57): *e.g.* $Fd3m$ with the inversion on a metal ion site for $\varepsilon = \frac{3}{8}$ and $\delta_1 = \delta_2 = \delta_3 = \frac{2n}{16}$; $Fd3m$ with the inversion between metal ion sites for $\varepsilon = \frac{3}{8}$ and $\delta_1 = \delta_2 = \delta_3 = \frac{2n+1}{16}$; $R3m$ for $\varepsilon = \frac{3}{8}$ and $\delta_1 = \delta_2 = \delta_3 \neq \frac{n}{16}$ (n an integer); $R\bar{3}m$ for $\varepsilon = \frac{4}{11}$ and $\delta_1 = \delta_2 = \delta_3 = \frac{n}{11}$; $R3m$ for $\varepsilon = \frac{4}{11}$ and $\delta_1 = \delta_2 = \delta_3 \neq \frac{n}{11}$ *etc.* The real test of incommensurability, however, is not whether ε apparently coincides with rational fractions such as $\frac{3}{8}$ or $\frac{4}{11}$ (15, 18), but rather whether or not all possible higher order harmonic satellite reflections can be observed *i.e.* is there 'overlap' or interaction between modulated intensities arising from independent subcell reflections (43).

There is most certainly no 'overlap' in the current case as only the first allowed satellite reflections of the form $\mathbf{G}_f \pm \varepsilon\langle 1\ 1\ 1\rangle^*$ can be observed over most of the composition range. Even at the highest Nb_2O_5 contents, where higher order harmonic satellite reflections become noticeable in DPs (Figure 6), only one or two higher order harmonic satellite reflections of the form $\mathbf{G}_f \pm \varepsilon\langle 2\ 2\ 0\rangle^*$ are ever observed in XRD data (Figure 14) (8, 48). Such structures are effectively incommensurate whatever the apparent value of ε, *i.e.* the parameters δ_1, δ_2 and δ_3 are not refineable.

A.3 Constraints on AMFs

The superspace group symmetry can now be used to constrain the form of the compositional and displacive AMFs given in Eqns. 1 and 2 above, *i.e.* to minimise the number of independent structural variables that need to be determined in any subsequent structure refinement. Consider, for example, the superspace centring operation $\{x_1, x_2, x_3, x_4 + \frac{1}{2}, x_5 + \frac{1}{2}, x_6\}$. The meaning in three-dimensional physical space of this symmetry operation (see, for example, Withers *et al.* (57)) is that for each atom μ in cell $\mathbf{T}$ there exists a symmetry related atom μ in cell $\mathbf{T}'$ such that

$$\delta f_\mu(\mathbf{r}_\mu + \mathbf{T}') = \delta f_\mu(\mathbf{r}_\mu + \mathbf{T})$$

and

$$\mathbf{u}_\mu(\mathbf{r}_\mu + \mathbf{T}') = \mathbf{u}_\mu(\mathbf{r}_\mu + \mathbf{T})$$

where

$$\varepsilon\mathbf{a}^*.(\mathbf{r}_\mu + \mathbf{T}') = \varepsilon\mathbf{a}^*.(\mathbf{r}_\mu + \mathbf{T}) + \tfrac{1}{2},$$

$$\varepsilon\mathbf{b}^*.(\mathbf{r}_\mu + \mathbf{T}') = \varepsilon\mathbf{b}^*.(\mathbf{r}_\mu + \mathbf{T}) + \tfrac{1}{2}$$

and

$$\varepsilon\mathbf{c}^*.(\mathbf{r}_\mu + \mathbf{T}') = \varepsilon\mathbf{c}^*.(\mathbf{r}_\mu + \mathbf{T}).$$

Substitution into Eqns. 1 and 2 above shows such relationships can only be satisfied if both $a_\mu(m\ n\ p)$ and $\varepsilon_{\mu\alpha}(m\ n\ p) = 0$ unless $m + n$ $(n + p, m + p)$ is even *i.e.* the first allowed, or 'primary', modulation waves have wave-vector $\mathbf{q}_i = \varepsilon\langle 1\ 1\ 1\rangle_f^*$. The fact that the only observed satellite reflections in XRD data over most of the composition range are of the form $\mathbf{G}_f \pm \varepsilon\langle 1\ 1\ 1\rangle^*$ suggests that the corresponding $\varepsilon\langle 1\ 1\ 1\rangle^*$ compositional and displacive modulation wave amplitudes are the major (if not the only) non-zero amplitudes. Similar considerations for the other type of superspace centring operation $\{x_1 + \frac{1}{2}, x_2 + \frac{1}{2}, x_3, x_4, x_5, x_6\}$ shows that **T** in Eqns. 1 and 2 above need not be limited to $u\mathbf{a}_f + v\mathbf{b}_f + w\mathbf{c}_f$ (u, v, w integers) but rather can be taken as representing all average structure Bravais lattice vectors including $\frac{1}{2}(\mathbf{a} + \mathbf{b})$ ($\frac{1}{2}(\mathbf{b} + \mathbf{c})$, $\frac{1}{2}(\mathbf{c} + \mathbf{a})$) *etc.*

Now consider rotational symmetry operations such as the superspace inversion operation $\{-x_1, -x_2, -x_3, -x_4 + 2\delta_1, -x_5 + 2\delta_2, -x_6 + 2\delta_3\}$. The meaning in real space of this superspace symmetry operation is that for each atom μ in cell **T** there exists a symmetry related atom μ' in cell **T'** such that

$$\delta f_{\mu'}(\mathbf{r}_\mu + \mathbf{T}') = \delta f_\mu(\mathbf{r}_\mu + \mathbf{T})$$

and

$$\mathbf{u}_{\mu'}(\mathbf{r}_\mu + \mathbf{T}') = i\mathbf{u}_\mu(\mathbf{r}_\mu + \mathbf{T})$$

where

$$\varepsilon\mathbf{a}^*.(\mathbf{r}_\mu + \mathbf{T}') = -\varepsilon\mathbf{a}^*.(\mathbf{r}_\mu + \mathbf{T}) + 2\delta_1,$$
$$\varepsilon\mathbf{b}^*.(\mathbf{r}_\mu + \mathbf{T}') = -\varepsilon\mathbf{b}^*.(\mathbf{r}_\mu + \mathbf{T}) + 2\delta_2$$

and

$$\varepsilon\mathbf{c}^*.(\mathbf{r}_\mu + \mathbf{T}') = -\varepsilon\mathbf{c}^*.(\mathbf{r}_\mu + \mathbf{T}) + 2\delta_3.$$

Substitution into Eqns. 1 and 2 shows that:

$$\theta_M(m\ n\ p) = -2\pi(m\delta_1 + n\delta_2 + p\delta_3);$$

$$\theta_{M\alpha}(m\ n\ p) = -90° - 2\pi(m\delta_1 + n\delta_2 + p\delta_3);$$
$$\theta_{O1}(m\ n\ p) = \theta_O(m\ n\ p) - 2\pi(m\delta_1 + n\delta_2 + p\delta_3);$$
$$\theta_{O2}(m\ n\ p) = -\theta_O(m\ n\ p) - 2\pi(m\delta_1 + n\delta_2 + p\delta_3);$$
$$\theta_{O1,\alpha}(m\ n\ p) = -90° + \theta_{O\alpha}(m\ n\ p) - 2\pi(m\delta_1 + n\delta_2 + p\delta_3); \text{ and}$$
$$\theta_{O2,\alpha}(m\ n\ p) = -90° - \theta_{O\alpha}(m\ n\ p) - 2\pi(m\delta_1 + n\delta_2 + p\delta_3).$$

Note the extra phase degree of freedom associated with the oxygen atom AMFs relative to the metal ion AMFs and the fact that compositional and displacive modulation waves associated with any particular modulation harmonic are always constrained to be 90° out of phase with respect to each other.

The original AMFs of Eqns. 1 and 2 above can thus be more generally written in the form

$$\delta f_\mu(t_1\ t_2\ t_3)/f_\mu^{av} = \Sigma_{mnp} a_\mu(m\ n\ p)\cos\{2\pi[m(t_1 - \delta_1) + n(t_2 - \delta_2) + p(t_3 - \delta_3)] + \varphi_\mu(m\ n\ p)\} =$$
$$\Sigma_{mnp}\mathrm{Re}\{A_\mu(m\ n\ p)\exp 2\pi i[m(t_1 - \delta_1) + n(t_2 - \delta_2) + p(t_3 - \delta_3)]\} \quad ...(3)$$

and

$$\mathbf{u}_\mu(t_1\ t_2\ t_3) = \Sigma_{\alpha=a,b,c}\Sigma_{mnp}\alpha\varepsilon_{\mu\alpha}(m\ n\ p)\sin\{2\pi[m(t_1 - \delta_1) + n(t_2 - \delta_2) + p(t_3 - \delta_3)] + \varphi_{\mu\alpha}(m\ n\ p)\} =$$
$$\Sigma_{mnp}\mathrm{Im}\{\mathbf{e}_\mu(m\ n\ p)\exp 2\pi i[m(t_1 - \delta_1) + n(t_2 - \delta_2) + p(t_3 - \delta_3)] \quad ...(4)$$

respectively. Note the requirement of time-reversal symmetry that $A_\mu(-m\ -n\ -p) = A_\mu(m\ n\ p)^*$ and $\mathbf{e}_\mu(-m\ -n\ -p) = -\mathbf{e}_\mu(m\ n\ p)^*$.

The additional constraints on these AMFs arising from each of the five rotational generating elements of the overall superspace group symmetry given earlier can be derived via the procedures outlined above. They are most succinctly written in terms of constraints on the complex compositional and displacement eigenvectors, $A_\mu(-m\ -n\ -p)$ and $\mathbf{e}_\mu(m\ n\ p)$, as follows:

$$A_M(m\ n\ p)^* = A_M(m\ n\ p),$$
$$A_{O2}(m\ n\ p)^* = A_{O1}(m\ n\ p) \equiv A_O(m\ n\ p),$$
$$\mathbf{e}_M(m\ n\ p)^* = -i\mathbf{e}_M(m\ n\ p),$$
$$\mathbf{e}_{O2}(m\ n\ p)^* = -i\mathbf{e}_{O1}(m\ n\ p) \equiv \mathbf{e}_O(m\ n\ p),$$
$$A_\mu(n\ m\ p) = A_\mu(m\ n\ p),$$
$$\mathbf{e}_\mu(n\ m\ p) = \mathrm{m}_{db}\mathbf{e}_\mu(m\ n\ p),$$
$$A_M(-m\ -n\ p)^* = (-1)^{(m+n)/2}A_M(m\ n\ p),$$
$$A_{O2}(-m\ -n\ p)^* = (-1)^{(m+n)/2}A_{O1}(m\ n\ p),$$
$$\mathbf{e}_M(-m\ -n\ p)^* = -(-1)^{(m+n)/2}m_z\,\mathbf{e}_M(m\ n\ p),$$
$$\mathbf{e}_{O2}(-m\ -n\ p)^* = -(-1)^{(m+n)/2}m_z\,\mathbf{e}_{O1}(m\ n\ p),$$
$$A_M(m\ -n\ -p)^* = (-1)^{(n+p)/2}A_M(m\ n\ p),$$
$$A_{O2}(m\ -n\ -p)^* = (-1)^{(n+p)/2}A_{O1}(m\ n\ p),$$

$$\mathbf{e}_M(m\ -n\ -p)^* = -(-1)^{(n+p)/2} m_x\, \mathbf{e}_M(m\ n\ p),$$
$$\mathbf{e}_{O2}(m\ -n\ -p)^* = -(-1)^{(n+p)/2} m_x\, \mathbf{e}_{O1}(m\ n\ p)$$

and

$$A_\mu(pmn) = A_\mu(m\ n\ p),$$
$$\mathbf{e}_\mu(pmn) = C_{31} + \mathbf{e}_\mu(m\ n\ p) \quad \ldots(5)$$

Application of these constraints in conjunction with Eqns. 3 and 4 then gives the final form of the symmetry constrained AMFs as follows:

$$\begin{aligned}\delta f_\mu(t_1\ t_2\ t_3)/f_\mu^{av} = a_\mu(1\ 1\ 1)\{&\cos(2\pi[+(t_1-\delta_1)+(t_2-\delta_2)+(t_3-\delta_3)]+\varphi_\mu(1\ 1\ 1))\\ &-\cos(2\pi[-(t_1-\delta_1)-(t_2-\delta_2)+(t_3-\delta_3)]+\varphi_\mu(1\ 1\ 1))\\ &-\cos(2\pi[-(t_1-\delta_1)+(t_2-\delta_2)-(t_3-\delta_3)]+\varphi_\mu(1\ 1\ 1))\\ &-\cos(2\pi[+(t_1-\delta_1)-(t_2-\delta_2)-(t_3-\delta_3)]+\varphi_\mu(1\ 1\ 1))\}\end{aligned}$$

$$\begin{aligned}+a_\mu(2\ 2\ 0)\{&\cos(2\pi[+2(t_1-\delta_1)+2(t_2-\delta_2)+0(t_3-\delta_3)]+\varphi_\mu(2\ 2\ 0))\\ &+\cos(2\pi[+0(t_1-\delta_1)+2(t_2-\delta_2)+2(t_3-\delta_3)]+\varphi_\mu(2\ 2\ 0))\\ &+\cos(2\pi[+2(t_1-\delta_1)+0(t_2-\delta_2)+2(t_3-\delta_3)]+\varphi_\mu(2\ 2\ 0))\\ &-\cos(2\pi[-2(t_1-\delta_1)+2(t_2-\delta_2)+0(t_3-\delta_3)]+\varphi_\mu(2\ 2\ 0))\\ &-\cos(2\pi[+0(t_1-\delta_1)-2(t_2-\delta_2)+2(t_3-\delta_3)]+\varphi_\mu(2\ 2\ 0))\\ &-\cos(2\pi[+2(t_1-\delta_1)+0(t_2-\delta_2)-2(t_3-\delta_3)]+\varphi_\mu(2\ 2\ 0))\}\end{aligned}$$

$$+ \ldots \text{higher order harmonic terms} \ldots(6)$$

for the compositional AMFs (where $\varphi_M(m\ n\ p) = 0°$ and $\varphi_{O2}(m\ n\ p) = -\varphi_{O1}(m\ n\ p) = -\varphi_O(m\ n\ p)$) and

$$\begin{aligned}\mathbf{u}_\mu(t_1\ t_2\ t_3) = \varepsilon_\mu(1\ 1\ 1)\{&(\mathbf{a}+\mathbf{b}+\mathbf{c})\sin(2\pi[+(t_1-\delta_1)+(t_2-\delta_2)+(t_3-\delta_3)]+\varphi_\mu(1\ 1\ 1))\\ &-(-\mathbf{a}-\mathbf{b}+\mathbf{c})\sin(2\pi[-(t_1-\delta_1)-(t_2-\delta_2)+(t_3-\delta_3)]+\varphi_\mu(1\ 1\ 1))\\ &-(-\mathbf{a}+\mathbf{b}-\mathbf{c})\sin(2\pi[-(t_1-\delta_1)+(t_2-\delta_2)-(t_3-\delta_3)]+\varphi_\mu(1\ 1\ 1))\\ &-(\mathbf{a}-\mathbf{b}-\mathbf{c})\sin(2\pi[+(t_1-\delta_1)-(t_2-\delta_2)-(t_3-\delta_3)]+\varphi_\mu(1\ 1\ 1))\}\end{aligned}$$

$$\begin{aligned}+\varepsilon_\mu(2\ 2\ 0)\{&(2\mathbf{a}+2\mathbf{b}+0\mathbf{c})\sin(2\pi[+2(t_1-\delta_1)+2(t_2-\delta_2)+0(t_3-\delta_3)]+\varphi_\mu(2\ 2\ 0))\\ &+(0\mathbf{a}+2\mathbf{b}+2\mathbf{c})\sin(2\pi[+0(t_1-\delta_1)+2(t_2-\delta_2)+2(t_3-\delta_3)]+\varphi_\mu(2\ 2\ 0))\\ &+(2\mathbf{a}+0\mathbf{b}+2\mathbf{c})\sin(2\pi[+2(t_1-\delta_1)+0(t_2-\delta_2)+2(t_3-\delta_3)]+\varphi_\mu(2\ 2\ 0))\\ &-(-2\mathbf{a}+2\mathbf{b}+0\mathbf{c})\sin(2\pi[-2(t_1-\delta_1)+2(t_2-\delta_2)+0(t_3-\delta_3)]+\varphi_\mu(2\ 2\ 0))\\ &-(0\mathbf{a}-2\mathbf{b}+2\mathbf{c})\sin(2\pi[+0(t_1-\delta_1)-2(t_2-\delta_2)+2(t_3-\delta_3)]+\varphi_\mu(2\ 2\ 0))\\ &-(2\mathbf{a}+0\mathbf{b}-2\mathbf{c})\sin(2\pi[+2(t_1-\delta_1)+0(t_2-\delta_2)-2(t_3-\delta_3)]+\varphi_\mu(2\ 2\ 0))\}\end{aligned}$$

$$+ \ldots \text{higher order harmonic terms} \ldots(7)$$

for the displacive AMFs (where $\varphi_M(m\ n\ p) = 0°$ and $\varphi_{O2}(m\ n\ p) = -\varphi_{O1}(m\ n\ p) = -\varphi_O(m\ n\ p)$).

Keep in mind that the reciprocal space average fractional coordinates $\bar{x}_4 \equiv t_1 = \mathbf{q}_1.(\mathbf{r}_\mu + \mathbf{T}) = \varepsilon\mathbf{a}^*.(\mathbf{r}_\mu + \mathbf{T})$, $\bar{x}_5 \equiv t_2 = \mathbf{q}_2.(\mathbf{r}_\mu + \mathbf{T}) = \varepsilon\mathbf{b}^*.(\mathbf{r}_\mu + \mathbf{T})$ and $\bar{x}_6 \equiv t_3 = \mathbf{q}_3.(\mathbf{r}_\mu + \mathbf{T}) = \varepsilon\mathbf{c}^*.(\mathbf{r}_\mu + \mathbf{T})$ in Eqns. 3-7 above are really simply labels specifying which particular primitive average structure unit cell is being referred to (43, 57) while the parameters δ_1, δ_2 and δ_3 simply represent the initial phases of the 'primary' ($\mathbf{q}_1 = \varepsilon\mathbf{a}^*$, $\mathbf{q}_2 = \varepsilon\mathbf{b}^*$, and $\mathbf{q}_3 = \varepsilon\mathbf{c}^*$) modulation waves. (In the language of superspace (44), the parameters δ_1, δ_2 and δ_3 define a real space section of six-dimensional hyper-space). Note that there is only one degree of freedom (an amplitude) associated with each of the ε<1 1 1>* and ε<2 2 0>* modulation waves for the metal atom site AMFs whereas there are two compositional degrees of freedom (an amplitude and a phase) associated with each of the ε<1 1 1>* and ε<2 2 0>* modulation waves for the oxygen atom AMFs.

Eqns. 3-7 can in fact be simplified on the basis of experimental observations. Consider, for example, the metal atom compositional AMF describing Bi/Nb metal atom ordering defined in Eqn. 3. Given the virtual complete absence of satellite reflections other than those of $\mathbf{G}_f \pm \varepsilon$<1 1 1>* type in XRD patterns (see Figure 6 of Miida and Tanaka (48) and Figure 14) over most of the solid solution range, it must clearly be an extremely good approximation to put all metal atom compositional modulation wave amplitudes other than a_M(1 1 1) to zero in Eqn. 6.

Consequently surfaces parallel to each other in hyper-space (*i.e.* in t_1, t_2, t_3 space) (Figure 25), on each of which the metal atom composition (analogous to height in topographic contour plots) is constant, are defined by equations of the form

$$\begin{aligned}
&\cos(2\pi[+ (t_1 - \delta_1) + (t_2 - \delta_2) + (t_3 - \delta_3)]) \\
&- \cos(2\pi[- (t_1 - \delta_1) - (t_2 - \delta_2) + (t_3 - \delta_3)]) \\
&- \cos(2\pi[- (t_1 - \delta_1) + (t_2 - \delta_2) - (t_3 - \delta_3)]) \\
&- \cos(2\pi[+ (t_1 - \delta_1) - (t_2 - \delta_2) - (t_3 - \delta_3)])
\end{aligned}$$

$$\begin{aligned}
&= 2\{\cos(2\pi[+ (t_1 - \delta_1) - (t_2 - \delta_2)])\cos(2\pi[+ (t_3 - \delta_3)]) \\
&+ \sin(2\pi[+ (t_1 - \delta_1) + (t_2 - \delta_2)])\sin(2\pi[+ (t_3 - \delta_3)])\} \\
&= \text{constant} \quad \ldots(8).
\end{aligned}$$

Consider also the oxygen atom compositional AMF (defined in Eqn. 6) describing oxygen vacancy ordering and how it might correlate with the metal atom ordering discussed above. The fact that the atomic scattering factor difference between Bi and Nb for X-rays, $(f_{Bi} - f_{Nb})$, is ~ 5.2 times the atomic scattering factor difference between an oxygen atom and a vacancy, *i.e.* f_O , (at $\theta = 0°$) ensures that metal atom ordering and associated structural relaxation makes the dominant contribution to the incommensurate satellite reflections in XRD. In neutron powder diffraction, however, the reverse is the case (as a result of the fact that $b_O \sim 4(b_{Bi} - b_{Nb})$, b a neutron scattering length). Figure 28 shows a neutron powder

diffraction profile (from $d = 2.5$ Å to 9.0 Å) of an $x = 0.18$ specimen collected at the 145 ° detector bank of POLARIS. As for XRD, $\mathbf{G}_f \pm \varepsilon\langle 1\ 1\ 1\rangle^*$ type satellite reflections dominate the neutron powder diffraction profile. It must therefore again be a good approximation to put all (oxygen atom) compositional modulation wave amplitudes other than those associated with the $\varepsilon\langle 1\ 1\ 1\rangle_f^*$ modulation waves (*i.e.* $a_O(1\ 1\ 1)$) to zero in Eqn. 6.

Consequently surfaces parallel to each other in hyper-space, on each of which the oxygen atom composition is constant, are this time defined by equations of the form

$$\begin{aligned}
&\cos(2\pi[+ (t_1 - \delta_1) + (t_2 - \delta_2) + (t_3 - \delta_3)] \pm \varphi_O(1\ 1\ 1)) \\
&- \cos(2\pi[- (t_1 - \delta_1) - (t_2 - \delta_2) + (t_3 - \delta_3)] \pm \varphi_O(1\ 1\ 1)) \\
&- \cos(2\pi[- (t_1 - \delta_1) + (t_2 - \delta_2) - (t_3 - \delta_3)] \pm \varphi_O(1\ 1\ 1)) \\
&- \cos(2\pi[+ (t_1 - \delta_1) - (t_2 - \delta_2) - (t_3 - \delta_3)] \pm \varphi_O(1\ 1\ 1)) \\
&= \text{constant} \quad \ldots(9).
\end{aligned}$$

References

1. T. Takahashi, H. Iwahara, *Mater. Res. Bull.* **13**, 1447-1453 (1978).
2. A. W. Sleight, *Science* **208**, 895-900 (1980).
3. G. Gattow, H. Schröder, *Z. Anorg. Allg. Chem.* **318**, 176-189 (1962).
4. H. A. Harwig, *Z. Anorg. Allg. Chem.* **444**, 151-166 (1978).
5. P. D. Battle, C. R. A. Catlow, J. Drennan, A. D. Murray, *J. Phys. C: Solid State Phys.* **16**, L561-L566 (1983).
6. S. Hull, R. I. Smith, W. I. F. David, A. C. Hannon, J. Mayers, R. Cywinski, *Physics* **B180&181**, 1000-1002 (1992).
7. R. M. Ibberson, W. I. F. David, K. S. Knight, "The High Resolution Diffractometer (HRPD) at ISIS - a User Guide." *RAL-92-031* (Rutherford Appleton Laboratory Report, 1992).
8. C. D. Ling, R. L. Withers, S. Schmid, J. G. Thompson, *J. Solid State Chem.* **137**, 42-61 (1998).
9. G. Gattow, H. Fricke, *Z. Anorg. Allg. Chem.* **324**, 287-296 (1962).
10. A. C. Skapski, D. Rogers, *J. Chem. Soc. Chem. Commun.*, 611-613 (1965).
11. J. G. Thompson, S. Schmid, R. L. Withers, A. D. Rae, J. D. Fitzgerald, *J. Solid State Chem.* **101**, 309-321 (1992).
12. M. Touboul, J. Lokaj, L. Tessier, V. Kettman, V. Vrabel, *Acta Cryst.* **C48**, 1176-1179 (1992).
13. D. J. Buttrey, D. A. Jefferson, J. M. Thomas, *Mater. Res. Bull.* **21**, 739-744 (1986).
14. W. Zhou, *J. Solid State Chem.* **108**, 381-394 (1994).
15. W. Zhou, D. A. Jefferson, J. M. Thomas, *Proc. Roy. Soc. London Ser.* **A406**, 173-182 (1986).
16. W. Zhou, D. A. Jefferson, J. M. Thomas, *J. Solid State Chem.* **70**, 129-136 (1987).
17. W. Zhou, D. A. Jefferson, M. Alario-Franco, J. M. Thomas, *J. Phys. Chem.* **91**, 512-514 (1987).
18. D. Tang, W. Zhou, *J. Solid State Chem.* **119**, 311-318 (1995).
19. W. Zhou, D. A. Jefferson, J. M. Thomas, *Geophys. Monogr.* **43**, 113-117 (1989).
20. J. Gopalakrishnan, A. Ramanan, C. N. R. Rao, D. A. Jefferson, D. J. Smith, *J. Solid State Chem.* **55**, 101-105 (1984).
21. W. Zhou, *J. Solid State Chem.* **101**, 1-17 (1992).
22. G. Pang, S. Feng, Y. Tang, C. Tan, R. Xu, *Chem. Mater.* **10**, 2446-2449 (1998).
23. W. Zhou, *J. Solid State Chem.* **87**, 44-54 (1990).
24. W. Zhou, *J. Solid State Chem.* **76**, 290-300 (1988).
25. O. Savborg, M. Lundberg, *J. Solid State Chem.* **57**, 135-142 (1985).
26. E. Aguardo, R. Enjalbert, J. M. Rojo, A. Castro, *Bol. Soc. Esp. Cerám. Vidrio* **34**, 417-420 (1995).
27. A. Watanabe, N. Ishizawa, M. Kato, *J. Solid State Chem.* **60**, 252-257 (1985).
28. R. N. Vannier, G. Mairesse, F. Abraham, G. Nowogrocki, *J. Solid State Chem.* **122**, 394-406 (1996).
29. S. Kashida, T. Hori, *J. Solid State Chem.* **122**, 358-363 (1995).
30. V. F. Katkov, I. V. Pruzhko, A. K. Kushnereva, *Inorganic Materials* **33**, 481-482 (1997).
31. E. M. Levin, R. S. Roth, *J. Research Natl. Bur. Standards* **68**A, 202 (1964).

32. R. S. Roth, J. Waring, *J. Research Natl. Bur. Standards* **66**A, 461 (1962).

33. M. Egashira, K. Matsuo, S. Kagawa, T. Seiyama, *J. Catal.* **58**, 409-418 (1979).

34. A. C. Larson, R. B. V. Dreele, *GSAS. The General Structure Analysis System* (Los Alamos National Laboratory, 1991).

35. E. M. Levin, R. S. Roth, *J. Research Natl. Bur. Standards* **68**A, 197-206 (1964).

36. E. T. Keve, A. C. Skapski, *J. Solid State Chem.* **8**, 159-165 (1973).

37. E. I. Speranskaya, *Neorg. Mater. (Russ.)* **6**, 138-140 (1970).

38. M. Huvé, R.-N. Vannier, G. Nowogrocki, G. Mairesse, G. V. Tendeloo, *J. Mater. Chem.* **6**, 1339-1345 (1996).

39. R. N. Vannier, G. Mairesse, F. Abraham, G. Nowogrocki, *J. Solid State Chem.* **103**, 441-446 (1993).

40. T. V. Panchenko, V. F. Katrov, V. K. Kostyuk, N. A. Truseeva, A. V. Schmal'ko, *Ukr. Fiz. Zh. (Russ. Ed.)* **28**, 1091-1093 (1983).

41. N. P. Smolyaninov, I. N. Belyaev, *Russ. J. Inorg. Chem.* **8**, 632-636 (1963).

42. A. A. Bush, V. G. Koshelayeva, Y. N. Venevtesv, *Jap. J. Appl. Phys.* **24**[Suppl. 24-2], 625-627 (1985).

43. J. M. Pérez-Mato, G. Madariaga, F. J. Zuñiga, A. G. Arribas, *Acta Cryst.* A**43**, 216-226 (1987).

44. S. Van Smaalen, *Cryst. Rev.* **4**, 79-202 (1995).

45. T. Jannsen, A. Janner, A. Looijenga-Vos, P. M. DeWolff, in *International Tables for Crystallography* A. J. C. Wilson, Ed. (Kluwer Academic Publishers, Dordrecht, 1992), vol. C, pp. 797.

46. R. L. Withers, Y. C. Feng, G. H. Lu, *J. Phys.: Condens. Matter* **2**, 3187-3200 (1990).

47. A. Yamamoto, *Acta Cryst.* B**38**, 1451-1456 (1982).

48. R. Miida, M. Tanaka, *Jpn. J. Appl. Phys.* **29**, 1132-1138 (1990).

49. R. L. Withers, J. G. Thompson, P. J. Barlow, J. C. Barry, *Aust. J. Chem.* **45**, 1375-1392 (1992).

50. A. Pring, T. Williams, R. L. Withers, *Amer. Miner.* **78**, 619-626 (1993).

51. C. D. Ling, R. L. Withers, J. G. Thompson, S. Schmid, *Acta Cryst.* B**55** (In press).

52. N. E. Brese, M. O'Keeffe, *Acta Cryst.* B**47**, 192-197 (1991).

53. R. L. Withers, C. D. Ling, S. Schmid, *Z. Krist.* **214** (In press).

54. H. G. von Schnering, R. Nesper, *Z. Phys.* B**83**, 407-412 (1991).

55. S. Andersson, S. T. Hyde, H. G. von Schnering, *Z. Krist.* **168**, 1-17 (1984).

56. L. Elcoro, J. M. Pérez-Mato, Structure of the Decagonal Quasicrystal AlNiCo, G. Chapuis, W. Paciorek, Eds., Aperiodic '94 (World Scientific, 1995).

57. R. L. Withers, S. Schmid, J. G. Thompson, *Prog. in Solid State Chem.* **26**, 1-96 (1998).

58. V. K. Trunov, V. A. Efremov, Y. A. Velikopodnyi, I. M. Averina, *Sov. Phys. Crystallogr.* **26**, 35-37 (1981).

59. C. D. Ling, S. Schmid, R. L. Withers, J. G. Thompson, N. Ishizawa, S. Kishimoto, *Acta Cryst.* B**55** (In press).

60. W. H. Zachariasen, *Acta. Cryst.* A**24**, 212-216 (1968).

61. S. R. Hall, H. D. Flack, J. M. Stewart, *Xtal3.2 Reference Manual* (Universities of Western Australia, Australia, Geneva, Switzerland and Maryland, USA, 1992).

62. B. G. Hyde, S. Andersson, *Inorganic Crystal Structures.* (Wiley, New York, 1989) pp. 257-271.

63. C. D. Ling, J. G. Thompson, R. L. Withers, S. Schmid, *J. Solid State Chem.* **142**, 33-40 (1999).

64. B. Aurivillius, *Arkiv. Kemi.* **2**, 519-527 (1950).

65. R. L. Withers, J. G. Thompson, A. D. Rae, *J. Solid State Chem.* **94**, 404-417 (1991).

66. R. Enjalbert, G. Hasselmann, J. Galy, *J. Solid State Chem.* **131**, 236-245 (1997).

67. R. N. Vannier, F. Abraham, G. Nowogrocki, G. Mairesse, *J. Solid State Chem.* **142**, 294-304 (1999).

68. D. J. Buttrey, T. Vogt, G. P. A. Yap, A. L. Rheingold, *Mater. Res. Bull.* **32**, 947-963 (1997).

69. F. Theobald, A. Laarif, A. W. Hewat, *Ferroelectrics* **56**, 219-237 (1984).

70. R. G. Teller, J. F. Brazdil, R. K. Grasselli, *Acta Cryst.* C**40**, 2001-2005 (1984).

71. A. F. Van den Elzen, G. D. Rieck, *Acta Cryst.* B**29**, 2463-2438 (1973).

72. T. Takahashi, H. Iwahara, T. Arao, *J. Appl. Electrochem.* **5**, 187-195 (1975).

73. A. Watanabe, *J. Solid State Chem.* **124**, 287-291 (1996).

74. A. Yamamoto, *Acta Cryst.* A**52**, 509-560 (1996).

75. L. Berg, G. Czack, V. Haase, H. Hein, H. Katscher, G. Kirchstein, H. K. Kugler, S. Ruprecht, Ed.s *Gmelin Handbuch der Anorganischen Chemie* (Springer-Verlag, Berlin, 1979), vol. W Erg. – Bd B 2, §3.2.11 pp. 74.

76. I. D. Brown, D. Altermatt, *Acta Cryst.* B**41**, 244-247 (1985).

77. I. D. Brown, *EUTAX v1.3*. (Department of Chemistry, Arizona State University, Tempe, Arizona, U.S.A., 1973).

78. B. G. Hyde, S. Andersson, *Inorganic Crystal Structures*. (Wiley, New York, 1989) pp. 344-349.